Energy-consistent formulations of the one-dimensional two-fluid model

Buist, J.F.H.

DOI
10.4233/uuid:1db9efbc-9494-4c5e-af78-08bc9ea84537

Publication date
2024

Document Version
Final published version

Citation (APA)
Buist, J. F. H. (2024). *Energy-consistent formulations of the one-dimensional two-fluid model*. [Dissertation (TU Delft), Delft University of Technology]. https://doi.org/10.4233/uuid:1db9efbc-9494-4c5e-af78-08bc9ea84537

Important note
To cite this publication, please use the final published version (if applicable).
Please check the document version above.

Energy-consistent formulations of the one-dimensional two-fluid model

Energy-consistent formulations of the one-dimensional two-fluid model

Proefschrift

ter verkrijging van de graad van doctor
aan de Technische Universiteit Delft,
op gezag van de Rector Magnificus prof. dr. ir. T. H. J. J. van der Hagen,
voorzitter van het College voor Promoties,
in het openbaar te verdedigen op
dinsdag 3 september 2024 om 15.00 uur

door

Jurriaan Frederick Hubert BUIST

Ingenieur in de Technische Natuurkunde,
Technische Universiteit Eindhoven,
geboren te Boxmeer

Dit proefschrift is goedgekeurd door de promotoren.

Samenstelling promotiecommissie bestaat uit:

Rector Magnificus	voorzitter
Prof. dr. ir. R. A. W. M. Henkes	Technische Universiteit Delft, promotor
Prof. dr. ir. C. W. Oosterlee	Universiteit Utrecht, promotor
Dr. ir. B. Sanderse	Centrum Wiskunde & Informatica, copromotor
Onafhankelijke leden:	
Prof. dr. ir. B. J. Boersma	Technische Universiteit Delft
Prof. dr. ir. B. Koren	Technische Universiteit Eindhoven
Prof. dr. ir. R. W. C. P. Verstappen	Rijksuniversiteit Groningen
Dr. S. T. Munkejord	SINTEF Energy Research, Noorwegen
Prof. dr. R. Pecnik	Technische Universiteit Delft, reservelid

Dr. S. B. Dubinkina (VU Amsterdam) heeft als begeleider in belangrijke mate aan de totstandkoming van het proefschrift bijgedragen.

This work is part of the Industrial Partnership Program (IPP) "Computational Science for Energy Research" (CSER) of the Dutch Research Council (NWO), with project number 15CSER017. The research work was carried out at Centrum Wiskunde & Informatica (CWI), the Dutch national institute for mathematics and computer science.

Style:	TU Delft House Style, with modifications by Moritz Beller
Printed by:	Gildeprint
Cover:	Graphs of growth rate versus wavelength for small perturbations to a steady state of the two-fluid model, when including different stabilizing effects.

ISBN 978-94-6496-155-3

An electronic version of this dissertation is available at
`http://repository.tudelft.nl/`.

It is important to realize that in physics today, we have no knowledge what energy is *... However, there are formulas for calculating some numerical quantity, and when we add it all together it gives ... always the same number.*

Richard Feynman, Lectures on Physics

Contents

Summary

Two-phase pipe flows are found in diverse industrial applications, such as cooling systems in nuclear reactors, processes in chemical plants, the production of oil and gas, and the transport of carbon dioxide which is captured to prevent its emission into the atmosphere. In many cases, the pipelines are too long to be analyzed using a full three-dimensional computational model, which would come with high computational cost. Therefore, the three-dimensional flow equations are averaged, yielding a one-dimensional model which only describes variations along the direction of flow. However, the simplification of three-dimensional reality to a one-dimensional model requires making assumptions, which can result in nonphysical behavior. Similarly, the process of discretizing the equations can yield a computational model with different properties than the continuous model. This thesis focuses on retaining energy conservation properties in both continuous and discrete versions of the one-dimensional model, yielding improved physical fidelity and nonlinear stability.

To provide insight into the model assumptions, the one-dimensional two-fluid model for stratified incompressible flow is derived from first principles. Integral mass and momentum balances are set up for the two fluids (phases) separately, with the two-fluid interface forming the boundary between the two control volumes, which together span the cross-section of the pipe. From the integral balances, a set of four partial differential equations follows: one mass and one momentum conservation equation for each fluid. These equations describe the evolution of the height of the interface, and of the cross-sectionally averaged velocity of each fluid.

The basic form of the resulting model (without source terms, diffusion, or surface tension) is analyzed in detail. A conserved energy is proposed, consisting of potential energy associated with the height of the interface, and kinetic energy associated with the averaged velocities. Taking the dot product of an energy gradient vector with the model equations yields an equation for the time derivative of the energy. The remaining terms in the equation are associated with the fluxes of mass and momentum, and for them to have conservative contributions to the energy equation, a set of compatibility conditions needs to be satisfied. It is shown that these conditions are indeed satisfied, proving that the proposed energy is a secondary conserved quantity of the one-dimensional two-fluid model.

Using a finite volume scheme on a staggered grid, the model is discretized in a general manner, leaving open the precise expressions for the numerical fluxes. A discrete form of the energy is proposed. Energy-conserving expressions for the numerical fluxes then follow from the discrete forms of the conditions for energy conservation. With these numerical fluxes, a discrete energy conservation equation is obtained from the discrete model, in the same way as the continuous energy equation is obtained from the continuous model.

The conditions for energy conservation are used to correct an inconsistency in a derived version of the one-dimensional two-fluid model, in which the pressure is eliminated through substitution. This pressure-free two-fluid model requires an explicit expression for the volumetric flow rate, which is typically set to zero, resulting in solutions that differ from those of the original model, and also in a lack of energy conservation. Using the demand for energy conservation, an expression for the volumetric flow rate is found that removes the inconsistency. Having been made fully consistent with the standard two-fluid model, the pressure-free model becomes a more efficient alternative, due to its lack of implicit constraints. This enables the use of fully explicit time integration methods, and results in reduced numerical error and reduced computational cost.

Additional physical effects beyond those of the basic model are included in the energy analysis. Each model term has an independent contribution to the energy equation, that is found by taking the dot product of the energy gradient vector with the model term. The contributions of streamwise gravity and surface tension are shown to be energy-conserving, while those of diffusion and friction are shown to be strictly dissipative. For each model term, a discretization is proposed such that its energy behavior is retained in the computational model.

Even without diffusion and friction being explicitly added to the model, energy must be dissipated in the presence of shocks. To this end a novel advective flux discretization is proposed, which is designed to conserve energy where the solution is smooth, and to provide numerical diffusion and resulting dissipation in the presence of sharp gradients. These properties are obtained by combining, using flux limiters, the original energy-conserving advective flux with a new strictly dissipative upwind advective flux.

The computational model formed by the discretization methods and modeling choices proposed in this work has two main advantages over the standard model. First, it possesses a bound on the mechanical energy, which can be interpreted as a nonlinear stability bound. Dissipating when necessary, but never increasing, the energy behavior of the computational model is physically sound. The dissipation can be quantified and monitored throughout the course of a numerical simulation. Second, the model possesses favorable linear stability properties. Physical long-wavelength instabilities are allowed to develop, while nonphysical short-wavelength instabilities are damped.

Together, these advantages result in accurate, bounded, and convergent numerical solutions. Physical instabilities grow and develop into shocks, at which point they reach a nonlinear bound and propagate without further growth. Shocks are resolved with neither numerical oscillations nor excessive numerical diffusion. A gradual and monotonic convergence of the solution is observed under highly unstable flow conditions, for which the standard model fails to converge.

These properties make the computational model robust, allowing it to be reliably used under a wide range of flow conditions. This robustness is obtained without compromising on the computational efficiency of the model. The work of this thesis therefore increases the viability of fully physics-based dynamical simulations in two-phase pipe flow engineering practice.

Samenvatting

Twee-fase stromingen in buizen komen voor in diverse industriële toepassingen, zoals koelsystemen in kerncentrales, processen in chemische fabrieken, de winning van olie en gas, en het transport van koolstofdioxide, wat wordt afgevangen om te voorkomen dat het wordt uitgestoten in de atmosfeer. In veel gevallen zijn de pijpleidingen te lang om te analyseren met volledig driedimensionale computersimulaties, wat te veel rekenkracht zou kosten. Daarom worden de driedimensionale stromingsvergelijkingen gemiddeld, wat een eendimensionaal model oplevert dat alleen variaties beschrijft langs de stromingsrichting. Een nadeel hiervan is dat het vereenvoudigen van de driedimensionale werkelijkheid tot een eendimensionaal model bepaalde aannames vergt, die kunnen leiden tot niet-fysisch gedrag. Vergelijkbaar hiermee is het probleem dat het discretiseren van de modelvergelijkingen kan leiden tot een computermodel met andere eigenschappen dan het analytische model. Dit proefschrift richt zich op het bewaren van energiebehoudseigenschappen in zowel continue als discrete versies van het eendimensionale model, wat leidt tot verbeterde fysische betrouwbaarheid en niet-lineaire stabiliteit.

Om inzicht te verschaffen in de modelvergelijkingen wordt het eendimensionale 'two-fluid model' voor gestratificeerde incompressibele stroming afgeleid vanuit fundamentele principes. Integrale massa- en impulsbalansen worden opgezet voor de twee fluïda (fasen, vloeistof of gas) afzonderlijk, met het contactoppervlak tussen de twee fluïda als grens tussen de twee controlevolumes, die samen de dwarsdoorsnede van de buis beslaan. Uit de integrale balansen volgt een set van vier partiële differentiaalvergelijkingen: één massa- en één impulsbehoudsvergelijking voor elk van de twee fluïda. Deze vergelijkingen beschrijven de ontwikkeling van de hoogte van het contactoppervlak tussen de twee fluïda, en van de over de dwarsdoorsnede gemiddelde snelheden van de twee fluïda.

Een basale vorm van het resulterende model (zonder brontermen, diffusie, of oppervlaktespanning) wordt in detail bestudeerd. Een behouden energie wordt geponeerd, bestaande uit potentiële energie gerelateerd aan de hoogte van het contactoppervlak, en kinetische energie gerelateerd aan de gemiddelde snelheden. Het nemen van het inwendig product van een energiegradiëntsvector met de modelvergelijkingen leidt tot een vergelijking voor de tijdsafgeleide van de energie. De overige termen van de vergelijkingen zijn gerelateerd aan de flux van massa en impuls, en deze termen leveren alleen conservatieve bijdragen aan de energievergelijking wanneer ze aan bepaalde voorwaarden voldoen. Het wordt aangetoond dat inderdaad aan deze voorwaarden wordt voldaan, wat bewijst dat de geponeerde energie een secundair behouden grootheid is van het eendimensionale two-fluid model.

Het model wordt op een algemene manier gediscretiseerd, gebruikmakend van een eindige-volume methode op een verspringend rooster, terwijl de uitdrukkingen voor de numerieke fluxes open worden gelaten. Een discrete vorm van de energie wordt voorgesteld. Energiebehoudende uitdrukkingen voor de numerieke fluxes volgen dan uit de discrete vormen van de voorwaarden voor energiebehoud. Met deze numerieke fluxes

kan een discrete energiebehoudsvergelijking worden afgeleid van het discrete model, op dezelfde manier waarop de continue energiebehoudsvergelijking werd afgeleid van het continue model.

De voorwaarden voor energiebehoud worden gebruikt om een inconsistentie te corrigeren in een afgeleide versie van het eendimensionale two-fluid model, waarin de druk wordt geëlimineerd door substitutie. Dit druk-vrije two-fluid model vraagt een expliciete uitdrukking voor het volumedebiet, die doorgaans op nul wordt gezet, wat leidt tot oplossingen die verschillen van die van het originele model, en ook tot een gebrek aan energiebehoud. Door gebruik te maken van de eis van energiebehoud wordt een uitdrukking gevonden voor het volumedebiet die de inconsistentie uit het model haalt. Na volledig consistent te zijn gemaakt met het standaard two-fluid model, is het druk-vrije model een efficiënter alternatief, doordat het vrij is van impliciete restricties op de oplossing. Dit maakt het mogelijk om een volledig expliciete tijdsintegratiemethode te gebruiken, en leidt tot een vermindering van de numerieke fout en de benodigde rekenkracht.

Aanvullende fysische effecten, voorbij die van de basale vorm van het model, worden toegevoegd aan de energieanalyse. Elke term in het model levert onafhankelijk een bijdrage aan de energievergelijking, die wordt gevonden door het inwendig product te nemen van de energiegradiëntsvector met de modelterm. Voor de bijdragen van zwaartekracht in de stromingsrichting en van oppervlaktespanning wordt aangetoond dat ze energiebehoudend zijn, terwijl voor diffusie en wrijving wordt aangetoond dat ze strikt dissipatief zijn. Voor elke modelterm wordt vervolgens een discretizatie voorgesteld zodanig dat de energiebehoudseigenschappen bewaard blijven in het computermodel.

Het computermodel dat wordt gevormd door de discretizatiemethoden en modelleringskeuzes die worden voorgesteld in dit werk heeft twee belangrijke voordelen ten opzichte van het standaardmodel. Ten eerste bezit het model een bovengrens voor de mechanische energie, die kan worden geïnterpreteerd als een niet-lineaire stabiliteitsgrens. De energie dissipeert wanneer nodig, maar neemt nooit toe, waarmee het voldoet aan fysische principes. De dissipatie kan worden gekwantificeerd en bijgehouden gedurende het verloop van een numerieke simulatie. Ten tweede bezit het model gunstige lineaire stabiliteitseigenschappen. Fysische instabiliteiten met lange golflengtes kunnen zich ongehinderd ontwikkelen, terwijl niet-fysische instabiliteiten met kleine golflengtes worden gedempt.

Samen leiden deze voordelen tot nauwkeurige, begrensde, en convergerende numerieke oplossingen. Fysische instabiliteiten groeien en ontwikkelen zich tot schokken, op welk punt ze een niet-lineaire stabiliteitsgrens bereiken en vervolgens propageren zonder verdere groei. De verkregen schokoplossingen vertonen noch numerieke oscillaties noch overmatige numerieke diffusie. Onder hoogst instabiele stromingscondities, waarvoor het standaardmodel niet convergeert, wordt een geleidelijke en monotone convergentie van de oplossing bereikt.

Deze eigenschappen maken het computermodel robuust, waardoor het betrouwbaar kan worden toegepast onder verschillende omstandigheden. De robuustheid wordt verkregen zonder in te leveren op rekenkundige efficiëntie. Het werk van dit proefschrift vergroot daarmee de haalbaarheid van volledig op fysica gebaseerde dynamische simulaties in de ingenieurspraktijk van twee-fase buisstromingen.

1 Introduction

In this thesis we design computational models for the stable and accurate prediction of the flow of two fluids through a pipe. Reliable and computationally efficient models for the full range of flow patterns appearing in two-phase pipe flow could greatly assist the design and control of pipeline systems in a variety of applications, minimizing costs and maximizing safety. The nature of two-phase pipe flow, with its complex flow patterns, and the nature of the accompanying one-dimensional equations, with their physical and nonphysical instabilities, make designing proper numerical models a real challenge. The approach of this thesis is based on a careful consideration of the energy conservation and dissipation properties of the discretized one-dimensional equations.

1.1 Two-phase pipe flow

Two-phase pipe flow refers to the simultaneous flow through a pipe of two phases (gas-liquid) of a certain substance, or more in general two different immiscible fluids (liquid-liquid or gas-liquid). These two fluids can interact in complicated ways, leading to increased complexity over single-phase flow. Depending on the flow conditions, the two fluids can arrange themselves in different ways. The different shapes that the flow can take have been categorized into different flow regimes, or flow patterns [82, 116]. Figure 1.1 depicts some of the different flow patterns that can arise in horizontal gas-liquid flow.

When the liquid flow rate is very large but the gas flow rate is low, the dispersed flow pattern is observed, in which a continuous liquid phase flows through the pipe, with small spherical gas bubbles dispersed in it. On the other hand, when the gas flow rate is very large but the liquid flow rate is low, the annular flow pattern is observed, in which the gas flows through the center, with the liquid wetting the perimeter of the pipe.

When both fluids flow at a low rate, the liquid and gas will separate due to the effect of gravity, leading to the stratified flow regime. At slightly higher flow rates, waves will appear at the interface between the gas and the liquid. At even higher flow rates, these waves can grow large and bridge the pipe, forming what is called a slug. A slug is a lump of liquid that locally fills the pipe and travels through it at high speed. Typically, the flow will develop multiple slugs in sequence, alternated with gas pockets. When slugs

grow through the growth of unstable waves, this is called 'hydrodynamic slugging' [54]. Alternatively, slugs may develop through the accumulation of liquid in dips in the pipe. This is known as 'terrain-induced slugging'.

This thesis will focus on the stratified and stratified wavy flow regimes in (nearly) horizontal pipe flow, working towards the transition to slug flow.

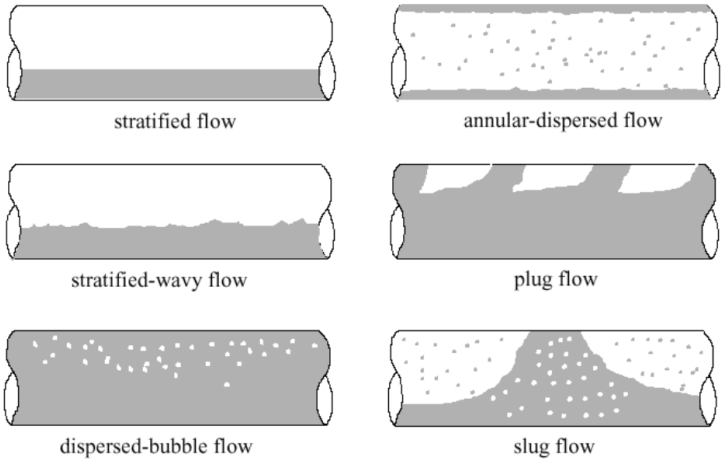

Figure 1.1: A possible classification of the different flow regimes in horizontal two-phase pipe flow [108].

1.2 Applications

Two-phase pipe flows are found in diverse industrial applications. An important driver of the modeling of two-phase pipe flow has been the field of nuclear reactor safety analysis [8, 9, 80]. In most nuclear power plants, water is used as a coolant, to carry off the heat produced by the nuclear reactions. During a typical reference failure mode called a loss-of-coolant accident (LOCA), a pipe carrying the cooling water ruptures. The pipe depressurizes and the water rapidly changes into a two-phase mixture of liquid and vapor, which spills out of the pipe. Due to the resulting lack of cooling, the temperature in the reactor may increase and more of the water may boil. This is a dangerous type of potential accident which must be well understood for specific reactor designs (including their countermeasures).

Another industry where much effort is put into the modeling of two-phase pipe flow, is the oil and gas industry [7, 33, 93]. In the exploitation of a reservoir, crude oil and associated gas are extracted simultaneously, with the possible additions of water and sand. The reservoirs are often located below deep and rough seas, where it is impractical to construct and operate the equipment needed to separate the fluids. Instead, the fluids are transported together, from the offshore well to a central processing facility, which may be located onshore. This transport takes place through long pipelines along the sea floor, which may be hundreds of kilometers in length (see Figure 1.2).

At processing facilities, a steady and predictable input of oil and gas is preferred. In contrast, when slugs form, the flow becomes highly intermittent. Slugs can threaten to

flood the separator with a sudden surge of liquid, exceeding the capacity of the separator [13, 38]. Therefore separators need to be somewhat oversized, or so-called slug catchers are needed to temporarily store the slug. A second issue is that slugs form a body of liquid that carry much momentum. At bends in the pipe, the direction of the slug is changed, and the pipe will experience a large reaction force. This necessitates extra reinforcement of the pipe and its restraints.

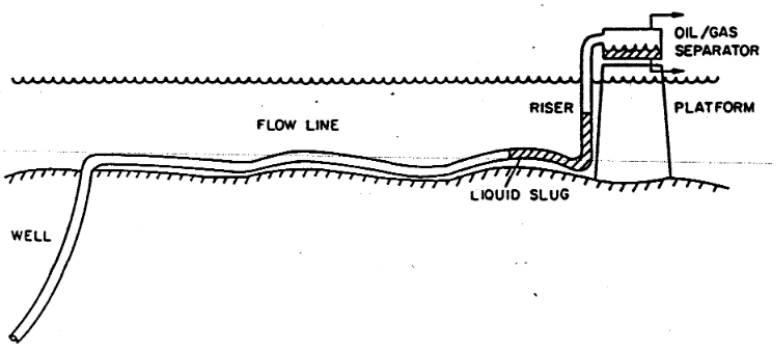

Figure 1.2: Schematic of a pipeline between an offshore well and a processing facility [13].

An application which has recently attracted much interest is the capture and storage of CO_2 [4]. Carbon dioxide is injected into the earth's subsurface, with the aim of preventing its emission into the atmosphere. Pipeline transport is needed in order to transport CO_2 in large quantities and over long distances. CO_2 is preferably transported at high pressure in liquid state (supercritical dense phase CO_2), but can transition into a gas when the pressure drops, for example due to frictional pressure losses, or when the CO_2 is injected in low-pressure subsurface reservoirs. This can give two-phase CO_2 transport in pipelines and in injection wells. The pressure decrease and phase change can be accompanied by a large drop in temperature that may render the pipe brittle and vulnerable to cracks.

For all these applications, computational modeling is important. First, for the design of pipeline systems. With computational models, the properties of a design can be analyzed, which enables efficient optimization. Designs can also be subjected to an extensive safety analysis, in which different scenarios are evaluated. This is particularly important in the nuclear industry.

Second, computational modeling can be used to monitor the flow in real time, through the creation of a so-called Digital Twin of the physical pipeline system. The Digital Twin is fed with real measurements, and uses computational modeling to fill in the gaps for the flow in between measurement points, and for properties of the flow that cannot be easily measured. It therefore provides a full picture of the real physical system. Additionally, it can be used to forecast the flow for a period of time in the future. These forecasts can be used for the control of a pipeline system, ensuring its steady and safe operation.

1

1.3 Modeling

Pipes are characterized by a much longer length scale along the axis of the pipe than in the radial direction. For some applications, the length of the pipe is on the scale of kilometers versus a diameter on the scale of decimeters. For such a geometry, data of every small fluctuation in the three-dimensional (3D) flow would be intractable. Instead, we are interested in variations along the pipe axis, for example of the pressure, the accumulation of the two fluids, and the mass fluxes. These quantities can be provided by a one-dimensional (1D) model. Such a model will have a much lower computational cost than a 3D model, which is important for the applications discussed above, which require either a large number of calculations for different conditions, or faster than real time calculations.

The one-dimensional two-fluid model (TFM) is a dynamic model for two-phase flow in pipes, which resolves only cross-sectionally averaged quantities. There are many variants of the model, but the basic idea, of two interacting fluids whose behavior is averaged to obtain a 1D model, was introduced by Wallis (1969) [127]. In this work we consider a version that models the stratified flow regime. It has the ability to dynamically simulate hydrodynamic instabilities, and has the potential to simulate the transition to slug flow, which may develop from these instabilities.

The full TFM is derived in chapter 2. It consists of two mass conservation equations and two momentum conservation equations. A basic form of the model, for horizontal stratified incompressible flow in a 2D channel (see Figure 1.3), is given by

$$\frac{\partial}{\partial t}\left(\rho_U H_U\right) + \frac{\partial}{\partial s}\left(\rho_U u_U H_U\right) = 0 \tag{1.1a}$$

$$\frac{\partial}{\partial t}\left(\rho_L H_L\right) + \frac{\partial}{\partial s}\left(\rho_L u_L H_L\right) = 0 \tag{1.1b}$$

$$\frac{\partial}{\partial t}\left(\rho_U u_U H_U\right) + \frac{\partial}{\partial s}\left(\rho_U u_U^2 H_U - \frac{1}{2}\rho_U g H_U^2\right) = -H_U \frac{\partial p}{\partial s} + \tau_U + \tau_{\text{int}} \tag{1.1c}$$

$$\frac{\partial}{\partial t}\left(\rho_L u_L H_L\right) + \frac{\partial}{\partial s}\left(\rho_L u_L^2 H_L + \frac{1}{2}\rho_L g H_L^2\right) = -H_L \frac{\partial p}{\partial s} + \tau_L - \tau_{\text{int}} \tag{1.1d}$$

Here s is the streamwise spatial coordinate, t is time, ρ_U and ρ_L are the densities of the upper and lower fluids respectively, H_U and H_L are the heights taken up by these fluids, u_U and u_L are the averaged velocities of these fluids, g is the acceleration of gravity, and p is the pressure. The source terms τ_U and τ_L represent the friction with the walls and τ_{int} represents the friction between the two fluids, acting at the interface. The *hold-up* of each fluid is defined as $\alpha_U = H_U/H$ and $\alpha_L = H_L/H$. The equations are subject to the constraint that the two fluids must together fill the channel:

$$\alpha_L + \alpha_U = 1.$$

For the applications discussed earlier, the drift-flux model [39, 83, 127, 132] is commonly used. This can be considered a simplification of the two-fluid model, which assumes equal pressures between the phases and requires a closure relation for the slip velocity (the difference between the two fluids' velocities). Closure relations are a typical characteristic of averaged and simplified models, in which not all of the relevant physics can be resolved, so that empirical correlations are needed to close the equations. The drift-flux model removes the Kelvin-Helmholtz instabilities present in the TFM [76], and can therefore not

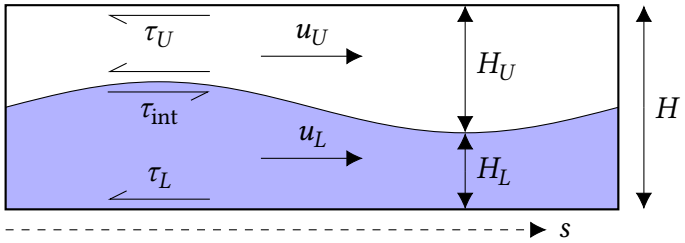

Figure 1.3: A schematic of stratified 1D two-fluid flow in a 2D channel.

be used to predict the transition to slug flow explicitly. Rather, the standard approach is to use flow regime maps to determine the current flow regime, and essentially switch models based on the flow regime [49]. A typical flow regime map is shown in Figure 1.4. Flow regime maps have a highly empirical nature, and are only strictly valid for steady-state flow [11].

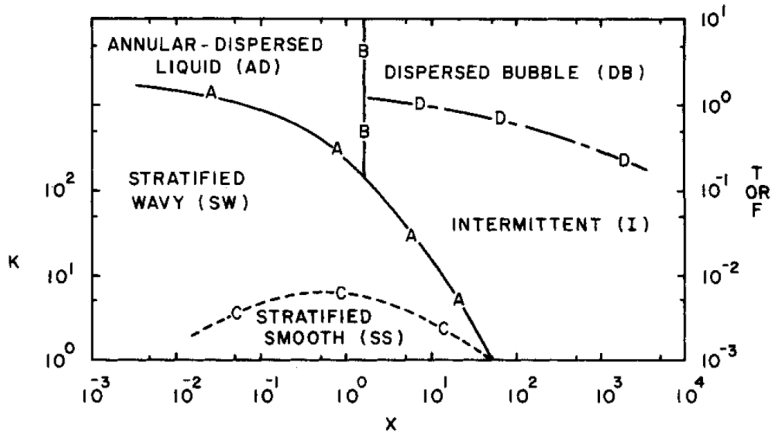

Figure 1.4: Generalized flow regime map of Taitel and Dukler [116]. Curves A & B are plotted against the dimensionless parameters X & F. Curve C is plotted against the dimensionless parameters X & K. Curve D is plotted against the dimensionless parameters X & T.

This thesis works towards a more fundamental approach, in which the transition from stratified flow to slug flow is predicted using solely the conservation equations of the TFM, with a minimal number of closure relations. Modeling slug flow in this way, with a natural evolution of the hold-up fractions to values of 0 and to 1, is called 'slug capturing' [60], as opposed to 'slug tracking' and 'empirical slug specification'.

The first difficulty with this is that the initial value problem for the basic model is only conditionally *well-posed* [81]. This means that it is well-posed for some flow states and *ill-posed* for others (i.e. when there is a large velocity difference between the two fluids). When the initial value problem for the equations is *ill-posed*, the smallest wavelengths present in the solution are unstable and will grow at an unbounded rate. In this case the solution is said to carry no physical meaning [74], and some authors interpret the ill-

posedness as the trigger for the transition to a different flow regime (slug or annular flow) [6, 17]. Slugs can also develop for flow states where the model is well-posed unstable, which means that perturbations will grow, but at a bounded rate. In principle, this can be modeled without special difficulty. However, when the state is well-posed unstable, there is a high risk that the solution travels into the ill-posed region of state space [106]. Therefore, in turn, the growth of slugs can be said to trigger the ill-posedness of the model.

A second issue with applying the TFM to slug capturing is that when one of the hold-ups becomes zero (meaning that one of the phases locally 'disappears'), the equation system becomes singular [131]. For example, if the gas hold-up becomes zero, the gas mass and momentum equations will admit infinitely many solutions for the gas velocity. Before reaching this singularity, the system will become 'stiff', so that a numerical algorithm for its advancement in time will run a high risk of being numerically unstable [67].

This thesis will tackle the issue of the instability of the two-fluid model, taking a crucial step towards a robust method for slug capturing.

1.4 Well-posedness

The Hadamard definition of a well-posed (or properly posed) problem is a problem for which [84, p. 27]

1. a solution exists,
2. the solution is unique, and
3. the solution depends in a continuous manner on the initial and boundary conditions.

For the two-fluid model, the issue is with the third condition.

The third condition is somewhat vague in this form. A rigorous definition (for an initial value problem) is given by Morton and Mayers [89, p. 158] and Richtmyer and Morton [100, p. 41]: There exists some constant K such that for any initial conditions $w'(x,0)$ and $w(x,0)$ the following holds:

$$\|w'(x,t) - w(x,t)\| \leq K \|w'(x,0) - w(x,0)\|, \quad \text{for } t \geq 0. \tag{1.2}$$

This means that the norm of the difference between two solutions, resulting from two different initial conditions, can be bounded by the norm of the difference between the initial conditions. This should hold for any fixed (finite) time t; K may be a function of t. The norm $\|\cdot\|$ is typically chosen to be the L^2 norm (over x). For linear partial differential equations, (1.2) is equivalent to the following condition [113, p. 206], which is often used in practice:

$$\|w(x,t)\| \leq K \|w(x,0)\|, \quad \text{for } t \geq 0. \tag{1.3}$$

A typical example where (1.2) is *not* satisfied is the Hadamard instability [30, p. 229]. Consider the following (linear) initial value problem (known as the Laplace equation in the context where t is a spatial variable)

$$\frac{\partial^2 u_n}{\partial t^2} + \frac{\partial^2 u_n}{\partial x^2} = 0, \tag{1.4}$$

with initial conditions

$$u_n(x,0) = 0, \quad \frac{\partial u_n}{\partial t}(x,0) = f_n(x) = \frac{\sin(nx)}{n^2}, \quad n = 1,2,3\ldots \tag{1.5}$$

The initial condition $f_n(x)$ converges to zero for $n \longrightarrow \infty$ (see Figure 1.5).

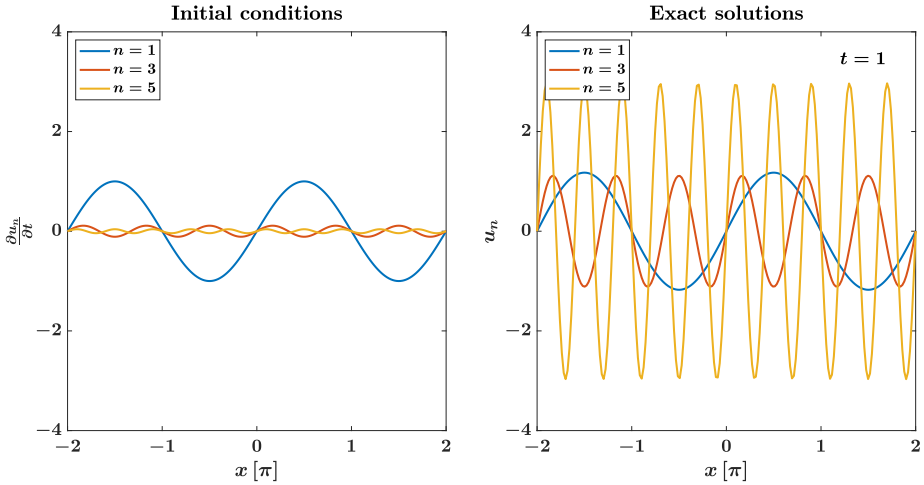

Figure 1.5: Initial conditions (1.5) (left), and exact solutions at finite time (1.6) (right), with different n.

An exact solution to this initial value problem is

$$u_n(x,t) = \sinh(nt)\frac{\sin(nx)}{n^2}. \tag{1.6}$$

The difference in norm between two initial conditions $u_n(x,0)$ and $u_{n+1}(x,0)$ defined by (1.5) is zero (since they are both zero):

$$\|u_{n+1}(x,0) - u_n(x,0)\| = 0 < \delta, \tag{1.7}$$

and for large n the difference in the time derivatives is similarly small:

$$\left\|\frac{\partial u_{n+1}}{\partial t}(x,0) - \frac{\partial u_n}{\partial t}(x,0)\right\| < \delta', \quad \text{with } \delta' \text{ a decreasing function of } n. \tag{1.8}$$

However, for fixed $0 < t < \infty$ and fixed $|x| < \infty$, the solution (1.6) explodes as $n \longrightarrow \infty$ (i.e. the short wavelength limit), and the series $u_{n+1}(x,t) - u_n(x,t)$ diverges: there is no bound for

$$\|u_{n+1}(x,t) - u_n(x,t)\|, \quad \text{at fixed } t. \tag{1.9}$$

The example violates the well-posedness criterion; there is no constant K such that (1.2) holds for all finite t and all n, since $\|u_{n+1}(x,t) - u_n(x,t)\| \longrightarrow \infty$ for $n \longrightarrow \infty$ (at fixed t), while $\|u_{n+1}(x,0) - u_n(x,0)\|$ remains zero (see Figure 1.6).

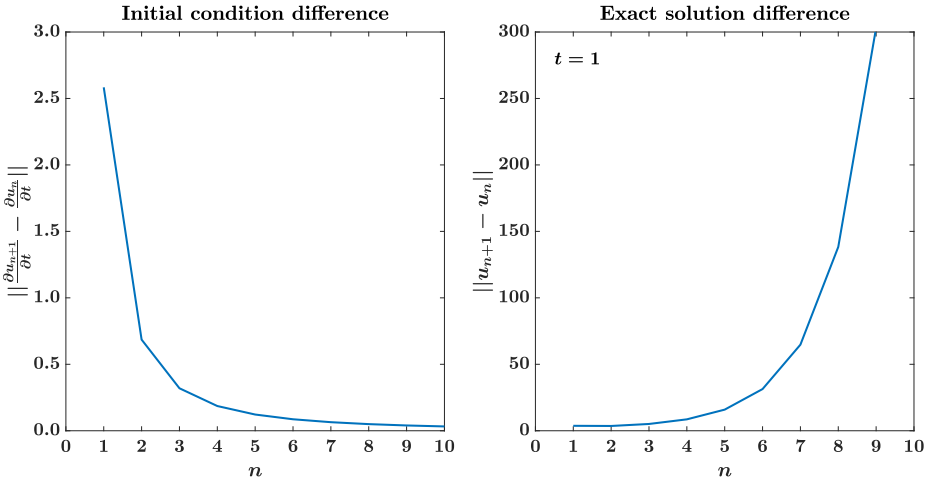

Figure 1.6: Difference in initial conditions (1.8) (left), and difference in exact solutions at fixed time (1.9) (right), as a function of n, for the initial value problem specified by (1.4) and (1.5). Here the L^2 norm is taken over the interval $[-2\pi, 2\pi]$.

One of the problems with an ill-posed model is that it cannot describe observable natural phenomena [30]. As Courant and Hilbert put it, data in nature can never be defined with infinite precision; a measurement will always involve small errors. An ill-posed initial value problem can amplify these measurement errors via an unbounded growth rate, so that for any moment past the initial point in time the predicted solution diverges completely.

This leads directly to another problem, when solving the model equations numerically. Though numerical viscosity can bound the wave growth rate at small wavelengths, the solution will not converge with grid refinement, since numerical viscosity is grid-dependent [8, 46, 60]. In fact, as stated by the Lax equivalence theorem [72], well-posedness of the (linear) initial value problem is one of the conditions (along with consistency and numerical stability) for convergence of the finite difference equations. If the (linear) initial value problem is ill-posed, then no numerical scheme that is consistent with the problem can be stable [100, p. 59]. Convergence is a crucial property for a reliable numerical model. If convergence is achieved, this can be regarded as proof that the model is well-posed.

1.5 Characteristic analysis

Since it is in general not possible to obtain exact solutions for the TFM, it is more difficult to judge its well-posedness. It is typically studied using two different techniques: characteristic analysis and linear stability analysis. These two analyses are well-defined for quasi-linear first-order systems of partial differential equations of the form

$$\mathbf{A}(\mathbf{w})\frac{\partial \mathbf{w}}{\partial t} + \mathbf{B}(\mathbf{w})\frac{\partial \mathbf{w}}{\partial x} = \mathbf{c}(\mathbf{w}), \tag{1.10}$$

with $\mathbf{w}$ the solution vector, t time, x a spatial coordinate, $\mathbf{A}$ and $\mathbf{B}$ square matrices, and $\mathbf{c}$ a vector of source terms. The TFM as given by (1.1) can be written in this form (see section 5.B). Systems that are higher order in $\partial\mathbf{w}/\partial x$ can be reformulated to fit this form through substitution. For example, equation (1.4) can be written in the form (1.10) with

$$p_n = \frac{\partial u_n}{\partial t}, \quad q_n = \frac{\partial u_n}{\partial x}, \quad \mathbf{w} = \begin{bmatrix} p_n \\ q_n \end{bmatrix}, \quad \mathbf{A} = \mathbf{I} = \begin{bmatrix} 1 & 0 \\ 0 & 1 \end{bmatrix}, \quad \mathbf{B} = \begin{bmatrix} 0 & 1 \\ -1 & 0 \end{bmatrix}, \text{ and } \mathbf{c} = \begin{bmatrix} 0 \\ 0 \end{bmatrix}. \tag{1.11}$$

Characteristic analysis yields the (generalized) eigenvalues and eigenvectors of (1.10). These can be used for classification. There are multiple possibilities (with different names in different texts) [50, 53, 68, 73, 129, 130], but a useful classification is the following:

- If there are no real eigenvalues, i.e. all eigenvalues are complex, the system is called *elliptic*.
- If the system has a mix of real and complex eigenvalues, the system is said to be *hybrid*.
- If all eigenvalues are real but the system does not have a full set of linearly independent eigenvectors, the system is called *parabolic*, or *weakly hyperbolic* if $\mathbf{A} = \mathbf{I}$.
- If all eigenvalues are real and the system has a full set of linearly independent (left) eigenvectors, the system is called *hyperbolic*, or *strongly hyperbolic* if $\mathbf{A} = \mathbf{I}$. A strongly hyperbolic system is *diagonalizable*.
- If additionally all eigenvalues are distinct, the system is called *totally hyperbolic* or *strictly hyperbolic*.

For linear systems that can be written in the form (1.10) with $\mathbf{A} = \mathbf{I}$, it can be rigorously proven that strong hyperbolicity is a necessary and sufficient condition for the initial value problem to be well-posed, in the sense that it satisfies (1.2) [50, 68]. Consider as an example equation (1.4), which written in the form (1.10) with substitutions (1.11), can be determined to be elliptic with eigenvalues $\lambda = \pm\sqrt{-1}$, and is clearly ill-posed.

For the basic incompressible two-fluid model as given by (1.1), characteristic analysis yields two eigenvalues that are real in a portion of state space where the difference between the velocities of the two fluids small, and complex where the velocity difference exceeds the Kelvin-Helmholtz stability criterion [74, 107]. The model is therefore said to be conditionally hyperbolic: it has a hyperbolic character when its eigenvalues are real, and a hybrid character when its eigenvalues are complex. This suggests that the model becomes unusable.

However, the TFM is highly nonlinear, and the extension of the proof of the connection between hyperbolicity and the satisfaction of (1.2) to nonlinear systems relies on a linearization principle, which requires that the solution is smooth [50, 68]. Some researchers [15, 65, 66, 69, 70] propose that "The Hadamard instability suggests that the initial value problem for a linear elliptic problem is meaningless. Nonlinear problems may nonetheless have features which mitigate this conclusion" [66].

Additionally, when higher order terms such as diffusion and surface tension are added to the model (see chapter 2), the characteristic analysis requires that these terms are reduced to first order terms. Montini [87] found that this process makes the results of the

characteristic analysis unreliable. In the limit of vanishing viscosity and surface tension, the results of the characteristic analysis do not reduce to those of the basic model without viscosity and surface tension.

Standard techniques for the analysis of nonlinear conservation laws with discontinuous solutions [73] are unfortunately not directly applicable due to the non-conservative (pressure) terms in the TFM [95, p. 274]. A further complication is that (in addition to the two previously discussed eigenvalues) the incompressible TFM carries two infinite eigenvalues, and the characteristics belonging to these eigenvalues correspond to constraints that should be satisfied instantaneously, at each moment in time [107]. For its quasilinear form (see section 5.B), the matrix $\mathbf{A}$ is not invertible. Even when the basic TFM has all real eigenvalues, it does not have a full set of linearly independent eigenvectors, so that it is strictly speaking only parabolic. This stands in contrast to the related shallow water or Saint-Venant equations, which are of fully conservative form and are strongly hyperbolic, making their analysis relatively straightforward.

1.6 Linear stability analysis

Linear stability analysis is a more straightforward way of studying the stability and well-posedness of the TFM. A general description of the technique is given by [95], and it has been applied to the TFM by amongst others [46, 74, 76, 96]. In a linear stability analysis, the system is linearized around a base state, and a linear system is solved for the evolution in time of a Fourier decomposition of a small perturbation to the base state. The results of the analysis are expressions for the angular frequency of the perturbation (known as dispersion relations), of which the imaginary component represents the growth (or damping) rate. These may depend on the wavelength of the perturbation, and on the current solution. In section 5.B the analysis and its results will be described in detail for the TFM.

In absence of source terms, linear stability analysis of a system of the form (1.10) gives the same result as its characteristic analysis [96]. This means that the eigenvalues found in the characteristic analysis are equal to the complex frequency divided by the wavenumber of the perturbation. In the limit of short wavelengths, the source term may be neglected in the linear stability analysis, so the two analyses are equivalent for short wavelengths. This means that the eigenvalues of the system will be real if and only if perturbations of vanishing wavelength do not grow. In contrast, when the eigenvalues are complex, perturbations of vanishing wavelength will have an infinite growth rate. There thus is an intimate connection between the linear stability analysis of (1.10) and its characteristic analysis.

The infinite growth rate of perturbations of vanishing wavelength, found by the linear stability analysis of the basic model when the velocity difference exceeds the Kelvin-Helmholtz stability criterion, stands in clear contrast to the well-posedness condition (1.2). For linear partial differential equations, the linear stability analysis is exact, and this result would be a clear proof of ill-posedness. However, for the nonlinear two-fluid model, linear stability analysis is an approximation that is valid only when the perturbation is small and the solution is smooth.

When higher order terms such as diffusion and surface tension are added to the model, the connection between the characteristic analysis and the linear stability analysis becomes unclear, because unlike the source terms these cannot be neglected at short wave-

lengths. For the characteristic analysis they need to be converted to first-order form, while in the linear stability analysis they can be left in higher order form. Higher order terms drastically alter the dispersion relations at short wavelengths, bounding the growth rate [94]. When both diffusion and surface tension are added, the growth rate becomes negative, leading to damping (see chapter 5). The instability of longer wavelength perturbations is unchanged, but their bounded growth rate does not contradict (1.2), and these are physical instabilities that should not be removed from the model.

For these reasons, the important question becomes what happens when instabilities grow large and form (non-smooth) shocks. This concerns the *nonlinear* stability of the model [76].

1.7 Energy stability

This thesis proposes to analyze the two-fluid model from the perspective of *energy stability* [112]. This is a property of the full nonlinear model.

As an example we will consider the inviscid incompressible Navier-Stokes equations (also known as the Euler equations), which can be averaged to obtain the TFM. These can be written as

$$\nabla \cdot \mathbf{u} = 0, \tag{1.12}$$

$$\frac{\partial \mathbf{u}}{\partial t} + \nabla \cdot (\mathbf{u} \otimes \mathbf{u}) + \frac{1}{\rho} \nabla p = 0. \tag{1.13}$$

The vector $\mathbf{u}$ represents the velocities in different directions, ρ is the density, and p is the pressure. We use the following vector identities:

$$\nabla \cdot (\mathbf{a} \otimes \mathbf{b}) = \mathbf{b}(\nabla \cdot \mathbf{a}) + (\mathbf{a} \cdot \nabla)\mathbf{b}, \quad \nabla \cdot (a\mathbf{b}) = a(\nabla \cdot \mathbf{b}) + (\mathbf{b} \cdot \nabla)\, a,$$
$$(\mathbf{b} \cdot \nabla)\, a = \mathbf{b} \cdot (\nabla a), \quad \nabla(\mathbf{a} \cdot \mathbf{b}) = (\nabla \mathbf{a}) \cdot \mathbf{b} + (\nabla \mathbf{b}) \cdot \mathbf{a}.$$

The derivation is based on [102]. Take the dot product of (1.13) with $\mathbf{u}$:

$$\mathbf{u} \cdot \frac{\partial \mathbf{u}}{\partial t} + \mathbf{u} \cdot (\nabla \cdot (\mathbf{u} \otimes \mathbf{u})) + \frac{1}{\rho} \mathbf{u} \cdot (\nabla p) = 0. \tag{1.14}$$

The time derivative term can be written as

$$\mathbf{u} \cdot \frac{\partial \mathbf{u}}{\partial t} = \frac{\partial}{\partial t} \left(\frac{1}{2} \mathbf{u} \cdot \mathbf{u} \right).$$

Using the vector identities, the advective term in (1.14) can be written as

$$\mathbf{u} \cdot (\nabla \cdot (\mathbf{u} \otimes \mathbf{u})) = \nabla \cdot \left(\frac{1}{2} (\mathbf{u} \cdot \mathbf{u}) \mathbf{u} \right) + \frac{1}{2} (\mathbf{u} \cdot \mathbf{u})(\nabla \cdot \mathbf{u}) = \nabla \cdot \left(\frac{1}{2} (\mathbf{u} \cdot \mathbf{u}) \mathbf{u} \right),$$

where in the last step we have substituted (1.12). Now, using the identities and assuming ρ constant, the pressure term can be written as

$$\frac{1}{\rho} \mathbf{u} \cdot (\nabla p) = \frac{1}{\rho} \nabla \cdot (p\mathbf{u}) - \frac{1}{\rho} p (\nabla \cdot \mathbf{u}) = \nabla \cdot \left(\frac{p}{\rho} \mathbf{u} \right).$$

1

Gathering terms, (1.14) becomes the local energy equation, for which a TFM equivalent will be derived in chapter 3:

$$\frac{\partial e}{\partial t} + \nabla \cdot \mathbf{h}_f + \nabla \cdot \mathbf{h}_p = 0, \tag{1.15}$$
$$\text{with} \quad e = \frac{1}{2}\mathbf{u}\cdot\mathbf{u}, \quad \mathbf{h}_f = \frac{1}{2}(\mathbf{u}\cdot\mathbf{u})\mathbf{u}, \quad \mathbf{h}_p = \frac{p}{\rho}\mathbf{u}.$$

Here e is the locally defined mechanical energy. The terms $\mathbf{h}_f$ and $\mathbf{h}_p$ are energy fluxes, describing the in- and outflow of energy from a point in space. This energy conservation equation is not part of the governing equations, but is a consequence of the mass and momentum conservation equations (1.12) and (1.13). Mechanical energy is a secondary conserved quantity, in relation to the primary conserved quantities of mass and momentum.

Note that in order to obtain (1.14), we took the dot product with

$$\mathbf{v} = \left[\frac{\partial e}{\partial \mathbf{u}}\right]^T = \mathbf{u}.$$

This will have a direct parallel in the analysis of the TFM.

Integrating (1.15) over the domain and applying Gauss' theorem yields the global energy equation (similar to [40, p. 160])

$$\frac{\mathrm{d}E}{\mathrm{d}t} + \oint_S \mathbf{h}_f \cdot \mathbf{n}\,\mathrm{d}S + \oint_S \mathbf{h}_p \cdot \mathbf{n}\,\mathrm{d}S = 0, \tag{1.16}$$

with integrals over the surface S, and a global energy

$$E = \int_V \frac{1}{2}\mathbf{u}\cdot\mathbf{u}\,\mathrm{d}V = \frac{1}{2}\|\mathbf{u}\|^2,$$

defined using an integral over the volume V. For periodic or closed boundaries ($\mathbf{u} = \mathbf{0}$), (1.16) reduces to

$$\frac{\mathrm{d}E}{\mathrm{d}t} = 0. \tag{1.17}$$

This equation has a direct interpretation as a form of nonlinear stability, since it sets a bound on the norm of the solution. It directly implies that the simplified well-posedness condition (1.3) is satisfied. When viscous diffusion terms are added to the model, a strictly negative dissipation term is added to the right-hand side of (1.17), and in chapter 5 the same will be shown to hold for the TFM.

For the Navier-Stokes equations, energy stability is therefore a useful analytical property. Additionally, it can be used to guide the design of numerical schemes, which should ideally retain this property. To achieve this, the discretization must be designed such that the steps made in the derivation of the continuous energy conservation equation can be repeated in the discrete setting, which requires that the discretization satisfies certain symmetries (the advection operator must be skew-symmetric and the gradient and divergence operators must be each other's negative transpose [29, 125]).

Energy-conserving schemes yield non-linearly stable numerical models [126]. They prevent nonlinear instability, which may otherwise arise due to the accumulation of numerical error stemming from the spatial discretization of the advective terms [29]. Energy-conserving schemes also add physical consistency, since they retain an additional property of the physical fluid flow equations. They add no artificial dissipation: all of the dissipation is due to the physical viscous terms. This is important for the accurate simulation of turbulent flow [51, 103].

1.8 Research goal and outline

Summarizing, the TFM has both a severe nonphysical instability leading to ill-posedness (for the short wavelengths), and a physical instability that is well-behaved (for the long wavelengths). These instabilities are important to understand for the continuous model, and to control for the numerical model. A lack of satisfactory methods for understanding and controlling these instabilities stands in the way of robust physics-based simulations of the wavy stratified flow regime and the transition to slug flow.

We have seen how ill-posedness manifests itself for an initial value problem, making the model nonphysical, and preventing convergence of numerical solutions. We have discussed the method of characteristic analysis, which yields clear results on the well-posedness of linear systems of partial differential equations, but is inconclusive for the nonlinear, non-conservative, and sometimes higher order TFM. We have discussed the method of linear stability analysis, which yields clear results for small perturbations to a smooth solution, but is inconclusive when perturbations grow large and develop into (discontinuous) shocks. Finally, we have discussed the energy method, which yields clear nonlinear stability results for the Navier-Stokes equations, and can be used to guide the design of non-linearly stable numerical models.

The goal of this thesis is to develop computationally efficient, accurate, and nonlinearly stable models and numerical methods for the simulation of waves and instabilities in two-phase pipe flow. We aim for the most physically fundamental model that the one-dimensional setting allows, based on the conservation equations, without unnecessary closure terms and artificial regularization. This will provide the basis for a robust and reliable computational model for slug capturing.

To this end, we formulate a concept of energy stability for the one-dimensional two-fluid model, aiming to replicate the benefits that this type of analysis offers to the Navier-Stokes equations. By studying the energy conservation properties of the TFM, we obtain a new perspective on its stability, in addition to the traditional approaches of characteristic analysis and linear stability analysis. This new perspective provides a new tool for analyzing solutions to the TFM. By analyzing the dissipation of energy, we gain insight into how shocks are bounded, providing a form of nonlinear stability to the linearly unstable model.

As a natural complement to the energy analysis of the TFM, this thesis develops an energy-consistent spatial discretization. This yields a numerical model with stability properties similar to those of the continuous model. By retaining the energy conservation properties of the continuous model, the numerical model gains an additional aspect of accuracy and physical fidelity.

After deriving the model in chapter 2, these developments are made in a few steps.

- First, chapter 3 sets up the basis of the *energy-conserving* framework. The energy conservation equation is derived for the basic model, without higher order terms. The derivation is conducted in a general manner, in order to guide the derivation of an energy-conserving spatial discretization. This discretization is obtained in a constructive manner. The energy is demonstrated to be conserved up to near machine precision for simulations of waves in a channel.
- Second, in chapter 4, the results of chapter 3 are applied to a new pressure-free version of the two-fluid model, the development of which the author contributed to in an article not included in this thesis [105]. The demand for energy conservation is used to remedy a prior discrepancy between the pressure-free and original models, and yields an *energy-consistent* model. Additionally, the streamwise gravity term is included in the energy-conserving framework, enabling energy-consistent simulations for inclined flow. The energy-consistent pressure-free two-fluid model (PFTFM) is more computationally efficient than the original TFM, and is free of the numerical error stemming from the solution of the pressure Poisson equation.
- Third, in chapter 5, the energy-consistent framework is extended with higher order effects which remedy the unbounded short wavelength linear instability of the basic model. This includes dissipative effects, which appear as strictly negative terms on the right hand side of the energy equation, yielding an *energy-stable* model. Energy-consistent discretizations of these terms are presented, with expressions for the numerical dissipation rates which are consistent with their continuous counterparts. Additionally, an energy-stable discretization of the advective terms is developed, that provides numerical dissipation near shocks when the grid resolution is too low to fully resolve the physical dissipation. The combination of stabilizing effects is shown to yield bounded shocks, and smoothly converging solutions, for conditions under which the basic TFM is ill-posed.

These chapters are directly based on the publications [20], [21], and [22], respectively. As a result, these chapters show some overlap in the introductions, and there are some small inconsistencies in notation between the different chapters.

2

Derivation of the two-fluid model

In this chapter we derive the one-dimensional two-fluid model for stratified incompressible flow, starting from first principles. It is important to understand the averaged nature of the model, as it sometimes has counter-intuitive implications. In literature, different derivations are available, based on different types of averaging. The different approaches include ensemble averaging [35], time averaging [58], and volume averaging [88]. These derivations are typically quite general, being performed for multidimensional disperse flows, and are only specified to one-dimensional flow at a later stage, as described for example in [76]. Here, we restrict the derivation to stratified one-dimensional flow in ducts, resulting in a simpler process and a more direct relation to the final model. This derivation provides insight into the meaning of the different terms in the model, and the model's limitations.

This chapter will start by introducing standard integral conservation laws, and the boundary conditions between two fluids in multiphase flow. Second, in section 2.2, the averaging procedure will be described, which will be applied to the mass conservation law in section 2.3. Section 2.4 will derive the momentum equations term-by-term. Finally, in section 2.5, the assumptions made during the derivation will be collected, providing a basis for a thorough understanding of the model.

2.1 Preliminaries

2.1.1 Integral balances

The incompressible two-fluid model is based on the principles of mass and momentum conservation. These are most fundamentally expressed as an integral balance over a control volume. The mass in the control volume can change due to a difference in the inflow and the outflow of mass at the boundaries. The momentum in the control volume can change due to inflows and outflows, and due to forces acting throughout the volume, or on the boundaries.

A standard integral mass balance [128] can be written as

$$\frac{\mathrm{d}}{\mathrm{d}t}\int_V \rho \,\mathrm{d}V + \oint_S \rho \mathbf{u}\cdot\mathbf{n}\,\mathrm{d}S = 0, \tag{2.1}$$

where $\mathrm{d}/\mathrm{d}t$ is a derivative with respect to time, $\int_V \mathrm{d}V$ is an integral over the control volume V, $\rho = \rho(\mathbf{x}, t)$ is the density ($\mathbf{x}$ representing coordinates in three-dimensional space and t representing time), $\oint_S \mathrm{d}S$ is an integral over the closed surface S bounding V, $\mathbf{u} = \mathbf{u}(\mathbf{x}, t)$ is the velocity vector and $\cdot\,\mathbf{n}$ is the dot product with the vector normal to the surface S, pointing outward. Figure 2.1 shows such a control volume, including an interface between two fluids. If the velocity is continuous at the interface (see section 2.1.2), the velocity field $\mathbf{u}(\mathbf{x}, t)$ can be defined as a continuous combined velocity field which encompasses both fluids.

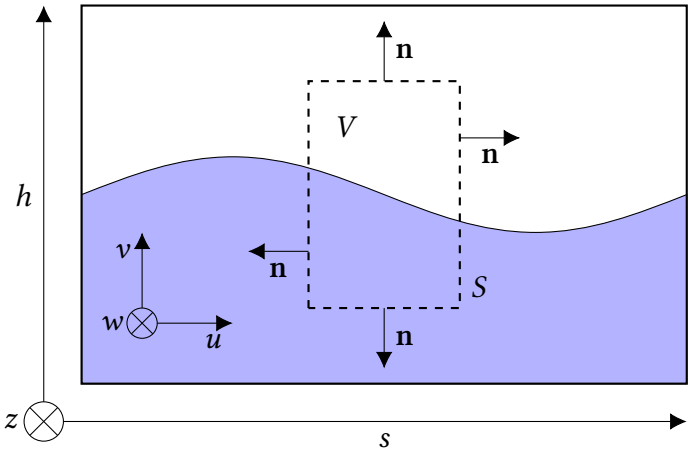

Figure 2.1: A schematic of a control volume V in two-phase flow. The control volume is bounded by S, with normal vectors pointing outward. The spatial coordinate vector $\mathbf{x}$ has components s, h, and z. The velocities in these directions are the components u, v, and w of $\mathbf{u}$, respectively.

The momentum balance, i.e. the Navier-Stokes equations in integral form [128], can be written as

$$\frac{\mathrm{d}}{\mathrm{d}t}\int_V \rho\mathbf{u}\,\mathrm{d}V + \oint_S \rho\mathbf{u}\,(\mathbf{u}\cdot\mathbf{n})\,\mathrm{d}S = -\oint_S p\mathbf{n}\,\mathrm{d}S + \oint_S \boldsymbol{\tau}\cdot\mathbf{n}\,\mathrm{d}S + \int_V \rho\mathbf{g}\,\mathrm{d}V, \tag{2.2}$$

where $p = p(\mathbf{x}, t)$ is the pressure, $\boldsymbol{\tau} = \boldsymbol{\tau}(\mathbf{u}(\mathbf{x}, t))$ is the stress tensor, and $\mathbf{g}$ is the gravity force vector. For a control volume containing an interface between two fluids, a term

$$+\int_V \mathbf{f}_\sigma \delta_{S_\mathrm{int}}\,\mathrm{d}V \tag{2.3}$$

can be added to the right-hand side of (2.2) [119, p. 42]. The surface tension term $\mathbf{f}_\sigma$ is added as a body force that acts only at the interface, which is marked by the delta function $\delta_{S_\mathrm{int}} = \delta(\mathbf{x} - \mathbf{x}_\mathrm{int})$. For constant surface tension σ, it can be written as

$$\mathbf{f}_\sigma \delta_{S_\mathrm{int}} = \sigma\kappa\mathbf{n}_\mathrm{int}\delta_{S_\mathrm{int}},$$

with $\mathbf{n}_\mathrm{int}$ the interface normal (pointing outward) and $\kappa = \nabla\cdot\mathbf{n}_\mathrm{int}$ the surface curvature.

A similar conservation equation as for mass and momentum can be formulated for energy. However, if the flow is assumed to be isothermal, an equation of state $\rho = f(p)$ suffices to close the system. If additionally the flow is assumed to be incompressible, ρ becomes a constant independent of p. The density may differ between the fluids, but each fluid and its density are simply advected with the flow field $\mathbf{u}$.

2.1.2 Interface conditions

The jump conditions at the interface between two fluids can be derived by considering a thin control volume including the interface, as depicted in Figure 2.2 [119]. The width of the control volume is defined to be zero, so that no mass can accumulate inside of it. The control volume travels with the interface at velocity $\mathbf{u}_{\text{int}}$. The integral mass balance (2.1) then leads to the so-called Rankine-Hugoniot condition

$$\rho_1 (\mathbf{u}_1 - \mathbf{u}_{\text{int}}) \cdot \mathbf{n}_{\text{int}} = \rho_0 (\mathbf{u}_0 - \mathbf{u}_{\text{int}}) \cdot \mathbf{n}_{\text{int}} = \dot{m}, \tag{2.4}$$

in which $\mathbf{u}_{\text{int}}$ is the interface velocity, $\mathbf{u}_1$ is the velocity of fluid 1, $\mathbf{u}_0$ is the velocity of fluid 0 and $\dot{m}$ is the mass flow across the interface. We will assume there to be no phase change, implying that mass cannot traverse the phase boundary, so that $\dot{m} = 0$. This leads to the interface condition

$$\mathbf{u}_{\text{int}} \cdot \mathbf{n}_{\text{int}} = \mathbf{u}_1 \cdot \mathbf{n}_{\text{int}} = \mathbf{u}_0 \cdot \mathbf{n}_{\text{int}}. \tag{2.5}$$

Assuming no slip between the fluids, this becomes

$$\mathbf{u}_1 = \mathbf{u}_0.$$

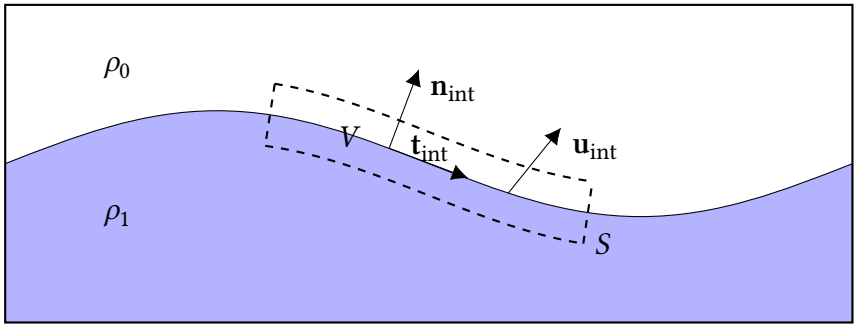

Figure 2.2: A schematic of thin control volume V with boundary S, centered around the interface. At the interface, the normal vector $\mathbf{n}_{\text{int}}$ points outward from fluid 1. Along the interface lies the tangent vector $\mathbf{t}_{\text{int}}$.

Applying the integral momentum balance (2.2) to the control volume in Figure 2.2, and substituting (2.5), yields another interface condition [119]:

$$(p_1 - p_0)\mathbf{n}_{\text{int}} - (\boldsymbol{\tau}_1 - \boldsymbol{\tau}_0) \cdot \mathbf{n}_{\text{int}} = \mathbf{f}_\sigma, \tag{2.6}$$

By taking dot products with $\mathbf{n}_{\text{int}}$ and $\mathbf{t}_{\text{int}}$, this is split into two different interface conditions:

$$p_1 - p_0 - \mathbf{n}_{\text{int}} \cdot (\boldsymbol{\tau}_1 - \boldsymbol{\tau}_0) \cdot \mathbf{n}_{\text{int}} = \sigma\kappa, \tag{2.7}$$

$$\mathbf{t}_{\text{int}} \cdot (\boldsymbol{\tau}_1 - \boldsymbol{\tau}_0) \cdot \mathbf{n}_{\text{int}} = 0. \tag{2.8}$$

The first of these interface conditions involves forces acting on the interface in the direction normal to the interface, and the second involves forces acting in the direction tangential to the interface. Surface tension is now included in the interface conditions, through which it can be included in the two-fluid model, where the interface forms the boundary between two control volumes. With such control volumes, surface tension must be left out of the momentum balance as given by (2.2).

2.2 Two-fluid model averaging

The central idea of the one-dimensional two-fluid model for stratified flow is to consider the flow of two fluids in a closed duct, and take the cross-sectional average of the flow, over the two fluids separately. Here this will be done by defining control volumes as depicted in Figures 2.3 and 2.4, and setting up integral mass and momentum balances for each one. Drawing such control volumes means that we assume that the interface height H_L can be given as a function of s (and t); nowhere is any of the lower fluid located above any of the upper fluid. The control volumes are bounded by the interface perimeter P_{int} and the wall perimeters P_L and P_U.

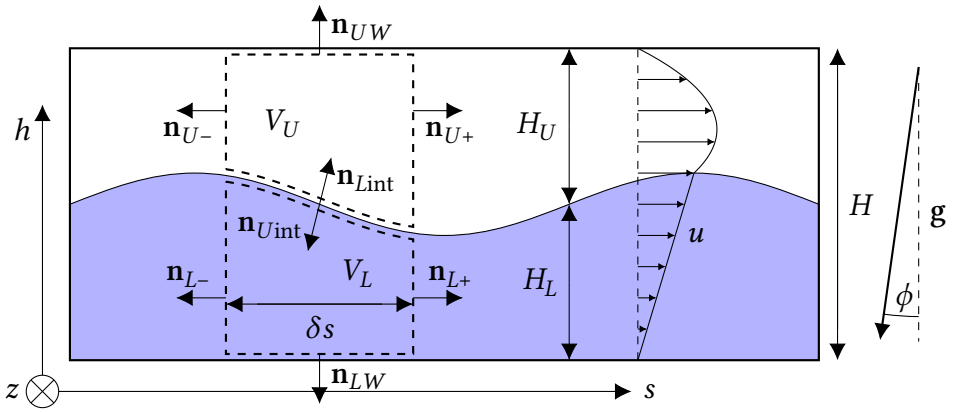

Figure 2.3: Side view of the control volumes used in the derivation of the 1D two-fluid model. V_U is the control volume for the upper fluid, V_L the control volume for the lower fluid, and the boundary between the two control volumes forms the interface. Mass and momentum can enter at boundaries normal to the streamwise direction, while the duct walls are impenetrable. A typical (unaveraged) velocity profile is pictured.

To derive the two-fluid model, the integral balances for the two control volumes are written in terms of volume and cross-sectional averages. Before averaging is applied, any locally defined flow variable ξ is a function of the streamwise coordinate s, the normal coordinate h, the horizontal coordinate z, and the time t: $\xi = \xi(s,h,z,t)$. Its cross-sectional average over the cross-section A_L occupied by the lower fluid will only be a function of s and t and is defined as

$$\langle \xi \rangle_L(s,t) = \frac{1}{A_L(s,t)} \int_{A_L(s,t)} \xi(s,h,z,t)\,\mathrm{d}A, \quad \text{with} \quad A_L(s,t) = \int_{A_L(s,t)} \mathrm{d}A,$$

in which $A_L(s,t)$ is the local size of the lower fluid's cross section, with $A_U(s,t)$ its equiv-

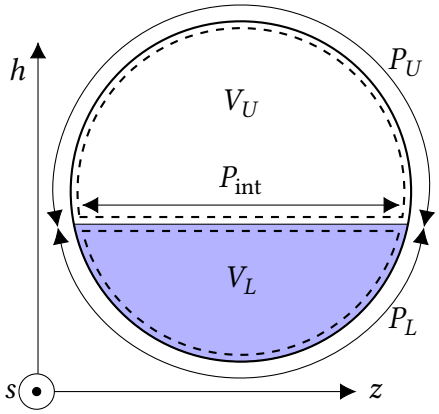

Figure 2.4: Cross section of the control volumes depicted in Figure 2.3. The control volumes V_U and V_L are bounded by the wall perimeters P_U and P_L, and the interface perimeter P_{int} between them.

alent for the upper fluid, adding up to the (constant) total duct cross section $A = A_L(s,t) + A_U(s,t)$. The volume average over the control volume V_L is defined similarly:

$$\{\xi\}_L(t) = \frac{1}{V_L(t)} \int_{V_L(t)} \xi(s,h,z,t)\,\mathrm{d}V, \quad \text{with} \quad V_L(t) = \int_{V_L(t)} \mathrm{d}V.$$

Note that the area integral can alternatively be written as

$$A_L(s,t) = \int_0^{H_L(s,t)} w(h)\,\mathrm{d}h,$$

with $w(h)$ the width of the duct as a function of the coordinate h, with $w(H_L) = P_{\text{int}}$.

The derivation that will be given in the following sections is based on the same principles as the derivation of the Saint-Venant equations [31].

2.3 Mass equations

We write (2.1) for the lower fluid control volume, which is bounded by the duct wall and by the interface. We split the surface integral into contributions of the four faces. This becomes

$$\frac{\mathrm{d}}{\mathrm{d}t}\int_{V_L} \rho\,\mathrm{d}V + \int_{S_{L\text{int}}} \rho(\mathbf{u}-\mathbf{u}_{\text{int}})\cdot\mathbf{n}\,\mathrm{d}S + \int_{S_{L+}} \rho\mathbf{u}\cdot\mathbf{n}\,\mathrm{d}S + \int_{S_{LW}} \rho\mathbf{u}\cdot\mathbf{n}\,\mathrm{d}S + \int_{S_{L-}} \rho\mathbf{u}\cdot\mathbf{n}\,\mathrm{d}S = 0,$$

in which the second integral takes the given form due to the fact that the boundary moves with the interfacial velocity. For the same reason, the volume of the control volume changes over time.

We assume that there is no mass transfer between the fluids, so (2.5) can be substituted, so that the contribution of the interface becomes zero. Since the wall face is impenetrable,

its contribution is also zero. Therefore, using the averaging definitions given above, the mass balance for the lower fluid control volume centered at s can be written as

$$\frac{\mathrm{d}}{\mathrm{d}t}\left(\{\rho\}_L(t)V_L(t)\right)+\langle\rho u\rangle_L(s+\delta s/2,t)\,A_L(s+\delta s/2,t) - \langle\rho u\rangle_L(s-\delta s/2,t)\,A_L(s-\delta s/2,t)=0.$$

For small δs, the volume average can be approximated by a cross-sectional average, and the volume can be approximated by $V_L(t)\approx A_L(s,t)\delta s$. Substituting these approximations, dividing by δs, and taking the limit $\delta s\longrightarrow 0$ yields

$$\frac{\partial}{\partial t}\left(\langle\rho\rangle_L(s,t)A_L(s,t)\right)+\frac{\partial}{\partial s}\left(\langle\rho u\rangle_L(s,t)A_L(s,t)\right)=0.$$

The last approximation in the derivation of the lower fluid's mass conservation equation is to equate the average of a product to the product of averages: $\langle\rho u\rangle_L\approx\langle\rho\rangle_L\langle u\rangle_L$. Finally, simplifying the notation of the cross-sectional averages to $\langle\xi\rangle_L(s,t)=\xi_L(s,t)$ yields

$$\frac{\partial}{\partial t}\left(\rho_L A_L\right)+\frac{\partial}{\partial s}\left(\rho_L u_L A_L\right)=0. \tag{2.9}$$

which is the conservative form of the mass conservation equation for the lower fluid in the TFM. The conservation equation for the mass of the upper fluid is derived in the same way and is given by

$$\frac{\partial}{\partial t}\left(\rho_U A_U\right)+\frac{\partial}{\partial s}\left(\rho_U u_U A_U\right)=0. \tag{2.10}$$

2.4 Momentum equations

The momentum conservation equation (2.2) has three vector components. In the two-fluid model, we only resolve the streamwise momentum equation, which is an equation for the cross-sectionally averaged streamwise velocities (per fluid). Along the h-direction the momentum equation will be simplified to a hydrostatic balance, and along the z-direction we will assume the pressure is uniform (see section 2.4.2). This implies that the (variation of) v and w are negligible, and through the continuity equation $\nabla\cdot\mathbf{u}=0$ ($\mathbf{u}$ being the combined velocity field before averaging), the conclusion is that the streamwise scale over which variations in the flow occur must be much larger than the normal and horizontal scales over which variations occur: $L\gg H$ [120, p. 51]. This is known as the *long wavelength assumption* [87, p. 79]. This does *not* mean that the (unaveraged) streamwise velocity cannot vary along the h and z axes: it surely will, see the velocity profile in Figure 2.3.

2.4.1 Advective terms

We write the advective part of (2.2) for the lower control volume, in the streamwise direction:

$$\frac{\mathrm{d}}{\mathrm{d}t}\int_{V_L}\rho u\,\mathrm{d}V+\int_{S_{L\mathrm{int}}}\rho u(\mathbf{u}-\mathbf{u}_{\mathrm{int}})\cdot\mathbf{n}\,\mathrm{d}S+\int_{S_{L+}}\rho u(\mathbf{u}\cdot\mathbf{n})\,\mathrm{d}S + \int_{S_{LW}}\rho u(\mathbf{u}\cdot\mathbf{n})\,\mathrm{d}S+\int_{S_{L-}}\rho u(\mathbf{u}\cdot\mathbf{n})\,\mathrm{d}S=0,$$

where $\mathbf{n}$ is the outward facing normal vector. For the same reasons as in the mass equations, the contributions of the interface and wall faces are zero. In terms of averages the equation can be written as

$$\frac{\mathrm{d}}{\mathrm{d}t}\left(\{\rho u\}_L(t)V_L(t)\right) + \left\langle \rho u^2 \right\rangle_L (s+\delta s/2,t)A_L(s+\delta s/2,t) - \left\langle \rho u^2 \right\rangle_L (s-\delta s/2,t)A_L(s-\delta s/2,t) = 0.$$

With the same procedure as taken for the mass equations, and additionally the assumption $\left\langle \rho u^2 \right\rangle_L \approx \left\langle \rho \right\rangle_L \left\langle u \right\rangle_L^2$, this becomes

$$\frac{\partial}{\partial t}\left(\rho_L u_L A_L\right) + \frac{\partial}{\partial s}\left(\rho_L u_L^2 A_L\right) = 0. \tag{2.11}$$

For the upper fluid we obtain

$$\frac{\partial}{\partial t}\left(\rho_U u_U A_U\right) + \frac{\partial}{\partial s}\left(\rho_U u_U^2 A_U\right) = 0. \tag{2.12}$$

2.4.2 Pressure terms

For the lower control volume, the pressure terms in (2.2) take the following form:

$$\oint_S \mathbf{e}_s \cdot p\mathbf{n}\,\mathrm{d}S = \int_{S_{L+}} \mathbf{e}_s \cdot p\mathbf{n}\,\mathrm{d}S + \int_{S_{L-}} \mathbf{e}_s \cdot p\mathbf{n}\,\mathrm{d}S + \int_{S_{\mathrm{Lint}}} \mathbf{e}_s \cdot p\mathbf{n}\,\mathrm{d}S + \int_{S_{LW}} \mathbf{e}_s \cdot p\mathbf{n}\,\mathrm{d}S, \tag{2.13}$$

in which $\mathbf{e}_s$ is the unit vector in the streamwise direction. We assume that the pipe is of constant cross-section, so that in the last term $\mathbf{e}_s \cdot \mathbf{n} = \mathbf{e}_s \cdot \mathbf{n}_{LW} = 0$, and it drops out. The first and second terms on the right-hand side can be written in terms of A_L:

$$\int_{S_{L+}} \mathbf{e}_s \cdot p\mathbf{n}\,\mathrm{d}S + \int_{S_{L-}} \mathbf{e}_s \cdot p\mathbf{n}\,\mathrm{d}S = \left\langle p \right\rangle_L (s+\delta s/2,t)A_L(s+\delta s/2,t) - \left\langle p \right\rangle_L (s-\delta s/2,t)A_L(s-\delta s/2,t).$$

For the third term, we note that an integral over the interface can be written as an integral over the perimeter P_{int} spanned by the interface, and the length of the control volume, in the following manner:

$$\int_{S_{\mathrm{Lint}}} \mathrm{d}S = \int_{s-\delta s/2}^{s+\delta s/2} \int_{P_{\mathrm{int}}} \mathrm{d}P \frac{\mathrm{d}s}{|\mathbf{e}_h \cdot \mathbf{n}_{\mathrm{Lint}}|},$$

with $|\mathbf{e}_h \cdot \mathbf{n}_{\mathrm{Lint}}| = \cos\zeta$, as depicted in Figure 2.5. Here we have assumed that the interface is flat along the z-coordinate. Next, note that $\mathbf{e}_s \cdot \mathbf{n}_{\mathrm{Lint}} = \cos(\pi/2-\zeta) = \sin\zeta$, and that $\partial H_L/\partial s = -\sin\zeta/\cos\zeta$. Using these relations, the third term on the right-hand side of (2.13) can be written in terms of the interface height H_L [104]:

$$\int_{S_{\mathrm{Lint}}} \mathbf{e}_s \cdot p\mathbf{n}\,\mathrm{d}S = \int_{S_{\mathrm{Lint}}} p\mathbf{e}_s \cdot \mathbf{n}\,\mathrm{d}P \frac{\mathrm{d}s}{|\mathbf{e}_h \cdot \mathbf{n}_{\mathrm{Lint}}|} = \int_{S_{\mathrm{Lint}}} p\frac{\mathbf{e}_s \cdot \mathbf{n}_{\mathrm{Lint}}}{|\mathbf{e}_h \cdot \mathbf{n}_{\mathrm{Lint}}|}\,\mathrm{d}P\,\mathrm{d}s = -\int_{S_{\mathrm{Lint}}} p\frac{\partial H_L}{\partial s}\,\mathrm{d}P\,\mathrm{d}s.$$

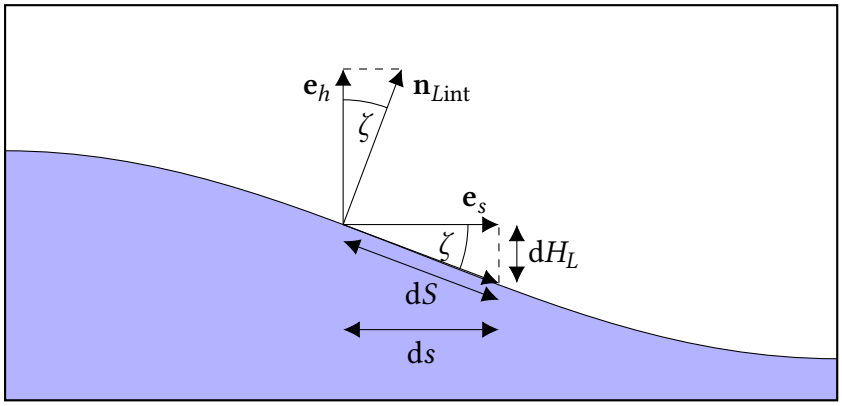

Figure 2.5: Illustration of the geometry of the integral over the interface.

Combining terms, dividing by δs, and taking its limit to zero, the right-hand side of (2.13) becomes

$$\begin{aligned}
\frac{\partial}{\partial s}\left(\langle p\rangle_L A_L\right) - \int_{P_{\text{int}}} p\frac{\partial H_L}{\partial s}\,\mathrm{d}P &= \frac{\partial}{\partial s}\left(\langle p\rangle_L A_L\right) - p_{\text{int},L}\frac{\partial H_L}{\partial s}\int_{P_{\text{int}}}\mathrm{d}P \\
&= \frac{\partial}{\partial s}\left(\langle p\rangle_L A_L\right) - p_{\text{int},L}\frac{\partial A_L}{\partial s} \\
&= \frac{\partial}{\partial s}\left(\left(\langle p\rangle_L - p_{\text{int},L}\right)A_L\right) + \frac{\partial}{\partial s}\left(p_{\text{int,L}}A_L\right) - p_{\text{int},L}\frac{\partial A_L}{\partial s} \\
&= \frac{\partial}{\partial s}\int_0^{H_L}(p - p_{\text{int,L}})w(h)\,\mathrm{d}h + A_L\frac{\partial p_{\text{int,L}}}{\partial s},
\end{aligned} \tag{2.14}$$

where we have assumed that p is independent of z and that the interface is flat along the cross section. Here $p_{\text{int},L}$ is the pressure at the interface, on the side of the lower fluid. Similarly, for the upper fluid, we have

$$\frac{\partial}{\partial s}\left(\langle p\rangle_U A_U\right) - \int_{P_{\text{int}}} p\frac{\partial H_U}{\partial s}\,\mathrm{d}P = \frac{\partial}{\partial s}\int_{H_L}^{H}(p - p_{\text{int,U}})\,w(h)\mathrm{d}h + A_U\frac{\partial p_{\text{int,U}}}{\partial s}, \tag{2.15}$$

with $p_{\text{int},U}$ the pressure at the interface on the side of the upper fluid.

We assume hydrostatic balance within the phases (which can be derived from the momentum equation in the h-direction if v or its acceleration is assumed negligible):

$$\begin{aligned}
p - p_{\text{int,L}} &= -g_n\rho_L(h - H_L), \\
p - p_{\text{int,U}} &= -g_n\rho_U(h - H_L),
\end{aligned}$$

with $g_n = g\cos(\phi)$ the normal component of gravity (see Figure 2.3). Substituting these

relations in the first terms of (2.14) and (2.15) yields

$$\frac{\partial}{\partial s}\int_0^{H_L}(p-p_{\text{int,L}})w(h)\,\mathrm{d}h = -\frac{\partial}{\partial s}\left(\rho_L g_n \widehat{H}_L\right),$$
$$\frac{\partial}{\partial s}\int_{H_L}^{H}(p-p_{\text{int,U}})w(h)\,\mathrm{d}h = -\frac{\partial}{\partial s}\left(\rho_U g_n \widehat{H}_U\right),$$

with $\widehat{H}_L$ and $\widehat{H}_U$ general geometric functions of A_L and A_U, respectively, for which definitions are given in Appendix A. These terms are known as the 'level gradient' or 'hydraulic gradient' terms, and describe the effect of the hydrostatic variation of the pressure.

Assuming that the pressure is continuous across the interface: $p_{\text{int,L}} = p_{\text{int,U}} = p_{\text{int}}$, the second terms of (2.14) and (2.15) can be simplified. The added terms on the right hand side of the momentum equations become (adding the minus signs present in (2.2) again)

$$\frac{\partial}{\partial s}\left(\rho_L g_n \widehat{H}_L\right) - A_L\frac{\partial p_{\text{int}}}{\partial s}, \tag{2.16}$$
$$\frac{\partial}{\partial s}\left(\rho_U g_n \widehat{H}_U\right) - A_U\frac{\partial p_{\text{int}}}{\partial s}. \tag{2.17}$$

2.4.3 Surface tension

Surface tension enters the equations through the interface condition (2.7). Instead of the assumption $p_{\text{int,L}} = p_{\text{int,U}} = p_{\text{int}}$, we allow the pressure to be discontinuous across the interface. The pressure difference is given by [87, 96]

$$\Delta p_{\text{int}} = p_{\text{int},U} - p_{\text{int},L} = -\sigma\kappa = \sigma\frac{\partial^2 H_L}{\partial s^2}\left[1+\left(\frac{\partial H_L}{\partial s}\right)^2\right]^{-3/2}.$$

This is the so-called Young-Laplace equation for the two-fluid model (in which the interface is assumed flat along z). Here we have left out the viscous terms in (2.7), which involve the interface-normal spatial derivative of the interface-normal velocity, and can typically be neglected with respect to the pressure terms [58]. Typically the assumption $(\partial H_L/\partial s \ll 1)^2$ will be made (see e.g. [6]) to approximate Δp_{int} as

$$\Delta p_{\text{int}} \approx \sigma\frac{\partial^2 H_L}{\partial s^2} \approx \frac{\sigma}{P_{\text{int}}}\frac{\partial^2 A_L}{\partial s^2}. \tag{2.18}$$

We revisit the derivation of section 2.4.2, and this time do not assume that the pressure is continuous across the interface. We choose to define the reference pressure as the interface pressure of the upper fluid, $p_{\text{int}} = p_{\text{int,U}}$, so that nothing changes in the upper momentum equation. Then the pressure term on the right hand side of the lower momentum equation can be expressed in terms of this reference pressure, and the pressure jump:

$$-A_L\frac{\partial p_{\text{int,}L}}{\partial s} = -A_L\frac{\partial}{\partial s}\left(p_{\text{int}} - \Delta p_{\text{int}}\right) = -A_L\frac{\partial p_{\text{int}}}{\partial s} + A_L\frac{\partial \Delta p_{\text{int}}}{\partial s}. \tag{2.19}$$

The result is a combination of the typical pressure term and an additional surface tension term, in which (2.18) should be substituted. This form of the surface tension is similar to that of [46].

2.4.4 Stress terms

For the lower control volume, the stress terms in (2.2) take the following form:

$$\oint_S \mathbf{e}_s \cdot \boldsymbol{\tau} \cdot \mathbf{n}\,\mathrm{d}S = \int_{S_{L\mathrm{int}}} \mathbf{e}_s \cdot \boldsymbol{\tau} \cdot \mathbf{n}\,\mathrm{d}S + \int_{S_{L+}} \mathbf{e}_s \cdot \boldsymbol{\tau} \cdot \mathbf{n}\,\mathrm{d}S + \int_{S_{LW}} \mathbf{e}_s \cdot \boldsymbol{\tau} \cdot \mathbf{n}\,\mathrm{d}S + \int_{S_{L-}} \mathbf{e}_s \cdot \boldsymbol{\tau} \cdot \mathbf{n}\,\mathrm{d}S, \quad (2.20)$$

where $\mathbf{n}$ is the outward facing normal vector. The relevant stresses are the stresses acting on the streamwise momentum balance, with $\mathbf{e}_h$ the unit vector in the h-direction, and $\mathbf{e}_z$ the unit vector in the z-direction:

$$\mathbf{e}_s \cdot \boldsymbol{\tau} \cdot \mathbf{n} = \tau_{ss}(\mathbf{e}_s \cdot \mathbf{n}) + \tau_{sh}(\mathbf{e}_h \cdot \mathbf{n}) + \tau_{sz}(\mathbf{e}_z \cdot \mathbf{n}).$$

Following the geometric analysis given in section 2.4.2, the interface term in (2.20) can be written as

$$\int_{S_{L\mathrm{int}}} \mathbf{e}_s \cdot \boldsymbol{\tau} \cdot \mathbf{n}\,\mathrm{d}S = \int_{s-\delta s/2}^{s+\delta s/2} \int_{P_{\mathrm{int}}} \frac{\mathbf{e}_s \cdot \boldsymbol{\tau} \cdot \mathbf{n}_{L\mathrm{int}}}{|\mathbf{e}_h \cdot \mathbf{n}_{L\mathrm{int}}|}\,\mathrm{d}P\,\mathrm{d}s.$$

Similarly, the wall term in (2.20) can be written as

$$\int_{S_{LW}} \mathbf{e}_s \cdot \boldsymbol{\tau} \cdot \mathbf{n}\,\mathrm{d}S = \int_{s-\delta s/2}^{s+\delta s/2} \int_{P_{\mathrm{int}}} \frac{\mathbf{e}_s \cdot \boldsymbol{\tau} \cdot \mathbf{n}_{LW}}{|\mathbf{e}_h \cdot \mathbf{n}_{LW}|}\,\mathrm{d}P\,\mathrm{d}s.$$

The streamwise terms can be written as

$$\int_{S_{L+}} \mathbf{e}_s \cdot \boldsymbol{\tau} \cdot \mathbf{n}\,\mathrm{d}S + \int_{S_{L-}} \mathbf{e}_s \cdot \boldsymbol{\tau} \cdot \mathbf{n}\,\mathrm{d}S = \langle \tau_{ss} \rangle_L (s+\delta s/2, t) A_L (s+\delta s/2, t) - \langle \tau_{ss} \rangle_L (s-\delta s/2, t) A_L (s-\delta s/2, t).$$

For the combined stress terms, dividing by δs yields

$$\int_{P_{\mathrm{int}}} \frac{\mathbf{e}_s \cdot \boldsymbol{\tau} \cdot \mathbf{n}_{L\mathrm{int}}}{|\mathbf{e}_h \cdot \mathbf{n}_{L\mathrm{int}}|}\,\mathrm{d}P + \int_{P_L} \frac{\mathbf{e}_s \cdot \boldsymbol{\tau} \cdot \mathbf{n}_{LW}}{|\mathbf{e}_h \cdot \mathbf{n}_{LW}|}\,\mathrm{d}P + \frac{\partial}{\partial s}\left(\langle \tau_{ss} \rangle_L A_L\right).$$

We define the perimeter-averaged stresses

$$\tau_{L\mathrm{int}} = \frac{1}{P_{\mathrm{int}}} \int_{P_{\mathrm{int}}} \frac{\mathbf{e}_s \cdot \boldsymbol{\tau} \cdot \mathbf{n}_{L\mathrm{int}}}{|\mathbf{e}_h \cdot \mathbf{n}_{L\mathrm{int}}|}\,\mathrm{d}P, \quad \tau_L = \frac{1}{P_L} \int_{P_L} \frac{\mathbf{e}_s \cdot \boldsymbol{\tau} \cdot \mathbf{n}_{LW}}{|\mathbf{e}_h \cdot \mathbf{n}_{LW}|}\,\mathrm{d}P,$$

which allows us to write the combined stress terms as

$$\tau_L P_L + \tau_{L\mathrm{int}} P_{\mathrm{int}} + \frac{\partial}{\partial s}\left(\langle \tau_{ss} \rangle_L A_L\right).$$

Likewise, for the upper control volume, we have

$$\tau_U P_U + \tau_{U\mathrm{int}} P_{\mathrm{int}} + \frac{\partial}{\partial s}\left(\langle \tau_{ss} \rangle_U A_U\right),$$

with

$$\tau_{U\mathrm{int}} = \frac{1}{P_{\mathrm{int}}} \int_{P_{\mathrm{int}}} \frac{\mathbf{e}_s \cdot \boldsymbol{\tau} \cdot \mathbf{n}_{U\mathrm{int}}}{|\mathbf{e}_h \cdot \mathbf{n}_{U\mathrm{int}}|}\,\mathrm{d}P, \quad \tau_U = \frac{1}{P_U} \int_{P_U} \frac{\mathbf{e}_s \cdot \boldsymbol{\tau} \cdot \mathbf{n}_{UW}}{|\mathbf{e}_h \cdot \mathbf{n}_{UW}|}\,\mathrm{d}P.$$

The tangential stresses present in (2.8) will typically dominate the normal stresses present in (2.7). Adding to this that the pressure terms in (2.7) have already been balanced against the surface tension terms, the two interface conditions determine that the stress must be continuous across the interface. Therefore, we can define a single interface stress

$$\tau_{\text{int}} = \tau_{U\text{int}} = \frac{1}{P_{\text{int}}} \int_{P_{\text{int}}} \frac{\mathbf{e}_s \cdot \boldsymbol{\tau} \cdot \mathbf{n}_{U\text{int}}}{|\mathbf{e}_h \cdot \mathbf{n}_{U\text{int}}|} \, \mathrm{d}P = -\tau_{L\text{int}} = -\frac{1}{P_{\text{int}}} \int_{P_{\text{int}}} \frac{\mathbf{e}_s \cdot \boldsymbol{\tau} \cdot \mathbf{n}_{L\text{int}}}{|\mathbf{e}_h \cdot \mathbf{n}_{L\text{int}}|} \, \mathrm{d}P.$$

With this sign convention, the stresses τ_L, τ_U, and τ_{int} are negative for the velocity profile given in Figure 2.3. Since the velocity field is not resolved, and $\boldsymbol{\tau}(\mathbf{u}(\mathbf{x}, t))$ is not known, closure relations need to be introduced for τ_L, τ_U, and τ_{int}, which express these stresses in terms of known cross-sectionally averaged variables. They are typically modeled in the following manner [116]:

$$\tau_L = -\frac{1}{2} f_L \rho_L u_L |u_L|, \quad \tau_U = -\frac{1}{2} f_U \rho_U u_U |u_U|, \quad \tau_{\text{int}} = -\frac{1}{2} f_{\text{int}} \rho_U (u_U - u_L) |u_U - u_L|,$$

in which f_L, f_U, and f_{int} are Fanning friction factors which require further closure relations. These can be based on experiments or numerical simulations (see [19] for an overview, and section 5.A for some specific examples).

The streamwise stress terms

$$\langle \tau_{ss} \rangle_L = \int_{A_L} \tau_{ss} \, \mathrm{d}A \quad \text{and} \quad \langle \tau_{ss} \rangle_U = \int_{A_U} \tau_{ss} \, \mathrm{d}A$$

also require closure. In [35, 63] the effective stresses are determined to be given by

$$\langle \tau_{ss} \rangle_L = \rho_L \nu_{\text{eff},L} \frac{\partial u_L}{\partial s} \quad \text{and} \quad \langle \tau_{ss} \rangle_U = \rho_U \nu_{\text{eff},U} \frac{\partial u_U}{\partial s},$$

which makes the associated terms in the model act as (momentum) diffusion along the streamwise axis. In [44, 46] the effective viscosity of each fluid is modeled as a combination of the material viscosity ν_m, and the turbulent viscosity ν_t:

$$\nu_{\text{eff}} = C_\epsilon (\nu_m + \nu_t),$$

with C_ϵ an adjustment factor to scale the dissipation of the 1D model so that it agrees with its multidimensional counterpart.

Finally, the contributions to the right-hand side of the momentum equations are given by

$$\tau_L P_L - \tau_{\text{int}} P_{\text{int}} + \frac{\partial}{\partial s} \left(\rho_L \nu_{\text{eff},L} A_L \frac{\partial u_L}{\partial s} \right), \tag{2.21}$$

$$\tau_U P_U + \tau_{\text{int}} P_{\text{int}} + \frac{\partial}{\partial s} \left(\rho_U \nu_{\text{eff},U} A_U \frac{\partial u_U}{\partial s} \right). \tag{2.22}$$

2.4.5 Gravity terms

The gravity terms in (2.2) take the following form:

$$\int_V \mathbf{e}_s \cdot \rho \mathbf{g} \, \mathrm{d}V = -\int_V \rho g_s \, \mathrm{d}V = -\{\rho g_s\}_L V_L = -\langle \rho g_s \rangle_L A_L \delta s = -\rho_L A_L g_s \delta s,$$

with $g_s = g \sin(\phi)$ the streamwise component of gravity. Dividing by δs yields

$$-\rho_L A_L g_s. \tag{2.23}$$

Likewise, for the upper fluid, we have

$$-\rho_U A_U g_s. \tag{2.24}$$

2.4.6 Combined results

Finally, we add the contributions from (2.16) (2.17), (2.19), (2.21), (2.22), (2.23), and (2.24) to the right-hand sides of (2.11) and (2.12) to obtain the momentum equations of the TFM. This yields

$$\begin{aligned}\frac{\partial}{\partial t}\left(\rho_L u_L A_L\right) + \frac{\partial}{\partial s}\left(\rho_L u_L^2 A_L - \rho_L g_n \widehat{H}_L\right) = -A_L \frac{\partial p}{\partial s} + \sigma A_L \frac{\partial^3 H_L}{\partial s^3} - \rho_L A_L g_s \\ + \tau_L P_L - \tau_{\text{int}} P_{\text{int}} + \frac{\partial}{\partial s}\left(\rho_L \nu_{\text{eff},L} A_L \frac{\partial u_L}{\partial s}\right)\end{aligned} \tag{2.25}$$

for the lower fluid, and

$$\begin{aligned}\frac{\partial}{\partial t}\left(\rho_U u_U A_U\right) + \frac{\partial}{\partial s}\left(\rho_U u_U^2 A_U - \rho_U g_n \widehat{H}_U\right) = -A_U \frac{\partial p}{\partial s} - \rho_U A_U g_s \\ + \tau_U P_U + \tau_{\text{int}} P_{\text{int}} + \frac{\partial}{\partial s}\left(\rho_U \nu_{\text{eff},U} A_U \frac{\partial u_U}{\partial s}\right).\end{aligned} \tag{2.26}$$

for the upper fluid, where we have redefined $p = p_{\text{int}}$. Often, the surface tension and diffusion terms in these equations will be left out, due to being short scale effects, that can be neglected due to the long-wavelength assumption. Together, (2.9), (2.10), (2.25) and (2.26) form the governing equations of the TFM. The volume constraint

$$A_L + A_U = A, \tag{2.27}$$

with A constant, closes the equations (which possess five unknowns).

2.5 Summary of the assumptions

The assumptions made in the derivation of the TFM can be summarized as follows:

- The flow is assumed to be isothermal, so no energy balance is needed as a part of the model.
- The interface height H_L can be given as a function of s; nowhere is any of the lower fluid located above any of the upper fluid. This means that waves cannot overturn, or at least that this cannot be modeled explicitly.

- There is no mass transfer between the two fluids. The fluids are immiscible, with a sharp interface that moves with the local fluid velocity.
- The average of a product is approximated by a product of averages: $\langle \xi^2 \rangle \approx \langle \xi \rangle \langle \xi \rangle$. A more advanced option is the introduction of momentum flux parameters [109].
- The duct cross section is constant along the streamwise axis, and constant in time.
- The flow is assumed to be incompressible, so that instead of using equations of state $\rho(p)$, we take ρ_U and ρ_L to be constants.
- Normal velocities are assumed negligible, so that along the h-direction the flow is in hydrostatic balance. The hydrostatic balance assumption reduces the two pressure variables to one variable p (defined at the interface).
- Along the z-direction the pressure is assumed constant. The velocity is negligible in the z-direction, and the interface is flat in the z-direction.
- The assumption of hydrostatic balance implies that the streamwise length scale of the flow is much larger than the normal length scale (i.e. the pipe diameter). This is called the long wavelength assumption [56, 87], and it is shared with the shallow water equations [71, p. 721]. It means that the 1D TFM does not accurately model short-wavelength phenomena.
- For wall and interface friction closure terms are introduced. These are usually formulated assuming steady state flow.

The resulting model is similar to the two-layer shallow water equations [1], with as important differences:

- The existence of the pressure as a variable in the TFM, and the presence of the volume constraint (2.27), which dictates that the fluids together fill the duct. The Poisson equation for the pressure enforces the constraint (see chapter 4).
- The use of arbitrary duct cross-sectional shapes (geometries). This means that in the relations
$$A_L = \int_0^{H_L} w(h)\,\mathrm{d}h \quad \text{and} \quad A_U = \int_{H_L}^{H} w(h)\,\mathrm{d}h,$$
the duct width $w(h)$ may be an arbitrary function of h. Two important examples are the 2D channel and the circular pipe, for which the relations between the cross sections and the fluid heights (H_L and H_U) are given in Appendix A.

In the rest of this thesis, we will work with the TFM as derived in this chapter. In chapter 3 we will analyze a basic form of the model, without source terms or higher order terms. Chapter 4 deals with a variant of the model in which the pressure is eliminated. Finally, chapter 5 analyzes the full model, with all of the physical terms included in this derivation. In each case, we will be bound by the assumptions listed here.

3

Energy-conserving formulation of the basic two-fluid model

We show that the one-dimensional (1D) two-fluid model (TFM) for stratified flow in channels and pipes (in its incompressible, isothermal form) satisfies an energy conservation equation, which arises naturally from the mass and momentum conservation equations that constitute the model. This result extends upon earlier work on the shallow water equations, with the important difference that we include non-conservative pressure terms in the analysis, and that we propose a formulation that holds for ducts with an arbitrary cross-sectional shape, with the 2D channel and circular pipe geometries as special cases.

The second novel result of this chapter is the formulation of a finite volume scheme for the TFM that satisfies a discrete form of the continuous energy equation. This discretization is derived in a manner that runs parallel to the continuous analysis. Due to the non-conservative pressure terms it is essential to employ a staggered grid, which requires careful consideration in defining the discrete energy and energy fluxes, and the relations between them and the discrete model. Numerical simulations confirm that the discrete energy is conserved.

This chapter is based on the article "Energy-conserving formulation of the two-fluid model for incompressible two-phase flow in channels and pipes", published in *Computers & Fluids*, 244:105533, 2022 [20].

3.1 Introduction

The one-dimensional (1D) two-fluid model (TFM) is a dynamic model for stratified flow in channels and pipes. It simplifies the full three-dimensional multiphase flow problem by resolving only the cross-sectionally averaged quantities (hold-ups, velocities, and pressure), which are often of practical interest. There are many variants of the model, but the basic idea, of two interacting fluids whose behavior is cross-sectionally averaged to obtain a 1D model, was introduced by Wallis (1969) [127] and Ishii (1975) [57]. The model has among others applications in the oil and gas industry [48], in CO_2 transport and storage [4], and in nuclear reactor safety analysis [8].

An unsolved issue with the basic version of the TFM is that the initial value problem for the governing equations is only conditionally well-posed [81]. This means that it is well-posed for some flow configurations and ill-posed for others (e.g. when there is a large velocity difference between the two fluids). Conventionally, ill-posedness of the TFM is demonstrated by a linear stability analysis which shows an unbounded growth rate for the smallest wavelengths, when the values of the model variables are such that the eigenvalues are complex. In this case the solution is said to carry no physical meaning [74]. However, when drawing conclusions on the well-posedness of the TFM, it is important to also consider its nonlinear aspects, and not only rely on a linearized analysis [70, 111]. Examples of studies that have included nonlinear effects in the TFM analysis can be found in [65, 76]. However, a complete nonlinear analysis, with implications for obtaining a robust discretization, is still missing.

In this work, we strive towards such a nonlinear analysis by presenting an expression for an energy which is conserved by the full (nonlinear) TFM, in its incompressible and isothermal form. This approach is motivated by the fact that for the incompressible Navier-Stokes equations such an analysis provides stability estimates [29, 103], and that for compressible equations it is closely related to the concept of entropy stability [114]. Important to note is that such an energy is not the thermodynamic energy for which a separate conservation equation exists in the compressible TFM. Rather, the considered energy conservation is an inherent property of the mass and momentum conservation equations that constitute the incompressible TFM: the energy is a secondary conserved quantity of the model. Its physical meaning is therefore the mechanical energy of the system (kinetic plus potential energy).

In order to derive this mechanical energy equation, we take the approach from [43], in which the dot product of the shallow water equations (SWE) and a vector of entropy variables is taken in such a way that a scalar energy equation results. However, an important difference with the SWE (and two-layer SWE [41]) is the presence of non-conservative pressure terms that are linked to the constraint that the fluid phases have to fill the cross section. Another important difference is that we consider arbitrary duct geometries, as opposed to the 1D SWE which in effect utilizes a planar channel geometry. Given these differences, the key challenge is thus to find a conserved energy and corresponding energy flux function for the TFM, and this will be the first main focus of this chapter.

The second focus of this chapter is to derive a spatial discretization which conserves a discrete version of the energy. Again, our approach is inspired by methods which have been developed for the SWE [42]. An important difference is that these methods are designed for collocated grids, while we will adapt them to a staggered grid. This is motivated

by the presence of the (non-conservative) pressure terms in the TFM, which makes the use of a staggered grid much more convenient (similar to the case of the incompressible Navier-Stokes equations [29]). However, the staggered grid introduces new challenges, for example in terms of the definitions of the energy and energy fluxes. We will formulate a discretization method that tackles these issues and yields, in a constructive manner, a new set of numerical fluxes on a staggered grid that is energy-conserving. Our approach adheres to the conservative form of the model, and therefore yields a discretization that satisfies the proper shock conditions. This discretization can also be viewed as an extension (to the TFM) of the staggered grid SWE discretization found in [122], although that discretization is derived using a rather different approach (based on a comparison to the compressible Euler equations and arguments on skew-symmetric operators).

Since our discretization takes the form of a finite volume scheme, mass and total momentum are also conserved, along with energy. These discrete conservation properties match the properties of the continuous equations, and improve the physical fidelity of long-term numerical simulations, by preventing artificial (numerical) damping or amplification of the flow. This will be illustrated in this chapter by a sloshing test case in a closed tank, which in absence of viscosity will constantly remain in motion, like an undamped pendulum.

This chapter is set up as follows. First, in section 3.2 we present the governing equations of the TFM. In section 3.3 we discuss the conditions for energy conservation, and introduce an energy and energy flux that satisfies these conditions, providing local and global energy conservation equations for the continuous TFM. We outline how the equations are discretized in section 3.4, while leaving open the specific form of the numerical fluxes. Then, in section 3.5, we present the discrete versions of the continuous conditions for energy conservation, and propose a set of new conservative numerical fluxes. Finally, in section 3.6 we present numerical results which demonstrate exact conservation of the aforementioned energy.

3.2 Governing equations

The 1D TFM, as considered in this work, describes the separated flow of a (heavier) lower fluid L and a (lighter) upper fluid U through a channel or pipe. It can be derived by applying a cross-sectional averaging procedure to the Navier-Stokes equations [59, 111]. An important assumption made in the derivation of the model is that the streamwise length scale is much larger than the normal length scale (i.e. the pipe diameter), which is referred to as the long wavelength assumption. As a consequence, along the normal direction the flow is in hydrostatic balance. We will omit source terms, such as wall friction, since such terms are sources or sinks of energy, and we are interested in the energy conservation properties of the core model. Good discussions of the assumptions underlying the TFM are given by [87, 90].

The cross-sectionally averaged equations can be written in the following concise form [106, 107] (with $\mathbf{q} = \mathbf{q}(s,t)$):

$$\frac{\partial \mathbf{q}}{\partial t} + \frac{\partial \mathbf{f}(\mathbf{q})}{\partial s} + \mathbf{j}(\mathbf{q})\frac{\partial p}{\partial s} = \mathbf{0}, \tag{3.1}$$

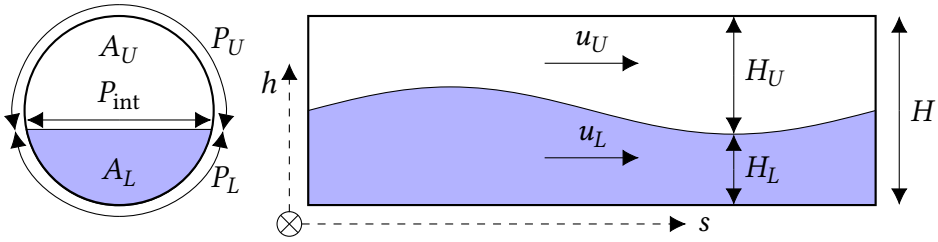

Figure 3.1: A schematic of stratified two-fluid flow in ducts (a circular pipe segment is shown as an example) described by the 1D TFM.

where $\mathbf{q}$ constitutes the vector of 'conserved' variables[1], namely the mass and momentum of each phase:

$$\mathbf{q}^T = \begin{bmatrix} q_1 & q_2 & q_3 & q_4 \end{bmatrix} = \begin{bmatrix} \rho_U A_U & \rho_L A_L & \rho_U u_U A_U & \rho_L u_L A_L \end{bmatrix}.$$

Here ρ_U and ρ_L are the densities, A_U and A_L are the cross sections, and u_U and u_L are the averaged velocities, all of the upper and lower fluids, respectively. The superscript T indicates a transpose. We consider the isothermal, incompressible case, so that ρ_U and ρ_L are constant.

The fluxes $\mathbf{f}$ describe convection of mass and momentum and gradients in the interface level. In terms of $\mathbf{q}$ they are given by

$$\mathbf{f}(\mathbf{q}) = \begin{bmatrix} q_3 \\ q_4 \\ \frac{q_3^2}{q_1} - \rho_U g_n \widehat{H}_U \\ \frac{q_4^2}{q_2} - \rho_L g_n \widehat{H}_L \end{bmatrix} = \begin{bmatrix} \rho_U u_U A_U \\ \rho_L u_L A_L \\ \rho_U u_U^2 A_U - \rho_U g_n \widehat{H}_U \\ \rho_L u_L^2 A_L - \rho_L g_n \widehat{H}_L \end{bmatrix}, \tag{3.2}$$

where $\widehat{H}_U = \widehat{H}_U(\mathbf{q})$ and $\widehat{H}_L = \widehat{H}_L(\mathbf{q})$ are geometric terms (to be discussed shortly), and g_n is the gravitational acceleration in the normal direction.

The fifth variable is the interface pressure p, and the non-conservative pressure terms are given by $\mathbf{j}(\partial p/\partial s)$ with

$$\mathbf{j}(\mathbf{q})^T = \begin{bmatrix} 0 & 0 & \frac{q_1}{\rho_U} & \frac{q_2}{\rho_L} \end{bmatrix} = \begin{bmatrix} 0 & 0 & A_U & A_L \end{bmatrix}.$$

The quantities $\widehat{H}_U = \widehat{H}_U(A_U(q_1, \rho_U))$ and $\widehat{H}_L = \widehat{H}_L(A_L(q_2, \rho_L))$ are geometry-dependent and are defined by

$$\widehat{H}_U \coloneqq \int_{A_U} (h - H_L)\,\mathrm{d}A, \qquad \widehat{H}_L \coloneqq \int_{A_L} (h - H_L)\,\mathrm{d}A. \tag{3.3}$$

Here the difference between the coordinate h and the two-fluid interface height H_L is integrated over the area A_U occupied by the upper fluid and the area A_L occupied by

[1]Note that the pressure term is not in conservative form, so q_3 and q_4 individually are not conserved, but $q_3 + q_4$ is.

the lower fluid, respectively. Using these general expressions, the model equations are valid for arbitrarily shaped cross sections. See Appendix A for evaluations of the integrals for the 2D channel and circular pipe geometries. The spatial derivatives of $\widehat{H}_U$ and $\widehat{H}_L$ that appear in the fluxes $\mathbf{f}$ are known as the level gradient terms, which result from the hydrostatic variation of the pressure.

Since the upper and lower fluid together fill the pipe, the system is subject to the volume constraint

$$\frac{q_1}{\rho_U} + \frac{q_2}{\rho_L} = A. \tag{3.4}$$

The entire system therefore consists of four evolution equations plus one constraint, and four 'conserved' variables plus the pressure. In our incompressible setting, a derived constraint can be obtained by differentiating the constraint (3.4) and substituting the mass equations, leading to [107]:

$$\frac{\partial}{\partial s}\left(\frac{q_3}{\rho_U} + \frac{q_4}{\rho_L}\right) = 0, \tag{3.5}$$

which can be integrated in space to give that the volumetric flow Q is constant in space, and a function of time only:

$$Q(\mathbf{q}) = \frac{q_3}{\rho_U} + \frac{q_4}{\rho_L} = Q(t). \tag{3.6}$$

This derived constraint, termed the volumetric flow constraint, can be seen as the incompressibility constraint for the TFM.

We can use these constraints to set up an equation for the pressure. The pressure equation is obtained by summing the momentum equations [107]:

$$\mathbf{l}^T \mathbf{j} \frac{\partial p}{\partial s} = -\mathbf{l}^T \left(\frac{\partial \mathbf{q}}{\partial t} + \frac{\partial \mathbf{f}}{\partial s}\right), \quad \text{with} \quad \mathbf{l}^T = \begin{bmatrix} 0 & 0 & \frac{1}{\rho_U} & \frac{1}{\rho_L} \end{bmatrix},$$

which can be expanded and rewritten with the definition of Q to yield

$$\left(\frac{q_1}{\rho_U^2} + \frac{q_2}{\rho_L^2}\right)\frac{\partial p}{\partial s} = -\frac{\mathrm{d}Q}{\mathrm{d}t} - \frac{\partial}{\partial s}\left(\frac{f_3}{\rho_U} + \frac{f_4}{\rho_L}\right).$$

Finally, taking the derivative of this equation to s and applying constraint (3.5) gives

$$\frac{\partial}{\partial s}\left(\left(\frac{q_1}{\rho_U^2} + \frac{q_2}{\rho_L^2}\right)\frac{\partial p}{\partial s}\right) = -\frac{\partial^2}{\partial s^2}\left(\frac{f_3}{\rho_U} + \frac{f_4}{\rho_L}\right). \tag{3.7}$$

This is a 'Poisson-type' equation for the pressure, which can be used in place of (3.4) to close the system of equations. In our numerical algorithm (discussed in section 3.4) we apply a discrete version of (3.7) in this manner.

3.3 Energy conservation equation for the continuous TFM

3.3.1 Outline: conditions for energy conservation

Having set-up the TFM governing equations, the first key objective of this chapter is to prove *local* and *global* energy equalities that are *implied* by this equation set. This is similar to the energy analyses for e.g. the incompressible Navier-Stokes equations [29], the SWE [115], and the two-layer SWE [41]. In all these models, no energy conservation equation is included in the model, but energy conservation follows from the mass and momentum conservation equations alone. It can therefore be said that the energy is a secondary conserved quantity.

Our proof of global energy conservation follows the approach in [42, 43] and starts by showing that a local energy conservation equation of the form

$$\frac{\partial e}{\partial t} + \frac{\partial}{\partial s}\left(h_f + h_p\right) = 0 \tag{3.8}$$

can be derived, purely based on manipulating the governing equations, given by (3.1). Here $e(\mathbf{q})$ is the local energy, and $h_f(\mathbf{q})$ and $h_p(\mathbf{q})$ are energy fluxes (to be detailed later). If (3.8) holds, then it can be integrated in space to yield

$$\frac{\mathrm{d}E}{\mathrm{d}t} = -\left[h_f + h_p\right]_{s_1}^{s_2} = 0, \tag{3.9}$$

where the last equality ('=0') holds in case of periodic or closed boundaries, and the global energy $E(t)$ is defined as

$$E(t) \coloneqq \int_{s_1}^{s_2} e \,\mathrm{d}s. \tag{3.10}$$

The key is therefore to obtain the local energy conservation equation (3.8). To achieve this, one first postulates an energy $e(\mathbf{q})$ (typically guided by physical considerations). Second, one calculates the vector of so-called entropy variables, defined as[2]

$$\mathbf{v}(\mathbf{q}) \coloneqq \left[\frac{\partial e}{\partial \mathbf{q}}\right]^T.$$

Taking the dot product of the system (3.1) with $\mathbf{v}$ leads to

$$\left\langle \mathbf{v}, \frac{\partial \mathbf{q}}{\partial t} \right\rangle + \left\langle \mathbf{v}, \frac{\partial \mathbf{f}}{\partial s} \right\rangle + \left\langle \mathbf{v}, \mathbf{j}\frac{\partial p}{\partial s} \right\rangle = 0, \tag{3.11}$$

in which we have ignored source terms (as indicated before), and the brackets denote a dot product over the vector elements:

$$\langle \mathbf{x}, \mathbf{y} \rangle \coloneqq \mathbf{x}^T \mathbf{y}.$$

The time derivative term can be written as

$$\left\langle \mathbf{v}, \frac{\partial \mathbf{q}}{\partial t} \right\rangle = \left(\frac{\partial e}{\partial \mathbf{q}}\right)\frac{\partial \mathbf{q}}{\partial t} = \frac{\partial e}{\partial t},$$

[2] We take the convention that $\partial e/\partial \mathbf{q}$ is a row vector, making $\mathbf{v}$ a column vector.

so (3.11) becomes an equation for the time evolution of the energy.

Given an expression for e, the art is to find an energy flux h_f that satisfies

$$\langle \mathbf{v}, \frac{\partial \mathbf{f}}{\partial s} \rangle = \frac{\partial h_f}{\partial s}, \tag{3.12}$$

since then the second term in (3.11) can be written in the (locally) conservative form given by (3.8). In order to get a condition solely referring to the relations between different functions of $\mathbf{q}$ (i.e. independent of s), the chain rule (valid for smooth solutions) is employed to convert (3.12) to:

$$\langle \mathbf{v}, \frac{\partial \mathbf{f}}{\partial \mathbf{q}} \rangle = \frac{\partial h_f}{\partial \mathbf{q}}. \tag{3.13}$$

This is the condition encountered in e.g. [42] and [43] for an energy flux h_f to conserve a given energy e (or, more generally: entropy function) of the SWE.

Likewise, we need to find a flux h_p such that the product of $\mathbf{v}$ and the pressure gradient can be written in conservative form:

$$\langle \mathbf{v}, \mathbf{j} \frac{\partial p}{\partial s} \rangle = \frac{\partial h_p}{\partial s}. \tag{3.14}$$

The difference between h_f and h_p lies in the fact that h_f is responsible for the spatially conservative terms of the governing equations, whereas h_p takes the non-conservative part into account. Perhaps surprisingly, we will show that these non-conservative terms $\mathbf{j}(\partial p/\partial s)$ can indeed be written in conservative form in the energy equation. An alternative formulation of condition (3.14) is given by

$$\frac{\partial}{\partial s} \left(\langle \mathbf{v}, \mathbf{j} \rangle p \right) - p \frac{\partial}{\partial s} \langle \mathbf{v}, \mathbf{j} \rangle = \frac{\partial h_p}{\partial s}. \tag{3.15}$$

In order for the local energy to be conserved, there must exist a h_p (for the given e and resulting $\mathbf{v}$) such that this condition is satisfied.

An important difference between this derivation and the derivation for the SWE as found in e.g. [43] is the non-conservative pressure term. Although the two-layer SWE [1] also features a non-conservative term, in the TFM the non-conservative term depends on a variable for which there is no evolution equation (namely the pressure). This pressure term is instead linked directly to the volume constraint (3.4) and volumetric flow constraint (3.6) [107], which are not present in the SWE. For a system in conservative form without source terms, (3.13) is the only condition. This condition is emphasized in literature (e.g. [73]) as the condition for the existence of an entropy function. The derivation of energy conservation for the conservative part of the TFM system thus matches the derivation of an entropy condition for a conservative hyperbolic system.

In summary, the task is to find a set e, h_f, and h_p, which satisfy conditions (3.12) and (3.14) for the current model with flux $\mathbf{f}$ and pressure terms $\mathbf{j}(\partial p/\partial s)$. The alternative conditions (3.13) and (3.15) yield results more directly and will therefore be used in the following section. The result is the local energy conservation equation (3.8), and global energy conservation then follows directly.

3.3.2 Choice of energy and energy fluxes

We will show that the mechanical energy

$$\boxed{e = \rho_U g_n \widetilde{H}_U + \rho_L g_n \widetilde{H}_L + \frac{1}{2}\frac{q_3^2}{q_1} + \frac{1}{2}\frac{q_4^2}{q_2}} \\ = \rho_U g_n \widetilde{H}_U + \rho_L g_n \widetilde{H}_L + \frac{1}{2}\rho_U A_U u_U^2 + \frac{1}{2}\rho_L A_L u_L^2, \tag{3.16}$$

is conserved by the TFM (in absence of source terms). Here $\widetilde{H}_U = \widetilde{H}_U(A_U(q_1, \rho_U))$ represents the center of mass of the upper fluid multiplied by A_U and $\widetilde{H}_L = \widetilde{H}_L(A_L(q_2, \rho_L))$ represents the center of mass of the lower fluid multiplied by A_L (see Appendix A), so that the first two terms can be recognized as the potential energy of the upper and lower fluid, respectively. The third and fourth terms represent the kinetic energy of the upper and lower fluid, respectively. Therefore, this energy e has a clear physical interpretation. Note that just as for the incompressible Navier-Stokes equations, the pressure does not contribute to the energy.

The entropy variables are given by

$$\mathbf{v} = \left[\frac{\partial e}{\partial \mathbf{q}}\right]^T = \begin{bmatrix} -\frac{1}{2}\frac{q_3^2}{q_1^2} + g_n \frac{\mathrm{d}\widetilde{H}_U}{\mathrm{d}A_U} \\ -\frac{1}{2}\frac{q_4^2}{q_2^2} + g_n \frac{\mathrm{d}\widetilde{H}_L}{\mathrm{d}A_L} \\ \frac{q_3}{q_1} \\ \frac{q_4}{q_2} \end{bmatrix} = \begin{bmatrix} -\frac{1}{2}\frac{q_3^2}{q_1^2} + g_n(H - H_U) \\ -\frac{1}{2}\frac{q_4^2}{q_2^2} + g_n H_L \\ \frac{q_3}{q_1} \\ \frac{q_4}{q_2} \end{bmatrix}, \tag{3.17}$$

with $H_U = H_U(A_U(q_1, \rho_U))$ and $H_L = H_L(A_L(q_2, \rho_L))$ representing the fluid layer thickness of the upper and lower fluids, respectively (see Appendix A). It is important that in the energy and energy flux terms concerning the upper fluid we use $\widehat{H}_U(A_U)$, $\widetilde{H}_U(A_U)$, and $H_U(A_U)$, while for the lower fluid we use $\widehat{H}_L(A_L)$, $\widetilde{H}_L(A_L)$, and $H_L(A_L)$. It is possible to use the volume constraint to change this functional dependence, but our choice leads to an elegant form of the energy conservation conditions.

The task is to find h_f and h_p. We start with h_p: the pressure term needs to satisfy (3.15). Straightforward evaluation gives

$$\langle \mathbf{v}, \mathbf{j} \rangle = \frac{q_3}{q_1}\frac{q_1}{\rho_U} + \frac{q_4}{q_2}\frac{q_2}{\rho_L} = Q,$$

with Q the volumetric flow rate given by (3.6). Because of the volumetric flow constraint (3.6), the second term of (3.15) vanishes, so that the condition on the pressure gradient evaluates to

$$\frac{\partial}{\partial s}(Qp) = \frac{\partial h_p}{\partial s},$$

and (3.15) is satisfied with

$$\boxed{h_p = Qp.} \tag{3.18}$$

We note that p is the pressure that enforces incompressibility – it does not include a driving pressure gradient (which would appear as a source term in the TFM governing equations). Therefore h_p is periodic in space in the case of periodic boundaries. In the case of closed boundaries, Q must be zero, meaning that $h_p = 0$ throughout the domain. This means that when integrating (3.8) over a closed or periodic domain, the terms involving h_p vanish, and thus this definition for h_p is compatible with global energy conservation as described by (3.9).

Note that alternatively, global energy conservation of the pressure terms could be proved by integrating (3.14) over the domain, and equating it to the integral of the second term on the left-hand side of (3.15). This equality can be seen as a parallel to a well-known property of the incompressible Navier-Stokes equations, namely that, apart from the minus sign, the gradient operator applied to the pressure is the adjoint of the divergence operator applied to the velocity field [123]. For both models, the final step to proving global energy conservation of the pressure terms is substituting the incompressibility constraint (here given by $\partial Q/\partial s = 0$).

The next task is to find h_f. Based on the form of h_f for the SWE and condition (3.13), we propose the following choice

$$\begin{aligned} \boxed{h_f = g_n q_3 (H - H_U) + g_n q_4 H_L + \frac{1}{2}\frac{q_3^3}{q_1^2} + \frac{1}{2}\frac{q_4^3}{q_2^2}} \\ = g_n q_3 (H - H_U) + g_n q_4 H_L + \frac{1}{2}\rho_U A_U u_U^3 + \frac{1}{2}\rho_L A_L u_L^3, \end{aligned} \tag{3.19}$$

which can be shown to satisfy condition (3.13) by computing:

$$\left[\left\langle \mathbf{v}, \frac{\partial \mathbf{f}}{\partial \mathbf{q}} \right\rangle\right]^T = \begin{bmatrix} -\frac{q_3^3}{q_1^3} - g_n \frac{\mathrm{d}\widehat{H}_U}{\mathrm{d}A_U}\frac{q_3}{q_1} \\ -\frac{q_4^3}{q_2^3} - g_n \frac{\mathrm{d}\widehat{H}_L}{\mathrm{d}A_L}\frac{q_4}{q_2} \\ \frac{3}{2}\frac{q_3^2}{q_1^2} + g_n \frac{\mathrm{d}H_U}{\mathrm{d}A_U} \\ \frac{3}{2}\frac{q_4^2}{q_2^2} + g_n \frac{\mathrm{d}\widetilde{H}_L}{\mathrm{d}A_L} \end{bmatrix}, \quad \left[\frac{\partial h_f}{\partial \mathbf{q}}\right]^T = \begin{bmatrix} -\frac{q_3^3}{q_1^3} - \frac{g_n}{\rho_U}\frac{\mathrm{d}H_U}{\mathrm{d}A_U} q_3 \\ -\frac{q_4^3}{q_2^3} + \frac{g_n}{\rho_L}\frac{\mathrm{d}H_L}{\mathrm{d}A_L} q_4 \\ \frac{3}{2}\frac{q_3^2}{q_1^2} + g_n (H - H_U) \\ \frac{3}{2}\frac{q_4^2}{q_2^2} + g_n H_L \end{bmatrix}.$$

The last two entries in these vectors are equal because of relations (A.5), derived in Appendix A. The first two entries are equal due to the geometric relations (A.6), which we repeat here in terms of the conserved variables $\mathbf{q}$:

$$\frac{\rho_U}{q_1}\frac{\mathrm{d}\widehat{H}_U}{\mathrm{d}A_U} = \frac{\mathrm{d}H_U}{\mathrm{d}A_U}, \qquad \frac{\rho_L}{q_2}\frac{\mathrm{d}\widehat{H}_L}{\mathrm{d}A_L} = -\frac{\mathrm{d}H_L}{\mathrm{d}A_L}. \tag{3.20}$$

These relations follow directly from the definitions of these geometric quantities and hold for arbitrary duct geometries. Note that, alternatively, condition (3.12) can be used (instead of (3.13)), which leads to the following conditions:

$$\frac{\rho_U}{q_1}\frac{\partial \widehat{H}_U}{\partial s} = \frac{\partial H_U}{\partial s}, \qquad \frac{\rho_L}{q_2}\frac{\partial \widehat{H}_L}{\partial s} = -\frac{\partial H_L}{\partial s}, \tag{3.21}$$

which may also be shown to be satisfied directly via application of Leibniz' rule to the definitions of $\widehat{H}_U$ and $\widehat{H}_L$. These last two conditions will play an important role in the discrete analysis in section 3.5.

In conclusion, we have proposed a novel set of e, h_f, and h_p for the TFM and have shown that the local energy conservation equation (3.8) is satisfied.

3.3.3 Reformulation in terms of the entropy potential and conditions on fluxes

Conditions (3.12) and (3.14), or their alternatives (3.13) and (3.15), were used in the previous section to find a combination of e, h_f and h_p for the continuous TFM, *given* the fluxes $\mathbf{f}$ from the governing equations. In section 3.5, we will instead aim to find discrete flux functions, *given* discretized versions of e, h_f and h_p (that are inspired by their continuous counterparts). Equation (3.12) is not a very useful formulation to find such numerical flux functions, because it is a condition imposed on the jump in $\mathbf{f}$, rather than $\mathbf{f}$ itself. Therefore, equation (3.12) is reformulated using the concept of the *entropy potential* [42, 115].

The entropy potential is defined to be related to $\mathbf{v}$, $\mathbf{f}$, and h_f in the following manner:

$$\psi \coloneqq \langle \mathbf{v}, \mathbf{f} \rangle - h_f. \tag{3.22}$$

With this definition, we can reformulate condition (3.12) using the product rule ($\frac{\partial}{\partial s}\langle \mathbf{v}, \mathbf{f} \rangle = \langle \frac{\partial \mathbf{v}}{\partial s}, \mathbf{f} \rangle + \langle \mathbf{v}, \frac{\partial \mathbf{f}}{\partial s} \rangle$) as:

$$\frac{\partial \psi}{\partial s} = \langle \frac{\partial \mathbf{v}}{\partial s}, \mathbf{f} \rangle. \tag{3.23}$$

The entropy potential can be directly calculated from its definition (3.22) and is given by:

$$\begin{aligned} \boxed{\psi = \langle \mathbf{v}, \mathbf{f} \rangle - h_f = -\rho_U g_n \widehat{H}_U \frac{q_3}{q_1} - \rho_L g_n \widehat{H}_L \frac{q_4}{q_2}} \\ = -\rho_U g_n \widehat{H}_U u_U - \rho_L g_n \widehat{H}_L u_L. \end{aligned} \tag{3.24}$$

Because this entropy potential is based on an h_f that satisfies (3.12), (3.23) is satisfied by construction. Nevertheless, we outline the details to convert (3.23) into conditions on the individual numerical fluxes, since they will be exactly mimicked by our discrete analysis in section 3.5. We first introduce the following notation for the fluxes, and split them into the following components:

$$\mathbf{f} = \begin{bmatrix} f_1(q_3) \\ f_2(q_4) \\ f_{3,a}(q_1, q_3) + g_n f_{3,g}(q_1) \\ f_{4,a}(q_2, q_4) + g_n f_{4,g}(q_2) \end{bmatrix}. \tag{3.25}$$

Here $f_{3,a}$ and $f_{4,a}$ are the momentum advection terms, and $f_{3,g}$ and $f_{4,g}$ are the level gradient terms (divided by g_n). These fluxes and the definitions for $\mathbf{v}$ (3.17) and ψ (3.24) can be substituted in (3.23). The resulting condition is first split into two conditions: one condition proportional to g_n, and one not proportional to g_n. This is done on the basis that

the mass and momentum advection terms *do not* depend on g_n in the continuous case (see (3.2)), and *should not* depend on g_n in the discrete case. These two conditions are split again on the basis that f_1 and f_3 should not depend on q_2 and q_4, and f_2 and f_4 should not depend on q_1 and q_3. We obtain the following four conditions:

$$-\frac{\partial}{\partial s}\left(\frac{1}{2}\frac{q_3^2}{q_1^2}\right)f_1 + \frac{\partial}{\partial s}\left(\frac{q_3}{q_1}\right)f_{3,a} = 0, \tag{3.26a}$$

$$-\frac{\partial}{\partial s}\left(\frac{1}{2}\frac{q_4^2}{q_2^2}\right)f_2 + \frac{\partial}{\partial s}\left(\frac{q_4}{q_2}\right)f_{4,a} = 0, \tag{3.26b}$$

$$\frac{\partial}{\partial s}\left(g_n(H-H_U)\right)f_1 + \frac{\partial}{\partial s}\left(\frac{q_3}{q_1}\right)g_n f_{3,g} = -\frac{\partial}{\partial s}\left(\rho_U g_n \widehat{H}_U \frac{q_3}{q_1}\right), \tag{3.26c}$$

$$\frac{\partial}{\partial s}\left(g_n H_L\right)f_2 + \frac{\partial}{\partial s}\left(\frac{q_4}{q_2}\right)g_n f_{4,g} = -\frac{\partial}{\partial s}\left(\rho_L g_n \widehat{H}_L \frac{q_4}{q_2}\right). \tag{3.26d}$$

As mentioned, these equations are by construction satisfied by the flux vector (3.2). One important remark is that after we reformulate in terms of ψ, the geometric conditions (3.21) encountered in section 3.3.2 still need to be satisfied in order for (3.26c) and (3.26d) to hold.

3.3.4 Comparison of the energy and energy fluxes to those of other models

Here we compare the expressions obtained for e and h_f to results from literature for other models, focusing on the case of a 2D channel geometry. The expression (3.16) for e for the channel geometry can be obtained by substitution of the channel-specific evaluations of $\widetilde{H}_U$ and $\widetilde{H}_L$ (Appendix A):

$$e_{\text{ch}} = \rho_U g_n H_U (H - \frac{1}{2}H_U) + \frac{1}{2}\rho_L g_n H_L^2 + \frac{1}{2}\rho_U u_U^2 H_U + \frac{1}{2}\rho_L u_L^2 H_L. \tag{3.27}$$

For a single layer fluid, such as the single layer SWE, only the third and fifth terms remain, and they are consistent with the SWE entropy function as discussed in [43] (without channel inclination).

To compare with two-layer SWE theory, we rewrite (3.27) using the volume constraint (3.4) to obtain

$$e_{\text{AK}} = \frac{1}{2}\rho_U g_n H_U^2 + \rho_U g_n H_U H_L + \frac{1}{2}\rho_L g_n H_L^2 + \frac{1}{2}\rho_L u_L^2 H_L + \frac{1}{2}\rho_U u_U^2 H_U.$$

This is the expression presented by Abgrall and Karni (AK) [1] and Fjordholm [41] as an entropy function for the two-layer SWE. The energy found in the present study can therefore be seen as a generalization of the two-layer SWE energy to arbitrary duct geometries.

When comparing our energy flux h_f for the TFM to the one for the two-layer SWE, it should be realized that the two-layer SWE can be obtained from the TFM by the choice $p = \rho_U g_n H_U$. This means that the pressure flux h_p of the TFM needs to be added to h_f in order to compare with the SWE expressions. In our notation, the two-layer SWE entropy

flux given by [1] is

$$h_{\mathrm{AK}} = \rho_U g_n u_U H_U^2 + \rho_U g_n (u_U + u_L) H_U H_L + \rho_L g_n u_L H_L^2 + \frac{1}{2}\rho_U u_U^3 H_U + \frac{1}{2}\rho_L u_L^3 H_L.$$

Our expression for h_f for a 2D channel is given by

$$h_{f,\mathrm{ch}} = \rho_U g_n u_U H_U (H - H_U) + \rho_L g_n u_L H_L^2 + \frac{1}{2}\rho_U u_U^3 H_U + \frac{1}{2}\rho_L u_L^3 H_L.$$

3

Upon adding $h_p = Qp = Q\rho_U g_n H_U$ to $h_{f,\mathrm{ch}}$, and after some rewriting, we see that our TFM energy flux is consistent with the two-layer SWE entropy flux:

$$h_{\mathrm{AK}} = h_{f,\mathrm{ch}} + h_p.$$

To conclude, our proposed energy (3.16) and energy fluxes (3.18) and (3.19) can be seen as a generalization of the two-layer SWE energy and energy flux to arbitrary duct cross sections.

3.4 Discretization of the governing equations

3.4.1 Semi-discrete model equations

The system of equations (3.1) is discretized using a finite volume method on a uniform staggered grid, sketched in Figure 3.2. This discretization naturally conserves mass for each fluid separately, and momentum for both fluids combined. The first two components of $\mathbf{q}$ (the phase masses) and the pressure are defined at the centers of N_p pressure volumes, which have a cell size of $\Delta s = L/N_p$. The last two components of $\mathbf{q}$ (the phase momenta) are defined at the centers of N_u velocity volumes.

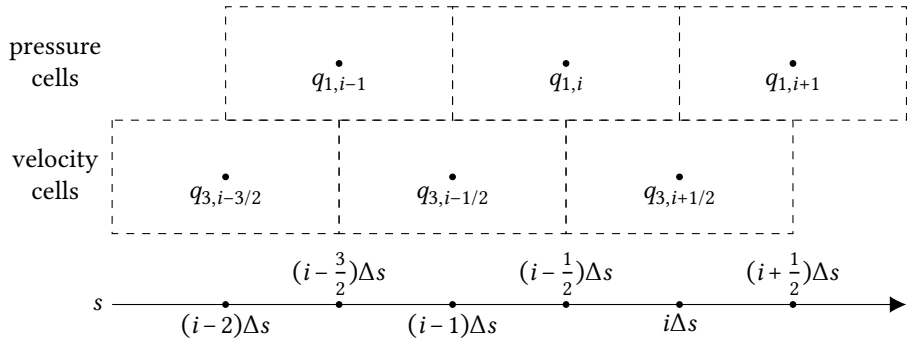

Figure 3.2: Staggered grid layout.

On this staggered grid we define a local discrete vector of unknowns as follows:

$$\mathbf{q}_i(t) \coloneqq \begin{bmatrix} q_{1,i}(t) \\ q_{2,i}(t) \\ q_{3,i-1/2}(t) \\ q_{4,i-1/2}(t) \end{bmatrix} = \begin{bmatrix} (\rho_U A_U \Delta s)_i \\ (\rho_L A_L \Delta s)_i \\ (\rho_U A_U u_U \Delta s)_{i-1/2} \\ (\rho_L A_L u_L \Delta s)_{i-1/2} \end{bmatrix} = \begin{bmatrix} \rho_U A_{U,i} \Delta s \\ \rho_L A_{L,i} \Delta s \\ \rho_U \overline{A}_{U,i-1/2} u_{U,i-1/2} \Delta s \\ \rho_L \overline{A}_{L,i-1/2} u_{L,i-1/2} \Delta s \end{bmatrix}.$$

The choice of using $i-1/2$ in the definition of $\mathbf{q}_i$ instead of $i+1/2$ is arbitrary. Note that $q_{1,i}(t) \approx q_1(s_i, t)$ (and similar for the other entries); the notation is on purpose kept very close to the notation of the continuous model, but can be distinguished due to the extra index which the discrete variables carry. Another notable difference is that the cell sizes are included in the discrete unknowns, so that they have units of mass and momentum.

The last equality in the above equation describes the relations of the discrete conservative variables to the discrete primitive variables (cross-sections and velocities). Here we have introduced the following notation for interpolation operators [42]:

$$\overline{a}_{i-1/2} \coloneqq \frac{1}{2}(a_{i-1} + a_i) \quad \overline{a}_i \coloneqq \frac{1}{2}\left(a_{i-1/2} + a_{i+1/2}\right). \tag{3.28}$$

The numerical scheme is implemented in terms of the conservative variables $q_{1,i}$ through $q_{4,i-1/2}$, but the primitive variables can be extracted in post-processing according to the given relations.

The notation with $\mathbf{q}_i$ as a discrete local vector of unknowns allows us to write the discrete scheme in vector form as

$$\frac{\mathrm{d}\mathbf{q}_i}{\mathrm{d}t} + \left(\mathbf{f}_{i+1/2} - \mathbf{f}_{i-1/2}\right) + \mathbf{j}_i\left(p_i - p_{i-1}\right) = \mathbf{0}. \tag{3.29}$$

Here, we have defined $\mathbf{f}_{i-1/2}$ and $\mathbf{j}_i$ as

$$\mathbf{f}_{i-1/2}(\mathbf{q}_{i-2}, \mathbf{q}_{i-1}, \mathbf{q}_i) \coloneqq \begin{bmatrix} f_{1,i-1/2}(\mathbf{q}_i) \\ f_{2,i-1/2}(\mathbf{q}_i) \\ f_{3,i-1}(\mathbf{q}_{i-2}, \mathbf{q}_{i-1}, \mathbf{q}_i) \\ f_{4,i-1}(\mathbf{q}_{i-2}, \mathbf{q}_{i-1}, \mathbf{q}_i) \end{bmatrix}, \quad \text{and} \quad \mathbf{j}_i(\mathbf{q}_{i-1}, \mathbf{q}_i) \coloneqq \begin{bmatrix} 0 \\ 0 \\ j_{3,i-1/2}(\mathbf{q}_{i-1}, \mathbf{q}_i) \\ j_{4,i-1/2}(\mathbf{q}_{i-1}, \mathbf{q}_i) \end{bmatrix}.$$

The numerical fluxes and numerical pressure terms are left undefined in this section, because we will define them based on the requirement of energy conservation, in section 3.5.

The pressure terms are non-conservative and are not written as the difference between an inflow and an outflow of the finite volume cell. However, with the staggered grid employed here, one can see that $q_{3,i-1/2}$ and $q_{4,i-1/2}$ are directly and naturally connected to the pressure at the neighboring grid cells. Analogous to the incompressible (multi-dimensional) single-phase Navier-Stokes equations (for which staggered grids are known to lead to strong coupling), this pressure-velocity coupling is necessary to prevent checkerboard patterns, and would be much more difficult to achieve on a collocated grid.

The system is closed by the volume constraint (compare to (3.4)):

$$\frac{q_{1,i}}{\rho_U \Delta s} + \frac{q_{2,i}}{\rho_L \Delta s} = A, \tag{3.30}$$

which implies the volumetric flow constraint (compare to (3.5))

$$Q_{i+1/2} - Q_{i-1/2} \coloneqq \frac{q_{3,i+1/2}}{\rho_U \Delta s} - \frac{q_{3,i-1/2}}{\rho_U \Delta s} + \frac{q_{4,i+1/2}}{\rho_L \Delta s} - \frac{q_{4,i-1/2}}{\rho_L \Delta s} = 0, \tag{3.31}$$

so that $Q_{i+1/2} = Q_{i-1/2} = Q(t)$, like in the continuous case. This step can only be made if we choose $f_{1,i-1/2} = q_{3,i-1/2}/\Delta s$ and $f_{2,i-1/2} = q_{4,i-1/2}/\Delta s$, and this will be used as a condition on the form of the numerical fluxes in section 3.5.4.

Just as in the continuous case, these constraints are used to set up a Poisson equation for the pressure. The semi-discrete momentum equations are first summed to obtain

$$\frac{1}{\Delta s}\mathbf{l}^T\mathbf{j}_i\left(p_i - p_{i-1}\right) = -\frac{1}{\Delta s}\mathbf{l}^T\left(\frac{\mathrm{d}\mathbf{q}_i}{\mathrm{d}t} + \left(\mathbf{f}_{i+1/2} - \mathbf{f}_{i-1/2}\right)\right), \quad \text{with} \quad \mathbf{l}^T = \begin{bmatrix} 0 & 0 & \frac{1}{\rho_U} & \frac{1}{\rho_L} \end{bmatrix}.$$

Expanding and substituting the definition of $Q_{i-1/2}$ yields

$$\frac{1}{\Delta s}\left(\frac{j_{3,i-1/2}}{\rho_U} + \frac{j_{4,i-1/2}}{\rho_L}\right)\left(p_i - p_{i-1}\right) = -\frac{\mathrm{d}Q_{i-1/2}}{\mathrm{d}t} - \frac{1}{\Delta s}\left(\frac{f_{3,i} - f_{3,i-1}}{\rho_U} + \frac{f_{4,i} - f_{4,i-1}}{\rho_L}\right).$$

After taking the difference between this equation and the same equation for index $i + 1/2$, and applying (3.31), we obtain the discrete version of (3.7):

$$\frac{1}{\Delta s^2}\left[\left(\frac{j_{3,i+1/2}}{\rho_U} + \frac{j_{4,i+1/2}}{\rho_L}\right)\left(p_{i+1} - p_i\right) - \left(\frac{j_{3,i-1/2}}{\rho_U} + \frac{j_{4,i-1/2}}{\rho_L}\right)\left(p_i - p_{i-1}\right)\right] = -\frac{1}{\Delta s^2}\left(\frac{f_{3,i+1} - 2f_{3,i} + f_{3,i-1}}{\rho_U} + \frac{f_{4,i+1} - 2f_{4,i} + f_{4,i-1}}{\rho_L}\right). \quad (3.32)$$

System (3.29) is discretized in time using the fourth-order semi-explicit Runge-Kutta method described in [107]. At each stage of the Runge-Kutta time step, a predictor-corrector algorithm is applied: the momentum equations are first solved without including the pressure terms, the discrete Poisson equation is solved for the pressure using these intermediate momenta, and the momenta are updated in a projection step using the calculated pressure. This ensures that the volume and volumetric flow constraints are satisfied at all stages. We solve (3.32) iteratively, using a preconditioned conjugate gradient method, which is run until the relative residual falls below the tolerance (10^{-12}), or until the maximum number of iterations is reached (50). The time integration method is fourth-order accurate for all variables, and requires a restriction to the CFL-number based on the eigenvalues of the TFM.

3.4.2 Boundary conditions

In the case of periodic boundaries, the domain is divided into N_p pressure volumes and $N_u = N_p$ velocity volumes. There are no special boundary points: the scheme as laid out in section 3.4.1 applies everywhere, looping around the domain.

For closed boundaries, there are N_p interior pressure points and $N_u = N_p - 1$ interior velocity points. The first interior pressure node is located at $s = \Delta s/2$, the first interior velocity node is located at $s = \Delta s$, and similarly for the last nodes at the end of the domain [107]. For both the pressure and velocity grids, there are boundary points in addition to the interior points, one at each side of the domain. When calculating the discrete energy on the velocity grid (see section 3.5.1), it is important to include the half-volumes between the boundary points and the first and last interior points.

At the boundary points, the mass fluxes ($\rho_U A_U u_U$ and $\rho_L A_L u_L$) are specified, and A_U and A_L follow via an analysis of the characteristics corresponding to the incoming and outgoing waves at the boundary. In the case of closed boundaries, as used in this work, the mass fluxes are set to zero. Note that the characteristic analysis incorporates the volume

constraint (3.30), and no boundary condition is needed for the pressure (the pressure at the boundaries has no influence on the solution in the interior). For more details on the implementation of the boundary conditions we refer to [107].

3.5 Energy-conserving spatial discretization of the TFM

3.5.1 Outline: conditions for discrete energy conservation

In the discrete case, just as in the continuous case, we want to satisfy a local and a global energy equality. The use of a staggered grid instead of the commonly used collocated grid (e.g. [42, 115]) makes it straightforward to obtain an energy-conserving discretization of the non-conservative pressure term, but introduces new challenges in terms of the definition of the discrete local energy, which is not unique anymore.

We choose to define the local energy at the velocity grid points, i.e. we choose $e_{i-1/2} = e(\mathbf{q}_{i-1}, \mathbf{q}_i)$, and are aiming for a discrete version of (3.8):

$$\frac{\mathrm{d}e_{i-1/2}}{\mathrm{d}t} + \left(h_{f,i} - h_{f,i-1}\right) + \left(h_{p,i} - h_{p,i-1}\right) = 0, \tag{3.33}$$

with $h_{f,i} = h_f(\mathbf{q}_{i-1}, \mathbf{q}_i)$ and $h_{p,i} = h_p(p_i)$ as the numerical energy fluxes. This choice means that the potential energy terms and q_1 and q_2 in the kinetic energy terms need to be interpolated, but q_3 and q_4 do not require interpolation. With this choice, we obtain energy-conserving expressions for $f_{3,i}$ and $f_{4,i}$ in a constructive manner (after choosing advantageous expressions for $f_{1,i-1/2}$ and $f_{2,i-1/2}$). It is also possible to define the energy at the pressure grid points, and obtain an energy-conserving discretization, but in that case it is necessary to substitute trial solutions for $f_{3,i}$ and $f_{4,i}$, and interpolation of the pressure is required in the expression for $h_{p,i}$ (see the remark at the end of section 3.5.4). We would like to emphasize that (3.33) is *not* being solved as an additional equation; instead it will be shown to be *a consequence* of the discrete mass and momentum equations given in section 3.4, if the numerical fluxes and $\mathbf{j}_i$ are chosen appropriately.

If (3.33) holds, it can be summed over all finite volumes to yield

$$\frac{\mathrm{d}E_h}{\mathrm{d}t} = \sum_{i=1}^{N_u} \frac{\mathrm{d}e_{i-1/2}}{\mathrm{d}t} = -\sum_{i=1}^{N_u} \left[\left(h_f + h_p\right)_i - \left(h_f + h_p\right)_{i-1}\right] = 0,$$

where the last equality should hold in the case of periodic or closed boundaries. Here we have defined the global discrete energy as the discrete counterpart of (3.10):

$$E_h(t) \coloneqq \sum_{i=1}^{N_u} e_{i-1/2}.$$

Like in the continuous case, the art is to find expressions for $e_{i-1/2}$, $h_{f,i}$ and $h_{p,i}$ such that equation (3.33) is satisfied. In addition, the numerical flux $\mathbf{f}_{i-1/2}$ needs to be constructed. We will outline the steps to obtain these quantities in a manner parallel to the continuous derivation in section 3.3.

First, we postulate an energy

$$e_{i-1/2} = e_{i-1/2}\left(\mathbf{q}_{i-1}, \mathbf{q}_i\right), \tag{3.34}$$

which will be based on the energy found for the continuous case. Note that the dependence could be expanded to additional grid points if required, but we will introduce an energy for which this is not necessary. Second, we calculate the vectors of entropy variables, defined as

$$\mathbf{v}_{i-1/2,i-1} \coloneqq \left[\frac{\partial e_{i-1/2}}{\partial \mathbf{q}_{i-1}}\right]^T, \quad \mathbf{v}_{i-1/2,i} \coloneqq \left[\frac{\partial e_{i-1/2}}{\partial \mathbf{q}_{i}}\right]^T.$$

Here the first index refers to the index of the energy, and the second index refers to the conservative variables to which derivatives are taken.

For the energy given by (3.34), the time derivative can be expressed as

$$\frac{\mathrm{d}e_{i-1/2}}{\mathrm{d}t} = \langle \mathbf{v}_{i-1/2,i-1}, \frac{\mathrm{d}\mathbf{q}_{i-1}}{\mathrm{d}t}\rangle + \langle \mathbf{v}_{i-1/2,i}, \frac{\mathrm{d}\mathbf{q}_{i}}{\mathrm{d}t}\rangle, \tag{3.35}$$

Here the brackets represent dot products over the vectors (at a certain grid point), just as in the continuous case. The right-hand side of equation (3.35) follows by substituting equation (3.29) for i and $i-1$:

$$\frac{\mathrm{d}e_{i-1/2}}{\mathrm{d}t} = \langle \mathbf{v}_{i-1/2,i-1}, [\![\mathbf{f}_{i-1}]\!]\rangle + \langle \mathbf{v}_{i-1/2,i-1}, \mathbf{j}_{i-1}\rangle [\![p_{i-3/2}]\!] + \langle \mathbf{v}_{i-1/2,i}, [\![\mathbf{f}_{i}]\!]\rangle + \langle \mathbf{v}_{i-1/2,i}, \mathbf{j}_{i}\rangle [\![p_{i-1/2}]\!], \tag{3.36}$$

where we have introduced the following notation for jump operators [42]:

$$[\![a_{i-1/2}]\!] \coloneqq a_i - a_{i-1}, \quad [\![a_i]\!] \coloneqq a_{i+1/2} - a_{i-1/2}. \tag{3.37}$$

Comparing with (3.33) we see that the energy fluxes $h_{f,i}$ and $h_{p,i}$ need to satisfy

$$\langle \mathbf{v}_{i-1/2,i-1}, [\![\mathbf{f}_{i-1}]\!]\rangle + \langle \mathbf{v}_{i-1/2,i}, [\![\mathbf{f}_{i}]\!]\rangle = \left[\!\!\left[h_{f,i-1/2}\right]\!\!\right], \tag{3.38}$$

$$\langle \mathbf{v}_{i-1/2,i-1}, \mathbf{j}_{i-1}\rangle [\![p_{i-3/2}]\!] + \langle \mathbf{v}_{i-1/2,i}, \mathbf{j}_{i}\rangle [\![p_{i-1/2}]\!] = [\![h_{p,i-1/2}]\!]. \tag{3.39}$$

These conditions are analogous to (3.12) and (3.14) for the continuous case, with discrete jumps corresponding to derivatives with respect to s. Together, conditions (3.38) and (3.39) guarantee that (3.36) can be written as (3.33), thus proving conservation of the discrete local energy (3.34).

The challenge is to find the proper combination of discrete expressions for $e_{i-1/2}$, $h_{f,i}$, $h_{p,i}$, and $\mathbf{f}_{i-1/2}$ which are consistent approximations to their continuous counterparts in such a way that the local energy conservation equation is satisfied. This is a difficult problem, since we have multiple degrees of freedom ($e_{i-1/2}$, $h_{f,i}$, $h_{p,i}$, and $\mathbf{f}_{i-1/2}$), and the solution might not be unique. To simplify the construction, we will use the concept of entropy potential introduced in section 3.3.3: after choosing a certain $e_{i-1/2}$ and $\psi_{i-1/2}$, this yields straightforward conditions on the fluxes $\mathbf{f}_{i-1/2}$ to be energy-conserving.

3.5.2 Choice of discrete energy and energy fluxes

In this section we propose an energy $e_{i-1/2}$, and verify that this energy is conserved by the pressure terms of the discrete model (energy conservation for the flux terms is treated in

section 3.5.3 and section 3.5.4). Recalling the continuous energy (3.16), we define a discrete energy $e_{i-1/2} = e_{i-1/2}(\mathbf{q}_{i-1}, \mathbf{q}_i)$:

$$\boxed{e_{i-1/2} = \rho_U g_n \widetilde{\overline{H}}_{U,i-1/2}\Delta s + \rho_L g_n \widetilde{\overline{H}}_{L,i-1/2}\Delta s + \frac{1}{2}\frac{q_{3,i-1/2}^2}{\overline{q}_{1,i-1/2}} + \frac{1}{2}\frac{q_{4,i-1/2}^2}{\overline{q}_{2,i-1/2}}} \tag{3.40}$$

$$= \rho_U g_n \widetilde{\overline{H}}_{U,i-1/2}\Delta s + \rho_L g_n \widetilde{\overline{H}}_{L,i-1/2}\Delta s + \frac{\rho_U}{2}\overline{A}_{U,i-1/2}u_{U,i-1/2}^2\Delta s + \frac{\rho_L}{2}\overline{A}_{L,i-1/2}u_{L,i-1/2}^2\Delta s.$$

Other choices are possible because on a staggered grid interpolation is required, and the interpolation may be carried out in various different ways[3]. Our choice (3.40) is one of the most straightforward choices for the energy that is consistent with the continuous definition, when the energy is defined at the velocity grid points, and leads to an elegant form of the energy-conserving discretization (see also the remark at the end of section 3.5.4).

We use identities given in Appendix A to calculate the $\mathbf{v}$ vectors. They are given by

$$\mathbf{v}_{i-1/2,i-1} = \left[\frac{\partial e_{i-1/2}}{\partial \mathbf{q}_{i-1}}\right]^T = \begin{bmatrix} -\frac{1}{4}\frac{q_{3,i-1/2}^2}{\overline{q}_{1,i-1/2}^2} + \frac{1}{2}g_n\left(H - H_{U,i-1}\right) \\ -\frac{1}{4}\frac{q_{4,i-1/2}^2}{\overline{q}_{2,i-1/2}^2} + \frac{1}{2}g_n H_{L,i-1} \\ 0 \\ 0 \end{bmatrix}, \tag{3.41}$$

and

$$\mathbf{v}_{i-1/2,i} = \left[\frac{\partial e_{i-1/2}}{\partial \mathbf{q}_{i}}\right]^T = \begin{bmatrix} -\frac{1}{4}\frac{q_{3,i-1/2}^2}{\overline{q}_{1,i-1/2}^2} + \frac{1}{2}g_n\left(H - H_{U,i}\right) \\ -\frac{1}{4}\frac{q_{4,i-1/2}^2}{\overline{q}_{2,i-1/2}^2} + \frac{1}{2}g_n H_{L,i} \\ \frac{q_{3,i-1/2}}{\overline{q}_{1,i-1/2}} \\ \frac{q_{4,i-1/2}}{\overline{q}_{2,i-1/2}} \end{bmatrix}, \tag{3.42}$$

and their sum is consistent with (3.17).

The pressure terms in (3.36) need to satisfy condition (3.39), which can be rewritten to obtain the discrete version of (3.15):

$$\left[\!\left[h_{p,i-1/2}\right]\!\right] = \left[\!\left[\overline{\langle \mathbf{v}_{i-1/2,i-1}, \mathbf{j}_{i-1}\rangle} p_{i-3/2}\right]\!\right] - \overline{\left(\left[\!\left[\langle \mathbf{v}_{i-1/2,i-1}, \mathbf{j}_{i-1}\rangle\right]\!\right] p_{i-3/2}\right)}$$
$$+ \left[\!\left[\overline{\langle \mathbf{v}_{i-1/2,i}, \mathbf{j}_{i}\rangle} p_{i-1/2}\right]\!\right] - \overline{\left(\left[\!\left[\langle \mathbf{v}_{i-1/2,i}, \mathbf{j}_{i}\rangle\right]\!\right] p_{i-1/2}\right)}. \tag{3.43}$$

On a staggered grid, it is straightforward to satisfy this condition by choosing for $\mathbf{j}_i$

$$\mathbf{j}_i = \frac{1}{\Delta s}\begin{bmatrix} 0 \\ 0 \\ \frac{\overline{q}_{1,i-1/2}}{\rho_U} \\ \frac{\overline{q}_{2,i-1/2}}{\rho_L} \end{bmatrix} = \begin{bmatrix} 0 \\ 0 \\ \overline{A}_{U,i-1/2} \\ \overline{A}_{L,i-1/2} \end{bmatrix}, \tag{3.44}$$

[3] In section 3.A we will show that the same results can be obtained with a global energy analysis, in which interpolation of the local potential energy to the velocity grid points is not needed.

since with this choice we have

$$\langle \mathbf{v}_{i-1/2,i-1}, \mathbf{j}_{i-1} \rangle = 0,$$

and

$$\langle \mathbf{v}_{i-1/2,i}, \mathbf{j}_i \rangle = \left(\frac{q_{3,i-1/2}}{\rho_U \Delta s} + \frac{q_{4,i-1/2}}{\rho_L \Delta s} \right) = Q_{i-1/2}.$$

Consequently, condition (3.43) can be written with the volumetric flow constraint (3.31) as

$$[\![h_{p,i-1/2}]\!] = [\![\overline{Q}_{i-1/2} p_{i-1/2}]\!] = [\![Q(t) p_{i-1/2}]\!], \tag{3.45}$$

so that (3.43) (and (3.39)) is satisfied when $h_{p,i}$ is given by

$$\boxed{h_{p,i} = Q(t) p_i.} \tag{3.46}$$

Note that our constraint-consistent time integration method enforces that the volumetric flow constraint is satisfied up to machine precision [107].

3.5.3 Reformulation in terms of the entropy potential and conditions on numerical fluxes

The objective of finding energy-conserving numerical fluxes is better served by reformulating condition (3.38) in terms of the entropy potential, because this results in an alternative, constructive, condition for finding energy-conserving fluxes. The fluxes are then based on the entropy potential $\psi_{i-1/2}$ instead of the energy flux $h_{f,i}$. Similar to section 3.3.3, we rewrite the left-hand side of (3.38) as:

$$\begin{aligned} \langle \mathbf{v}_{i-1/2,i-1}, [\![\mathbf{f}_{i-1}]\!] \rangle + \langle \mathbf{v}_{i-1/2,i}, [\![\mathbf{f}_i]\!] \rangle = [\![\langle \overline{\mathbf{v}}_{i-1/2,i-1}, \mathbf{f}_{i-1} \rangle]\!] + [\![\langle \overline{\mathbf{v}}_{i-1/2,i}, \mathbf{f}_i \rangle]\!] \\ - \overline{\langle [\![\mathbf{v}_{i-1/2,i-1}]\!], \mathbf{f}_{i-1} \rangle} - \overline{\langle [\![\mathbf{v}_{i-1/2,i}]\!], \mathbf{f}_i \rangle}, \end{aligned} \tag{3.47}$$

which can be interpreted as a discrete version of the product rule $\langle \mathbf{v}, \frac{\partial \mathbf{f}}{\partial s} \rangle = \frac{\partial}{\partial s} \langle \mathbf{v}, \mathbf{f} \rangle - \langle \frac{\partial \mathbf{v}}{\partial s}, \mathbf{f} \rangle$. We have made use of the following definitions:

$$\begin{aligned} \overline{\mathbf{v}}_{i,i-1/2} &= \frac{1}{2} \left(\mathbf{v}_{i-1/2,i-1} + \mathbf{v}_{i+1/2,i} \right), & \overline{\mathbf{v}}_{i,i+1/2} &= \frac{1}{2} \left(\mathbf{v}_{i-1/2,i} + \mathbf{v}_{i+1/2,i+1} \right), \\ [\![\mathbf{v}_{i,i-1/2}]\!] &= \mathbf{v}_{i+1/2,i} - \mathbf{v}_{i-1/2,i-1}, & [\![\mathbf{v}_{i,i+1/2}]\!] &= \mathbf{v}_{i+1/2,i+1} - \mathbf{v}_{i-1/2,i}. \end{aligned}$$

These definitions are such that we only interpolate or take jumps between $\mathbf{v}$ vectors with the same relative indices.

Instead of directly choosing ψ, it is more natural to use the last terms in (3.47) and define the jump in ψ (similar to (3.23)) as

$$[\![\psi_i]\!] = \langle [\![\mathbf{v}_{i,i-1/2}]\!], \mathbf{f}_{i-1/2} \rangle + \langle [\![\mathbf{v}_{i,i+1/2}]\!], \mathbf{f}_{i+1/2} \rangle, \tag{3.48}$$

since this leads to the following 'implied' definition of ψ:

$$[\![\overline{\psi}_{i-1/2}]\!] = \overline{[\![\psi_{i-1/2}]\!]} = \frac{1}{2} [\![\psi_{i-1}]\!] + \frac{1}{2} [\![\psi_i]\!] = [\![\langle \overline{\mathbf{v}}_{i-1/2,i-1}, \mathbf{f}_{i-1} \rangle]\!] + [\![\langle \overline{\mathbf{v}}_{i-1/2,i}, \mathbf{f}_i \rangle]\!] - \left[\!\!\left[h_{f,i-1/2} \right]\!\!\right], \tag{3.49}$$

which is consistent with (3.22). The advantage of (3.48) over (3.38) is that we have a condition on the flux itself, rather than on the jump in the flux. Once $e_{i-1/2}$ and $\psi_{i-1/2}$ have been chosen and $\mathbf{f}_{i-1/2}$ has been derived, $h_{f,i}$ can be determined from

$$h_{f,i} = \langle \overline{\mathbf{v}}_{i,i-1/2}, \mathbf{f}_{i-1/2} \rangle + \langle \overline{\mathbf{v}}_{i,i+1/2}, \mathbf{f}_{i+1/2} \rangle - \overline{\psi}_i. \tag{3.50}$$

We note that this expression is similar to the collocated grid setting, where one has $h_{f,i-1/2} = \langle \overline{\mathbf{v}}_{i-1/2}, \mathbf{f}_{i-1/2} \rangle - \overline{\psi}_{i-1/2}$ [42]. The difference lies in a shift in indices (because our energy is defined at $i-1/2$ instead of i), and in the way the term $\langle \mathbf{v}, \mathbf{f} \rangle$ is approximated.

We propose now the following discrete entropy potential for the equations:

$$\boxed{\psi_{i-1/2}(\mathbf{q}_{i-1}, \mathbf{q}_i) = -\rho_U g_n \overline{\widehat{H}}_{U,i-1/2} \frac{q_{3,i-1/2}}{\overline{q}_{1,i-1/2}} - \rho_L g_n \overline{\widehat{H}}_{L,i-1/2} \frac{q_{4,i-1/2}}{\overline{q}_{2,i-1/2}}} \tag{3.51}$$

$$= -\rho_U g_n \overline{\widehat{H}}_{U,i-1/2} u_{U,i-1/2} - \rho_L g_n \overline{\widehat{H}}_{L,i-1/2} u_{L,i-1/2}.$$

This is a straightforward discretization of (3.24). Given the expressions for $\mathbf{v}$ ((3.41) and (3.42)), condition (3.48) can now be evaluated to yield the numerical fluxes $\mathbf{f}_{i-1/2}$. In order to be able to derive from the (scalar) condition (3.48) multiple equations for the individual numerical fluxes, we split $f_{3,i-1}$ and $f_{4,i-1}$ into an advective component (denoted by subscript a) and a level gradient (or gravity) component (denoted by subscript g): $f_{3,i-1} = f_{3,i-1,a} + g_n f_{3,i-1,g}$ and $f_{4,i-1} = f_{4,i-1,a} + g_n f_{4,i-1,g}$.

As a consequence, condition (3.48) can be split into the following four separate conditions by collecting terms featuring g_n and those not featuring g_n, and by using the functional dependencies assumed for the fluxes:

$$-\left[\!\left[\frac{1}{2} \frac{q_{3,i}^2}{\overline{q}_{1,i}^2} \right]\!\right] \overline{f}_{1,i} + \left[\!\left[\frac{q_{3,i}}{\overline{q}_{1,i}} \right]\!\right] f_{3,i,a} = 0, \tag{3.52a}$$

$$-\left[\!\left[\frac{1}{2} \frac{q_{4,i}^2}{\overline{q}_{2,i}^2} \right]\!\right] \overline{f}_{2,i} + \left[\!\left[\frac{q_{4,i}}{\overline{q}_{2,i}} \right]\!\right] f_{4,i,a} = 0, \tag{3.52b}$$

$$\overline{\left(\left[\!\left[g_n \left(H - H_{U,i}\right) \right]\!\right] f_{1,i}\right)} + \left[\!\left[\frac{q_{3,i}}{\overline{q}_{1,i}} \right]\!\right] g_n f_{3,i,g} = -\left[\!\left[\rho_U g_n \overline{\widehat{H}}_{U,i} \frac{q_{3,i}}{\overline{q}_{1,i}} \right]\!\right], \tag{3.52c}$$

$$\overline{\left(\left[\!\left[g_n H_{L,i} \right]\!\right] f_{2,i}\right)} + \left[\!\left[\frac{q_{4,i}}{\overline{q}_{2,i}} \right]\!\right] g_n f_{4,i,g} = -\left[\!\left[\rho_L g_n \overline{\widehat{H}}_{L,i} \frac{q_{4,i}}{\overline{q}_{2,i}} \right]\!\right]. \tag{3.52d}$$

These conditions have been obtained analogously to their continuous equivalents (3.26). In the continuous case, the fluxes were known and these conditions were satisfied by construction. In the discrete case, these conditions will be used in the next section to determine the numerical fluxes.

3.5.4 Derivation of energy-conserving numerical fluxes for the TFM

System (3.52) is a system of four equations for six unknowns. This leaves the mass fluxes $f_{1,i-1/2}$ and $f_{2,i-1/2}$ free to be chosen arbitrarily, with the expressions for $f_{3,i}$ and $f_{4,i}$ depending on this choice. This observation has been made previously for the (isothermal)

compressible Euler equations [62, 124], of which the advective terms have a similar mathematical form to those of the TFM. We take the following choice for $f_{1,i-1/2}$ and $f_{2,i-1/2}$:

$$\boxed{f_{1,i-1/2} = \frac{q_{3,i-1/2}}{\Delta s} \quad \text{and} \quad f_{2,i-1/2} = \frac{q_{4,i-1/2}}{\Delta s},} \tag{3.53}$$

which is motivated by the fact that it requires no interpolation (so that the mass and momentum equations are directly coupled), and moreover is such that the discrete Poisson equation (3.32) follows naturally from the discrete volumetric flow constraint (3.31) (which is used in our time integration method [107]).

Substituting $f_{1,i-1/2}$ in (3.52a) and $f_{2,i-1/2}$ in (3.52b) yields directly

$$\boxed{f_{3,i,a} = \frac{1}{\Delta s}\overline{\left(\frac{q_{3,i}}{\overline{q}_{1,i}}\right)}\overline{q}_{3,i} \quad \text{and} \quad f_{4,i,a} = \frac{1}{\Delta s}\overline{\left(\frac{q_{4,i}}{\overline{q}_{2,i}}\right)}\overline{q}_{4,i}.} \tag{3.54}$$

To get the gravity component of $f_{3,i}$ and $f_{4,i}$, substitution of $f_{2,i-1/2}$ in (3.52d) leads to

$$\frac{1}{2}\left[\!\left[H_{L,i-1/2}\right]\!\right]\frac{q_{4,i-1/2}}{\Delta s} + \frac{1}{2}\left[\!\left[H_{L,i+1/2}\right]\!\right]\frac{q_{4,i+1/2}}{\Delta s} + \left[\!\left[\frac{q_{4,i}}{\overline{q}_{2,i}}\right]\!\right] f_{4,i,g} = \rho_L\overline{\widehat{H}}_{L,i-1/2}\frac{q_{4,i-1/2}}{\overline{q}_{2,i-1/2}} - \rho_L\overline{\widehat{H}}_{L,i+1/2}\frac{q_{4,i+1/2}}{\overline{q}_{2,i+1/2}}.$$

After significant rewriting, this yields the following expression for the gravity component of $f_{4,i}$:

$$f_{4,i,g} = -\rho_L\widehat{H}_{L,i} - \overline{\left[\left(\rho_L\frac{\left[\!\left[\widehat{H}_{L,i}\right]\!\right]}{\overline{q}_{2,i}} + \frac{\left[\!\left[H_{L,i}\right]\!\right]}{\Delta s}\right)q_{4,i}\right]}\left[\!\left[\frac{q_{4,i}}{\overline{q}_{2,i}}\right]\!\right]^{-1}, \tag{3.55}$$

and a similar expression holds for $f_{3,i,g}$ (but with a minus sign instead of the plus sign).

The first term on the right-hand side is easily recognized as the discrete counterpart of $-\rho_L\widehat{H}_L$. In order for the discrete expression to be practical and match the continuous expression, the second term must vanish, and we require the following conditions to be satisfied:

$$\left[\!\left[\widehat{H}_{U,i-1/2}\right]\!\right] = \frac{\overline{q}_{1,i-1/2}}{\rho_U\Delta s}\left[\!\left[H_{U,i-1/2}\right]\!\right], \qquad \left[\!\left[\widehat{H}_{L,i-1/2}\right]\!\right] = -\frac{\overline{q}_{2,i-1/2}}{\rho_L\Delta s}\left[\!\left[H_{L,i-1/2}\right]\!\right]. \tag{3.56}$$

In the continuous case a continuous version of these conditions, given by (3.21), is also required, and these can be shown to be satisfied exactly via manipulation of the continuous derivatives. The same manipulation is not possible with discrete jumps, so that in the discrete case these conditions are not satisfied in general, and the second term in (3.55) does not generally vanish. This means that we cannot obtain a practical energy-conserving discretization for arbitrary geometries (at least not with the conventional staggered-grid finite volume method that we have employed).

Even though conditions (3.56) are not generally exactly satisfied in the discrete case, we can show that they are approximately satisfied for arbitrary duct geometries, and that they are exactly satisfied for specific geometries such as a channel. This can be shown by evaluating both sides of (3.56) using Taylor series. We expand $\widehat{H}_{L,i-1}$ and $H_{L,i-1}$ into Taylor series around $A_L = A_{L,i}$, and expand $A_{L,i-1}$ around $s = s_i$. These Taylor series are combined to obtain expressions for $\left[\!\left[\widehat{H}_{L,i-1/2}\right]\!\right]$, $\left[\!\left[H_{L,i-1/2}\right]\!\right]$, and $\left[\!\left[A_{L,i-1/2}\right]\!\right]$. With these expressions the left-hand side of (3.56) (for the lower fluid) evaluates to

$$\left[\!\left[\widehat{H}_{L,i-1/2}\right]\!\right] = -\left(\frac{\mathrm{d}\widehat{H}_L}{\mathrm{d}A_L}\right)_i \left(A_{L,i-1} - A_{L,i}\right) - \frac{1}{2}\left(\frac{\mathrm{d}^2\widehat{H}_L}{\mathrm{d}A_L^2}\right)_i \left(A_{L,i-1} - A_{L,i}\right)^2 - \frac{1}{6}\left(\frac{\mathrm{d}^3\widehat{H}_L}{\mathrm{d}A_L^3}\right)_i \left(A_{L,i-1} - A_{L,i}\right)^3 + O(\Delta s^4), \quad (3.57)$$

where $(.)_i$ indicates $(.)$ evaluated at $A_{L,i}$. The right-hand side of (3.56) evaluates to

$$-\frac{\overline{q}_{2,i-1/2}}{\rho_L \Delta s}\left[\!\left[H_{L,i-1/2}\right]\!\right] = \frac{1}{2}\left(\frac{\mathrm{d}H_L}{\mathrm{d}A_L}\right)_i \left(A_{L,i-1}^2 - A_{L,i}^2\right) + \frac{1}{4}\left(\frac{\mathrm{d}^2H_L}{\mathrm{d}A_L^2}\right)_i \left(A_{L,i-1} + A_{L,i}\right)\left(A_{L,i-1} - A_{L,i}\right)^2 + \frac{1}{12}\left(\frac{\mathrm{d}^3H_L}{\mathrm{d}A_L^3}\right)_i \left(A_{L,i-1} + A_{L,i}\right)\left(A_{L,i-1} - A_{L,i}\right)^3 + O(\Delta s^4). \quad (3.58)$$

At this point we apply relation (A.6) from Appendix A to the discrete quantities used here:

$$\left(\frac{\mathrm{d}\widehat{H}_L}{\mathrm{d}A_L}\right)_i = -A_{L,i}\left(\frac{\mathrm{d}H_L}{\mathrm{d}A_L}\right)_i,$$

and from this we can derive

$$\left(\frac{\mathrm{d}^2\widehat{H}_L}{\mathrm{d}A_L^2}\right)_i = -\left(\frac{\mathrm{d}H_L}{\mathrm{d}A_L}\right)_i - A_{L,i}\left(\frac{\mathrm{d}^2H_L}{\mathrm{d}A_L^2}\right)_i, \quad \text{and} \quad \left(\frac{\mathrm{d}^3\widehat{H}_L}{\mathrm{d}A_L^3}\right)_i = -2\left(\frac{\mathrm{d}^2H_L}{\mathrm{d}A_L^2}\right)_i - A_{L,i}\left(\frac{\mathrm{d}^3H_L}{\mathrm{d}A_L^3}\right)_i.$$

Substitution of these relations in (3.57), and comparison of the result to (3.58) yields

$$\left[\!\left[\widehat{H}_{L,i-1/2}\right]\!\right] = -\frac{\overline{q}_{2,i-1/2}}{\rho_L \Delta s}\left[\!\left[H_{L,i-1/2}\right]\!\right] + \frac{1}{12}\left(\frac{\mathrm{d}^2H_L}{\mathrm{d}A_L^2}\right)_i \left(A_{L,i-1} - A_{L,i}\right)^3 + O(\Delta s^4). \quad (3.59)$$

This derivation can be carried out with similar results for the upper fluid.

These relations show that for arbitrary duct geometries, the geometric conditions (3.56) are satisfied only approximately in the discrete case. This stands in contrast to the continuous case, where the equivalent geometric conditions are satisfied exactly (for arbitrary geometries).

Fortunately, for a 2D channel geometry $\mathrm{d}H_L/\mathrm{d}A_L = 1$ and $\mathrm{d}^2H_L/\mathrm{d}A_L^2 = 0$, and all higher order derivatives are zero, so in this case (3.56) is exactly satisfied. This means that the 2D channel geometry is an important special case for which we obtain the following conservative numerical fluxes:

$$\boxed{f_{3,i,g} = -\rho_U \widehat{H}_{U,i} \quad \text{and} \quad f_{4,i,g} = -\rho_L \widehat{H}_{L,i}.} \quad (3.60)$$

These fluxes are energy-conserving for other geometries with $\mathrm{d}^2 H_L/\mathrm{d}A_L^2 = 0$, but not for geometries with curved sides, such as the pipe geometry.

The final collection of energy-conserving numerical fluxes is given by (3.53), (3.54), and (3.60). Of these, (3.53) and (3.60) are locally exact, and (3.54) involves second order accurate central interpolation. Together they form the numerical flux vector

$$\mathbf{f}_{i-1/2} = \begin{bmatrix} \frac{q_{3,i-1/2}}{\Delta s} \\ \frac{q_{4,i-1/2}}{\Delta s} \\ \frac{1}{\Delta s}\overline{\left(\frac{q_{3,i-1}}{\overline{q}_{1,i-1}}\right)}\overline{q}_{3,i-1} - \rho_U g_n \widehat{H}_{U,i-1} \\ \frac{1}{\Delta s}\overline{\left(\frac{q_{4,i-1}}{\overline{q}_{2,i-1}}\right)}\overline{q}_{4,i-1} - \rho_L g_n \widehat{H}_{L,i-1} \end{bmatrix} = \begin{bmatrix} \rho_U \overline{A}_{U,i-1/2} u_{U,i-1/2} \\ \rho_L \overline{A}_{L,i-1/2} u_{L,i-1/2} \\ \rho_U \overline{u}_{U,i-1}\overline{\left(\overline{A}_{U,i-1} u_{U,i-1}\right)} - \rho_U g_n \widehat{H}_{U,i-1} \\ \rho_L \overline{u}_{L,i-1}\left(\overline{A}_{L,i-1} u_{L,i-1}\right) - \rho_L g_n \widehat{H}_{L,i-1} \end{bmatrix}. \tag{3.61}$$

Here the flux is rendered in terms of primitive variables only for ease of interpretation; the implementation of the numerical flux (and of the discrete energy) in the numerical code is completely in terms of the conservative variables.

Remark 1. The difficulty to satisfy condition (3.56) for arbitrary cross-sectional geometries is not dependent on the choice of $\psi_{i-1/2}$, nor is it due to the interpolation of the potential energy to the velocity grid points (as needed on a staggered grid). This is shown in section 3.A by applying a global energy analysis.

Remark 2. The proposed discrete energy (3.40) is a consistent approximation to (3.16) which is conserved by the numerical fluxes given by (3.61). However, it is not unique. For example, an alternative definition is

$$e_i(\mathbf{q}_{i-1}, \mathbf{q}_i, \mathbf{q}_{i+1}) = \rho_U g_n \widetilde{H}_{U,i} \Delta s + \rho_L g_n \widetilde{H}_{L,i} \Delta s + \frac{1}{2}\overline{\left(\frac{q_{3,i}^2}{\overline{q}_{1,i}}\right)} + \frac{1}{2}\overline{\left(\frac{q_{4,i}^2}{\overline{q}_{2,i}}\right)}. \tag{3.62}$$

In this formulation the energy is defined on the pressure grid, and the energy conservation conditions and local energy conservation equation can be adapted to accommodate for this. With a similar change in the entropy potential, it is again possible to derive a set of energy-conserving numerical fluxes, which turn out to be the same as those given by (3.61). As the issue of the geometric relations also persists with this choice, there seems no clear advantage over our proposed formulation.

Remark 3. It is possible to show that, with our discretization of the advective terms, the advective contribution to the global energy equation (given by a sum over the domain of the left-hand side of (3.38), minus gravitational terms) can be written as

$$\mathbf{u}_{U,h}^T \mathbf{C}_U \mathbf{u}_{U,h} + \mathbf{u}_{L,h}^T \mathbf{C}_L \mathbf{u}_{L,h},$$

where $\mathbf{u}_{U,h} = [u_{U,1/2} \dots u_{U,N_u-1/2}]^T$ and similar for $\mathbf{u}_{L,h}$, and with $\mathbf{C}_U = \mathbf{C}_U(\mathbf{f}_{1,h}, \mathbf{u}_{U,h})$ and $\mathbf{C}_L = \mathbf{C}_L(\mathbf{f}_{2,h}, \mathbf{u}_{L,h})$ being skew-symmetric matrices. From this it can be shown that the advective terms conserve global energy. In [122], this principle is used to derive a similar discretization of the advective terms for the SWE.

3.6 Numerical experiments

We perform numerical experiments for a 2D channel geometry, with the goal of verifying conservation of the discrete global energy, as discussed in section 3.5.1:

$$\frac{\mathrm{d}E_h}{\mathrm{d}t} = 0.$$

The model for which we perform the experiments will not include source terms such as wall friction and interface friction, or diffusion, since these would lead to dissipation of energy in the continuous analysis. The test cases are chosen such that no discontinuities appear, for which the continuous analysis is invalid, since this would also necessitate dissipation of energy. Furthermore, the numerical experiments performed in this section will all be in the 'well-posed regime' of the TFM, meaning that the initial conditions are chosen such that the eigenvalues of the model are real, and remain so.

We use the discretization as outlined in section 3.4, with the numerical fluxes given by (3.61). The vector $\mathbf{j}_i$ of the pressure term is given by (3.44). We noted earlier that the scheme is spatially exactly energy-conserving, but not temporally. However, we can still obtain energy conservation by taking the time step sufficiently small. The difference between the initial energy E_h^0 and the final energy $E_h^{N_t}$ after N_t time steps should then be in the order of the machine precision, and we shall term this difference the 'energy error'.

3.6.1 Gaussian perturbation in a periodic domain

We consider a test case with periodic boundaries, so that effectively we do not need to take the boundaries into account. We introduce a perturbation in the hold-up $\alpha_L = A_L/A$ of the form

$$\alpha_L(s) = \alpha_{L,0} + \Delta\alpha_L(s), \qquad \Delta\alpha_L(s) = \Delta\widehat{\alpha}_L \exp\left[-\frac{1}{2}\left(\frac{s - L/2}{\sigma}\right)^2\right],$$

with $\Delta\widehat{\alpha}_L = 0.2$ and $\sigma = L/10$, and L the length of the domain. This produces a Gaussian perturbation centered at the middle of the domain. The initial velocities are left at zero, which ensures exact initial satisfaction of the volumetric flow constraint (3.6) (in fact, $Q = 0$).

We use parameters similar to those used in the Thorpe experiment [117], as described by [77]. They are given by Table 3.1. The choice for a high upper fluid density is deliberate: it ensures that all terms in the expression for e, (3.40), are significant. Additionally, at large density ratios (i.e. low upper fluid density) the flow becomes more violent and the formation of shocks becomes more likely, the treatment of which is outside the scope of this chapter.

We employ $N_p = N_u = 40$ finite volumes with $\Delta s = L/N_p$ and let the simulations run until $t = 30\,\mathrm{s}$, with $\Delta t = 0.001\,\mathrm{s}$. The perturbation splits symmetrically into a left-traveling and a right-traveling wave, which travel through the periodic boundaries, to eventually come together in the middle and reform the initial perturbation approximately. We show the evolution of the hold-up and velocity in Figure 3.3, roughly up to the point that the waves meet at the boundaries of the domain.

Table 3.1: Parameters for the Gaussian perturbation test case.

Parameter	Symbol	Value	Units
Lower fluid density	ρ_L	1000	$\mathrm{kg\,m^{-3}}$
Upper fluid density	ρ_U	780	$\mathrm{kg\,m^{-3}}$
Acceleration of gravity	g	9.8	$\mathrm{m\,s^{-2}}$
Channel inclination	ϕ	0	degrees
Domain length	L	1.83	m
Channel height	H	0.03	m
Initial lower fluid hold-up	$\alpha_{L,0}$	0.5	–
Initial lower fluid velocity	$u_{L,0}$	0	$\mathrm{m\,s^{-1}}$
Initial upper fluid velocity	$u_{U,0}$	0	$\mathrm{m\,s^{-1}}$

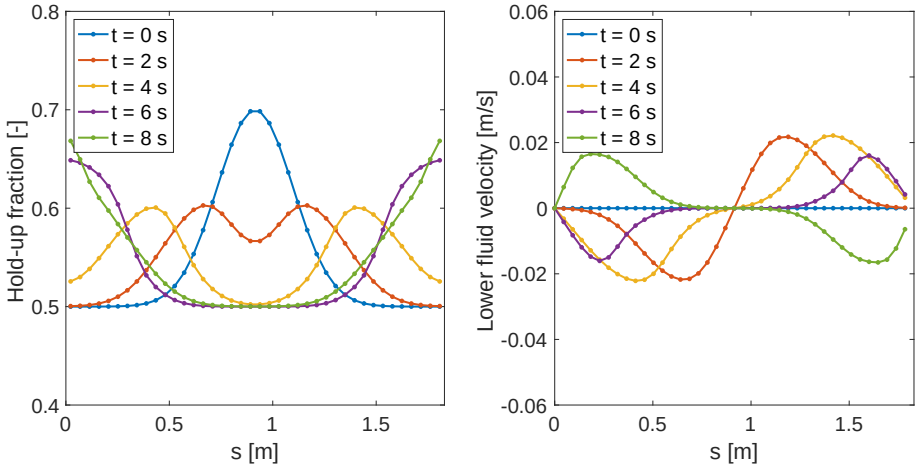

Figure 3.3: The initial evolution of the Gaussian perturbation, up to the point that the boundaries are met. Left: lower fluid hold-up. Right: lower fluid velocity.

In this test case we have a significant exchange between kinetic and potential energy, which can be seen in Figure 3.4 (left panel). The total energy is conserved up to machine precision, as can be seen in the right panel of the figure. The mass of each phase and total momentum are also conserved, and the volume constraint and volumetric flow constraint are satisfied, up to machine precision (see also [107]). As time progresses, nonlinear effects start to play a role, leading to more irregular behavior of the potential and kinetic energy as a function of time. The sum of the two stays exactly constant, confirming our theoretical derivations, and showing that our newly proposed numerical fluxes for the TFM lead indeed to an energy-conserving discretization method.

We give further evidence that the energy is conserved exactly by the spatial discretization, and limited only by a temporal error, by plotting the convergence of the energy error with refinement of the time step, and with refinement of the grid. The first plot in Figure 3.5 shows a fourth order convergence rate with Δt, in agreement with the fourth

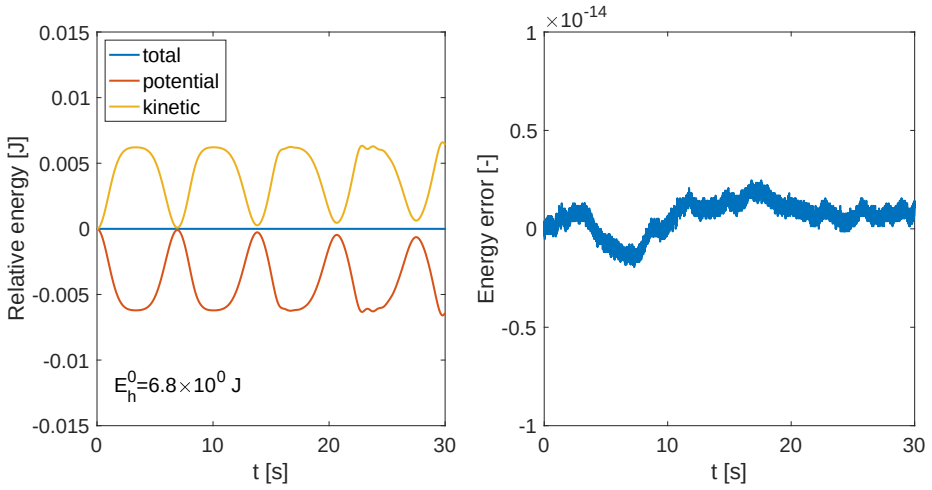

Figure 3.4: Conserved quantities for the Gaussian perturbation test case. Left: potential, kinetic and total energy relative to their initial values. Right: $\left(E_h - E_h^0\right)/E_h^0$.

order accuracy of the Runge-Kutta time integration method. The convergence continues up to machine precision, which is reached around $\Delta t = 0.001$ s, as was used for the results in Figure 3.4. The second plot in Figure 3.5 shows that when using a small enough time step, the same (minimal) level of error is obtained, irrespective of spatial resolution.

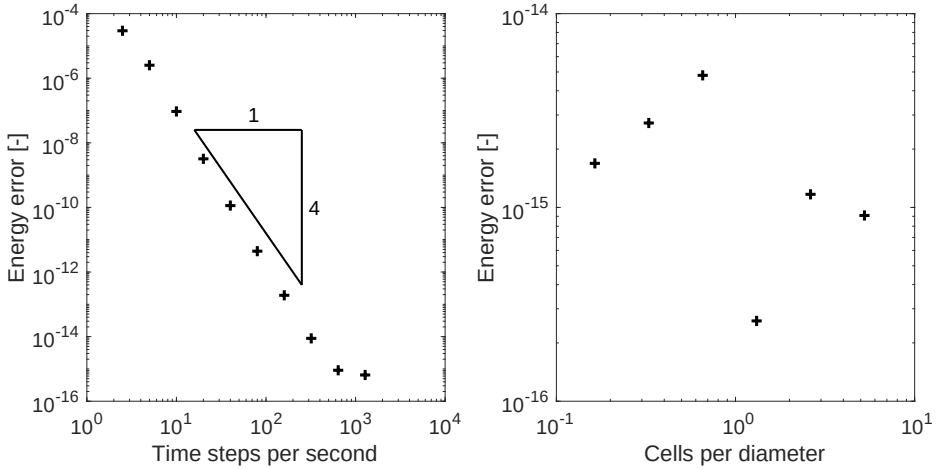

Figure 3.5: Convergence of the energy error $\left(E_h^{N_t} - E_h^0\right)/E_h^0$ for the Gaussian perturbation test case. Left: constant $N_p = 40$. Right: constant $\Delta t = 0.0001$ s.

3.6.2 Sloshing in a closed tank

We now consider a test case with closed (solid-wall) boundaries, for which energy conservation is expected to hold because the fluxes h_f and h_p involve multiplication with q_3 and q_4, which are zero at the boundaries. The test case features a closed rectangular tank in which the two fluids are brought out of equilibrium, so that sloshing occurs. The parameters are identical to those of the previous test case, see Table 3.1, except that the initial condition for the hold-up perturbation is different. It is given by

$$\alpha_L(s) = \alpha_{L,0} + \Delta\alpha_L(s), \qquad \Delta\alpha_L(s) = \Delta\widehat{\alpha}_L \frac{s - L/2}{L/2},$$

with $\Delta\widehat{\alpha}_L = 0.2$. This yields a straight slanted interface, with $\alpha_L = 0.3$ at the left boundary and $\alpha_L = 0.7$ at the right boundary: see Figure 3.6.

This is not a typical sloshing case, since the TFM was designed to model long-wavelength phenomena, and indeed we have taken $L \gg H$. Therefore we are not able to explicitly capture typical sloshing phenomena such as wave breaking. However, the effect of such small-scale phenomena on the averaged flow may be included in the model via closure terms [55]. With accurate closure terms, the TFM can closely match DNS results, as shown in [18]. This is not included here, as this would lead to dissipation of energy and not allow us to show the energy-conserving properties of our proposed numerical discretization.

Like in the first test case, initially the total energy of the system consists of only potential energy. Under the influence of gravity (via the level gradient terms) the interface starts to flatten, which is achieved via a right-running and a left-running wave, that emanate from the left and right boundary, respectively. Around $t = 7\,\mathrm{s}$ the interface is almost completely flat, and all potential energy has been converted into kinetic energy, and the interface starts to slant ('slosh') again in the opposite direction. Figure 3.6 shows this behavior up to approximately the point that the lower fluid reaches its maximum height at the left boundary. Note that the evolution of the hold-up fraction is not exactly symmetric, amongst others because the wave speed in the 'deep' part is different from the wave speed in the 'shallow' part. Also in this test case, the mass of each phase is conserved up to machine precision, but there is a (physical) inflow of momentum at the boundaries, due to the level gradient terms.

Figure 3.7 shows the exchange of potential and kinetic energy as a function of time. Similar to the previous test case, exact energy conservation is achieved with our proposed spatial discretization, if the time step is fine enough (here $\Delta t = 0.005\,\mathrm{s}$, and $N_p = 40$). If the time step is not fine enough, a (small) energy error is made, which converges with fourth order upon time step refinement, as is shown in Figure 3.8. The ability to conserve energy in this closed system is an important step in order to obtain fidelity in the simulation results. Non-energy-conserving schemes, e.g. schemes that dissipate energy, would introduce artificial (numerical) damping of the sloshing movement and incur a loss in the liquid height reached at the boundaries. In a way, the sloshing movement can be compared to a moving pendulum [91], for which it is well-known that conservation of the total energy (the Hamiltonian) is an important property that should be mimicked upon discretization in order to achieve realistic long-time behavior.

Figure 3.9 shows results for a test case using the same parameters, but in a circular pipe geometry, with a diameter corresponding to the height of the 2D channel (0.03 m). A

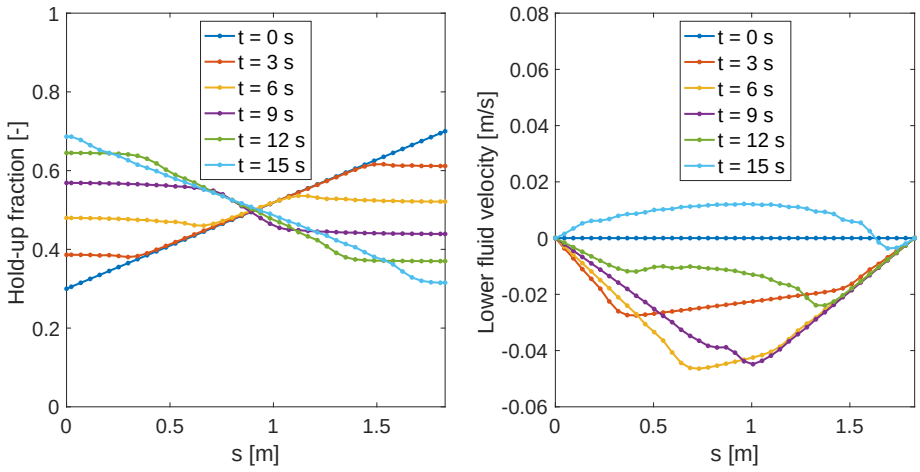

Figure 3.6: The initial evolution of the sloshing simulation, approximately up to the point that the lower fluid reaches its maximum height at the left boundary. Left: lower fluid hold-up. Right: lower fluid velocity.

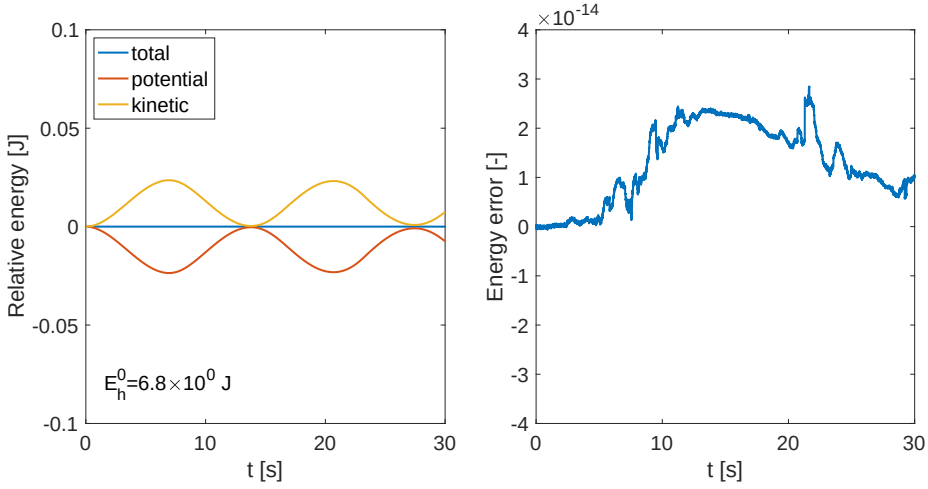

Figure 3.7: Conserved quantities for the sloshing test case. Left: potential, kinetic and total energy relative to their initial values. Right: $\left(E_h - E_h^0\right)/E_h^0$.

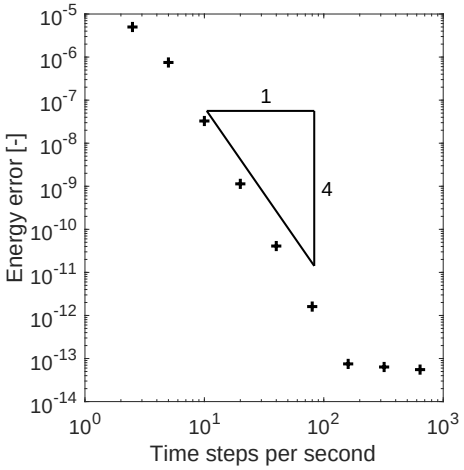

Figure 3.8: Convergence of the energy error $\left(E_h^{N_t} - E_h^0\right)/E_h^0$ with time step, for the sloshing test case.

similar sloshing motion takes place, and the exchange of potential and kinetic energy is similar to that shown in Figure 3.7 for the channel. However, for the pipe geometry, we observe a spatial discretization error in the total energy, stemming from the extra terms in (3.59). Though the energy error comes out positive at $t = 30\,\mathrm{s}$, the long-term trend is towards dissipation. Fortunately, for this case with $N_p = 40$ and $\Delta t = 0.005\,\mathrm{s}$, the energy error incurred by our proposed discretization remains relatively small and the effect on the solution is limited.

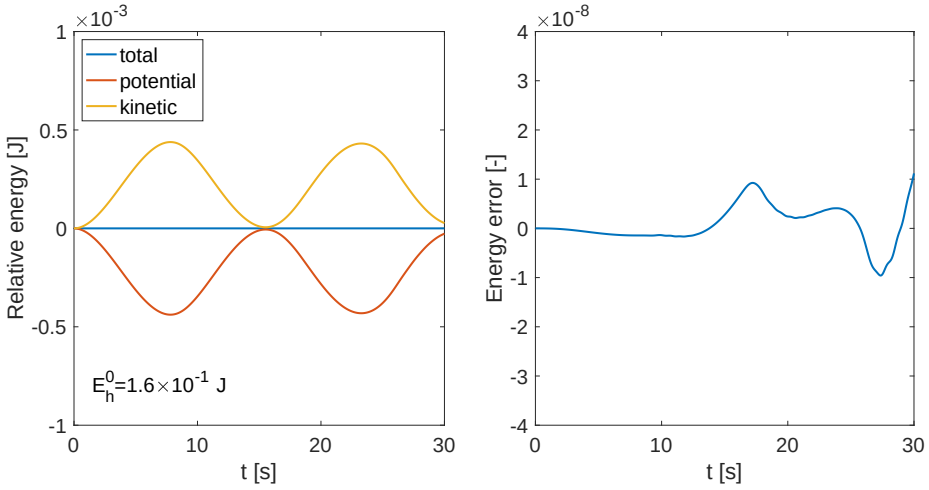

Figure 3.9: Conserved quantities for the sloshing test case, but in a circular pipe geometry. Left: potential, kinetic and total energy relative to their initial values. Right: $\left(E_h - E_h^0\right)/E_h^0$.

3.6.3 Traveling wave

Finally, we perform a test case with a traveling wave in a periodic domain. The flow is unidirectional and stratified, with a velocity and density difference between the two fluids. We consider a steady base state, upon which a small periodic perturbation is introduced, of which we study the evolution in time. This case is similar to test cases examining the Kelvin-Helmholtz instability, such as in [74, 107]. However, here the perturbation will be stable since the flow is inviscid and in the (linearly) well-posed regime.

Most of the parameters are again identical to those given by Table 3.1, but the initial conditions for the hold-up and the fluid velocities are different. We set $\alpha_{L,0} = 0.4$ and $u_{L,0} = 1$. For u_U we take $u_{U,0} = 1.187$ (which is the value that would result in a steady flow with wall and interface friction[4]).

In order to construct an initial perturbation that results in a traveling wave, we conduct a linear stability analysis of the TFM [74]. The analysis is conducted in terms of its primitive variables in the form

$$\mathbf{w}^T = \begin{bmatrix} \alpha_L & u_L & u_G & p \end{bmatrix}. \tag{3.63}$$

As exact solutions we obtain waves of the form

$$\Delta\mathbf{w} = \mathrm{Re}\left(\Delta\hat{\mathbf{w}} \exp\left[i(\omega t - ks)\right]\right), \tag{3.64}$$

with $\Delta\hat{\mathbf{w}}$ the amplitude of the perturbation in each variable. The relative amplitudes in $\Delta\hat{\mathbf{w}}$ are such that $\Delta\hat{\mathbf{w}}$ is an eigenvector corresponding to one of two dispersion relations $\omega(k)$.

The initial perturbation is defined as (3.64), with $t = 0$. We take a wavenumber of $k = 2\pi/L\,\mathrm{m}^{-1}$ and calculate the corresponding angular frequencies, of which one is selected. The chosen mode is

$$\omega = 3.982\,\mathrm{s}^{-1}.$$

Setting $\Delta\hat{\alpha}_L = 1 \cdot 10^{-2}$, the amplitudes of the other variables are calculated so that $\Delta\hat{\mathbf{w}}$ is an eigenvector corresponding to this mode:

$$\left(\Delta\hat{\mathbf{w}}\right)^T = \begin{bmatrix} 1.00 \cdot 10^{-2} & 3.99 \cdot 10^{-3} & 4.51 \cdot 10^{-3} & -2.30 \end{bmatrix}.$$

This ensures that the other mode is not present in the initial perturbation, so that we can study the isolated behavior of one mode. A projection step is then performed in order to make the initial condition satisfy the constraints (see section 3.4).

The initial condition is shown in Figure 3.10, along with its evolution in time, which is computed up to $t = 30\,\mathrm{s}$. Setting the initial condition this way yields a wave traveling to the right at velocity $\omega/k = 1.16\,\mathrm{m\,s}^{-1}$, which remains of approximately constant amplitude since the flow is inviscid and in the well-posed regime, so that ω has no imaginary component. The traveling wave can deform due to the nonlinear character of the governing equations, which is neglected in the linear stability analysis. This is made apparent by the snapshots of the solution shown in Figure 3.10, which are separated by an integer number of wave periods: at the time of the last snapshot the wave has traveled through the domain 18 times. The solutions do not completely overlap and we see wave steepening taking place.

[4]For this we take the Churchill friction model [28] with viscosities of $\mu_U = 1.5 \cdot 10^{-3}$ Pa s and $\mu_L = 1 \cdot 10^{-3}$ Pa s.

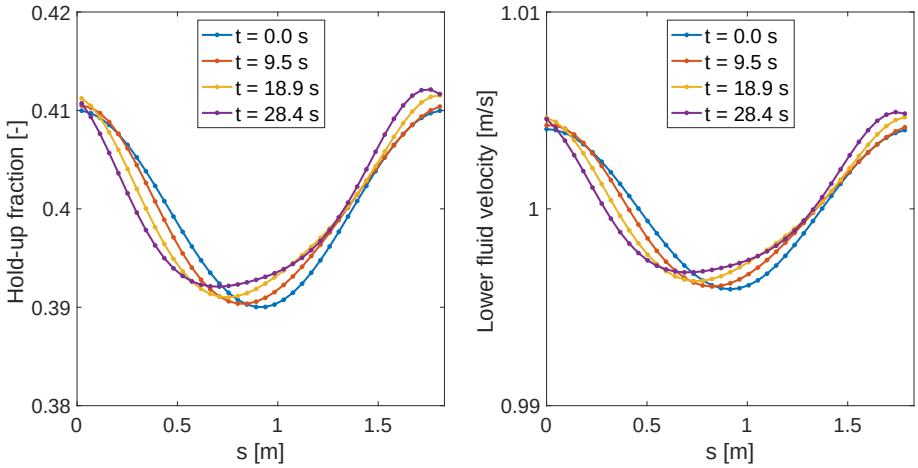

Figure 3.10: The initial perturbation travels to the right with time. Consecutive snapshots are separated by a time interval of 6 wave periods. Left: lower fluid hold-up. Right: lower fluid velocity.

Figure 3.11 shows the evolution of the energy. In this case, the exchange between kinetic and potential energy is small relative to the total energy of the base state. This is due to the fact that the wave is roughly constant in time, up to a displacement which does not change the energy.

The total energy can again be seen to remain constant up to a high precision. Like before, this is achieved by using a small time step ($\Delta t = 0.005\,\mathrm{s}$), with a modest spatial resolution ($N_p = N_u = 40$). Figure 3.12 shows how the energy converges with time step refinement. The convergence rate is fourth order over a wide range of time steps (matching the order of the time integration method), demonstrating that also for this test case, the spatial discretization conserves energy. While the solution moves away from the stable traveling wave predicted by linear analysis, its energy remains constant with time.

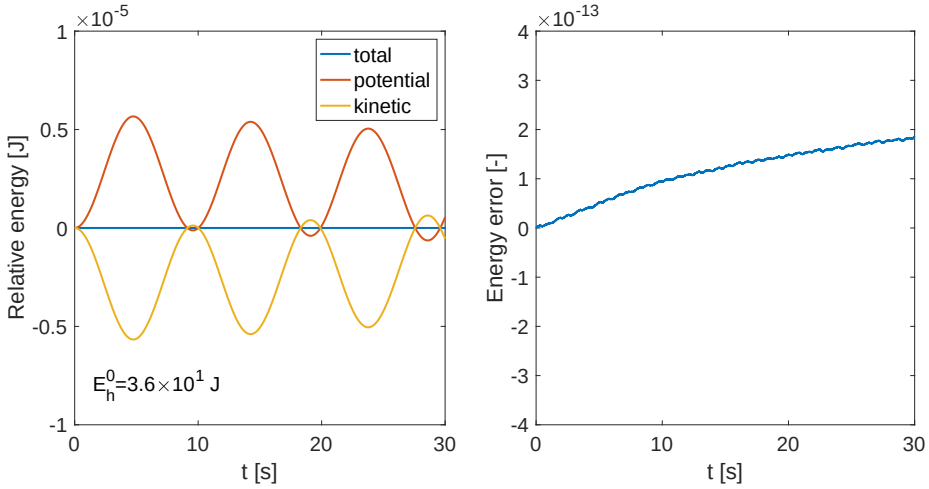

Figure 3.11: Conserved quantities for the traveling wave test case. Left: potential, kinetic and total energy relative to their initial values. Right: $\left(E_h - E_h^0\right)/E_h^0$.

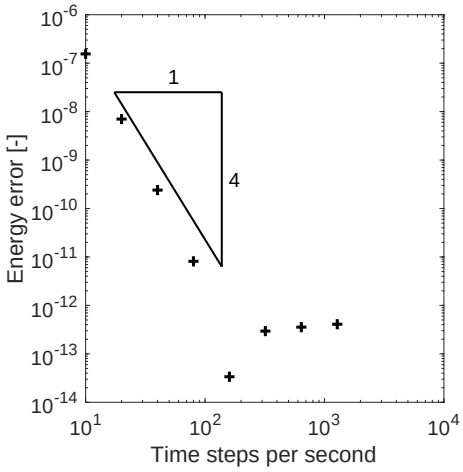

Figure 3.12: Convergence of the energy error $\left(E_h^{N_t} - E_h^0\right)/E_h^0$ with time step, for the traveling wave test case.

3.7 Conclusions

In this chapter, we have derived the result that the total mechanical energy (sum of kinetic and potential energy) is a secondary conserved quantity of the incompressible and isothermal TFM. This result is in line with the well-known fact that multi-dimensional incompressible frictionless flow equations conserve mechanical energy. Our novel insight is that this conservation statement still holds after averaging: the averaging procedure used to obtain the 1D TFM does not interfere with the energy conservation property. The approach was based on the formulation of entropy variables and an entropy potential, similar to what is commonly done for the SWE, but with two main differences: (i) we have included a non-conservative pressure term in our analysis, which is shown to be energy-conserving, and (ii) we have obtained our results independent of the duct geometry, which may be a 2D channel or a circular pipe, or any other closed cross-sectional duct shape.

The second novel result of this chapter is a set of numerical fluxes that conserve a discrete form of the mechanical energy. A discretization on a staggered grid was proposed in order to keep the energy conservation property of the non-conservative pressure terms in a discrete sense. Although the use of a staggered grid implies that the choice of a discrete energy and entropy potential is not unique, we were able to propose a combination which is such that the discrete analysis is consistent with and analogous to the continuous analysis. However, one important difference between the continuous and discrete cases remains, namely in the analysis of the level gradient terms (for arbitrary geometries). A geometric relation between the potential energy and the interface height is satisfied exactly in the continuous case, but only approximately in the discrete case. Fortunately, for the specific case of the 2D channel geometry, the condition is satisfied *exactly*, and the discrete level gradient reduces to a form which parallels the continuous form perfectly. For other geometries, such as the pipe, a small numerical energy error persists in the discrete analysis.

Our theoretical derivations are supported by numerical experiments, which show that the proposed energy is indeed exactly conserved by our new spatial discretization in both periodic and closed domains. Building on previous work [107], the discretization also conserves mass and momentum, has strong coupling between momentum and pressure, and is constraint-consistent. In these experiments the temporal error was negligible (due to a combination of high-order time integration and small time steps), but for future work it is suggested to also make the time integration method energy-conserving [103].

Our energy-conserving formulation of the TFM provides a foundation for investigating the nonlinear stability of the model. For related models, the energy acts as a norm or a convex entropy function of the solution, providing stability bounds, and it should be investigated if the TFM energy has similar implications. While we have only considered smooth solutions, in general cases discontinuities may appear, at which energy should be dissipated [61]. Failure of a numerical scheme to do so leads to numerical oscillations. As a first option, an energy-consistent discretization of the wall and interface friction, and streamwise diffusion due to molecular and turbulent viscosity [46, 126], could be considered. Alternatively, a carefully chosen numerical diffusion operator could be added to the scheme to obtain the required dissipation at shocks [24, 43].

Appendix
3.A Global energy analysis

The main text has described a way to derive the *local* semi-discrete energy conservation equation given by (3.33). In the case of periodic or closed boundaries, this can be integrated in space to yield global energy conservation. In this section, we directly derive the global energy conservation equation without the intermediate step of the local energy. This allows us to skip the step of choosing an entropy potential, which means that the derivation will contain less assumptions. On the other hand, the obtained conditions on the numerical fluxes are not constructive, because they are conditions for the 'jumps' of the numerical fluxes, rather than for a single numerical flux at one discrete point. Therefore, the global analysis is not used as a replacement, but as a validation of the local analysis.

The scheme (3.29) described in section 3.4 for a certain pressure volume i and velocity volume $i-1/2$ can be extended to describe the evolution of the entire state vector $\mathbf{q}_h$:

$$\frac{\mathrm{d}\mathbf{q}_h}{\mathrm{d}t} + \mathbf{f}_h + \mathbf{j}_h = \mathbf{0}, \tag{3.65}$$

where $\mathbf{q}_h = [q_{1,1} \dots q_{1,N}, q_{2,1} \dots q_{2,N}, q_{3,1/2} \dots q_{3,N-1/2}, q_{4,1/2} \dots q_{4,N-1/2}]^T$, and similar expressions for $\mathbf{f}_h$ and $\mathbf{j}_h$. For simplicity we only discuss periodic boundary conditions, for which $N_p = N_u = N$.

Similar to the local entropy variable $\mathbf{v}$ we define the global entropy variable

$$\mathbf{v}_h \coloneqq \left[\frac{\mathrm{d}E_h}{\mathrm{d}\mathbf{q}_h}\right]^T.$$

Taking the inner product of $\mathbf{v}_h$ and (3.65), the first term yields

$$\left\langle \mathbf{v}_h, \frac{\mathrm{d}\mathbf{q}_h}{\mathrm{d}t} \right\rangle = \frac{\mathrm{d}E_h}{\mathrm{d}t}.$$

Thus, to obtain global discrete energy conservation, given by $\frac{\mathrm{d}E_h}{\mathrm{d}t} = 0$, we need the following conditions on $\mathbf{f}_h$ and $\mathbf{j}_h$:

$$\langle \mathbf{v}_h, \mathbf{f}_h \rangle = 0, \tag{3.66}$$

$$\langle \mathbf{v}_h, \mathbf{j}_h \rangle = 0. \tag{3.67}$$

In order to evaluate $\mathbf{v}_h$, we note that

$$\frac{\partial E_h}{\partial \mathbf{q}_i} = \frac{\partial e_{i-1/2}}{\partial \mathbf{q}_i} + \frac{\partial e_{i+1/2}}{\partial \mathbf{q}_i} = \mathbf{v}_{i-1/2,i} + \mathbf{v}_{i+1/2,i} = \begin{bmatrix} -\frac{1}{2}\overline{\left(\frac{q_{3,i}^2}{q_{1,i}^2}\right)} + g_n\left(H - H_{U,i}\right) \\ -\frac{1}{2}\overline{\left(\frac{q_{4,i}^2}{q_{2,i}^2}\right)} + g_n H_{L,i} \\ \overline{\frac{q_{3,i-1/2}}{q_{1,i-1/2}}} \\ \overline{\frac{q_{4,i-1/2}}{q_{2,i-1/2}}} \end{bmatrix}, \tag{3.68}$$

and $\mathbf{v}_h$ follows by assembling this expression for all grid points (ordered by equation, like $\mathbf{q}_h$). The pressure condition (3.67) then evaluates to

$$\langle \mathbf{v}_h, \mathbf{j}_h \rangle = \sum_{i=1}^{N} Q_{i-1/2} \left(p_i - p_{i-1} \right) = \sum_{i=1}^{N} \left(Q_{i+1/2} - Q_{i-1/2} \right) p_i = 0,$$

and is thus satisfied because Q is uniform in space.

The flux condition (3.66) evaluates to

$$\begin{aligned}\langle \mathbf{v}_h, \mathbf{f}_h \rangle = \sum_{i=1}^{N} &\left(-\frac{1}{2} \overline{\left(\frac{q_{3,i}^2}{\overline{q}_{1,i}^2} \right)} + g_n \left(H - H_{U,i} \right) \right) \left(f_{1,i+1/2} - f_{1,i-1/2} \right) \\ &+ \left(-\frac{1}{2} \overline{\left(\frac{q_{4,i}^2}{\overline{q}_{2,i}^2} \right)} + g_n H_{L,i} \right) \left(f_{2,i+1/2} - f_{2,i-1/2} \right) + \left(\frac{q_{3,i-1/2}}{\overline{q}_{1,i-1/2}} \right) \left(f_{3,i} - f_{3,i-1} \right) + \left(\frac{q_{4,i-1/2}}{\overline{q}_{2,i-1/2}} \right) \left(f_{4,i} - f_{4,i-1} \right).\end{aligned}$$

We split this condition into two conditions: one proportional to g_n and one not proportional to g_n:

$$\langle \mathbf{v}_h, \mathbf{f}_h \rangle = \langle \mathbf{v}_h, \mathbf{f}_h \rangle_a + \langle \mathbf{v}_h, \mathbf{f}_h \rangle_g.$$

The advective condition is given by

$$\begin{aligned}\langle \mathbf{v}_h, \mathbf{f}_h \rangle_a = \sum_{i=1}^{N} \Bigg[&-\frac{1}{2} \overline{\left(\frac{q_{3,i}^2}{\overline{q}_{1,i}^2} \right)} \left(f_{1,i+1/2} - f_{1,i-1/2} \right) - \frac{1}{2} \overline{\left(\frac{q_{4,i}^2}{\overline{q}_{2,i}^2} \right)} \left(f_{2,i+1/2} - f_{2,i-1/2} \right) \\ &+ \left(\frac{q_{3,i-1/2}}{\overline{q}_{1,i-1/2}} \right) \left(f_{3,i,a} - f_{3,i-1,a} \right) + \left(\frac{q_{4,i-1/2}}{\overline{q}_{2,i-1/2}} \right) \left(f_{4,i,a} - f_{4,i-1,a} \right) \Bigg].\end{aligned}$$

Substituting (3.53) yields an equation that can be rewritten as

$$\begin{aligned}\langle \mathbf{v}_h, \mathbf{f}_h \rangle_a = \sum_{i=1}^{N} \Bigg[&\frac{1}{2} \left(\frac{q_{3,i-1/2}^2}{\overline{q}_{1,i-1/2}^2} \frac{q_{3,i-1/2}}{\Delta s} - \frac{q_{3,i+1/2}^2}{\overline{q}_{1,i+1/2}^2} \frac{q_{3,i+1/2}}{\Delta s} \right) + \frac{1}{2} \left(\frac{q_{4,i-1/2}^2}{\overline{q}_{2,i-1/2}^2} \frac{q_{4,i-1/2}}{\Delta s} - \frac{q_{4,i+1/2}^2}{\overline{q}_{2,i+1/2}^2} \frac{q_{4,i+1/2}}{\Delta s} \right) \\ &+ \left(\frac{q_{3,i+1/2}}{\overline{q}_{1,i+1/2}} - \frac{q_{3,i-1/2}}{\overline{q}_{1,i-1/2}} \right) \overline{\left(\frac{q_{3,i}}{\overline{q}_{1,i}} \right)} \frac{\overline{q}_{3,i}}{\Delta s} + \left(\frac{q_{3,i-1/2}}{\overline{q}_{1,i-1/2}} \right) \left(f_{3,i,a} - f_{3,i-1,a} \right) \\ &+ \left(\frac{q_{4,i+1/2}}{\overline{q}_{2,i+1/2}} - \frac{q_{4,i-1/2}}{\overline{q}_{2,i-1/2}} \right) \overline{\left(\frac{q_{4,i}}{\overline{q}_{2,i}} \right)} \frac{\overline{q}_{4,i}}{\Delta s} + \left(\frac{q_{4,i-1/2}}{\overline{q}_{2,i-1/2}} \right) \left(f_{4,i,a} - f_{4,i-1,a} \right) \Bigg].\end{aligned}$$

Here, the sum over the entries on the first lines evaluates to zero, since each term has a matching term of opposite sign and index shifted by 1 (even the boundary terms, in case of periodic boundaries). In order for this to also hold for the terms in the second and third lines, we need to satisfy the condition

$$\left(\frac{q_{3,i+1/2}}{\overline{q}_{1,i+1/2}} - \frac{q_{3,i-1/2}}{\overline{q}_{1,i-1/2}} \right) \overline{\left(\frac{q_{3,i}}{\overline{q}_{1,i}} \right)} \frac{\overline{q}_{3,i}}{\Delta s} + \left(\frac{q_{3,i-1/2}}{\overline{q}_{1,i-1/2}} \right) f_{3,i,a} = \left(\frac{q_{3,i+1/2}}{\overline{q}_{1,i+1/2}} \right) f_{3,i,a},$$

and similar for $f_{4,i,a}$. These are indeed satisfied with our choice (3.54).

The condition proportional to g_n, after substitution of (3.53), is given by

$$\langle \mathbf{v}_h, \mathbf{f}_h \rangle_g = \sum_{i=1}^{N} \Bigg[g_n \left(H - H_{U,i}\right) \left(\frac{q_{3,i+1/2}}{\Delta s} - \frac{q_{3,i-1/2}}{\Delta s} \right) + g_n H_{L,i} \left(\frac{q_{4,i+1/2}}{\Delta s} - \frac{q_{4,i-1/2}}{\Delta s} \right) + g_n \left(\frac{q_{3,i-1/2}}{\overline{q}_{1,i-1/2}} \right) \left(f_{3,i,g} - f_{3,i-1,g} \right) + g_n \left(\frac{q_{4,i-1/2}}{\overline{q}_{2,i-1/2}} \right) \left(f_{4,i,g} - f_{4,i-1,g} \right) \Bigg],$$

and it can be rewritten as

$$\langle \mathbf{v}_h, \mathbf{f}_h \rangle_g = \sum_{i=1}^{N} \Bigg[g_n \frac{\Delta s \left(f_{3,i,g} - f_{3,i-1,g} \right) - \left(H - H_{U,i}\right) \overline{q}_{1,i-1/2}}{\overline{q}_{1,i-1/2}} \frac{q_{3,i-1/2}}{\Delta s} + g_n \left(H - H_{U,i}\right) \frac{q_{3,i+1/2}}{\Delta s} + g_n \frac{\Delta s \left(f_{4,i,g} - f_{4,i-1,g} \right) - H_{L,i} \overline{q}_{2,i-1/2}}{\overline{q}_{2,i-1/2}} \frac{q_{4,i-1/2}}{\Delta s} + g_n H_{L,i} \frac{q_{4,i+1/2}}{\Delta s} \Bigg].$$

Now, in order for this to be conservative, we need the first term in each line to be equal but opposite in sign to the second term in each line (shifted in index by 1). This yields the following conditions:

$$[\![f_{3,i-1/2,g}]\!] = -\frac{\overline{q}_{1,i-1/2}}{\Delta s} [\![H_{U,i-1/2}]\!], \qquad [\![f_{4,i-1/2,g}]\!] = \frac{\overline{q}_{2,i-1/2}}{\Delta s} [\![H_{L,i-1/2}]\!], \tag{3.69}$$

which upon substitution of (3.60) reduce to the geometric conditions (3.56).

In conclusion, the results of the global discrete analysis are consistent with our local discrete analysis. The additional insight from the global analysis is that the geometric conditions (3.69) or (3.56) are *independent of the choice of the entropy potential.* Rather, they follow directly from our assumed form (3.60) of the numerical fluxes (which can be seen as a simplification of the full form (3.55), which was obtained using the entropy potential). This confirms that the choice of entropy potential does not limit the results.

Remark 4. The global energy analysis can also be performed without requiring interpolation of the potential energy to the velocity grid points, as needed in the definition of $e_{i-1/2}$ given by (3.40). Instead, one can directly define

$$E_h = \sum_{i=1}^{N_p} \left(\rho_U g_n \widetilde{H}_{U,i} \Delta s + \rho_L g_n \widetilde{H}_{L,i} \Delta s \right) + \sum_{i=1}^{N_u} \left(\frac{1}{2} \frac{q_{3,i-1/2}^2}{\overline{q}_{1,i-1/2}} + \frac{1}{2} \frac{q_{4,i-1/2}^2}{\overline{q}_{2,i-1/2}} \right).$$

It can be verified that this leads to the same $\mathbf{v}_h$ as given by (3.68), and consequently the geometric condition (3.69) remains present.

4

Energy-consistent formulation of the pressure-free two-fluid model

The pressure-free two-fluid model (PFTFM) is a recent reformulation of the one-dimensional two-fluid model (TFM) for stratified incompressible flow in ducts (including pipes and channels), in which the pressure is eliminated through intricate use of the volume constraint. The disadvantage of the PFTFM was that the volumetric flow rate had to be specified as an input, even though it is an unknown quantity in case of periodic boundary conditions.

In this chapter, we derive an expression for the volumetric flow rate that is based on the demand for energy (and momentum) conservation. This leads to PFTFM solutions that match those of the TFM, justifying the validity and necessity of the derived choice of volumetric flow rate. Furthermore, we extend an energy-conserving spatial discretization of the TFM, in the form of a finite volume scheme, to the PFTFM. We propose a discretization of the volumetric flow rate that yields discrete momentum and energy conservation. The discretization is extended with an energy-conserving discretization of the source terms related to gravity acting in the streamwise direction.

Our numerical experiments confirm that the discrete energy is conserved for different problem settings, including sloshing in an inclined closed tank, and a traveling wave in a periodic domain. The PFTFM solutions and the volumetric flow rates match the TFM solutions, with reduced computation time, and with exact momentum and energy conservation.

This chapter is based on the article "Energy-consistent formulation of the pressure-free two-fluid model", published in *International Journal for Numerical Methods in Fluids*, 95(5):869–898, 2023 [21].

4.1 Introduction

The one-dimensional two-fluid model (TFM) is a cross-sectionally averaged model for two-phase flow in ducts [127]. The term 'duct' is used generally to describe a closed conduit with arbitrary cross-sectional shape, including for example cylindrical pipes and 2D channels. The TFM's one-dimensional nature makes it useful for applications where the interest is in cross-sectionally averaged quantities for very long ducts, for which the computational cost needs to be minimized. Important applications include oil and gas or CO_2 transport through pipelines [4, 48] and nuclear reactor safety analysis [8].

We consider the incompressible form of the TFM, for (separated) stratified flow, assuming a hydrostatic balance between the fluids [5]. One reason this model is of interest, is its potential to dynamically simulate the transition from stratified flow to slug flow [60, 67]. This stands in contrast to for example the drift-flux model, where the two velocities are not modelled separately: instead a closure relation is introduced for their difference [39, 83]. The transition to slug flow can occur through hydrodynamic instabilities that arise naturally in the TFM [6, 74, 76]. However, the physical instability of the model is connected to a loss of hyperbolicity, an issue for which different interpretations and circumvention strategies have been proposed [34, 35, 81, 97, 111].

This issue is shared with the two-layer shallow water equations (TLSWE), as described for example by Chiapolino and Saurel [27]. Both models include one mass equation and one momentum equation for each fluid (totalling four conservation equations). Whereas the TLSWE describe open channel flow, the TFM describes flow in a duct that is closed at the top. This introduces a constraint to the model, named the volume constraint, describing the demand that the two fluids must together fill the duct. While in the TLSWE the pressure is completely determined by the ambient pressure and the hydrostatic pressure, in the closed duct of the TFM the pressure can vary independently as a fifth variable, and a Poisson equation for it follows from the volume constraint and the derived volumetric flow constraint, which describes the incompressible nature of the flow. Furthermore, the TFM describes flow in ducts with arbitrarily shaped cross-sections.

The constraints and the non-dynamic pressure variable complicate the numerical solution of the TFM, and its (nonlinear) stability analysis. The four equations of the TFM can be combined into two to form the fixed flux model (FFM), by taking the sum of the mass equations, and the difference of the momentum equations, which eliminates the pressure [56, 76, 78, 92]. In the process, smoothness of the solution is assumed, and as a result the model has incorrect jump conditions for shocks [2]. In addition, the volumetric flow rate is often assumed to be constant in time, which excludes unsteady inflow boundary conditions, and which is incorrect in case of periodic boundary conditions. Similar two-equation models have been given by Keyfitz et al. [66] and Etrati et al. [36], and a comparable approach has been taken for a two-layer shallow water model with rigid-lid assumption [86], which describes flow in a closed channel. A different two-equation two-fluid model was derived by Jones and Prosperetti [64], in which the volumetric flow constraint is used to eliminate both the pressure and the mass equations. Like the FFM, this model assumes smoothness of the solution, and the volumetric flow rate needs to be prescribed.

In a recent article by Sanderse et al. [105], it was shown how a four-equation pressure-free two-fluid model (PFTFM) can be derived, by eliminating the pressure using the volume constraint, but otherwise leaving the model in its original conservative form. This model

requires no constraints, exhibits the correct shock relations, and allows a time-dependent volumetric flow rate.

An open issue with the PFTFM was that the volumetric flow rate needed to be prescribed, although for periodic boundary conditions it is a priori not known what value to take: it is a free parameter. Without an appropriate prescription for this free parameter, the solutions of the TFM and the PFTFM, when starting from identical initial conditions, will diverge in time [105], which means that the PFTFM solution will be incorrect. In this work, the demand for energy conservation is used to find an appropriate expression for the rate of change of the volumetric flow rate. Since it is known that the TFM solution conserves energy (see chapter 3), replicating this property in the PFTFM naturally yields a PFTFM solution consistent with that of the TFM.

Due to the manner in which the PFTFM is derived from the TFM, it is natural to apply mass- and momentum conserving discretizations of the TFM to the PFTFM (unlike for two-equation models which are not formulated as mass and momentum conservation equations per fluid). In the present chapter, we will show that, starting from our previously presented staggered grid energy-conserving discretization of the TFM (see chapter 3), an energy-conserving semi-discrete form of the PFTFM can be derived. This includes an expression for the rate of change of volumetric flow rate, as a function of the current solution throughout the domain. This discretization can be compared to energy-conserving discretizations of the shallow water equations, on a staggered grid [122], or on a collocated grid [41, 43]. These discretizations improve the stability of numerical solutions.

We extend the discretization with a streamwise potential energy conserving discretization of the streamwise gravity source terms, to make the discretization more complete and extend its applicability to more general cases. The discretization of these terms is similar to an existing staggered-grid energy-conserving discretization of terms in the SWE that describe the influence of a non-flat bottom topography [122]. However, in the SWE, the bottom topography is added to a level domain, while in the TFM the spatial coordinate follows the inclination of the duct.

This chapter is set up as follows. Section 2 introduces the TFM and the PFTFM, and shows how the latter is derived from the former. It points out the step in the derivation where, if the PFTFM's free parameter is not set correctly, the models could diverge. In section 3, we analyse the energy behavior of the continuous PFTFM, as a means to find an expression for the free parameter, which removes the discrepancy between the TFM and the PFTFM. Additionally, it is demonstrated that the streamwise gravity terms can be included in an energy-conserving framework. Section 4 is the semi-discrete counterpart of section 2, and derives the semi-discrete PFTFM from the semi-discrete energy-conserving TFM, before discussing both models' incorporation of the flow constraints. Section 5 uses semi-discrete energy conservation as a guide to find a semi-discrete expression for the free parameter, and introduces the energy-conserving discretization of the streamwise gravity terms. Finally, in section 6, we present the results of numerical experiments, which show that with our proposed expression for the free parameter, and with our proposed discretization, the PFTFM solution matches that of the TFM perfectly.

4.2 Formulation of the two-phase flow models

4.2.1 Introduction to the two-fluid model

The one-dimensional incompressible two-fluid model for stratified flow in channels and pipes can be derived by setting up integral mass and momentum balances for two control volumes: one spanning a section of the duct occupied by the upper fluid, and the other spanning a section of the duct occupied by the lower fluid (see Figure 4.1). Taking the limit in which the length of the control volumes goes to zero yields a set of equations for upper and lower fluid cross-sections A_U and A_L, and the cross-sectionally averaged velocities u_U and u_L [59, 111]. These are functions of time t and the axial coordinate s. In this derivation, a few assumptions are made; one of the most important being that variations along the streamwise direction typically occur over distances larger than the duct diameter, resulting in an assumption of hydrostatic balance in the normal direction [56, 87].

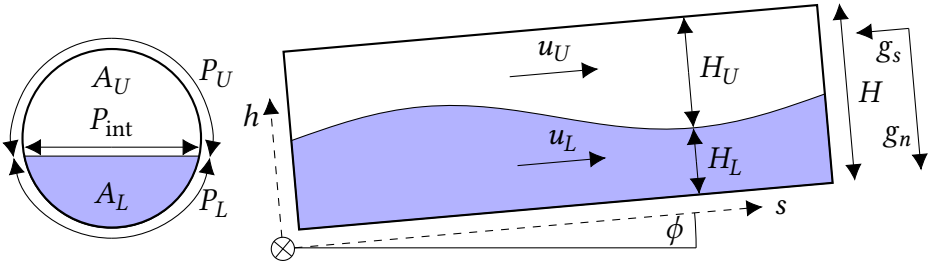

Figure 4.1: A schematic of stratified two-fluid flow in ducts (a circular pipe segment is shown as an example) described by the one-dimensional TFM.

The cross-sectionally averaged equations can be written in terms of the conservative variables $\mathbf{q}(s,t)$ (see chapter 3):

$$\frac{\partial \mathbf{q}}{\partial t} + \frac{\partial \mathbf{f}(\mathbf{q})}{\partial s} + \mathbf{j}(\mathbf{q})\frac{\partial p}{\partial s} = \mathbf{c}(\mathbf{q}), \tag{4.1}$$

with

$$\mathbf{q}^T = \begin{bmatrix} q_1 & q_2 & q_3 & q_4 \end{bmatrix} = \begin{bmatrix} \rho_U A_U & \rho_L A_L & \rho_U u_U A_U & \rho_L u_L A_L \end{bmatrix}. \tag{4.2}$$

The cross-sections are multiplied by the upper and lower fluid densities, ρ_U and ρ_L, in order to obtain a mass per unit length, and the velocities are multiplied by the cross-sections and densities to obtain a momentum per unit length. In (4.1), the fluxes are given by

$$\mathbf{f}(\mathbf{q})^T = \begin{bmatrix} f_1(\mathbf{q}) & f_2(\mathbf{q}) & f_3(\mathbf{q}) & f_4(\mathbf{q}) \end{bmatrix} = \begin{bmatrix} q_3 & q_4 & \frac{q_3^2}{q_1} - \rho_U g_n \widehat{H}_U & \frac{q_4^2}{q_2} - \rho_L g_n \widehat{H}_L \end{bmatrix}.$$

Here $\widehat{H}_U = \widehat{H}_U(\mathbf{q})$ and $\widehat{H}_L = \widehat{H}_L(\mathbf{q})$ are geometric terms which are measures for the potential energy relative to the interface height, defined in Appendix A. The gravitational acceleration in the normal direction is represented by $g_n = g\cos(\phi)$, with ϕ the angle at which the duct is inclined.

The pressure p appearing in the equations is the pressure at the interface. It is preceded by the vector $\mathbf{j}$, which is given by

$$\mathbf{j}(\mathbf{q})^T = \begin{bmatrix} 0 & 0 & \frac{q_1}{\rho_U} & \frac{q_2}{\rho_L} \end{bmatrix}.$$

Neglecting friction and surface tension, the source terms are given by

$$\mathbf{c}(\mathbf{q})^T = \begin{bmatrix} c_1(\mathbf{q}) & c_2(\mathbf{q}) & c_3(\mathbf{q}) & c_4(\mathbf{q}) \end{bmatrix} = \begin{bmatrix} 0 & 0 & -\frac{q_1}{\rho_U}\frac{\partial p_{\text{body}}}{\partial s} - g_s q_1 & -\frac{q_2}{\rho_L}\frac{\partial p_{\text{body}}}{\partial s} - g_s q_2 \end{bmatrix}.$$

Gravity in the streamwise direction is represented by $g_s = g\sin(\phi)$ (see Figure 4.1), and a driving pressure gradient $\partial p_{\text{body}}/\partial s$ may be imposed in case of periodic boundary conditions.

The system of equations (4.1) is subject to the volume constraint

$$\frac{q_1}{\rho_U} + \frac{q_2}{\rho_L} = A, \tag{4.3}$$

which through differentiation to t and substitution of the mass conservation equations can be converted into the volumetric flow constraint:

$$\frac{\partial Q}{\partial s} = 0, \tag{4.4}$$

with

$$Q(\mathbf{q}) \coloneqq \frac{q_3}{\rho_U} + \frac{q_4}{\rho_L} = u_U A_U + u_L A_L. \tag{4.5}$$

Since $Q = Q(\mathbf{q})$ and $\mathbf{q} = \mathbf{q}(s,t)$, Q depends on t through $\mathbf{q}$ (but not on s due to (4.4)). We can use these constraints to set up an equation for the pressure. Typically, this equation is obtained by summing the momentum equations as follows [107]:

$$\mathbf{l}^T\mathbf{j}\frac{\partial p}{\partial s} = -\mathbf{l}^T\left(\frac{\partial \mathbf{q}}{\partial t} + \frac{\partial \mathbf{f}}{\partial s} - \mathbf{c}\right), \quad \text{with} \quad \mathbf{l}^T = \begin{bmatrix} 0 & 0 & \frac{1}{\rho_U} & \frac{1}{\rho_L} \end{bmatrix}, \tag{4.6}$$

and substituting (4.5) and using (4.4) to get

$$\frac{\partial p}{\partial s} = -\frac{1}{\mathbf{l}^T\mathbf{j}}\left(\mathbf{l}^T\frac{\partial \mathbf{f}}{\partial s} + \dot{Q} - \mathbf{l}^T\mathbf{c}\right), \tag{4.7}$$

with

$$\dot{Q} \coloneqq \frac{\mathrm{d}Q}{\mathrm{d}t} = \frac{\partial Q}{\partial t} = \frac{1}{\rho_U}\frac{\partial q_3}{\partial t} + \frac{1}{\rho_L}\frac{\partial q_4}{\partial t}. \tag{4.8}$$

Finally, taking the derivative of (4.6) to s and applying (4.4) gives a Poisson equation for the pressure, which can be used instead of the volume constraint to close the model, acting as the fifth equation of the TFM (in addition to (4.1)):

$$\frac{\partial}{\partial s}\left(\mathbf{l}^T\mathbf{j}\frac{\partial p}{\partial s}\right) = -\frac{\partial}{\partial s}\left(\mathbf{l}^T\frac{\partial \mathbf{f}}{\partial s} - \mathbf{l}^T\mathbf{c}\right). \tag{4.9}$$

4.2.2 Pressure-free two-fluid model

The pressure-free two-fluid model (PFTFM) was introduced by Sanderse et al. [105]. It is a form of the incompressible two-fluid model from which the pressure has been eliminated. To this end, (4.7) is multiplied by $\mathbf{j}$ and rewritten as

$$\mathbf{j}\frac{\partial p}{\partial s} = -\mathbf{B}\left(\frac{\partial \mathbf{f}}{\partial s} - \mathbf{c}\right) - \mathbf{k}\dot{Q}, \tag{4.10}$$

with

$$\mathbf{B}(\mathbf{q}) = \frac{\mathbf{j}\mathbf{l}^T}{\mathbf{l}^T\mathbf{j}} = \frac{1}{\hat{\rho}}\begin{bmatrix} 0 & 0 & 0 & 0 \\ 0 & 0 & 0 & 0 \\ 0 & 0 & \frac{\rho_L}{\rho_U}q_1 & q_1 \\ 0 & 0 & q_2 & \frac{\rho_U}{\rho_L}q_2 \end{bmatrix}, \quad \mathbf{k}(\mathbf{q}) = \frac{\mathbf{j}}{\mathbf{l}^T\mathbf{j}} = \frac{1}{\hat{\rho}}\begin{bmatrix} 0 \\ 0 \\ \rho_L q_1 \\ \rho_U q_2 \end{bmatrix}, \tag{4.11}$$

$$\hat{\rho}(\mathbf{q}) = \frac{\rho_L^2 q_1 + \rho_U^2 q_2}{\rho_U \rho_L} = \rho_U \rho_L \mathbf{l}^T\mathbf{j}.$$

Substitution of (4.10) in (4.1) then yields the pressure-free two-fluid model

$$\frac{\partial \mathbf{q}'}{\partial t} + \mathbf{A}(\mathbf{q}')\frac{\partial \mathbf{f}(\mathbf{q}')}{\partial s} - \mathbf{k}(\mathbf{q}')\dot{K}(t) = \mathbf{A}(\mathbf{q}')\mathbf{c}(\mathbf{q}'), \quad \text{with} \quad \mathbf{A}(\mathbf{q}) = \mathbf{I} - \mathbf{B}(\mathbf{q}). \tag{4.12}$$

Here, the term $\mathbf{k}\dot{Q}$ (appearing in (4.10)) has been replaced by $\mathbf{k}\dot{K}$. This has been done because in this model, $\dot{K} = \dot{K}(t)$ is a free parameter that needs to be set. We cannot use the local definition in terms of $\partial\mathbf{q}'/\partial t$ (given by (4.8)), since substituting this definition would result in a singular system.[1] Instead, the rate of change of the volumetric flow rate needs to be specified explicitly, as a function that is independent of s. This directly enforces the volumetric flow constraint (see section 4.2.4), without need for the pressure and its Poisson equation.

We have given $\mathbf{q}'$ an apostrophe in order to distinguish the solution of the PFTFM from the solution of the TFM, given by $\mathbf{q}$. The transformation from TFM to PFTFM will normally not change the solution (meaning that the original solution $\mathbf{q}(s,t)$ will still satisfy the transformed equations), unless $\dot{K}(t)$ is set such that it differs from the $\dot{Q}(t)$ corresponding to $\mathbf{q}(s,t)$. In this case, with both models starting from the same initial conditions $\mathbf{q}(s,t_0) = \mathbf{q}'(s,t_0)$, the solutions to the TFM and PFTFM will diverge over time so that $\mathbf{q}(s,t) \neq \mathbf{q}'(s,t)$.

The derivation described in this subsection relies on the existence of an s-independent value for the volumetric flow rate, which is guaranteed by (4.4) for this one-dimensional model. In multidimensional incompressible flow, the divergence-free constraint does not determine a unique volumetric flow rate, so this method cannot be applied; see Lteif [79] for a similar conclusion regarding the two-layer shallow water equations with a rigid lid.

4.2.3 Boundary conditions

The boundary conditions are important to consider due to their relevance to the volumetric flow rate. At the boundaries, q_3 and q_4 are set, and the remaining variables follow via characteristic analysis [107]. This holds both for the TFM and the PFTFM.

[1] To see this, note that this model can also be obtained by taking the product of $\mathbf{A}$ and (4.1). $\mathbf{A}$ is a projection matrix satisfying $\mathbf{A}^2 = \mathbf{A}$, and it is singular. The term $\mathbf{A}\partial\mathbf{q}/\partial t$ needs to be split in the following manner: $\mathbf{A}\partial\mathbf{q}/\partial t = \partial\mathbf{q}/\partial t - \mathbf{B}\partial\mathbf{q}/\partial t = \partial\mathbf{q}'/\partial t - \mathbf{k}\dot{K}$.

Consider a domain bounded by s_1 and s_2. For a closed domain, the boundary conditions are given by $q_3(s_1,t)=0$, $q_4(s_1,t)=0$, $q_3(s_2,t)=0$, and $q_4(s_2,t)=0$. This directly determines $Q=Q(\mathbf{q})$ at the boundaries through (4.5), and through (4.4) this determines Q throughout the domain.

For inflow boundary conditions, q_3 and q_4 at s_1 and s_2 may be (known) functions of time. Therefore, Q may be a function of time (through $\mathbf{q}(s,t)$), but it is again fully determined by the boundary conditions. Through (4.4), Q will be determined for the full domain, also at an outflow boundary where q_3 and q_4 depend on the solution in the interior.

In case of periodic boundaries, the boundary conditions are $q_3(s_1,t)=q_3(s_2,t)$ and $q_4(s_1,t)=q_4(s_2,t)$. While this illustrates that Q at s_1 will be equal to Q at s_2, these boundary conditions do not determine the actual value of Q. As a result, Q can vary freely with time. The degree to which it varies depends on the specifics of the initial conditions and the parameter values. For the TFM, Q can be seen as a component of the solution, for which the model equations must be solved.

4.2.4 The problem of setting the volumetric flow rate

For the PFTFM, it is necessary to set the (rate of change of the) volumetric flow rate as an input to the system of equations through the free parameter $\dot{K}=\dot{K}(t)$. This is the cost of eliminating the pressure $p=p(s,t)$ as a variable [105]. By taking the dot product of (4.12) with $\mathbf{l}$ and substituting

$$\frac{q_3'}{\rho_U}+\frac{q_4'}{\rho_L}=Q(\mathbf{q}')=Q',$$

we find that

$$\dot{Q}'=\dot{K}, \tag{4.13}$$

which makes clear that the value we set for K determines the actual volumetric flow rate of the PFTFM solution. This holds throughout the domain, which directly implies that the PFTFM solution satisfies the volumetric flow constraint (4.4), if the initial conditions satisfy the volumetric flow constraint. Similarly, take the dot product of (4.12) with $\begin{bmatrix}1/\rho_U & 1/\rho_L & 0 & 0\end{bmatrix}$ to find

$$\frac{\partial A'}{\partial t}=-\frac{\partial Q'}{\partial s}=0,$$

with A defined as a function of $\mathbf{q}'$ by (4.3). If care is taken that the initial conditions satisfy the constraints, this equation demonstrates that the volume constraint is also naturally satisfied by the PFTFM.

Due to the discussion in section 4.2.3, for closed and inflow boundaries it is clear how to set $\dot{K}$, but for periodic boundaries it is a priori unclear. In related models, the problem of setting the volumetric flow rate for periodic domains is usually avoided by assuming $\dot{Q}'=0$ [56, 76]. The same assumption has been made (at a later stage in the derivation) by Sanderse et al. [105], where in case of periodic boundaries the setting $\dot{K}=0$ has been used. However, this simplification yields differences between PFTFM and TFM solutions: we have $\dot{K}(t)=\dot{Q}'(t)\neq\dot{Q}(t)$ and $\mathbf{q}'(s,t)\neq\mathbf{q}(s,t)$. Considering the TFM to be the ground truth, this renders PFTFM solutions incorrect. In this work we will introduce an expression for $\dot{K}$ based on the demand for momentum and energy conservation, that resolves this discrepancy.

4.3 New improvements based on analysis of the continuous PFTFM

4.3.1 Energy conservation for the continuous model

As stated above, an expression for the free parameter $\dot{K}$ can be determined based on the demand for energy conservation. To this end, we will first give an outline of the steps required to prove that the mechanical energy is a secondary conserved quantity of the PFTFM, based on our proof of energy conservation for the regular two-fluid model, as given in chapter 3. In general, the process involves defining an expression for the mechanical energy, and (based on this expression) manipulating the governing equations of the model to obtain a local energy conservation equation, from which global energy conservation trivially follows.

Given an expression for the mechanical energy $e(\mathbf{q})$, we can define the vector of entropy variables, following Fjordholm et al. [42], as

$$\mathbf{v}(\mathbf{q}) \coloneqq \left[\frac{\partial e}{\partial \mathbf{q}}\right]^T.$$

Taking the dot product of this energy with the governing equations given by (4.12) yields

$$\langle \mathbf{v}, \frac{\partial \mathbf{q}}{\partial t}\rangle + \langle \mathbf{v}, \mathbf{I}\frac{\partial \mathbf{f}}{\partial s}\rangle - \langle \mathbf{v}, \mathbf{B}\frac{\partial \mathbf{f}}{\partial s}\rangle - \langle \mathbf{v}, \mathbf{k}\dot{K}\rangle + \langle \mathbf{v}, \mathbf{B}\mathbf{c}\rangle = \langle \mathbf{v}, \mathbf{c}\rangle, \tag{4.14}$$

where we have omitted the apostrophes, but emphasize that $\mathbf{q}$ refers to the PFTFM solution. The first term of this equation reduces to

$$\langle \mathbf{v}, \frac{\partial \mathbf{q}}{\partial t}\rangle = \left(\frac{\partial e(\mathbf{q})}{\partial \mathbf{q}}\right)\frac{\partial \mathbf{q}}{\partial t} = \frac{\partial e(\mathbf{q})}{\partial t},$$

which makes (4.14) an equation for $\partial e/\partial t$.

Now, if the remaining terms can be written in conservative form, meaning that they can be written as the one-dimensional divergence of some yet to be defined energy fluxes h_f and h_p (it will be determined in the current and the following subsection that this is indeed possible for the proposed model):

$$\langle \mathbf{v}, \frac{\partial \mathbf{f}}{\partial s}\rangle = \frac{\partial h_f}{\partial s}, \tag{4.15}$$

$$-\langle \mathbf{v}, \mathbf{B}\rangle\frac{\partial \mathbf{f}}{\partial s} - \langle \mathbf{v}, \mathbf{k}\rangle\dot{K} + \langle \mathbf{v}, \mathbf{B}\rangle\mathbf{c} = \frac{\partial h_p}{\partial s}, \tag{4.16}$$

then (4.14) reduces to the local energy conservation equation

$$\frac{\partial e}{\partial t} + \frac{\partial}{\partial s}\left(h_f + h_p\right) = \langle \mathbf{v}, \mathbf{c}\rangle, \tag{4.17}$$

showing how the energy $e(s,t)$ at a specific point in space changes due to an inflow or outflow, or due to source terms. Therefore, (4.15) and (4.16) are the conditions which need to be verified in order to prove energy conservation for the PFTFM. In the case of periodic

boundaries the difference between the energy flux at the left boundary and the energy flux at the right boundary must be zero, and in case of closed boundaries the boundary values of the energy fluxes must themselves be zero. Therefore, for both periodic and closed boundaries, integrating (4.17) over the domain yields the global energy conservation equation

$$\frac{\mathrm{d}E}{\mathrm{d}t} = -\left[h_f + h_p\right]_{s_1}^{s_2} + \int_{s_1}^{s_2} \langle \mathbf{v}, \mathbf{c} \rangle \,\mathrm{d}s = \int_{s_1}^{s_2} \langle \mathbf{v}, \mathbf{c} \rangle \,\mathrm{d}s, \quad \text{with} \quad E(t) \coloneqq \int_{s_1}^{s_2} e \,\mathrm{d}s. \tag{4.18}$$

Since the pressure-free two-fluid model is directly derived from the original two-fluid model and describes the same physics, we expect that it conserves the same energy as the original two-fluid model. This energy was presented in chapter 3 and is given by

$$e(\mathbf{q}) = \rho_U g_n \widetilde{H}_U + \rho_L g_n \widetilde{H}_L + \frac{1}{2}\frac{q_3^2}{q_1} + \frac{1}{2}\frac{q_4^2}{q_2}. \tag{4.19}$$

Here $\widetilde{H}_U = \widetilde{H}_U(A_U(q_1, \rho_U))$ and $\widetilde{H}_L = \widetilde{H}_L(A_L(q_2, \rho_L))$ are general geometric terms representing the centers of mass of the upper and lower fluids, respectively (see Appendix A). From this energy, we can calculate the entropy variables as

$$\mathbf{v}(\mathbf{q})^T = \left[-\frac{1}{2}\frac{q_3^2}{q_1^2} + g_n \frac{\mathrm{d}\widetilde{H}_U}{\mathrm{d}A_U} \quad -\frac{1}{2}\frac{q_4^2}{q_2^2} + g_n \frac{\mathrm{d}\widetilde{H}_L}{\mathrm{d}A_L} \quad \frac{q_3}{q_1} \quad \frac{q_4}{q_2} \right].$$

It was already proven in chapter 3 that the flux terms of the TFM are energy-conserving, and the condition (4.15) takes entirely the same form for the PFTFM as for the TFM. Therefore, we state that (4.15) holds with

$$h_f(\mathbf{q}) = g_n q_3 \frac{\mathrm{d}\widetilde{H}_U}{\mathrm{d}A_U} + g_n q_4 \frac{\mathrm{d}\widetilde{H}_L}{\mathrm{d}A_L} + \frac{1}{2}\frac{q_3^3}{q_1^2} + \frac{1}{2}\frac{q_4^3}{q_2^2}. \tag{4.20}$$

This can be proven by simply evaluating the left-hand side (LHS) of (4.15), applying product and chain rules, and substituting geometric relations (A.7)[2]. It is possible to substitute (A.5) in (4.20), but we shall keep the current notation, in which the contributions from both fluids take the same form. Note that each term in (4.20) contains a multiplication with a velocity, so that h_f will be zero at closed boundaries, and there will indeed be no contribution to the global energy balance (4.18) in this case.

4.3.2 Determining the PFTFM free parameter based on energy conservation

The proof of energy conservation for the remaining terms in the PFTFM differs from the proof of energy conservation for the pressure terms of the TFM, since condition (4.16) differs from its TFM equivalent. Therefore, we reintroduce apostrophes to distinguish the PFTFM solution from the TFM solution, which may differ in case $\dot{K}$ is set incorrectly. This difference in solutions also stands in the way of proving energy conservation, but it turns out that these two issues can be resolved by a single approach. This approach is to set $\dot{K}$ based on the demand for global energy conservation.

[2]In this derivation g_n is assumed to be constant along s.

The LHS of (4.16) can be evaluated using $\langle \mathbf{v}(\mathbf{q}'), \mathbf{j}(\mathbf{q}') \rangle = Q'$ and substituting definitions (4.11), which yields

$$-\langle \mathbf{v}(\mathbf{q}'), \mathbf{B}(\mathbf{q}') \rangle \frac{\partial \mathbf{f}(\mathbf{q}')}{\partial s} - \langle \mathbf{v}(\mathbf{q}'), \mathbf{k}(\mathbf{q}') \rangle \dot{K} + \langle \mathbf{v}(\mathbf{q}'), \mathbf{B}(\mathbf{q}') \rangle \mathbf{c}(\mathbf{q}') = -\frac{Q'}{\mathbf{1}^T \mathbf{j}(\mathbf{q}')} \left(\mathbf{1}^T \frac{\partial \mathbf{f}(\mathbf{q}')}{\partial s} + \dot{K} - \mathbf{1}^T \mathbf{c}(\mathbf{q}') \right). \quad (4.21)$$

For closed and inflow boundary conditions, $\dot{Q}'$ is determined by the boundary conditions in the same way for the PFTFM as for the TFM, so we have $\dot{K} = \dot{Q}$ and $\mathbf{q}' = \mathbf{q}$, and resubstituting (4.7) in (4.21) and by extension in the LHS of (4.16) leads to the conclusion that (4.16) holds with

$$h_p = Qp, \quad (4.22)$$

matching the TFM. However, due to arguments given in section 4.2, for periodic boundary conditions generally $\dot{K} \neq \dot{Q}$ and $\mathbf{q}' \neq \mathbf{q}$, and (4.7) cannot be substituted, since it is valid only for solutions of the TFM.

In general, the RHS of (4.21) can be integrated over the domain to yield the contribution to the global energy balance (4.18):

$$\frac{\mathrm{d}E}{\mathrm{d}t} = -\left[h_f\right]_{s_1}^{s_2} + \int_{s_1}^{s_2} \frac{Q'}{\mathbf{1}^T \mathbf{j}(\mathbf{q}')} \left(\mathbf{1}^T \frac{\partial \mathbf{f}(\mathbf{q}')}{\partial s} + \dot{K} - \mathbf{1}^T \mathbf{c}(\mathbf{q}') \right) \mathrm{d}s + \int_{s_1}^{s_2} \langle \mathbf{v}, \mathbf{c} \rangle \, \mathrm{d}s, \quad (4.23)$$

in which the advective and gravitational flux terms are encapsulated in the energy flux h_f (this was discussed above) and are therefore energy-conserving, and the expected contribution of the source terms will be examined in section 4.3.4. Our key insight now is that (for periodic boundary conditions) $\dot{K}$ can be *chosen* to make the pressure terms of the model energy-conserving. To determine the value for $\dot{K}$, we demand that the pressure terms are *globally* energy-conserving, meaning that they should not contribute to the global energy balance:

$$\int_{s_1}^{s_2} -\frac{Q'}{\mathbf{1}^T \mathbf{j}(\mathbf{q}')} \left(\mathbf{1}^T \frac{\partial \mathbf{f}(\mathbf{q}')}{\partial s} + \dot{K} - \mathbf{1}^T \mathbf{c}(\mathbf{q}') \right) \mathrm{d}s = 0. \quad (4.24)$$

Applying (4.4) leads to

$$\dot{K} = -\left(\int_{s_1}^{s_2} \frac{\mathbf{1}^T}{\mathbf{1}^T \mathbf{j}(\mathbf{q}')} \frac{\partial \mathbf{f}(\mathbf{q}')}{\partial s} \mathrm{d}s - \int_{s_1}^{s_2} \frac{\mathbf{1}^T}{\mathbf{1}^T \mathbf{j}(\mathbf{q}')} \mathbf{c}(\mathbf{q}') \mathrm{d}s \right) \Big/ \left(\int_{s_1}^{s_2} \frac{\mathrm{d}s}{\mathbf{1}^T \mathbf{j}(\mathbf{q}')} \right). \quad (4.25)$$

This is the value $\dot{K}$ should be set to in order to achieve global energy conservation, for periodic boundary conditions, when $\dot{Q}$ is unknown. We note that a similar expression was derived by Milewski et al. [86], for a two-layer shallow water model with a rigid lid, but the approximation $\dot{K}(t) = 0$ was made for the analysis and computations. We will use the precise expression (4.25), meaning that $\dot{K}$ is set as a function of the global solution at time t. With this choice, (4.23) reduces to (4.18). Using the proof that with this choice the PFTFM is equivalent to the TFM (see section 4.3.3), (4.24) can be written as $\left[Qp\right]_{s_1}^{s_2} = \left[h_p\right]_{s_1}^{s_2}$.

For the case of periodic boundaries, the new and improved PFTFM consists of (4.12) supplemented by (4.25), making it a combined system of differential and integral equations. For other boundary conditions, the PFTFM consists of (4.12) supplemented by a function $\dot{K} = \dot{K}(t)$, which is determined by the (possibly time-dependent) boundary conditions. These methods of setting $\dot{K}$ lead to a volumetric flow rate matching that of the original TFM solution: $\dot{K}(t) = \dot{Q}(t)$ (see section 4.3.3). It can be proven that with the changes made, and as long as consistent initial conditions are used, TFM solutions satisfy the PFTFM model equations, and vice versa (see section 4.3.3). Therefore, the solutions to the PFTFM must be locally energy-conserving (with $h_p = Qp$) and momentum-conserving (see section 4.A).

4.3.3 Equivalence of PFTFM and TFM solutions

Given a solution $\mathbf{q}'(s,t)$, (4.25) provides a unique value for $\dot{K}(t) = \dot{Q}'(t)$ in order to obtain a progression of the solution in time that is globally energy-conserving. In the derivation of the PFTFM from the TFM given in section 4.2.2, the solution is unchanged, up to the step of setting the rate of change of volumetric flow rate as an explicit parameter $\dot{K}(t)$, instead of leaving it as a part of the solution in the form $\dot{Q}(\partial \mathbf{q}'/\partial t)$ (given by (4.8)). This will change the solution if $\dot{K} \neq \dot{Q}$, but if $\dot{K} = \dot{Q}$, we change nothing in this step, and the transformation from TFM to PFTFM can be freely reversed. Since we have found the unique expression for $\dot{K} = \dot{Q}'$ that will progress the solution in an energy-conserving manner, and we know that the TFM is energy-conserving and $\dot{Q}$ will progress the solution $\mathbf{q}$ in an energy-conserving manner, it follows that, with identical initial conditions $\mathbf{q}'(s,t_0) = \mathbf{q}(s,t_0)$, we have $\dot{K}(t_0) = \dot{Q}(t_0)$, and the progression of the solutions must be identical so that at all further times we have $\mathbf{q}'(s,t) = \mathbf{q}(s,t)$ and $\dot{K}(t) = \dot{Q}(t)$.

The equivalence of solutions to the TFM and PFTFM can be verified by checking that solutions to the TFM satisfy the PFTFM model equations, and vice versa. First consider a solution $\mathbf{q}(s,t)$, $p(s,t)$, $\dot{Q}(\partial \mathbf{q}/\partial t) = \dot{Q}(t)$, which satisfies the TFM model equations (4.1) and the volume constraint (4.3), and its derived constraints. To check if this solution also satisfies the PFTFM model equations, we substitute $\mathbf{q}$ in the PFTFM system (4.12), and check if the following expression evaluates to zero:

$$\begin{aligned}\frac{\partial \mathbf{q}}{\partial t} + \big(\mathbf{I} - \mathbf{B}(\mathbf{q})\big)\frac{\partial \mathbf{f}(\mathbf{q})}{\partial s} - \mathbf{k}(\mathbf{q})\dot{K}(t) - \big(\mathbf{I} - \mathbf{B}(\mathbf{q})\big)\mathbf{c}(\mathbf{q}) \\ = \frac{\partial \mathbf{q}}{\partial t} + \frac{\partial \mathbf{f}(\mathbf{q})}{\partial s} - \mathbf{c}(\mathbf{q}) - \frac{\mathbf{j}(\mathbf{q})}{\mathbf{l}^T\mathbf{j}(\mathbf{q})}\left(\mathbf{l}^T\frac{\partial \mathbf{f}(\mathbf{q})}{\partial s} + \dot{K} - \mathbf{l}^T\mathbf{c}(\mathbf{q})\right)\end{aligned} \tag{4.26}$$

Clearly, if the following substitution can be made:

$$-\frac{\mathbf{j}(\mathbf{q})}{\mathbf{l}^T\mathbf{j}(\mathbf{q})}\left(\mathbf{l}^T\frac{\partial \mathbf{f}(\mathbf{q})}{\partial s} + \dot{K} - \mathbf{l}^T\mathbf{c}(\mathbf{q})\right) = \mathbf{j}(\mathbf{q})\frac{\partial p}{\partial s}, \tag{4.27}$$

then (4.26) reduces to the original TFM equations (which $\mathbf{q}$ and p were defined to satisfy), and therefore it evaluates to zero. For the TFM we know from (4.7) that (4.27) holds if $\dot{K}$ is replaced by $\dot{Q}$. In this case, it is trivial to set $\dot{K}(t) = \dot{Q}(t)$, since we know $\dot{Q}(t)$ as a part of the TFM solution. Therefore, the substitution given by (4.27) can be made, (4.26) reduces to zero, and the TFM solution satisfies the PFTFM model equations.

Now, we consider a solution $\mathbf{q}'(s,t)$, $\dot{Q}(\partial\mathbf{q}'/t) = \dot{Q}'(t) = \dot{K}(t)$ which satisfies the PFTFM model equations, and check if it satisfies the TFM model equations and its constraints. Substituting this solution in the TFM system (4.1) requires an expression for the pressure, so as a trial solution, we calculate the pressure based on (4.7) and the PFTFM solution. The result is:

$$\begin{aligned}\frac{\partial \mathbf{q}'}{\partial t} + \frac{\partial \mathbf{f}(\mathbf{q}')}{\partial s} + \mathbf{j}(\mathbf{q}')\frac{\partial p'}{\partial s} - \mathbf{c}(\mathbf{q}') &= \frac{\partial \mathbf{q}'}{\partial t} + \frac{\partial \mathbf{f}(\mathbf{q}')}{\partial s} - \frac{\mathbf{j}(\mathbf{q}')}{\mathbf{l}^T\mathbf{j}(\mathbf{q}')}\left(\mathbf{l}^T\frac{\partial \mathbf{f}(\mathbf{q}')}{\partial s} + \dot{Q}' - \mathbf{l}^T\mathbf{c}(\mathbf{q}')\right) - \mathbf{c}(\mathbf{q}') \\ &= \frac{\partial \mathbf{q}'}{\partial t} + \left(\mathbf{I} - \mathbf{B}(\mathbf{q}')\right)\frac{\partial \mathbf{f}(\mathbf{q}')}{\partial s} - \mathbf{k}(\mathbf{q}')\dot{K} - \left(\mathbf{I} - \mathbf{B}(\mathbf{q}')\right)\mathbf{c}(\mathbf{q}') \\ &= 0, \end{aligned} \tag{4.28}$$

where we have used (4.13). This demonstrates that, using (4.7) to define the pressure gradient as a function of the solution, the PFTFM solution satisfies the TFM model equations, *for any* $\dot{K}$. However, this does not take into account the boundary conditions. For closed or mass inflow boundaries, $\dot{K}$ should agree with the inflow set at the boundaries. For periodic boundary conditions, p' should be periodic, meaning that

$$p'(s_2) - p'(s_1) = \int_{s_1}^{s_2} \frac{\partial p'}{\partial s}\,\mathrm{d}s = \int_{s_1}^{s_2} -\frac{1}{\mathbf{l}^T\mathbf{j}(\mathbf{q}')}\left(\mathbf{l}^T\frac{\partial \mathbf{f}(\mathbf{q}')}{\partial s} + \dot{K} - \mathbf{l}^T\mathbf{c}(\mathbf{q}')\right)\mathrm{d}s = 0,$$

leading again to the demand that $\dot{K}$ should be set by (4.25). The proof is completed by referring back to section 4.2.4, where it has already been demonstrated that the PFTFM satisfies the volume and volumetric flow constraints, as long as the initial conditions are consistent.

To summarize, if $\dot{K}$ is set by (4.25), and the initial conditions satisfy the constraints, then any solution to the TFM satisfies the PFTFM, and any solution to the PFTFM satisfies the TFM. Therefore, we can conclude that the two models yield equivalent solutions.

4.3.4 Conservative formulation of the streamwise gravity source terms

A second addition to the PFTFM that we propose in this chapter is an energy-conserving discretization of the source terms related to gravity in the streamwise direction. We first need to show that the continuous model conserves streamwise potential energy, before constructing a discretization to mimic this property (the latter will be discussed in section 4.5.3). This addition extends upon the discretization presented in chapter 3 and can be applied just as well to the TFM. The goal of this addition is to make the energy-conserving discretization more complete and extend its applicability to more general cases (i.e. inclined flow).

The source terms can be split into different components, one of which is the streamwise gravity term $\mathbf{c}_g$:

$$\mathbf{c}_g^T = \begin{bmatrix} 0 & 0 & -g\sin(\phi)q_1 & -g\sin(\phi)q_2 \end{bmatrix}.$$

The term $\mathbf{c}_g$ can be incorporated in the energy-conserving formulation by adding a streamwise potential energy term to the energy (based on physical considerations):

$$e_{\text{new}} = e + e_g = e + gy\left(q_1 + q_2\right),$$

with

$$y(s) = y_1 + \int_{s_1}^{s} \sin(\phi(s'))\,\mathrm{d}s', \quad \text{and} \quad \frac{\mathrm{d}y}{\mathrm{d}s} = \sin(\phi(s)).$$

For this energy, the vector of entropy variables becomes

$$\mathbf{v}_{\text{new}} = \mathbf{v} + \mathbf{v}_g, \quad \text{with} \quad \mathbf{v}_g^T = \begin{bmatrix} gy(s) & gy(s) & 0 & 0 \end{bmatrix}.$$

If e_{new} is to be conserved, in the absence of other source terms, a new expression for h_f is required such that the following holds (compare to (4.15))[3]

$$\langle \mathbf{v}_{\text{new}}, \frac{\partial \mathbf{f}}{\partial s} \rangle - \langle \mathbf{v}_{\text{new}}, \mathbf{c}_g \rangle = \frac{\partial h_{\text{new}}}{\partial s}, \tag{4.29}$$

Regarding (4.16), nothing is changed, since only the terms in $\mathbf{v}$ that pertain to q_1 and q_2 are different than before, and (4.16) contains only terms pertaining to q_3 and q_4. If (4.29) is satisfied, then the energy conservation equation becomes

$$\frac{\partial e_{\text{new}}}{\partial t} + \frac{\partial}{\partial s}\left(h_{\text{new}} + h_p\right) = \langle \mathbf{v}_{\text{new}}, \mathbf{c}_{\text{rem}} \rangle, \tag{4.30}$$

in which $\mathbf{c}_{\text{rem}}$ is the remainder of the source terms; it contains all source terms except for $\mathbf{c}_g$. This equation differs from (4.17) through the changed expressions for e and h_f and a part of the source terms being removed from the right-hand side (RHS). It can be integrated over the domain to yield

$$\frac{\mathrm{d}E}{\mathrm{d}t} = -\left[h_{\text{new}} + h_p\right]_{s_1}^{s_2} + \int_{s_1}^{s_2} \langle \mathbf{v}_{\text{new}}, \mathbf{c}_{\text{rem}} \rangle \,\mathrm{d}s. \tag{4.31}$$

The extra terms on the LHS of (4.29), relative to (4.15), are given by

$$gy(s)\left(\frac{\partial q_3}{\partial s} + \frac{\partial q_4}{\partial s}\right) + g\sin(\phi(s))\left(q_3 + q_4\right) = \frac{\partial}{\partial s}\left(gy(s)\left(q_3 + q_4\right)\right).$$

Therefore, (4.29) is satisfied with

$$h_{\text{new}} = h_f + h_g = h_f + gy(s)\left(q_3 + q_4\right), \tag{4.32}$$

and (4.30) holds with e_{new} and h_{new}.

The derived h_{new} is zero at closed boundaries, so that the boundary terms in (4.31) disappear and the global energy remains constant. However, h_{new} is not periodic in the case of periodic boundaries with different $y(s)$ at each boundary. The difference in $y(s)$ between the boundaries makes the domain non-periodic. The change in energy resulting from the difference between $h_{\text{new}}(s_1)$ and $h_{\text{new}}(s_2)$ can potentially be balanced by a driving pressure gradient, which appears as a source term in the global energy conservation equation (4.31).

In conclusion, we have shown that the streamwise potential energy can be added to the energy, so that the amended energy is conserved (with appropriate boundary conditions). In contrast, remaining source terms such as the driving pressure gradient act as source terms in the energy equation.

[3]Note that h_{new} is the new version of h_f (and not for example of $h_f + h_p$). The notation has been changed with respect to the original publication, in order to make it more consistent between the chapters of this thesis.

4.4 Discretization of the two-phase flow models

4.4.1 Semi-discrete form of the two-fluid model

We have shown how the continuous PFTFM, derived from the continuous TFM, can be adapted with an appropriate expression for the volumetric flow rate. This leads to solutions matching the TFM, and energy conservation. We will now use these insights to obtain a semi-discrete PFTFM with the same properties, making use of the energy-conserving discretization of the TFM given in chapter 3.

To this end we must first derive the semi-discrete PFTFM from the semi-discrete TFM, mimicking the derivation of the continuous PFTFM from the continuous TFM in section 4.2. We choose this route rather than directly discretizing the continuous PFTFM, because the chosen route ensures that the energy-conserving discretization of the TFM is applied to the PFTFM consistently (i.e. that the correct discretizations of $\mathbf{B}$ and $\mathbf{k}$ are obtained). Such a consistent application of the TFM energy-conserving discretization to the PFTFM will ensure energy conservation, since this makes the semi-discrete PFTFM a reformulation of the energy-conserving semi-discrete TFM, for which energy conservation has already been demonstrated in chapter 3.

Therefore we first present the semi-discrete form of the TFM, as given in chapter 3. We have a staggered grid with N_p 'pressure volumes' and N_u 'velocity volumes', shown in Figure 4.2. Our semi-discrete vector of unknowns

$$\mathbf{q}_i(t) = \begin{bmatrix} q_{1,i}(t) \\ q_{2,i}(t) \\ q_{3,i-1/2}(t) \\ q_{4,i-1/2}(t) \end{bmatrix} = \begin{bmatrix} (\rho_U A_U \Delta s)_i \\ (\rho_L A_L \Delta s)_i \\ (\rho_U A_U u_U \Delta s)_{i-1/2} \\ (\rho_L A_L u_L \Delta s)_{i-1/2} \end{bmatrix} \tag{4.33}$$

is based on its continuous equivalent (4.2), but includes an extra factor Δs so that the unknowns become quantities of mass or momentum. The quantities of mass are defined at the pressure volumes and the quantities of momentum are defined at the velocity volumes.

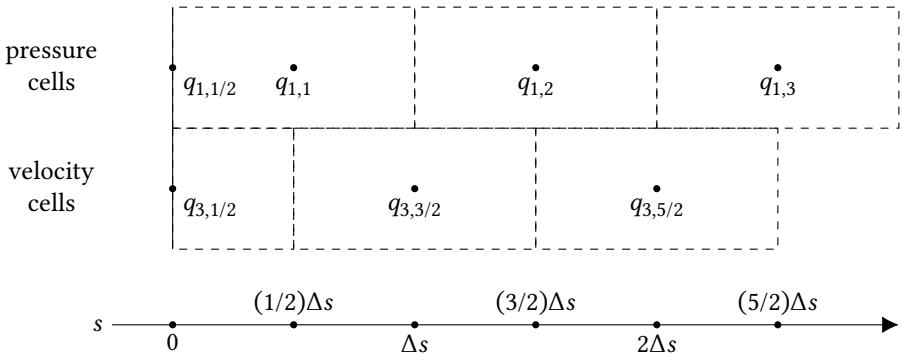

Figure 4.2: Staggered grid layout, with a left boundary.

With a line over the variable indicating interpolation:

$$\overline{a}_{i-1/2} = \frac{1}{2}(a_{i-1} + a_i), \quad \overline{a}_i = \frac{1}{2}\left(a_{i-1/2} + a_{i+1/2}\right),$$

and with brackets indicating a jump:

$$[\![a_{i-1/2}]\!] = a_i - a_{i-1}, \quad [\![a_i]\!] = a_{i+1/2} - a_{i-1/2},$$

the semi-discrete finite volume scheme can be written as

$$\frac{\mathrm{d}\mathbf{q}_i}{\mathrm{d}t} + [\![\mathbf{f}_i]\!] + \mathbf{j}_i [\![p_{i-1/2}]\!] = \mathbf{c}_i \Delta s, \tag{4.34}$$

with

$$\mathbf{f}_{i-1/2}(\mathbf{q}_{i-2}, \mathbf{q}_{i-1}, \mathbf{q}_i) = \begin{bmatrix} \frac{q_{3,i-1/2}}{\Delta s} \\ \frac{q_{4,i-1/2}}{\Delta s} \\ \frac{1}{\Delta s}\overline{\left(\frac{q_{3,i-1}}{\overline{q}_{1,i-1}}\right)}\overline{q}_{3,i-1} - \rho_U g_n \widehat{H}_{U,i-1} \\ \frac{1}{\Delta s}\overline{\left(\frac{q_{4,i-1}}{\overline{q}_{2,i-1}}\right)}\overline{q}_{4,i-1} - \rho_L g_n \widehat{H}_{L,i-1} \end{bmatrix}, \tag{4.35}$$

$$\mathbf{j}_i^T(\mathbf{q}_{i-1}, \mathbf{q}_i) = \frac{1}{\Delta s}\begin{bmatrix} 0 & 0 & \frac{\overline{q}_{1,i-1/2}}{\rho_U} & \frac{\overline{q}_{2,i-1/2}}{\rho_L} \end{bmatrix}, \tag{4.36}$$

$$\mathbf{c}_i^T(\mathbf{q}_{i-1}, \mathbf{q}_i) = \begin{bmatrix} 0 & 0 & -\frac{\overline{q}_{1,i-1/2}}{\rho_U \Delta s}\frac{\partial p_{\text{body}}}{\partial s} - g\frac{[\![y_{i-1/2}]\!]}{\Delta s}\frac{\overline{q}_{1,i-1/2}}{\Delta s} & -\frac{\overline{q}_{2,i-1/2}}{\rho_L \Delta s}\frac{\partial p_{\text{body}}}{\partial s} - g\frac{[\![y_{i-1/2}]\!]}{\Delta s}\frac{\overline{q}_{2,i-1/2}}{\Delta s} \end{bmatrix}. \tag{4.37}$$

The volume constraint

$$\frac{q_{1,i}}{\rho_U \Delta s} + \frac{q_{2,i}}{\rho_L \Delta s} = A \tag{4.38}$$

closes the equations. Through differentiation to t and substitution of the mass conservation equations (with fluxes given by (4.35)), it implies the volumetric flow constraint

$$[\![Q_i]\!] = 0, \tag{4.39}$$

with

$$Q_{i-1/2}(\mathbf{q}_i) \coloneqq \frac{q_{3,i-1/2}}{\rho_U \Delta s} + \frac{q_{4,i-1/2}}{\rho_L \Delta s}. \tag{4.40}$$

Just as in the continuous case, this constraint can be used to formulate an equation for the pressure. The discrete momentum equations can be summed as follows:

$$\frac{1}{\Delta s}\mathbf{l}^T \mathbf{j}_i [\![p_{i-1/2}]\!] = -\frac{1}{\Delta s}\mathbf{l}^T\left(\frac{\mathrm{d}\mathbf{q}_i}{\mathrm{d}t} + [\![\mathbf{f}_i]\!] - \mathbf{c}_i \Delta s\right), \quad \text{with} \quad \mathbf{l}^T = \begin{bmatrix} 0 & 0 & \frac{1}{\rho_U} & \frac{1}{\rho_L} \end{bmatrix}. \tag{4.41}$$

Substituting (4.40) yields an equation for the pressure that compares to (4.7):

$$\frac{[\![p_{i-1/2}]\!]}{\Delta s} = -\frac{1}{\mathbf{l}^T \mathbf{j}_i}\left(\mathbf{l}^T \frac{[\![\mathbf{f}_i]\!]}{\Delta s} + \dot{Q}_{i-1/2} - \mathbf{l}^T \mathbf{c}_i\right). \tag{4.42}$$

Taking the difference of (4.42) with a shifted version of itself and applying (4.39) yields

$$\frac{1}{\Delta s}\left[\mathbf{l}^T \mathbf{j}_{i+1}\frac{[\![p_{i+1/2}]\!]}{\Delta s} - \mathbf{l}^T \mathbf{j}_i \frac{[\![p_{i-1/2}]\!]}{\Delta s}\right] = -\frac{\mathbf{l}^T}{\Delta s}\left(\frac{[\![\mathbf{f}_{i+1}]\!]}{\Delta s} - \frac{[\![\mathbf{f}_i]\!]}{\Delta s}\right) + \mathbf{l}^T \frac{[\![\mathbf{c}_{i+1/2}]\!]}{\Delta s}. \tag{4.43}$$

This is the discrete version of (4.9).

4.4.2 Semi-discrete form of the pressure-free two-fluid model

Having presented an energy-conserving discretization of the TFM and its constraints, we can derive the pressure-free version of it, following the approach of section 4.2.2. Like in section 4.2.2, we multiply (4.42) by $\mathbf{j}_i$ to obtain

$$\mathbf{j}_i \frac{[\![p_{i-1/2}]\!]}{\Delta s} = -\mathbf{B}_i \left(\frac{[\![\mathbf{f}_i]\!]}{\Delta s} - \mathbf{c}_i \right) - \mathbf{k}_i \dot{Q}_{i-1/2}, \tag{4.44}$$

with

$$\mathbf{B}_i(\mathbf{q}_{i-1}, \mathbf{q}_i) = \frac{\mathbf{j}_i \mathbf{l}^T}{\mathbf{l}^T \mathbf{j}_i} = \frac{1}{\hat{\rho}_{i-1/2} \Delta s} \begin{bmatrix} 0 & 0 & 0 & 0 \\ 0 & 0 & 0 & 0 \\ 0 & 0 & \frac{\rho_L}{\rho_U} \overline{q}_{1,i-1/2} & \overline{q}_{1,i-1/2} \\ 0 & 0 & \overline{q}_{2,i-1/2} & \frac{\rho_U}{\rho_L} \overline{q}_{2,i-1/2} \end{bmatrix}, \tag{4.45}$$

$$\mathbf{k}_i(\mathbf{q}_{i-1}, \mathbf{q}_i) = \frac{\mathbf{j}_i}{\mathbf{l}^T \mathbf{j}_i} = \frac{1}{\hat{\rho}_{i-1/2} \Delta s} \begin{bmatrix} 0 \\ 0 \\ \rho_L \overline{q}_{1,i-1/2} \\ \rho_U \overline{q}_{2,i-1/2} \end{bmatrix}, \tag{4.46}$$

$$\hat{\rho}_{i-1/2}(\mathbf{q}_{i-1}, \mathbf{q}_i) = \frac{\rho_L^2 \overline{q}_{1,i-1/2} + \rho_U^2 \overline{q}_{2,i-1/2}}{\rho_U \rho_L \Delta s} = \rho_U \rho_L \mathbf{l}^T \mathbf{j}_i.$$

Substitution of (4.44) in (4.34) then yields the semi-discrete pressure-free two-fluid model

$$\frac{\mathrm{d}\mathbf{q}_i'}{\mathrm{d}t} + \mathbf{A}_i' [\![\mathbf{f}_i']\!] - \mathbf{k}_i' \dot{K} \Delta s = \mathbf{A}_i' \mathbf{c}_i' \Delta s, \quad \text{with} \quad \mathbf{A}_i = \mathbf{I} - \mathbf{B}_i, \tag{4.47}$$

where the apostrophes denote (dependence on) the PFTFM solution as opposed to the TFM solution (e.g. $\mathbf{f}_i' = \mathbf{f}_i(\mathbf{q}_{i-1}', \mathbf{q}_i')$). Here $\dot{K}$ must be set as an input to the model, as discussed in section 4.2.2.

4.4.3 Boundary conditions

For periodic domains, in a sense there are no boundaries. The scheme (4.47) continuously applies to all grid points, where it is understood that the left-most point of the domain and the right-most point of the domain are neighbours. There are an equal number of pressure volumes N_p and velocity volumes N_u.

For closed domains, if there are N_p pressure volumes, there are $N_u = N_p - 1$ full velocity volumes. At each side of the domain, there is an additional boundary point, and there is distance of $\Delta s/2$ between these points and the boundary of the closest velocity volume (see Figure 4.2). At the boundary points, we prescribe the boundary conditions in weak form. If the first interior pressure grid point is given an index of 1 and the last is given an index of N_p, this means that we prescribe $\mathrm{d}q_{3,1/2}/\mathrm{d}t = 0$, $\mathrm{d}q_{4,1/2}/\mathrm{d}t = 0$, $\mathrm{d}q_{3,N_p+1/2}/\mathrm{d}t = 0$, $\mathrm{d}q_{4,N_p+1/2}/\mathrm{d}t = 0$ (the initial conditions should be prescribed such that $q_{3,1/2} = 0$, $q_{4,1/2} = 0$, $q_{3,N_p+1/2} = 0$, $q_{4,N_p+1/2} = 0$ for closed boundaries). The boundary values of $\mathrm{d}q_{1,1/2}/\mathrm{d}t$, $\mathrm{d}q_{2,1/2}/\mathrm{d}t$, $\mathrm{d}q_{1,N_p+1/2}/\mathrm{d}t$, $\mathrm{d}q_{2,N_p+1/2}/\mathrm{d}t$ then follow via an analysis of the characteristics, as explained by Sanderse and Veldman [107].

In case of inflow boundaries, the treatment is generally the same as for closed boundaries, but the time derivatives of the momenta can be set to some predefined function of time instead of zero (and similar for their initial values). The disadvantage of prescribing the boundary conditions in weak form as opposed to strong form is the introduction of a time integration error at the boundaries. However, weak boundary conditions are necessary for consistency with the prescription of the volumetric flow rate in weak form (through the parameter $\dot{K}$) [105].

4.4.4 Discrete aspects of enforcing the constraints

Regarding the connection between the volumetric flow rate and the boundary conditions, the same arguments apply as in the continuous case. Through definition (4.40), the volumetric flow rate is determined by closed or inflow boundary conditions, but not by periodic boundary conditions. Through (4.39) this is extended to the entire domain.

For the TFM, the volume constraint (4.38) and the volumetric flow constraint (4.39) are enforced using a predictor-corrector algorithm involving the solution of the pressure Poisson equation (4.43), as a part of a semi-explicit Runge-Kutta method [107]. When running the TFM (for the purpose of comparing results to the PFTFM), we will solve the (implicit) pressure Poisson equation using a preconditioned conjugate gradient method. Satisfaction of the volume constraint is in turn necessary for total momentum conservation, and satisfaction of the volumetric flow constraint is necessary for energy conservation (see chapter 3). Total mass conservation is a property of the finite volume scheme and does not depend on the pressure Poisson equation.

For the PFTFM, just as in the continuous case, one can take the dot product of (4.47) with $(1/\Delta s)\mathbf{l}$ and substitute (4.40) to find

$$\dot{Q}'_{i-1/2} = \dot{K},$$

and this holds for any index, which shows that the volumetric flow constraint (4.39) is satisfied naturally by the PFTFM, as long as the initial condition satisfies the constraint. Similarly, take the dot product of (4.47) with $(1/\Delta s)\begin{bmatrix}1/\rho_U & 1/\rho_L & 0 & 0\end{bmatrix}$ to find

$$\frac{\mathrm{d}A'_i}{\mathrm{d}t} = -\frac{1}{\Delta s}\left[\!\left[Q'_i\right]\!\right] = 0, \quad \text{with} \quad A'_i = A'_{U,i} + A'_{L,i} = A,$$

implying that the volume constraint is also naturally satisfied by the PFTFM, as long as the initial conditions satisfy the constraints.

This shows how both models incorporate the volumetric flow constraint to determine the volumetric flow rate throughout the domain. The downside of the TFM is that it requires the solution of an extra equation (the pressure Poisson equation (4.43)), which adds to the computation time. Additionally, it introduces a numerical error which reduces the accuracy to which the constraints are satisfied, and as a result reduces the accuracy to which momentum and energy are conserved. In contrast, the time integration of the PFTFM can be performed in a fully explicit manner, and we will use a standard four-stage, fourth-order Runge-Kutta method [23]. The downside of the PFTFM is that the volumetric flow rate must be set explicitly through $\dot{K}$. This issue will be resolved for the discrete model in the following section, analogously to the continuous model.

4.5 Converting new improvements to the semi-discrete setting

4.5.1 Energy conservation for the semi-discrete model

To find an appropriate semi-discrete expression for the volumetric flow rate, we will use the demand for global energy conservation, as we have for the continuous model. Therefore we must study energy conservation for the semi-discrete model. Just as for the continuous model, a local energy conservation equation can be derived from the equations for mass and momentum conservation that constitute the model.

The derivation starts by defining the discrete mechanical energy $e_{i-1/2}$, from which the discrete vectors of entropy variables can be calculated:

$$\mathbf{v}_{i-1/2,i-1} \coloneqq \left[\frac{\partial e_{i-1/2}}{\partial \mathbf{q}_{i-1}}\right]^T, \quad \mathbf{v}_{i-1/2,i} \coloneqq \left[\frac{\partial e_{i-1/2}}{\partial \mathbf{q}_i}\right]^T.$$

Taking the sum of the dot products of $\mathbf{v}_{i-1/2,i-1}$ and $\mathbf{v}_{i-1/2,i}$ with the systems (4.47) for $\mathbf{q}_{i-1}$ and $\mathbf{q}_i$, respectively, yields the local energy conservation equation (with $h_{f,i}$ and $h_{p,i}$ as energy fluxes)

$$\frac{\mathrm{d}e_{i-1/2}}{\mathrm{d}t} + [\![h_{f,i-1/2}]\!] + [\![h_{p,i-1/2}]\!] = \langle \mathbf{v}_{i-1/2,i-1}, \mathbf{c}_{i-1}\Delta s\rangle + \langle \mathbf{v}_{i-1/2,i}, \mathbf{c}_i \Delta s\rangle, \tag{4.48}$$

under the following conditions:

$$\left\langle \mathbf{v}_{i-1/2,i-1}, [\![\mathbf{f}_{i-1}]\!]\right\rangle + \left\langle \mathbf{v}_{i-1/2,i}, [\![\mathbf{f}_i]\!]\right\rangle = \left[\!\left[h_{f,i-1/2}\right]\!\right], \tag{4.49}$$

$$\begin{aligned} &-\langle \mathbf{v}_{i-1/2,i-1}, \mathbf{B}_{i-1}\rangle [\![\mathbf{f}_{i-1}]\!] - \langle \mathbf{v}_{i-1/2,i}, \mathbf{B}_i\rangle [\![\mathbf{f}_i]\!] - \langle \mathbf{v}_{i-1/2,i-1}, \mathbf{k}_{i-1}\rangle \dot{K}\Delta s \\ &\quad - \langle \mathbf{v}_{i-1/2,i}, \mathbf{k}_i\rangle \dot{K}\Delta s + \langle \mathbf{v}_{i-1/2,i-1}, \mathbf{B}_{i-1}\rangle \mathbf{c}_{i-1}\Delta s + \langle \mathbf{v}_{i-1/2,i}, \mathbf{B}_i\rangle \mathbf{c}_i \Delta s = [\![h_{p,i-1/2}]\!]. \end{aligned} \tag{4.50}$$

This means that if the LHS of (4.49) and (4.50) can be written in conservative form, i.e. as the difference between an ingoing and an outgoing flux for the grid point $i-1/2$, then the scheme is energy-conserving. Therefore, (4.49) and (4.50) are the conditions for semi-discrete local energy conservation for the PFTFM, and are the discrete analogues of (4.15) and (4.16).

In case of periodic or closed boundaries, 'integrating' (summing) (4.48) over the domain yields the global energy conservation equation

$$\frac{\mathrm{d}E_h}{\mathrm{d}t} = \sum_{i=1}^{N_u} \left[\langle \mathbf{v}_{i-1/2,i-1}, \mathbf{c}_{i-1}\Delta s\rangle + \langle \mathbf{v}_{i-1/2,i}, \mathbf{c}_i \Delta s\rangle\right], \quad \text{with} \quad E_h(t) \coloneqq \sum_{i=1}^{N_u} e_{i-1/2}(t).$$

We now consider a specific energy, and verify if the conditions for energy conservation are satisfied. Since the semi-discrete pressure-free two-fluid model is directly derived from the semi-discrete two-fluid model, it should conserve the same energy (if the volumetric

flow rate is set correctly). The energy which was shown to be conserved by the TFM in chapter 3 is given by

$$e_{i-1/2} = \rho_U g_n \overline{\widetilde{H}}_{U,i-1/2} \Delta s + \rho_L g_n \overline{\widetilde{H}}_{L,i-1/2} \Delta s + \frac{1}{2} \frac{q_{3,i-1/2}^2}{\overline{q}_{1,i-1/2}} + \frac{1}{2} \frac{q_{4,i-1/2}^2}{\overline{q}_{2,i-1/2}}.$$

From this definition, the entropy variables can be calculated as

$$\mathbf{v}_{i-1/2,i-1} = \begin{bmatrix} -\frac{1}{4} \frac{q_{3,i-1/2}^2}{\overline{q}_{1,i-1/2}^2} + \frac{1}{2} g_n \left(\frac{\mathrm{d}\widetilde{H}_U}{\mathrm{d}A_U} \right)_{i-1} \\ -\frac{1}{4} \frac{q_{4,i-1/2}^2}{\overline{q}_{2,i-1/2}^2} + \frac{1}{2} g_n \left(\frac{\mathrm{d}\widetilde{H}_L}{\mathrm{d}A_L} \right)_{i-1} \\ 0 \\ 0 \end{bmatrix}, \quad \mathbf{v}_{i-1/2,i} = \begin{bmatrix} -\frac{1}{4} \frac{q_{3,i-1/2}^2}{\overline{q}_{1,i-1/2}^2} + \frac{1}{2} g_n \left(\frac{\mathrm{d}\widetilde{H}_U}{\mathrm{d}A_U} \right)_{i} \\ -\frac{1}{4} \frac{q_{4,i-1/2}^2}{\overline{q}_{2,i-1/2}^2} + \frac{1}{2} g_n \left(\frac{\mathrm{d}\widetilde{H}_L}{\mathrm{d}A_L} \right)_{i} \\ \frac{q_{3,i-1/2}}{\overline{q}_{1,i-1/2}} \\ \frac{q_{4,i-1/2}}{\overline{q}_{2,i-1/2}} \end{bmatrix}.$$

Condition (4.49) takes exactly the same form for the PFTFM as for the TFM, and does not involve the pressure or the volumetric flow rate. Since our semi-discrete PFTFM was derived from the energy-conserving semi-discrete TFM that was shown to satisfy this condition (see chapter 3), and consequently uses the same expressions for the numerical flux (given by (4.35)), it is clear that this condition will be satisfied for the PFTFM as well. This can be verified via a direct evaluation of the LHS of (4.49), making use of a discrete product rule and a discrete counterpart of (A.7).[4] This will show that (4.49) holds with

$$\begin{aligned} h_{f,i} = &\overline{\left[g_n \overline{\left(\frac{\mathrm{d}\widetilde{H}_U}{\mathrm{d}A_U} \right)}_i \frac{q_{3,i}}{\Delta s} \right]} + \left(\left[\overline{\left(\frac{q_{3,i}}{\overline{q}_{1,i}} \right)} \right]^2 - \frac{1}{2} \overline{\left(\frac{q_{3,i}^2}{\overline{q}_{1,i}^2} \right)} \right) \frac{\overline{q}_{3,i}}{\Delta s} + \frac{1}{4} \rho_U g_n \left[\left[\frac{q_{3,i}}{\overline{q}_{1,i}} \left[\left[\widehat{H}_{U,i} \right] \right] \right] \right] \\ &+ \overline{\left[g_n \overline{\left(\frac{\mathrm{d}\widetilde{H}_L}{\mathrm{d}A_L} \right)}_i \frac{q_{4,i}}{\Delta s} \right]} + \left(\left[\overline{\left(\frac{q_{4,i}}{\overline{q}_{2,i}} \right)} \right]^2 - \frac{1}{2} \overline{\left(\frac{q_{4,i}^2}{\overline{q}_{2,i}^2} \right)} \right) \frac{\overline{q}_{4,i}}{\Delta s} + \frac{1}{4} \rho_L g_n \left[\left[\frac{q_{4,i}}{\overline{q}_{2,i}} \left[\left[\widehat{H}_{L,i} \right] \right] \right] \right]. \end{aligned}$$

Since the last terms in each line vanish for $\Delta s \longrightarrow 0$, this discrete definition of h_f is consistent with the continuous definition given by (4.20). Condition (4.49) being satisfied proves that the flux terms of the semi-discrete PFTFM are energy-conserving.

4.5.2 Determining the PFTFM free parameter based on energy conservation

We now turn to condition (4.50), which needs to be satisfied for the 'pressure terms' of the semi-discrete PFTFM to be energy-conserving. In contrast to condition (4.49), condition (4.50) is unique to the PFTFM, and it hinges on a correct expression for $\dot{K}$. We again use apostrophes to distinguish the PFTFM solution from the TFM solution, and to distinguish

[4] Unlike their continuous versions, the discrete geometric conditions are only satisfied exactly by geometries with $\mathrm{d}^2 H_L / \mathrm{d}A_L^2 = 0$ (for example the 2D channel geometry). For other geometries, such as the cylindrical pipe geometry, these conditions are satisfied up to a numerical error of order $(\Delta s)^3$ (see chapter 3).

functions of the PFTFM solution from functions of the TFM solution. With $\mathbf{j}_i$ defined by (4.36), we obtain

$$\left\langle \mathbf{v}'_{i-1/2,i-1}, \mathbf{j}'_{i-1} \right\rangle = 0, \quad \left\langle \mathbf{v}'_{i-1/2,i}, \mathbf{j}'_{i} \right\rangle = \left(\frac{q'_{3,i-1/2}}{\rho_U \Delta s} + \frac{q'_{4,i-1/2}}{\rho_L \Delta s} \right) = Q'_{i-1/2}.$$

Therefore, similar to (4.21), the LHS of (4.50) evaluates to

$$-\frac{Q'_{i-1/2}}{\mathbf{1}^T \mathbf{j}'_i} \left(\mathbf{1}^T [\![\mathbf{f}'_i]\!] + \dot{K} \Delta s - \mathbf{1}^T \mathbf{c}'_i \Delta s \right).$$

For boundary conditions for which the volumetric flow is known a priori (closed or inflow boundaries), and $\dot{K}$ is set accordingly so that $\dot{K} = \dot{Q}$, we can resubstitute the discrete pressure equation (4.42) to show that (4.50) holds with $h_{p,i} = Q' p_i$, where we have used (4.39): the volumetric flow rate must be constant with s (and it is for the PFTFM, see section 4.4.4).

Just as for the continuous model, in case of periodic boundary conditions, $\dot{Q}$ is an a priori unknown function of the solution. We again set $\dot{K}$ such that the considered terms conserve energy globally:

$$\sum_{i=1}^{N_u} -\frac{Q'_{i-1/2}}{\mathbf{1}^T \mathbf{j}'_i} \left(\mathbf{1}^T [\![\mathbf{f}'_i]\!] + \dot{K} \Delta s - \mathbf{1}^T \mathbf{c}'_i \Delta s \right) = 0.$$

Using (4.39) again, this leads to

$$\dot{K} = -\left(\sum_{i=1}^{N_u} \frac{\mathbf{1}^T}{\mathbf{1}^T \mathbf{j}'_i} [\![\mathbf{f}'_i]\!] - \sum_{i=1}^{N_u} \frac{\mathbf{1}^T}{\mathbf{1}^T \mathbf{j}'_i} \mathbf{c}'_i \Delta s \right) \Big/ \left(\sum_{i=1}^{N_u} \frac{\Delta s}{\mathbf{1}^T \mathbf{j}'_i} \right). \tag{4.51}$$

At each time step $\dot{K}$ should be set to the current value of the RHS of this expression. A standard explicit Runge-Kutta time integration method can be used, in which case $\dot{K}$ should be calculated similarly at each stage. Setting the time derivative of the volumetric flow rate as described here corresponds to the 'option A' time discretization from Sanderse et al. [105].

The alternative is to set K at each time step ('option B'), requiring a specific and careful adaptation of the Runge-Kutta method. This second option does not fit in our framework of semi-discrete energy conservation, of which the purpose is to ensure that the spatial discretization does not introduce an energy error. Therefore it is concerned only with how the different terms in the model relate to each other instantaneously at any given moment in time. In the semi-discrete model formulation only $\dot{K}$ is present, as opposed to K, and therefore we can only impose conditions on $\dot{K}$.

The novel energy-conserving semi-discrete PFTFM consists of (4.47), with fluxes given by (4.35), and with $\dot{K}$ determined by (4.51) in case of periodic boundary conditions. For other boundary conditions, $\dot{K}$ is determined by the mass inflow set at the boundaries. Standard time integration methods can be applied to the semi-discrete PFTFM; we use a classic four-stage fourth-order Runge-Kutta method [23]. All the relations needed to implement the model are summarized in section 4.C.

With consistent initial conditions, the PFTFM will naturally satisfy the constraints (see section 4.4.4) and conserve momentum exactly with time (see section 4.B). Via the same arguments as given for the continuous model in section 4.3, the solution to the semi-discrete PFTFM will match that of the semi-discrete TFM, with $\dot{K} = \dot{Q}$. Between the fully discrete models, a very small difference remains, due to the details of the constraint-consistent time integration method of the TFM, involving a predictor-corrector algorithm and the solution of the pressure Poisson equation (4.43), instead of a direct evaluation of (4.51).

4.5.3 Conservative discretization of the streamwise gravity source terms

In section 4.3.4 it was shown that for the continuous model, the streamwise potential energy can be included in the local energy conservation equation. Only a carefully chosen discretization will replicate this property in the discrete setting. In this subsection, we shall pose such a discretization and show that it conserves the streamwise potential energy together with the normal potential energy and the kinetic energy.

We propose the following discretization for the streamwise gravity terms:

$$\mathbf{c}_{g,i}^T = \begin{bmatrix} 0 & 0 & -g\frac{[\![y_{i-1/2}]\!]}{\Delta s}\frac{\overline{q}_{1,i-1/2}}{\Delta s} & -g\frac{[\![y_{i-1/2}]\!]}{\Delta s}\frac{\overline{q}_{2,i-1/2}}{\Delta s} \end{bmatrix},$$

implying that the channel inclination has been discretized as

$$\left[\sin(\phi)\right]_{i-1/2} = \frac{[\![y_{i-1/2}]\!]}{\Delta s}.$$

The streamwise potential energy is added to the local energy, which becomes

$$e_{\text{new},i-1/2} = e_{i-1/2} + g\overline{\left(y_{i-1/2}\left(q_{1,i-1/2} + q_{2,i-1/2}\right)\right)}. \tag{4.52}$$

Other discretizations for the source terms and the energy are conceivable, but we will show that this particular set is energy-conserving, in conjunction with the discretization of the core model that was shown to be energy-conserving in the previous subsection.

Our chosen discretization implies that y is defined on the pressure grid, and $\sin(\phi)$ is defined on the velocity grid. This choice is natural since it implies that the streamwise potential energy is defined on the pressure grid and is interpolated as a whole to the velocity grid, which matches the treatment of the normal potential energy terms. This is particularly useful at the boundaries in a non-periodic domain, where velocity half-volumes are present which require this interpolation to proceed differently (see Figure 4.2). The potential energy of these half-volumes is determined only from the nearest interior grid point: $e_{p,1/2} = (1/2)e_{p,1}$ and $e_{p,N_p+1/2} = (1/2)e_{p,N_p}$. Treating the boundaries this way ensures that the act of interpolating the potential energy from the pressure to the velocity grid does not change the global potential energy. The kinetic energy is calculated directly from the boundary values without interpolation (masses and momenta are both available here).

In the proof of energy conservation, condition (4.49) is amended to

$$\begin{aligned}\left\langle \mathbf{v}_{\text{new},i-1/2,i-1}, [\![\mathbf{f}_{i-1}]\!] \right\rangle + \left\langle \mathbf{v}_{\text{new},i-1/2,i}, [\![\mathbf{f}_i]\!] \right\rangle \\ - \left\langle \mathbf{v}_{\text{new},i-1/2,i-1}, \mathbf{c}_{g,i-1}\Delta s \right\rangle - \left\langle \mathbf{v}_{\text{new},i-1/2,i}, \mathbf{c}_{g,i}\Delta s \right\rangle = [\![h_{\text{new},i-1/2}]\!]. \end{aligned} \tag{4.53}$$

The discrete condition on h_p, given by (4.50), remains unchanged. If the conditions are satisfied, the energy conservation equation becomes

$$\frac{\mathrm{d}e_{\mathrm{new},i-1/2}}{\mathrm{d}t} + [\![h_{\mathrm{new},i-1/2}]\!] + [\![h_{p,i-1/2}]\!] = \langle \mathbf{v}_{\mathrm{new},i-1/2,i-1}\,, \mathbf{c}_{\mathrm{rem},i-1}\Delta s\rangle + \langle \mathbf{v}_{\mathrm{new},i-1/2,i}\,, \mathbf{c}_{\mathrm{rem},i}\Delta s\rangle, \tag{4.54}$$

in which $\mathbf{c}_{\mathrm{rem},i}$ contains the remaining source terms. This equation can be integrated over the domain to yield the new global energy conservation equation

$$\frac{\mathrm{d}E_h}{\mathrm{d}t} = \sum_{i=1}^{N_u} \left[\langle \mathbf{v}_{\mathrm{new},i-1/2,i-1}\,, \mathbf{c}_{\mathrm{rem},i-1}\Delta s\rangle + \langle \mathbf{v}_{\mathrm{new},i-1/2,i}\,, \mathbf{c}_{\mathrm{rem},i}\Delta s\rangle\right],$$

in which the streamwise gravity terms have been removed from the right-hand side.

For the energy given by (4.52), the entropy variables are

$$\mathbf{v}_{\mathrm{new},i-1/2,i-1} = \mathbf{v}_{i-1/2,i-1} + \mathbf{v}_{g,i-1/2,i-1} \quad \text{with} \quad \mathbf{v}_{g,i-1/2,i-1}^T = \left[\tfrac{1}{2}gy_{i-1} \quad \tfrac{1}{2}gy_{i-1} \quad 0 \quad 0\right],$$

$$\mathbf{v}_{\mathrm{new},i-1/2,i} = \mathbf{v}_{i-1/2,i} + \mathbf{v}_{g,i-1/2,i} \quad \text{with} \quad \mathbf{v}_{g,i-1/2,i}^T = \left[\tfrac{1}{2}gy_{i} \quad \tfrac{1}{2}gy_{i} \quad 0 \quad 0\right].$$

Evaluating the LHS of (4.53) shows that there are only a few additional terms compared to those that were already shown to be conservative in the previous subsection. It can be shown that these additional terms can be written as

$$\left[\!\!\left[\left(g\overline{y}_{i-1/2}\left(\frac{q_{3,i-1/2}}{\Delta s} + \frac{q_{4,i-1/2}}{\Delta s}\right)\right)\right]\!\!\right] - \left[\!\!\left[\frac{1}{4}\left[\!\!\left[g\,[\![y_{i-1/2}]\!]\left(\frac{q_{3,i-1/2}}{\Delta s} + \frac{q_{4,i-1/2}}{\Delta s}\right)\right]\!\!\right]\right]\!\!\right].$$

Therefore (4.53) is satisfied with

$$h_{\mathrm{new},i} = h_{f,i} + h_{g,i} = h_{f,i} + \overline{\left(g\overline{y}_i\left(\frac{q_{3,i}}{\Delta s} + \frac{q_{4,i}}{\Delta s}\right)\right)} - \frac{1}{4}\left[\!\!\left[g\,[\![y_i]\!]\left(\frac{q_{3,i}}{\Delta s} + \frac{q_{4,i}}{\Delta s}\right)\right]\!\!\right],$$

which remains consistent with the continuous expression (4.32), and completes the amended local energy conservation equation (4.54).

In conclusion, we have shown that with a particular discretization of the source terms related to streamwise gravity, and a particular definition of the discrete streamwise potential energy, it can be shown that this energy is conserved in conjunction with the normal potential energy and the kinetic energy. Therefore, with this particular discretization, the conservation properties of the continuous model (which were discussed in section 4.3) apply to the semi-discrete model.

4.6 Numerical experiments

We conduct numerical experiments in order to confirm the properties of the proposed discretization of the PFTFM. The first test case has periodic boundaries. It will be used to test the new expression for $\dot{K}$ and its implementation in a fully explicit Runge-Kutta method. The test will demonstrate that the TFM and PFTFM solutions are now equivalent up to a small numerical error. Additionally, it will show that with the proposed adaptation, momentum and energy are conserved up to high precision.

The second test case has closed boundaries and an inclined domain, and will be used to test the proposed conservative discretization of the streamwise gravity terms. Both test cases are chosen such that for the continuous model the global energy remains constant, so that the discretization can be tested by verifying that

$$\frac{\mathrm{d}E_h}{\mathrm{d}t} = 0.$$

The spatial discretization should conserve energy exactly, with a residual temporal error that decreases as the time step is reduced. The non-dimensional energy error will be defined as $\left(E_h - E_h^0\right)/E_h^0$, with E_h^0 the energy of the initial condition.

The test cases are limited to the 2D channel geometry, since the discretization is not exactly energy-conserving for the circular pipe geometry (see the footnote in section 4.5.1). The parameters of the cases are chosen such that they avoid discontinuities, which would require the addition of diffusion to the numerical scheme in order to mitigate oscillations.

The TFM with the hydrostatic pressure assumption, as given in section 4.2.1, is only conditionally hyperbolic [6, 87]. This means that, for certain configurations of the flow variables, the eigenvalues can become complex. As a result, a linear stability analysis will show an unbounded growth rate for perturbations of vanishing wavelength, which is unphysical, and can lead to a lack of convergence of numerical solutions [46, 74]. Since the PFTFM has the same eigenvalues as the TFM [105], it retains this property. In the test cases considered here, the region of state space where the model attains complex eigenvalues is avoided by the choice of parameters and initial conditions. This implies that the velocity difference between the lower and upper fluid is kept small (below the inviscid Kelvin-Helmholtz stability criterion).

4.6.1 Traveling wave

This case is a modified version of a case featured in chapter 3. In this case, we initialize a sine-shaped perturbation to two fluids in steady state stratified flow in a (level) periodic domain. The parameters of the case are inspired by the Thorpe experiment [117], and are given in Table 4.1.

Table 4.1: Parameters for the traveling wave test case.

Parameter	Symbol	Value	Units
Lower fluid density	ρ_L	1000	$\mathrm{kg\,m^{-3}}$
Upper fluid density	ρ_U	780	$\mathrm{kg\,m^{-3}}$
Acceleration of gravity	g	9.8	$\mathrm{m\,s^{-2}}$
Channel inclination	ϕ	0	degrees
Domain length	L	1.83	m
Channel height	H	0.03	m

The base state is defined by $\alpha_{L,0} = 0.4$, $u_{L,0} = 1\,\mathrm{m\,s^{-1}}$, $u_{U,0} = 1.187\,\mathrm{m\,s^{-1}}$, and $p_0 = 10^5\,\mathrm{Pa}$, with $\alpha_L = A_L/A$ being the 'hold-up'. This set of parameters would result in a steady state flow when including wall and interface friction.[5] To this state, we add perturbations ac-

[5]Using the Churchill friction model [28] with viscosities of $\mu_U = 1.5 \cdot 10^{-3}\ \mathrm{kg\,m^{-1}\,s^{-1}}$ and $\mu_L = 1 \cdot 10^{-3}\ \mathrm{kg\,m^{-1}\,s^{-1}}$.

cording to:

$$\alpha_L(s) = \alpha_{L,0} + \Delta\widehat{\alpha}_L \cos(ks), \qquad u_U(s) = u_{U,0} + \Delta\hat{u}_U \cos(ks),$$
$$u_L(s) = u_{L,0} + \Delta\hat{u}_L \cos(ks), \qquad p(s) = p_0 + \Delta\hat{p} \cos(ks),$$

with $k = 2\pi/L$. In the absence of source terms, and for real values of[6]

$$\frac{\omega}{k} = \frac{\frac{\rho_L u_L}{\alpha_L} + \frac{\rho_U u_U}{\alpha_U} \pm \sqrt{\left(\frac{\rho_L}{\alpha_L} + \frac{\rho_U}{\alpha_U}\right)\left(\rho_L - \rho_U\right) g_n \frac{A}{P_{\text{int}}} - \frac{\rho_L \rho_U}{\alpha_L \alpha_U}\left(u_U - u_L\right)^2}}{\frac{\rho_L}{\alpha_L} + \frac{\rho_U}{\alpha_U}}, \tag{4.55}$$

these perturbations give rise to exact solutions to the linearized model [74] of the form

$$\alpha_L(s,t) = \alpha_{L,0} + \Delta\widehat{\alpha}_L \cos(ks - \omega t), \qquad u_U(s,t) = u_{U,0} + \Delta\hat{u}_U \cos(ks - \omega t),$$
$$u_L(s,t) = u_{L,0} + \Delta\hat{u}_L \cos(ks - \omega t), \qquad p(s,t) = p_0 + \Delta\hat{p} \cos(ks - \omega t),$$

where the relative magnitudes of the perturbations are given by

$$\Delta\widehat{\alpha}_L = \Delta\widehat{\alpha}_L, \qquad \Delta\hat{u}_U = -\frac{(\omega/k) - u_U}{\alpha_U}\Delta\widehat{\alpha}_L,$$
$$\Delta\hat{u}_L = \frac{(\omega/k) - u_L}{\alpha_L}\Delta\widehat{\alpha}_L, \qquad \Delta\hat{p} = \rho_L\left(\frac{\left[(\omega/k) - u_L\right]^2}{\alpha_L} - g_n\frac{A}{P_{\text{int}}}\right)\Delta\widehat{\alpha}_L$$

We set $\Delta\widehat{\alpha}_L = 0.05$ and calculate the remaining components of the perturbation according to the expressions given above, selecting the value for ω/k corresponding to the plus sign in (4.55). A projection step is performed on this perturbed state, to yield a set of initial conditions that satisfies the constraints. In the linear approximation, these initial conditions lead to a single wave travelling to the right at constant amplitude. In the full nonlinear model, the wave deforms over time, which can be seen by plotting the solution at integer multiples of the wave period Lk/ω (Figure 4.3).

Figure 4.4 shows the difference between the TFM and the PFTFM results for two components of the global solution: the potential energy and the volumetric flow rate. The results show that by setting $\dot{K}$ as described in section 4.5.2, the correct volumetric flow rate is obtained by the PFTFM, which matches that of the TFM (for reference, the initial value of the volumetric flow rate is $Q^0 = 3.3 \cdot 10^{-2}\,\mathrm{m^2\,s^{-1}}$, and the variation in Q over the course of the 30 second simulation is of order $10^{-7}\,\mathrm{m^2\,s^{-1}}$). The agreement in potential energy is also excellent. This resolves the issue reported in Sanderse et al. [105], where the authors observed an unjustified difference in volumetric flow rate between TFM and PFTFM solutions, with an accompanying difference in local solutions. Having repaired the volumetric flow rate, the simulations exhibit near machine precision agreement in local solutions between TFM and PFTFM (not shown). This agreement is independent of time step.

This near-identical solution is obtained at a significant reduction of computational expense: the wall-clock time for the PFTFM is 232 seconds while for the TFM it is 733

[6]For the channel geometry, we substitute $A = H$ and $P_{\text{int}} = 1$.

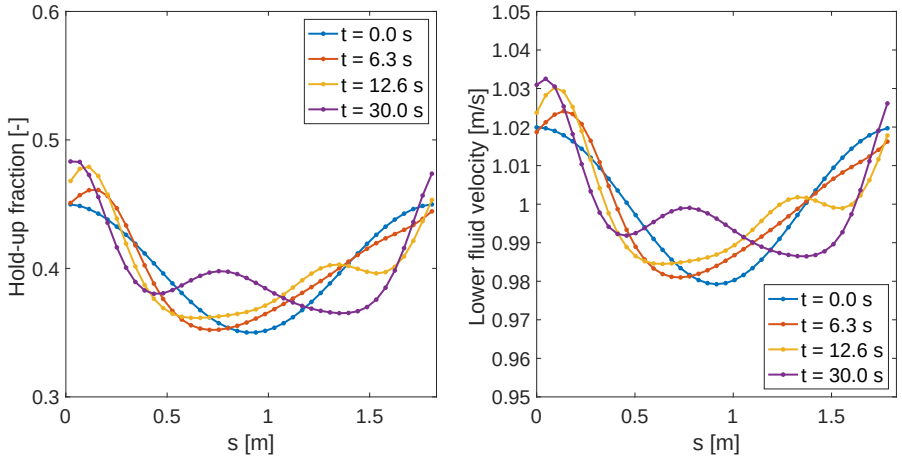

Figure 4.3: Solution to the traveling wave test case at different points in time, with $N_p = 40$ and $\Delta t = 5 \cdot 10^{-4}$ s.

seconds. This is roughly consistent with the results shown in Sanderse et al. [105], where it was already concluded that the PFTFM saves computing time by not having to solve the Poisson equation for the pressure. This conclusion proves to remain valid even though in that work a direct solver was used for the pressure Poisson equation instead of the iterative (conjugate gradient) solver used here.

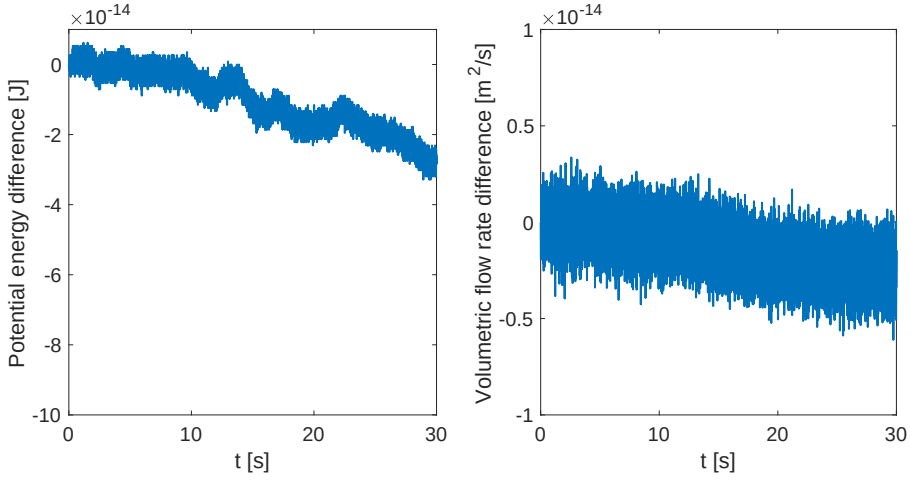

Figure 4.4: Comparison of solutions to the traveling wave test case obtained using the TFM and the PFTFM. Left: potential energy difference $E_{h,p,\text{PFTFM}} - E_{h,p,\text{TFM}}$. Right: volumetric flow rate difference $Q_{\text{PFTFM}} - Q_{\text{TFM}}$.

The energy behavior is shown in Figure 4.5, for a simulation with a resolution of $N_p = 40$ and a time step of $\Delta t = 5 \cdot 10^{-4}$ s. The exact solution of the linearized model has constant kinetic and potential energy since it is an unchanging travelling wave, but the

computed solution shows a somewhat erratic exchange between kinetic energy and a potential solution, at a period of a bit under four times the wave period. This exchange is small relative to the base energy, around the level of the spatial numerical error. Despite this irregular exchange, the total energy is conserved to great precision, confirming the energy-conserving properties of our discretization. If $\dot{K}$ is not set as described in section 4.5.2, but is set incorrectly to $\dot{K} = 0$, this leads to a total energy error that is many orders of magnitude larger than the error shown here.

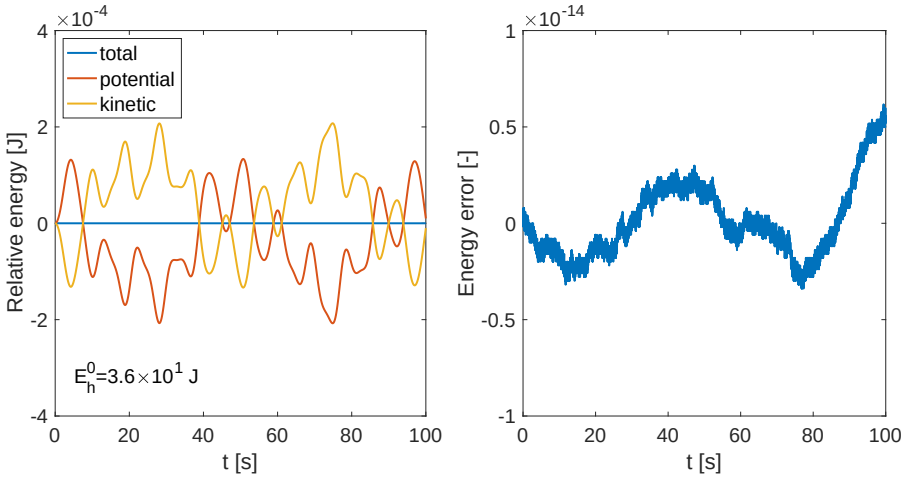

Figure 4.5: Conserved quantities for the traveling wave test case. Left: potential, kinetic and total energy relative to their initial values. Right: $\left(E_h - E_h^0\right)/E_h^0$.

It was discussed in section 4.4.4 that the absence of the Poisson equation for the pressure in the formulation of the discrete PFTFM may lead to improved momentum and energy conservation when compared to the TFM. This is demonstrated in Figure 4.6, where we show the conservation errors made by both models, varying the time step. Both models are solved with a resolution of $N_p = 40$, and for the Poisson equation the TFM uses a preconditioned conjugate gradient solver set to a tolerance at the order of machine precision (10^{-15}), so that it converges to the smallest possible residual (within a maximum of 50 iteration steps). The error in momentum conservation is constant with time step for both models, but is consistently larger for the TFM, and this can be ascribed to an increased volume constraint error. Regarding the energy, both models initially converge to fourth order with time step, but the PFTFM converges further, before also levelling off at a significantly smaller error than the TFM. This indicates that the remaining error in the pressure Poisson solve forms a limiting factor to the accuracy of energy conservation for the TFM.

4.6.2 Sloshing in a closed tank

This is a modified version of a test case presented by Sanderse and Veldman [107]. In this test case, a section of duct is bounded at the left and right ends by closed boundaries, forming a closed tank. Two fluids, with the density of water and air, are initialized at rest with a horizontal boundary between them. At $t = 0$, the tank is set at an incline, causing

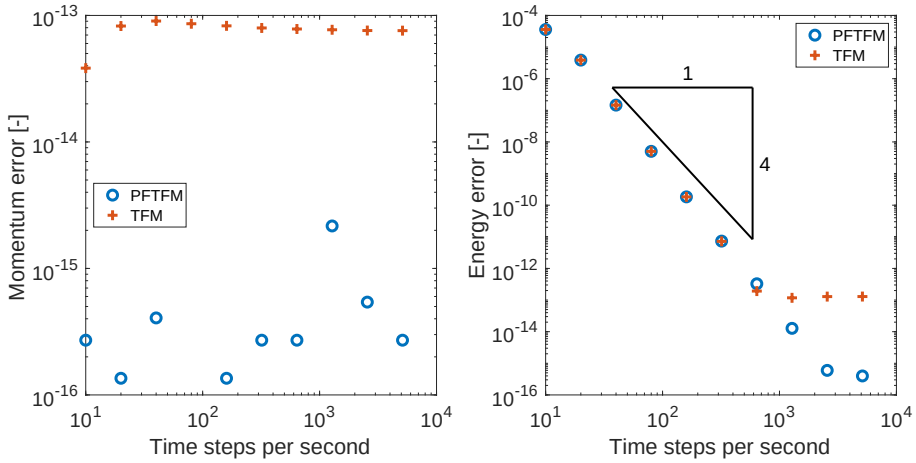

Figure 4.6: Convergence with time step of the error in conserved quantities for the traveling wave test case, run by the PFTFM and TFM. Left: momentum error $\left(M_h - M_h^0\right)/M_h^0$. Right: energy error $\left(E_h - E_h^0\right)/E_h^0$.

the water to start flowing towards the lower end of the tank, pushing the air towards the higher end.

This case tests the performance of our discretization of the source terms associated with the streamwise gravity, which was given in section 4.5.3. Here it was shown that with an appropriate discretization of these terms, and including the streamwise potential energy in the energy definition, the streamwise gravity does not act as a source term in the energy balance. Therefore, we expect to find spatially exact conservation of energy.

The parameters of this case are given in Table 4.2. The experiment differs from the reference case [107] due to the absence of wall and interface friction, the reduction of the inclination from 2 to 1 degrees, and the change of duct geometry from circular pipe to 2D channel. The number of pressure cells taken for the discretization is $N_p = 80$, just as in the reference case [107].

Table 4.2: Parameters for the sloshing test case.

Parameter	Symbol	Value	Units
Lower fluid density	ρ_L	1000	$\mathrm{kg\,m^{-3}}$
Upper fluid density	ρ_U	1.1614	$\mathrm{kg\,m^{-3}}$
Acceleration of gravity	g	9.8	$\mathrm{m\,s^{-2}}$
Channel inclination	ϕ	1	degrees
Domain length	L	1	m
Channel height	H	0.1	m
Initial lower fluid hold-up	$\alpha_{L,0}$	0.5	–

Figure 4.7 shows the different components of the solution in a space-time plot. At the start of the simulation, the results show waves in the hold-up emanating from both sides

of the tank. From the right boundary, an expansion wave travels to the left, reducing the hold-up. From the left boundary, a compression wave travels to the right. The expansion wave is faster than the compression wave, reaching the left boundary around $t = 1.3$, while the compression wave reaches the right boundary at $t = 1.7$. Figure 4.8 shows the solution at the points in time when a wave front meets a boundary. The waves reflect at the boundaries, and when they meet again the compression wave gains amplitude. This repeats itself at future encounters between the two waves, building up towards a shock wave.

The discontinuity which is being formed leads to the onset of numerical oscillations, which can be observed starting around $t = 4\,\mathrm{s}$. The numerical oscillations may be eliminated through the addition of physical (molecular and turbulent) viscosity [46], (grid-independent) artificial diffusion [14, 56], or (grid-dependent) numerical viscosity [42]. This is outside the scope of this chapter, since here we are interested in demonstrating the energy conservation property of the discretization, which would be spoiled by adding viscosity. Our discretization can serve as an energy-conserving basis to which energy-dissipating terms may be added.

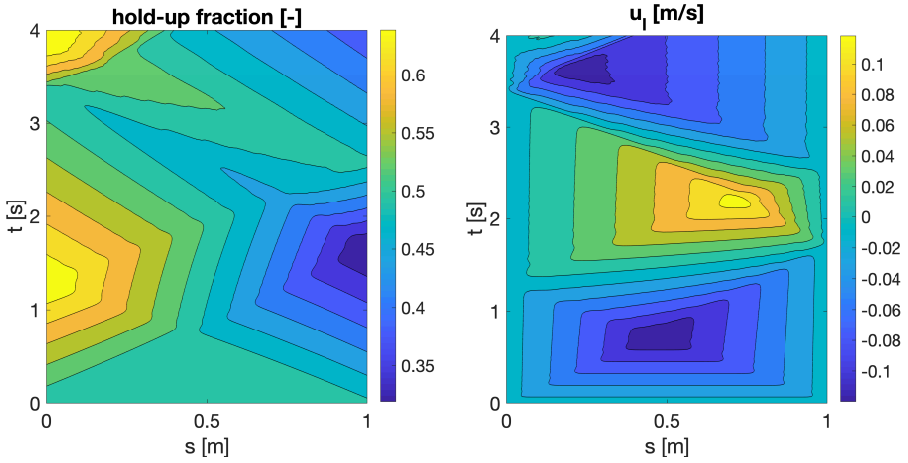

Figure 4.7: Solution to the sloshing test case shown in space and time, with $N_p = 80$ and $\Delta t = 10^{-4}\,\mathrm{s}$.

Figure 4.9 shows that, with a small time step of $\Delta t = 10^{-4}\,\mathrm{s}$, the total energy is conserved up to machine precision while potential and kinetic energy are exchanged. The potential energy includes the normal potential energy and the streamwise potential energy. It is due to the streamwise potential energy present in the initial condition, which is converted into kinetic energy, that motion is initiated. In these simulations there is no damping (except for minute damping due to time integration error), so the fluids will continue sloshing for as long as the simulation is run.

Figure 4.10 shows that the energy error converges to high precision with time step, while remaining roughly constant with grid resolution. The convergence with respect to time is approximately fourth order, corresponding to the order of the Runge-Kutta time integration scheme. This demonstrates that the spatial discretization is exactly energy conserving and that the remaining error is only temporal.

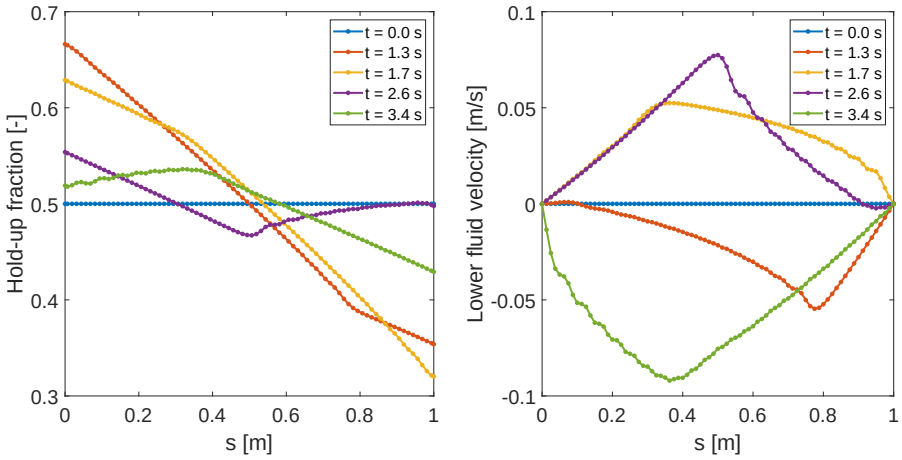

Figure 4.8: Solution to the sloshing test case at different points in time, with $N_p = 80$ and $\Delta t = 10^{-4}$ s.

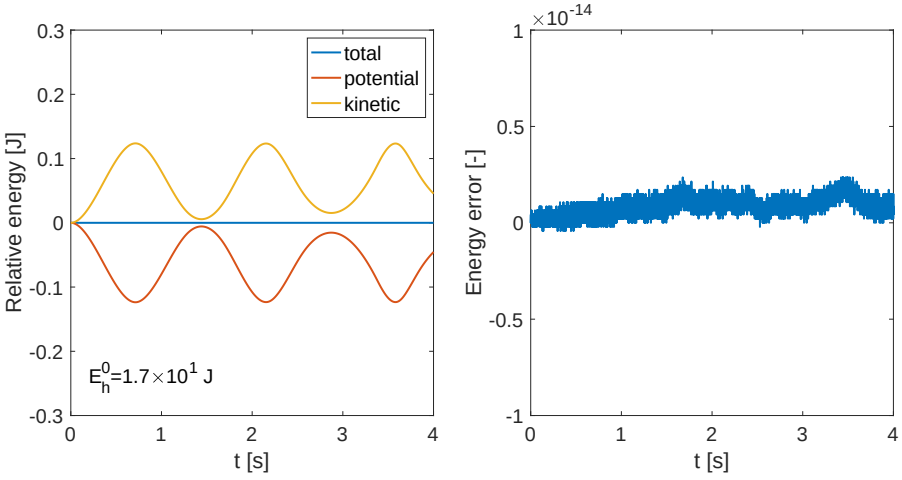

Figure 4.9: Conserved quantities for the sloshing test case. Left: potential, kinetic and total energy relative to their initial values. Right: $\left(E_h - E_h^0\right)/E_h^0$.

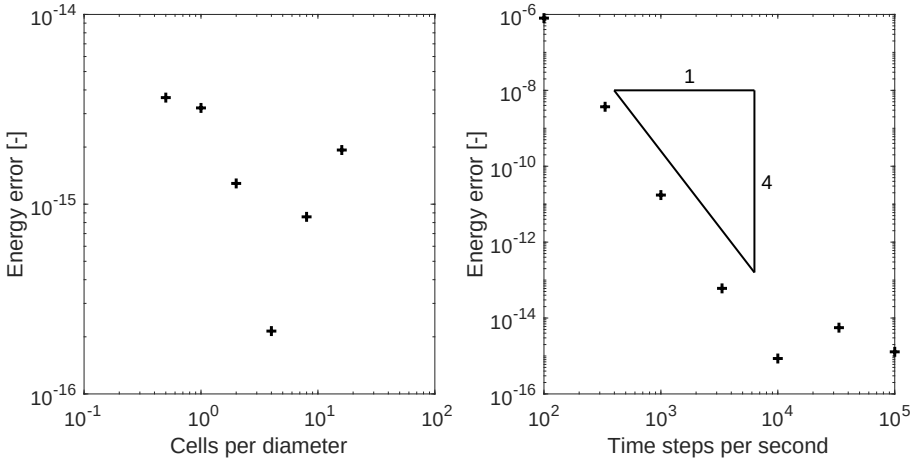

Figure 4.10: Convergence of the energy error $\left(E_h - E_h^0\right)/E_h^0$ for the sloshing test case. Left: constant $\Delta t = 10^{-4}$ s. Right: constant $N_p = 80$.

Finally, we verify that the solution of the PFTFM matches the solution of the TFM. Since the volumetric flow rate is known a priori ($Q = 0$ and $\dot{Q} = 0$), this is achieved without difficulty. This is demonstrated in Figure 4.11 by comparing the potential and kinetic energy obtained by the TFM and the PFTFM. The difference between the two models is near the order of machine precision (and the same holds for the local solutions). Again the PFTFM saves computing time by not having to solve the Poisson equation for the pressure: the wall-clock time for the PFTFM is 208 seconds while for the TFM it is 665 seconds.

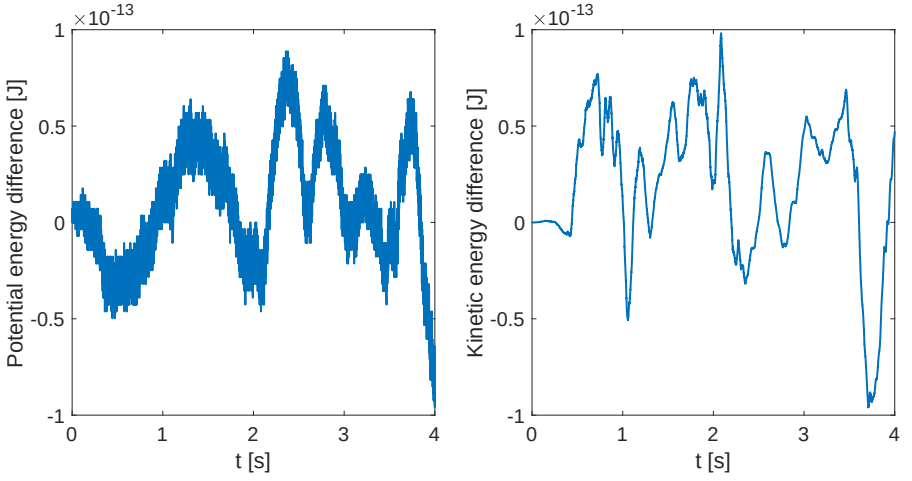

Figure 4.11: Comparison of solutions to the sloshing test case obtained using the TFM and the PFTFM. Left: potential energy difference $E_{h,p,\mathrm{PFTFM}} - E_{h,p,\mathrm{TFM}}$. Right: kinetic energy difference $E_{h,k,\mathrm{PFTFM}} - E_{h,k,\mathrm{TFM}}$.

4.7 Conclusions

In this chapter, we have removed the discrepancy between the pressure-free two-fluid model and the original two-fluid model from which it is derived. For periodic boundaries, this requires setting the rate of change of the volumetric flow rate based on the demand of global energy and momentum conservation. This change resolves the issues of disagreement between PFTFM and TFM solutions and of energy conservation in a combined approach. Our approach may inspire similar improvements to other pressure-eliminated versions of the TFM, such as the FFM. The PFTFM stands out from other pressure-eliminated versions of the TFM in that mass, momentum, and energy conserving discretizations of the TFM can be directly applied, and in the fact that it preserves the correct shock relations.

Additionally, the energy-conserving framework of chapter 3 was extended: the streamwise potential energy and its related source terms were included in the energy-conserving formulation. The amended energy is conserved in inclined domains without friction. We have presented an energy-conserving discretization of these source terms and their associated energy, extending the energy conservation properties of the previously presented discretization.

It was shown how a semi-discrete version of the PFTFM can be derived from the TFM, directly demonstrating how the energy-conserving discretization of the TFM presented in chapter 3 can be applied to the PFTFM. In the framework of this semi-discrete PFTFM, a discrete equivalent of the new expression for the (rate of change of the) volumetric flow rate was derived, based on the demand for discrete global energy conservation. This addition completes the energy-conserving discretization of the PFTFM for the important case of periodic boundary conditions. With the proposed discretization, the discrepancy between PFTFM and TFM solutions, observed in numerical simulations in Sanderse et al. [105], is removed for the discrete model.

The PFTFM modified and discretized as shown in this work conserves mass, momentum, and energy, without needing to account for implicit constraints, making the time integration fully explicit (standard explicit Runge-Kutta methods can be applied). Thus solutions are obtained that are equivalent to solutions of the TFM (down to machine precision), at significantly reduced computational cost. Removing the error attributable to the pressure Poisson solve in the TFM leads to slightly more precise conservation of momentum and energy for the PFTFM. A small temporal error remains present in the energy, which may be resolved in future work by developing an energy-conserving time integration method for the PFTFM.

In their current form, the model and its discretization contain no numerical or physical diffusion. This omission is necessary to achieve exact conservation of energy, but has the effect that discontinuities cannot be correctly resolved. To resolve this, our model could be extended with diffusion terms as found in e.g. Fullmer et al. [46], by including them in the source term vector. These should be a strictly dissipative addition to the energy-conserving discrete model, and should produce the dissipation required at discontinuities, without excessive dissipation where the solution is smooth.

The elimination of constraints and of the non-conservative pressure terms brings the model closer in mathematical form to related models such as the two-layer shallow water equations (TLSWE). Like the TLSWE, the TFM is only conditionally hyperbolic. This can be explained by the fact that both models describe the flow of two discrete fluids with a

sharp interface, under hydrostatic balance. The PFTFM and the modifications we propose in this chapter do not resolve the hyperbolicity issue. However, the PFTFM's energy-conserving formulation, and its increased mathematical similarity to the TLSWE, may facilitate the application of techniques developed for dealing with complex eigenvalues and instability for the TLSWE [16, 25].

Appendix

4.A Momentum conservation and the PFTFM free parameter

We now show that expression (4.25) can also be derived by demanding conservation of total (upper + lower fluid) momentum $m(\mathbf{q}) = q_3 + q_4$. To obtain the evolution equation for total momentum, (4.12) needs to be multiplied with $\mathbf{z} = \begin{bmatrix}0 & 0 & 1 & 1\end{bmatrix}$, instead of $\mathbf{v}$ which is used to obtain the evolution equation for the energy. Performing this multiplication yields

$$\frac{\partial m(\mathbf{q}')}{\partial t} = -\left(\langle \mathbf{z}, \frac{\partial \mathbf{f}(\mathbf{q}')}{\partial s}\rangle - \langle \mathbf{z}, \mathbf{B}(\mathbf{q}')\rangle \frac{\partial \mathbf{f}(\mathbf{q}')}{\partial s} - \langle \mathbf{z}, \mathbf{k}(\mathbf{q}')\rangle \dot{K} + \langle \mathbf{z}, \mathbf{B}(\mathbf{q}')\rangle \mathbf{c}(\mathbf{q}')\right) + \langle \mathbf{z}, \mathbf{c}(\mathbf{q}')\rangle$$

Substituting (4.11), $\langle \mathbf{z}, \mathbf{j}(\mathbf{q}')\rangle = A$ (assumed constant), and integrating over the domain leads to

$$\frac{\mathrm{d}M'}{\mathrm{d}t} = -\int_{s_1}^{s_2} \frac{\partial}{\partial s}\left(f_3(\mathbf{q}') + f_4(\mathbf{q}')\right) \mathrm{d}s + \int_{s_1}^{s_2} \frac{A}{\mathbf{l}^T \mathbf{j}(\mathbf{q}')}\left(\mathbf{l}^T \frac{\partial \mathbf{f}(\mathbf{q}')}{\partial s} + \dot{K} - \mathbf{l}^T \mathbf{c}(\mathbf{q}')\right) \mathrm{d}s + \int_{s_1}^{s_2} \left(c_3(\mathbf{q}') + c_4(\mathbf{q}')\right) \mathrm{d}s, \quad (4.56)$$

$$\text{with} \quad M' = \int_{s_1}^{s_2} m(\mathbf{q}')\, \mathrm{d}s.$$

The first term on the RHS is in conservative form and is therefore zero for periodic boundary conditions. The last term on the RHS is the expected contribution to the momentum due to source terms. The second term gives the contribution from the pressure terms, and is the equivalent of (4.24) for momentum. In case of periodic boundary conditions and in absence of source terms, only this term remains, and it is easy to see that demanding global momentum conservation leads to the previously derived expression (4.25), which is such that $\dot{K} = \dot{Q}$.

However, for closed boundary conditions, the first term on the RHS of (4.56) is nonzero, since, unlike h_f as given by (4.20), f_3 and f_4 are generally nonzero at closed boundaries (due to the gravitational terms). Therefore, unlike energy, momentum should not be conserved in case of closed boundaries, and momentum conservation cannot be used to derive an expression for $\dot{K}$. We have $Q' = 0$ and therefore (4.24) is zero regardless of $\dot{K}$. This means that energy conservation also cannot be used to derive an expression for $\dot{K}$. Instead, $\dot{K}$ is simply determined by the boundary conditions as described in section 4.2.3, which trivially leads to $\dot{K} = \dot{Q}$ (and the same holds for inflow boundaries). Therefore, for all boundary

conditions, (4.7) can be resubstituted and the global momentum balance becomes

$$\frac{\mathrm{d}M}{\mathrm{d}t} = -\left[f_3(\mathbf{q}) + f_4(\mathbf{q})\right]_{s_1}^{s_2} - \left[Ap\right]_{s_1}^{s_2} + \int_{s_1}^{s_2} c_3(\mathbf{q}) + c_4(\mathbf{q})\,\mathrm{d}s,$$

matching that of the TFM.

4.B Momentum conservation for the discrete PFTFM

Just as in the continuous case, it can be shown that our expression (4.51) for $\dot{K}$ (applied in the case of periodic boundary conditions) leads to total momentum conservation (in addition to energy conservation). The semi-discrete equation for the conservation of local momentum $m'_{i-1/2} = m(\mathbf{q}'_i) = q'_{3,i-1/2}(t) + q'_{4,i-1/2}(t)$ can be derived by taking the inner product of $\mathbf{z} = \begin{bmatrix}0 & 0 & 1 & 1\end{bmatrix}$ and (4.47):

$$\frac{\mathrm{d}m'_{i-1/2}}{\mathrm{d}t} = -\left(\langle \mathbf{z},\, [\![\mathbf{f}'_i]\!]\rangle - \langle \mathbf{z}, \mathbf{B}'_i\rangle\, [\![\mathbf{f}'_i]\!] - \langle \mathbf{z}, \mathbf{k}'_i\rangle \dot{K}\Delta s + \langle \mathbf{z}, \mathbf{B}'_i\rangle \mathbf{c}'_i \Delta s\right) + \langle \mathbf{z}, \mathbf{c}'_i \Delta s\rangle,$$

and the global momentum equation is derived by summing over the domain:

$$\frac{\mathrm{d}M'_h}{\mathrm{d}t} = -\sum_{i=1}^{N_u} [\![f'_{3,i-1/2} + f'_{4,i-1/2}]\!] + \sum_{i=1}^{N_u} \frac{A}{\mathbf{l}^T\mathbf{j}'_i}\left(\mathbf{l}^T [\![\mathbf{f}'_i]\!] + \dot{K}\Delta s - \mathbf{l}^T\mathbf{c}'_i\Delta s\right) + \sum_{i=1}^{N_u}\left(c'_{3,i-1/2}\Delta s + c'_{4,i-1/2}\Delta s\right),$$

$$\text{with} \quad M_h(t) \coloneqq \sum_{i=1}^{N_u} m_{i-1/2}(t).$$

Here we have substituted $\langle \mathbf{z}, \mathbf{j}'_i\rangle = \overline{A}_{U,i-1/2} + \overline{A}_{L,i-1/2} = A$, which means that the volume constraint (4.38) must remain satisfied, as it is for the PFTFM (see section 4.4.4). For periodic boundary conditions, setting $\dot{K}$ according to (4.51) leads to global momentum conservation, in absence of source terms. With $\dot{K} = \dot{Q}$, substituting (4.42) leads to

$$\frac{\mathrm{d}M_h}{\mathrm{d}t} = -\left(f_{3,N_p+1/2} + f_{4,N_p+1/2} - f_{3,1/2} - f_{4,1/2}\right) - \left(Ap_{N_p+1/2} - Ap_{1/2}\right) + \sum_{i=1}^{N_u}\left(c_{3,i-1/2}\Delta s + c_{4,i-1/2}\Delta s\right),$$

which is a momentum balance matching that of the TFM.

In contrast to energy, total momentum is conserved regardless of the discretization of the numerical fluxes, due to the nature of the finite volume scheme (just like total mass). In addition, it is conserved by a simple forward Euler time discretization, and by extension also by explicit Runge-Kutta methods. The proof for this is simple since $\mathbf{z}$ contains only constants, so that the following holds:

$$\langle \mathbf{z}, \frac{\mathrm{d}\mathbf{q}}{\mathrm{d}t}\rangle = \langle \mathbf{z}, \frac{\mathbf{q}_i^{n+1} - \mathbf{q}_i^n}{\Delta t}\rangle = \frac{m_{i-1/2}^{n+1} - m_{i-1/2}^n}{\Delta t},$$

with n denoting the temporal index and Δt the time step. For the energy, no such relation holds, since $\mathbf{v}_{i-1/2,i-1}$ and $\mathbf{v}_{i-1/2,i}$ are functions of the solution, which vary with time. Moreover, since the energy is not a quadratic function of the solution, standard energy-conserving time integration methods such as implicit midpoint [52] are also not energy-conserving.

4.C Summary of the discrete model

We summarize all the relations needed to implement the energy-conserving PFTFM. The basis of the model is (4.47), which describes the evolution of the variables (4.33), which are defined on the staggered grid pictured in Figure 4.2. The matrices $\mathbf{A}_i$ and $\mathbf{B}_i$ and the vector $\mathbf{k}_i$ are defined by the vectors $\mathbf{j}_i$ and $\mathbf{l}^T$ according to (4.45) and (4.46), which are in turn defined by (4.36) and (4.41). The fluxes $\mathbf{f}_i$ are defined by (4.35), and the difference of these fluxes should be taken:

$$[\![\mathbf{f}_i]\!] = \mathbf{f}_{i+1/2} - \mathbf{f}_{i-1/2}.$$

The source term vector, including a driving pressure gradient and streamwise gravity, is given by (4.37).

The PFTFM does not include constraints or an equation for the pressure. Instead it is necessary to define the rate of change of the volumetric flow rate, $\dot{K}$. For closed boundaries, this is simply $\dot{K} = 0$. For an inflow boundary, we have

$$\dot{K} = \frac{1}{\rho_U}\frac{\mathrm{d}q_{3,1/2}}{\mathrm{d}t} + \frac{1}{\rho_L}\frac{\mathrm{d}q_{4,1/2}}{\mathrm{d}t},$$

where $q_{3,1/2}$ and $q_{4,1/2}$ are the (prescribed) left boundary values of $q_3 = \rho_U u_U A_U$ and $q_4 = \rho_L u_L A_L$, respectively. For periodic boundaries, $\dot{K}$ is given by (4.51).

For closed or inflow boundaries, the boundary values of $\mathrm{d}q_3/\mathrm{d}t$ and $\mathrm{d}q_4/\mathrm{d}t$ are prescribed, and the boundary values of $\mathrm{d}q_1/\mathrm{d}t$ and $\mathrm{d}q_2/\mathrm{d}t$ follow from a characteristic boundary treatment described in Sanderse and Veldman [107].

The system (4.47) describes the problem locally and should be used to compose the global problem, over the whole domain. The resulting system, consisting of the semi-discrete governing equations with the semi-discrete expression for $\dot{K}$, can be integrated in time using standard explicit time integration methods. In this work, we use a classic four-stage fourth-order Runge-Kutta method [23]. Further details on the time integration, including how to prevent constraint drift, are given in Sanderse et al. [105].

5

Energy-stable formulation of the extended two-fluid model

In this chapter we present a complete framework for the energy-stable simulation of stratified incompressible flow in channels, using the one-dimensional two-fluid model. Building on earlier energy-conserving work on the basic two-fluid model, our new framework includes diffusion, friction, and surface tension. We show that surface tension can be added in an energy-conserving manner, and that diffusion and friction have a strictly dissipative effect on the energy.

We then propose spatial discretizations for these terms such that a semi-discrete model is obtained that has the same conservation properties as the continuous model. Additionally, we propose a new energy-stable advective flux scheme that is energy-conserving in smooth regions of the flow and strictly dissipative where sharp gradients appear. This is obtained by combining, using flux limiters, a previously developed energy-conserving advective flux with a novel first-order upwind scheme that is shown to be strictly dissipative.

The complete framework, with diffusion, surface tension, and a bounded energy, is linearly stable to short wavelength perturbations, and exhibits nonlinear damping near shocks. The model yields smoothly converging numerical solutions, even under conditions for which the basic two-fluid model is ill-posed. With our explicit expressions for the dissipation rates, we are able to attribute the nonlinear damping to the different dissipation mechanisms, and compare their effects.

This chapter is based on the article "Energy-stable discretization of the one-dimensional two-fluid model", published in *International Journal of Multiphase Flow*, 174:104756, 2024 [22].

5.1 Introduction

The one-dimensional two-fluid model (TFM) is a cross-sectionally averaged model for two-phase flow in pipes and channels. Velocities and phase fractions are resolved only along the main direction of flow, for each fluid separately. This yields an efficient model that is useful when calculations are needed quickly, or when many calculations need to be made. It is most commonly used for flow assurance in oil and gas or CO_2 transport [4, 48], and for safety analysis of steam-water flows in nuclear reactors [8]. In this chapter we consider the incompressible and isothermal form of the TFM. Note that the one-dimensional model discussed in this work, with averages taken over the portions of the pipe or channel cross section occupied by each fluid, differs from multi-dimensional two-fluid models with a local averaging, as described for example by Chahed et al. [26].

The TFM possesses the ability to dynamically simulate the Kelvin-Helmholtz instability which arises at the interface between two fluids flowing at different velocities. This is a valuable property since it is essential in predicting the transition from stratified flow to slug flow, a type of flow which is typically unwanted due to the large loads it places on the pipe [38]. However, for the basic TFM, when the difference between the two fluids' velocities is large, the instability is unphysically severe. Linear stability analysis shows an unbounded growth rate at short wavelengths, leading to the conclusion that the model is ill-posed [34, 35, 87]. For the basic model, with only first-order terms, the results of the linear stability analysis can be compared to those of a characteristic analysis: short wavelength unbounded instability implies complex eigenvalues [96].

The stability issue is intertwined with a modeling issue. Due to the averaged one-dimensional nature of the TFM, not all small-scale dynamics of the instability can be resolved, and there is uncertainty on how to model their effect on the averaged flow. The TFM implicitly carries the *long wavelength assumption*, implying that the TFM can only accurately model perturbations with a wavelength longer than the fluid depth [56, 87]. It is precisely at the poorly modeled short wavelengths that the catastrophic instability takes place.

The issue has led some researchers to use regularizing terms such as an artificial interfacial pressure force which completely eliminates the instability, for both long and short wavelengths [9, 37, 75]. Others have proposed regularizing terms which only eliminate instability below a desired cut-off wavelength, in the form of artificial diffusion, added both to mass and momentum equations [14, 56]. Finally, researchers strive for stabilization through the systematic inclusion of missing physics [35, 76]. One example is the introduction by Song and Ishii [110] of momentum flux parameters, which are intended to take into account the effect of the non-uniformity of the velocity profile. Montini [87] showed that these can extend the region of state space for which the TFM is well-posed, but unphysically high parameter values are required to stabilize the model for all relevant flow conditions. Other physical stabilizing effects, such as molecular or turbulent diffusion (in axial direction) [44] and surface tension [96], specifically target the short scales.

Beyond the question of the growth of small perturbations, which is answered by linear stability analysis, lies the question of the growth of large perturbations, for which the full nonlinear behavior of the model must be taken into account [76]. For related models, namely the single-layer and two-layer shallow water equations, the mechanical energy acts as an entropy function, and as a nonlinear bound on the solution [15, 42, 121]. An

energy conservation equation can be derived from the governing (mass and momentum conservation) equations, leading to the conclusion that energy is a secondary conserved quantity of the model, following the terminology of Veldman [125]. Energy-conserving discretization schemes, in which the energy conservation property of the continuous equations is retained, have been designed in order to prevent numerical instability [47, 122]. In chapter 3 we showed that the basic TFM satisfies an energy conservation equation like the shallow water equations, and developed an energy-conserving finite volume scheme which satisfies a semi-discrete energy conservation equation.

However, in the presence of shocks, the derivation of the energy conservation equation for the continuous model no longer holds, and energy needs to be dissipated [61]. Whereas for the compressible Euler equations the Rankine-Hugoniot relations prescribe the conservation of energy in shocks, for models like the shallow water equations and the isothermal TFM the Rankine-Hugoniot relations only involve conservation of mass and momentum, since these models do not solve an energy equation. Rather, the TFM must satisfy an energy inequality in the presence of shocks, much like the entropy inequality that holds for the compressible Euler equations. Energy-conserving schemes without dissipation will produce numerical oscillations in the presence of shocks. Therefore energy-stable schemes are designed, by taking an energy-conserving scheme as a baseline, and adding strictly dissipative terms, which can only cause a decrease of the energy [24, 43]. These dissipative terms typically take the form of numerical diffusion which is proportional to grid cell size, and preferably dissipate the minimum required amount of energy, and only in the vicinity of shocks, where it is needed.

The TFM requires mechanisms both for dissipation in shocks, and for suppression of the unbounded linear instability. Following the approach of Fullmer et al. [46], we achieve these effects through the addition of axial (momentum) diffusion and surface tension. In this work, we fit these effects, along with wall and interface friction, into our energy-consistent framework (see chapter 3). Diffusion and friction are shown to be strictly dissipative, surface tension is shown to be energy-conserving, and we present a spatial discretization of these terms that retains these properties. Importantly, we propose a novel discretization of the advective flux that is energy stable, with numerical dissipation acting near discontinuities in the solution.

The extended framework possesses bounded linear growth rates (with damping at short wavelengths), and possesses a nonlinear bound on the energy. It possesses multiple mechanisms for dissipation, which can be quantified using explicit expressions for the various dissipation rates. The energy-stable nature of the semi-discrete model, consistent with its continuous counterpart, provides additional fidelity in the accuracy of the numerical solution. The framework yields grid-converged numerical solutions, with well-resolved shocks, for flow states for which the basic TFM is linearly ill-posed.

The analysis of the continuous model is given in section 5.2, starting with a review of the basic model and its energy behavior, followed by the results for the extended model, and then a detailed analysis of each term separately. In section 5.3, these steps are repeated for the semi-discrete model, with the addition of an analysis of the newly proposed advective flux discretization, showing that it is energy stable. The stability of the TFM is discussed in detail in section 5.4, in order to motivate the additions to the basic model. In section 5.5, the energy and stability properties predicted by analysis are verified using

numerical experiments. We test the capability to model a traveling wave, and a growing wave which develops into a shock, and take a detailed look at the different components of the dissipation near the shock. Our conclusions are given in section 5.6.

5.2 Energy conservation and the continuous TFM

5.2.1 Governing equations for the basic model

The one-dimensional two-fluid model (TFM) is a cross-sectionally averaged model for two-phase flow in a closed conduit [59, 111]. The conduit can take different forms, such as a pipe with a circular cross section, as depicted in Figure 5.1, a duct with a rectangular cross section, or (more abstractly) a two-dimensional channel with a cross section of zero width. In all cases, the model can be obtained by defining control volumes for the two fluids separately, which are assumed to be stratified with a sharp interface between them, and setting up integral mass and momentum balances for these control volumes. No energy balance is needed, since the flow is assumed to be isothermal [90]. Additionally, the flow is assumed to be incompressible. The mass and momentum balances are divided by their length Δs, the limit $\Delta s \longrightarrow 0$ is taken, and the resulting equations are written in terms of cross-sectionally averaged variables, which are functions only of the streamwise coordinate s and time t. An important assumption made in this process is that the streamwise length scale over which variations in the flow occur must be much larger than the normal length scale over which variations occur; this is known as the long wavelength assumption [56, 87]. The long wavelength assumption implies that along the normal direction the flow is in hydrostatic balance.

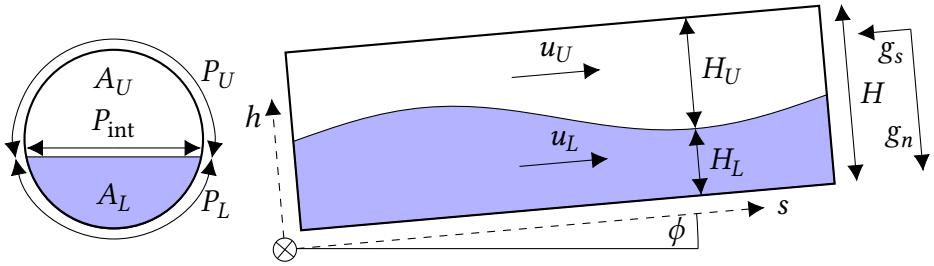

Figure 5.1: A schematic of stratified two-fluid flow in ducts (a circular pipe segment is shown as an example) described by the one-dimensional TFM.

The model, in conservative form, is given by (see chapter 3):

$$\frac{\partial \mathbf{q}}{\partial t} + \frac{\partial \mathbf{f}(\mathbf{q})}{\partial s} + \mathbf{j}(\mathbf{q})\frac{\partial p}{\partial s} = \mathbf{0}, \tag{5.1}$$

with the conservative variables $\mathbf{q}(s,t)$ representing a mass per unit length or momentum per unit length:

$$\mathbf{q}^T = \begin{bmatrix} q_1 & q_2 & q_3 & q_4 \end{bmatrix} = \begin{bmatrix} \rho_U A_U & \rho_L A_L & \rho_U u_U A_U & \rho_L u_L A_L \end{bmatrix}.$$

The conservative variables can be written in terms of the primitive variables, namely the cross-sections A_U and A_L (related to the heights H_U and H_L) which are occupied by the up-

per and lower fluids respectively, the densities ρ_U and ρ_L of each fluid, and the streamwise (averaged) velocities u_U and u_L. In (5.1), the fluxes are given by

$$\mathbf{f}(\mathbf{q})^T = \begin{bmatrix} f_1(\mathbf{q}) & f_2(\mathbf{q}) & f_3(\mathbf{q}) & f_4(\mathbf{q}) \end{bmatrix} = \begin{bmatrix} q_3 & q_4 & \frac{q_3^2}{q_1} - \rho_U g_n \widehat{H}_U & \frac{q_4^2}{q_2} - \rho_L g_n \widehat{H}_L \end{bmatrix}.$$

Here $\widehat{H}_U = \widehat{H}_U(\mathbf{q})$ and $\widehat{H}_L = \widehat{H}_L(\mathbf{q})$ are geometric quantities, defined in Appendix A, which are part of the terms known as the level gradients, which describe the effect of the variation of the hydrostatic pressure along s. The symbol $g_n = g\cos(\phi)$ represents the normal component of gravity, ϕ being the pipe inclination angle.

The pressure p appearing in the equations denotes the pressure at the interface between the two fluids. Its derivative is weighted by the vector $\mathbf{j}$, which is given by

$$\mathbf{j}(\mathbf{q})^T = \begin{bmatrix} 0 & 0 & \frac{q_1}{\rho_U} & \frac{q_2}{\rho_L} \end{bmatrix}.$$

Since the upper and lower fluid together fill the pipe with cross-section A, the system is subject to the volume constraint

$$\frac{q_1}{\rho_U} + \frac{q_2}{\rho_L} = A,$$

which implies the volumetric flow constraint (see chapter 4)

$$\frac{\partial Q}{\partial s} = 0, \quad \text{with} \quad Q(\mathbf{q}) = \frac{q_3}{\rho_U} + \frac{q_4}{\rho_L} = u_U A_U + u_L A_L. \tag{5.2}$$

5.2.2 Energy conservation for the basic model

In this subsection, we give a concise derivation of the energy equation of the basic TFM, based on the work of chapter 3. The results given in this subsection are not novel, but serve as a necessary basis for the extended energy analysis of later subsections.

The basic TFM has been shown to conserve the following mechanical energy:

$$e_b(\mathbf{q}) = \rho_U g_n \widetilde{H}_U + \rho_L g_n \widetilde{H}_L + \frac{1}{2}\frac{q_3^2}{q_1} + \frac{1}{2}\frac{q_4^2}{q_2}. \tag{5.3}$$

Here $\widetilde{H}_U = \widetilde{H}_U(A_U(q_1, \rho_U))$ and $\widetilde{H}_L = \widetilde{H}_L(A_L(q_2, \rho_L))$ are geometric terms representing the centers of mass of the upper and lower fluids respectively (see Appendix A). Given a mechanical energy $e_b(\mathbf{q})$, we can define the following vector:

$$\mathbf{v}_b(\mathbf{q})^T \coloneqq \left[\frac{\partial e_b}{\partial \mathbf{q}}\right] = \begin{bmatrix} -\frac{1}{2}\frac{q_3^2}{q_1^2} + g_n \frac{\mathrm{d}\widetilde{H}_U}{\mathrm{d}A_U} & -\frac{1}{2}\frac{q_4^2}{q_2^2} + g_n \frac{\mathrm{d}\widetilde{H}_L}{\mathrm{d}A_L} & \frac{q_3}{q_1} & \frac{q_4}{q_2} \end{bmatrix}. \tag{5.4}$$

Taking the dot product of this vector with the governing equations given by (5.1) yields

$$\langle \mathbf{v}_b, \frac{\partial \mathbf{q}}{\partial t} \rangle + \langle \mathbf{v}_b, \frac{\partial \mathbf{f}}{\partial s} \rangle + \langle \mathbf{v}_b, \mathbf{j}\frac{\partial p}{\partial s} \rangle = 0. \tag{5.5}$$

Using the geometric relations (A.7), the volumetric flow constraint (5.2), and assuming g_n to be constant along s, it can be shown that these terms can be written in conservative form (see chapter 3):

$$\langle \mathbf{v}_b, \frac{\partial \mathbf{q}}{\partial t} \rangle = \frac{\partial e_b}{\partial t}, \quad \langle \mathbf{v}_b, \frac{\partial \mathbf{f}}{\partial s} \rangle = \frac{\partial h_f}{\partial s}, \quad \langle \mathbf{v}_b, \mathbf{j}\frac{\partial p}{\partial s} \rangle = \frac{\partial h_p}{\partial s},$$

with

$$h_f = g_n q_3 \frac{\mathrm{d}\widetilde{H}_U}{\mathrm{d}A_U} + g_n q_4 \frac{\mathrm{d}\widetilde{H}_L}{\mathrm{d}A_L} + \frac{1}{2}\frac{q_3^3}{q_1^2} + \frac{1}{2}\frac{q_4^3}{q_2^2}, \tag{5.6}$$

and

$$h_p = Qp. \tag{5.7}$$

In the upcoming energy analysis of the additional model terms, we will follow the same structure, and use the insight that the dot product of $\mathbf{v}_b$ with the additional model term yields its contribution to the energy equation.

Since each term in (5.5) can be written in conservative form, it reduces to the local energy conservation equation

$$\frac{\partial e_b}{\partial t} + \frac{\partial h_b}{\partial s} = 0, \tag{5.8}$$

with $h_b = h_f + h_p$, which describes how the energy $e_b(s,t)$ at a specific point in space changes due to an inflow or outflow. In case of periodic or closed boundaries, integrating this equation over a section of pipe yields the global energy conservation equation

$$\frac{\mathrm{d}E_b}{\mathrm{d}t} = -\left[h_b\right]_{s_1}^{s_2} = 0, \quad \text{with} \quad E_b(t) = \int_{s_1}^{s_2} e_b \,\mathrm{d}s. \tag{5.9}$$

This shows that the mechanical energy is a secondary conserved quantity of the TFM (in contrast to the primary conserved quantities of mass and momentum).

5.2.3 Energy equation for the extended model

Having set up the basic TFM and its energy conservation equation, we will extend it in an energy-consistent manner, with three additions that make it linearly well-posed and energy stable. We will show, in the following subsections, that friction and diffusion have a strictly dissipative effect, while surface tension can be added in an energy-conserving manner. Previously (in chapter 4), the energy-conserving nature of streamwise gravity and the energy input due to a driving pressure gradient have been demonstrated.

The model, extended with all the additional terms, is given by

$$\boxed{\frac{\partial \mathbf{q}}{\partial t} + \frac{\partial \mathbf{f}}{\partial s} + \mathbf{j}\frac{\partial p}{\partial s} = \frac{\partial \mathbf{d}}{\partial s} + \mathbf{s} + \mathbf{c}_g + \mathbf{c}_f + \mathbf{c}_p} \tag{5.10}$$

with $\partial \mathbf{d}/\partial s$ representing diffusion, $\mathbf{c}_f$ representing friction, and $\mathbf{s}$ representing surface tension. The expressions for these terms will be given in (5.16), (5.20), and (5.25), respectively. The extended model includes the following contributions from streamwise gravity, indicated in Figure 5.1 with $g_s = g\sin(\phi)$:

$$\mathbf{c}_g^T = \begin{bmatrix} 0 & 0 & -g\sin(\phi)q_1 & -g\sin(\phi)q_2 \end{bmatrix},$$

and from a constant driving pressure gradient, which can be applied in cases with periodic boundary conditions in order to balance against streamwise gravity and friction:

$$\mathbf{c}_p^T = \begin{bmatrix} 0 & 0 & -\frac{q_1}{\rho_U}\frac{\partial p_{\text{body}}}{\partial s} & -\frac{q_2}{\rho_L}\frac{\partial p_{\text{body}}}{\partial s} \end{bmatrix}.$$

The driving pressure gradient acts as a body force, and is independent of the variable pressure p which acts to make the flow satisfy the volume and volumetric flow constraints.

For the extended model given by (5.10), the following energy conservation equation will be derived:

$$\boxed{\frac{\partial e}{\partial t} + \frac{\partial h}{\partial s} = -\epsilon + c_p} \tag{5.11}$$

with

$$e = e_b + e_g + e_\sigma, \tag{5.12}$$

$$h = h_b + h_g + h_d + h_\sigma, \tag{5.13}$$

$$\epsilon = \epsilon_d + \epsilon_f. \tag{5.14}$$

Equation (5.11) is the first main novel result of this work. It shows that the mechanical energy e, which consists of kinetic, potential, and surface energy, is locally conserved except for the dissipating effects of diffusion and friction. The upcoming subsections will give the expressions (5.18) for h_d, (5.19) for ϵ_d, (5.23) for ϵ_f, and (5.31) for e_σ and h_σ. Contributions from streamwise gravity are present in the energy and the energy flux (see chapter 4):

$$e_g = gy\big(q_1 + q_2\big), \quad h_g = gy\big(q_3 + q_4\big), \quad \text{with} \quad \frac{\mathrm{d}y}{\mathrm{d}s} = \sin(\phi(s)),$$

while the driving pressure gradient adds a source term:

$$c_p = -Q\frac{\partial p_{\text{body}}}{\partial s},$$

which is strictly positive in a flow which is aligned with its driving pressure gradient, e.g. $Q > 0$ and $\partial p_{\text{body}}/\partial s < 0$. This term differs from the others in that it represents an externally applied force, and therefore does not adhere to the strictly dissipative behavior of the flow itself.

Upon integrating the local energy equation over a periodic domain, the conservative term $\partial h/\partial s$ in (5.11) vanishes. Besides conservative terms, the new energy equation has an explicit sink term $-\epsilon$ which remains present in the global energy equation:

$$\boxed{\frac{\mathrm{d}E}{\mathrm{d}t} = -\mathcal{E} + C_p} \quad \text{with} \quad E(t) = \int_{s_1}^{s_2} e\,\mathrm{d}s, \quad \mathcal{E} = \int_{s_1}^{s_2} \epsilon\,\mathrm{d}s, \tag{5.15}$$

$$C_p = \int_{s_1}^{s_2} c_p\,\mathrm{d}s = -Q\frac{\partial p_{\text{body}}}{\partial s}L,$$

with $L = s_2 - s_1$ the length of the domain. Disregarding the (optional) externally supplied energy source, the energy-conserving basic model has been supplemented with a sink term which will shown to be strictly negative, leading to the dissipation of energy, and an energy-stable model.

Each addition to the model independently results in additional terms in the energy equation. The combined result of all these additions was given here. In the following subsections, the novel terms in (5.11) will be derived separately.

5.2.4 Physical diffusion

Our first novel contribution in the continuous setting is that we show that adding viscous diffusion terms to the TFM has a strictly dissipative effect, which can be quantified using an expression for the dissipation rate. We refer to these viscous terms as "physical diffusion" in contrast to the artificial diffusion of [14, 45, 56], and the numerical diffusion which will be discussed in section 5.3. The physical diffusion terms naturally appear in the derivation of the model, but are typically neglected due to the long wavelength assumption, with the argument that the TFM cannot accurately resolve the scale at which these terms act. However, they are important in bounding the linear instability of short wavelength perturbations (see section 5.4), and in bounding nonlinear shocks through dissipation (see section 5.5.4).

In the TFM, physical diffusion takes the form of the term $\partial \mathbf{d}/\partial \mathbf{s}$ as included in (5.10), with $\mathbf{d}$ given by [46, 87]

$$\mathbf{d}^T = \begin{bmatrix} 0 & 0 & \nu_{\text{eff},U} q_1 \frac{\partial}{\partial s}\frac{q_3}{q_1} & \nu_{\text{eff},L} q_2 \frac{\partial}{\partial s}\frac{q_4}{q_2} \end{bmatrix}. \tag{5.16}$$

5

We use the effective viscosity model of Fullmer et al. [44], which combines the material viscosity ν_m with a turbulent viscosity ν_t. This serves as a closure term for small scale fluctuations that are not resolved by the model:

$$\nu_{\text{eff}} = C_\epsilon (\nu_m + \nu_t),$$

with C_ϵ an adjustment factor. The parameters ν_t and C_ϵ are empirical: they can be based on fully resolved (higher dimensional) simulations, specific to a given test case. Physical diffusion conserves momentum, since it can be written in conservative form.

We now consider the effect of physical diffusion on the energy. Unlike the addition of streamwise gravity, the addition of diffusion does not change the energy definition. There is a contribution of the extra terms to the left hand side (LHS) of the energy equation, which is given by

$$-\langle \mathbf{v}_b, \frac{\partial \mathbf{d}}{\partial s} \rangle,$$

with $\mathbf{v}_b$ given by (5.4). Some manipulation yields (for smooth solutions)

$$-\langle \mathbf{v}_b, \frac{\partial \mathbf{d}}{\partial s} \rangle = -\frac{q_3}{q_1}\frac{\partial}{\partial s}\left(\nu_{\text{eff},U} q_1 \frac{\partial}{\partial s}\frac{q_3}{q_1}\right) - \frac{q_4}{q_2}\frac{\partial}{\partial s}\left(\nu_{\text{eff},L} q_2 \frac{\partial}{\partial s}\frac{q_4}{q_2}\right) = \frac{\partial h_d}{\partial s} + \epsilon_d, \tag{5.17}$$

with

$$h_d = -\nu_{\text{eff},U} q_1 \frac{1}{2}\frac{\partial}{\partial s}\frac{q_3^2}{q_1^2} - \nu_{\text{eff},L} q_2 \frac{1}{2}\frac{\partial}{\partial s}\frac{q_4^2}{q_2^2}, \tag{5.18}$$

$$\epsilon_d = \nu_{\text{eff},U} q_1 \left(\frac{\partial}{\partial s}\frac{q_3}{q_1}\right)^2 + \nu_{\text{eff},L} q_2 \left(\frac{\partial}{\partial s}\frac{q_4}{q_2}\right)^2. \tag{5.19}$$

The terms included in the energy flux h_d are energy-conserving, since they can be written in conservative form. The remaining terms, collected in ϵ_d, are not conservative. They are strictly positive, since $\nu_{\text{eff},U}$, q_1, $\nu_{\text{eff},L}$, and q_2 must be positive, and the square

of the differential terms must be positive. Therefore, when moved to the right hand side (RHS), it becomes clear that $-\epsilon_d$ is a strictly negative sink term. In conclusion, we have proven analytically that physical diffusion leads to dissipation of the energy given by (5.12), with dissipation rate ϵ_d.

5.2.5 Friction terms

Our second novel contribution in the continuous setting is that we prove that wall and interface friction add a strictly dissipative sink term to the energy equation. The friction term $\mathbf{c}_f$ can be added to the model as in (5.10), with

$$\mathbf{c}_f^T = \begin{bmatrix} 0 & 0 & \tau_U P_U + \tau_{\text{int}} P_{\text{int}} & \tau_L P_L - \tau_{\text{int}} P_{\text{int}} \end{bmatrix}. \tag{5.20}$$

The wall stresses τ_U and τ_L represent the shear stresses acting at the pipe perimeters P_U and P_L, that are in contact with the upper and lower fluids, respectively. The interface stress τ_{int} represents the shear stress at the interface P_{int} between the two fluids. The stress terms in the model are the averaged effect of local stresses on the averaged flow, and in order to express these in terms of the averaged variables, closure relations are required. These typically take the following form [116]:

$$\tau_L = -\frac{1}{2} f_L \rho_L u_L |u_L|, \quad \tau_U = -\frac{1}{2} f_U \rho_U u_U |u_U|, \quad \tau_{\text{int}} = -\frac{1}{2} f_{\text{int}} \rho_U (u_U - u_L)|u_U - u_L|, \tag{5.21}$$

in which f_L, f_U, and f_{int} are friction factors that require further closure relations, which are functions of the solution $\mathbf{q}$ (see section 5.A).

We now consider the effect of wall and interface friction on the energy. The contribution of the extra terms to the RHS of the energy equation is

$$+\langle \mathbf{v}_b, \mathbf{c}_f \rangle,$$

with $\mathbf{v}_b$ given by (5.4). Carrying out the multiplication, substituting (5.21), and some rewriting yields

$$\langle \mathbf{v}_b, \mathbf{c}_f \rangle = \frac{q_3}{q_1}(\tau_U P_U + \tau_{\text{int}} P_{\text{int}}) + \frac{q_4}{q_2}(\tau_L P_L - \tau_{\text{int}} P_{\text{int}}) = -\epsilon_f, \tag{5.22}$$

with

$$\epsilon_f = \frac{1}{2} f_U \rho_U \left(\frac{q_3}{q_1}\right)^2 \left|\frac{q_3}{q_1}\right| P_U + \frac{1}{2} f_L \rho_L \left(\frac{q_4}{q_2}\right)^2 \left|\frac{q_4}{q_2}\right| P_L + \frac{1}{2} f_{\text{int}} \rho_U \left(\frac{q_3}{q_1} - \frac{q_4}{q_2}\right)^2 \left|\frac{q_3}{q_1} - \frac{q_4}{q_2}\right| P_{\text{int}}. \tag{5.23}$$

Since f_U, f_L, f_{int}, ρ_U, ρ_L, P_U, P_L, and P_{int} must be positive, and the rest of the terms are either quadratic or absolute, all three terms in (5.23) must be positive. Therefore, $-\epsilon_f$ will act as a sink in the energy equation, which represents the dissipation of energy due to friction. In conclusion, we have proven analytically that wall and interface friction have a strictly dissipative effect on the energy given by (5.12).

5.2.6 Surface tension

Our third novel contribution in the continuous setting is that we show that surface tension can be added to the TFM in such a way that the total energy is conserved. Surface tension is an important addition since it makes the model linearly well-posed (see section 5.4). However, if surface tension were to be added in a non-conservative manner, it would spoil the energy-stable nature of the model. Therefore, it is key to find an energy-conserving form of the surface tension.

The effect of surface tension in the TFM is typically modeled through its effect on the pressure. This effect is to introduce a discontinuity in the pressure at the interface. The pressure difference is given by [87, 96]

$$\Delta p = -\sigma\kappa = \sigma \frac{\partial^2 H_L}{\partial s^2} \left[1 + \left(\frac{\partial H_L}{\partial s} \right)^2 \right]^{-3/2}, \tag{5.24}$$

with σ the surface tension and κ the streamwise curvature of the interface, with the interface assumed flat along the other direction. This is the Young-Laplace equation for the TFM.

Similar to [46], we include the effect of this pressure difference through the term $\mathbf{s}$ in (5.10), with

$$\mathbf{s}^T = \begin{bmatrix} 0 & 0 & 0 & \frac{q_2}{\rho_L} \frac{\partial \Delta p}{\partial s} \end{bmatrix}. \tag{5.25}$$

This is a general way to write the surface tension. Typically in literature [6, 46, 87, 96], the assumption $(\partial H_L/\partial s)^2 \ll 1$ will be made to approximate (5.24) as:

$$\Delta p \approx \sigma \frac{\partial^2 H_L}{\partial s^2} \approx \frac{\sigma}{P_{\text{int}}} \frac{\partial^2 A_L}{\partial s^2}. \tag{5.26}$$

Note that for the specific case of a 2D channel geometry ($P_{\text{int}} = 1$, $A_L = H_L$), the two approximations in (5.26) are equivalent.

We note that, unlike the basic model, surface tension of the form given by (5.25) is not momentum-conserving, as it cannot be written in conservative form. This is caused by the one-dimensional nature of the model and stands in contrast to higher-dimensional, unaveraged models, where surface tension does conserve momentum [99].

Though (5.25) is not momentum-conserving, it can still be energy-conserving, and we aim to find a set of expressions for Δp and the surface energy such that the contribution of surface tension to the energy conservation equation is of conservative form. Physically, the surface tension is associated with an energy, proportional to the surface area, that is conserved in combination with the mechanical energy [99]. The surface area in the one-dimensional two-fluid model (see Figure 5.1) will depend on $\partial H_L/\partial s = P_{\text{int}}^{-1} \partial A_L/\partial s$, and P_{int}. Therefore, we introduce the following general form for the surface energy:

$$e_\sigma = e_\sigma(S_{\text{int}}, P_{\text{int}}), \quad \text{with} \quad S_{\text{int}} = \frac{\partial A_L}{\partial s}, \tag{5.27}$$

with the functional dependencies specified as

$$q_2 = q_2(A_L), \quad P_{\text{int}} = P_{\text{int}}(A_L), \quad S_{\text{int}} = S_{\text{int}}(s,t), \quad A_L = A_L(s,t).$$

The additional term on the LHS of the energy equation due to surface tension as given by (5.25) is

$$-\langle \mathbf{v}_b, \mathbf{s} \rangle = -\frac{q_4}{\rho_L} \frac{\partial \Delta p}{\partial s}.$$

In order for the model addition to be energy-conserving, the following condition must hold:

$$-\frac{q_4}{\rho_L} \frac{\partial \Delta p}{\partial s} = \frac{\partial h_\sigma}{\partial s} + \frac{\partial e_\sigma}{\partial t}, \tag{5.28}$$

for in this case the addition to the energy equation will be of conservative form. We will now derive a relation between Δp and e_σ such that (5.28) holds.

The time derivative of the energy given by (5.27) is defined by

$$\frac{\partial e_\sigma}{\partial t} = \frac{\partial e_\sigma}{\partial S_{\text{int}}} \frac{\partial S_{\text{int}}}{\partial t} + \frac{\partial e_\sigma}{\partial P_{\text{int}}} \frac{\partial P_{\text{int}}}{\partial t},$$

and under the assumption of smooth solutions, and through substitution of the mass conservation equation for the lower fluid (the second equation of (5.1)), can be rewritten in the following manner:

$$\begin{aligned}
\frac{\partial e_\sigma}{\partial t} &= \frac{\partial e_\sigma}{\partial S_{\text{int}}} \frac{\partial}{\partial s} \left(\rho_L^{-1} \frac{\partial q_2}{\partial t} \right) + \frac{\partial e_\sigma}{\partial P_{\text{int}}} \frac{\mathrm{d} P_{\text{int}}}{\mathrm{d} A_L} \rho_L^{-1} \frac{\partial q_2}{\partial t} \\
&= -\frac{\partial e_\sigma}{\partial S_{\text{int}}} \frac{\partial}{\partial s} \left(\rho_L^{-1} \frac{\partial q_4}{\partial s} \right) - \frac{\partial e_\sigma}{\partial P_{\text{int}}} \frac{\mathrm{d} P_{\text{int}}}{\mathrm{d} A_L} \rho_L^{-1} \frac{\partial q_4}{\partial s} \\
&= -\frac{\partial h_\sigma}{\partial s} - \frac{q_4}{\rho_L} \frac{\partial \Delta p}{\partial s},
\end{aligned}$$

with

$$h_\sigma = \frac{1}{\rho_L} \left(\frac{\partial e_\sigma}{\partial S_{\text{int}}} \frac{\partial q_4}{\partial s} - q_4 \frac{\partial}{\partial s} \left(\frac{\partial e_\sigma}{\partial S_{\text{int}}} \right) + q_4 \frac{\partial e_\sigma}{\partial P_{\text{int}}} \frac{\mathrm{d} P_{\text{int}}}{\mathrm{d} A_L} \right),$$

and

$$\Delta p = \frac{\partial}{\partial s} \left(\frac{\partial e_\sigma}{\partial S_{\text{int}}} \right) - \frac{\partial e_\sigma}{\partial P_{\text{int}}} \frac{\mathrm{d} P_{\text{int}}}{\mathrm{d} A_L}. \tag{5.29}$$

For an energy of the general form (5.27), and a surface tension of the general form (5.25), (5.29) is the relation between the specific forms of Δp and e_σ, that needs to be satisfied in order to achieve energy conservation.

We now must find a set of expressions for Δp and e_σ, that – first – satisfies (5.29) and – second – makes physical sense. The most straightforward way to do this is to propose an energy based on physical considerations, substitute this in (5.29), and check if the resulting expression for Δp compares to our expectation, which is that it take a form similar to (5.24) or (5.26). From a physical point of view, the energy should be given by σ times the surface area, which can be expressed as

$$e_\sigma(S_{\text{int}}, P_{\text{int}}) = \sigma P_{\text{int}} \sqrt{1 + \left(\frac{\partial H_L}{\partial s} \right)^2} = \sigma P_{\text{int}} \sqrt{1 + \left(P_{\text{int}}^{-1} \frac{\partial A_L}{\partial s} \right)^2} = \sigma P_{\text{int}} \sqrt{1 + \left(P_{\text{int}}^{-1} S_{\text{int}} \right)^2}.$$

However, substituting this in (5.29) yields an expression for Δp that does not relate to (5.24) or (5.26), and therefore cannot be physically justified. Mimicking the conventional approach of taking approximations such as (5.26), we take the second order Taylor expansion of this energy around $S_{\text{int}} = 0$:

$$e_\sigma(S_{\text{int}}, P_{\text{int}}) \approx \sigma\left(P_{\text{int}} + \frac{1}{2}P_{\text{int}}^{-1}S_{\text{int}}^2\right).$$

Substituting this energy in (5.29) yields the following expression for Δp:

$$\Delta p_{\text{int}} = \frac{\sigma}{P_{\text{int}}}\frac{\partial S_{\text{int}}}{\partial s} - \sigma\left(1 + \frac{1}{2}P_{\text{int}}^{-2}S_{\text{int}}^2\right)\frac{\mathrm{d}P_{\text{int}}}{\mathrm{d}A_L}, \tag{5.30}$$

of which the first term can be recognized in (5.26), but the second term cannot.

When the scope is reduced from arbitrary geometries to the specific case of the 2D channel geometry, for which $P_{\text{int}} = 1$ and $A_L = H_L$, (5.30) does match (5.26) exactly. This means that for the channel geometry, the combination

$$e_\sigma = \sigma\left(1 + \frac{1}{2}\left(\frac{\partial H_L}{\partial s}\right)^2\right), \quad \Delta p = \sigma\frac{\partial^2 H_L}{\partial s^2}, \quad \text{with} \quad h_\sigma = \frac{\sigma}{\rho_L}\left(\frac{\partial q_4}{\partial s}\frac{\partial H_L}{\partial s} - q_4\frac{\partial^2 H_L}{\partial s^2}\right), \tag{5.31}$$

is energy-conserving, and it can be justified physically, since e_σ is an approximation of σ times the surface area, and Δp is an approximation of the Young-Laplace equation. This expression for Δp can be substituted in (5.25) to obtain an energy-conserving form of the surface tension.

We have therefore found a form of the surface tension $\mathbf{s}$, and an associated surface energy e_σ, with which the basic model can be extended, while retaining its energy-conserving behavior. For the 2D channel geometry, this turned out to be equivalent to a standard form, often used in literature.

5.3 Energy conservation and the semi-discrete TFM

5.3.1 Semi-discrete equations for the basic model

With the energy analysis for the continuous model complete, we will continue to propose a discretization that inherits the energy properties of the three additions to the model on the discrete level. In order to obtain the same conservation properties for the discrete model as for the continuous model, the model must be discretized in a specific manner. Therefore, the energy analysis guides the discretization. In this subsection, we will first summarize the previously found energy-conserving discretization of the basic model (see chapter 3), to which energy-consistent discretizations of the additional model terms will be added.

We define the unknowns of the semi-discrete TFM on a staggered grid, depicted in Figure 5.2, in the following manner:

$$\mathbf{q}_i(t) \coloneqq \begin{bmatrix} q_{1,i}(t) \\ q_{2,i}(t) \\ q_{3,i-1/2}(t) \\ q_{4,i-1/2}(t) \end{bmatrix} = \begin{bmatrix} (\rho_U A_U \Delta s)_i \\ (\rho_L A_L \Delta s)_i \\ (\rho_U A_U u_U \Delta s)_{i-1/2} \\ (\rho_L A_L u_L \Delta s)_{i-1/2} \end{bmatrix}, \tag{5.32}$$

We introduce the following notation to denote central interpolation and jumps respectively:

$$\overline{a}_{i-1/2} \coloneqq \frac{1}{2}(a_{i-1} + a_i), \quad \overline{a}_i \coloneqq \frac{1}{2}\left(a_{i-1/2} + a_{i+1/2}\right), \tag{5.33}$$

$$[\![a_{i-1/2}]\!] \coloneqq a_i - a_{i-1}, \quad [\![a_i]\!] \coloneqq a_{i+1/2} - a_{i-1/2}. \tag{5.34}$$

The primitive variables can be extracted from (5.32) through the following relations:

$$A_{U,i} = \frac{q_{1,i}}{\rho_U \Delta s}, \quad A_{L,i} = \frac{q_{2,i}}{\rho_L \Delta s}, \quad u_{U,i-1/2} = \frac{q_{3,i-1/2}}{\overline{q}_{1,i-1/2}}, \quad u_{L,i-1/2} = \frac{q_{4,i-1/2}}{\overline{q}_{2,i-1/2}}. \tag{5.35}$$

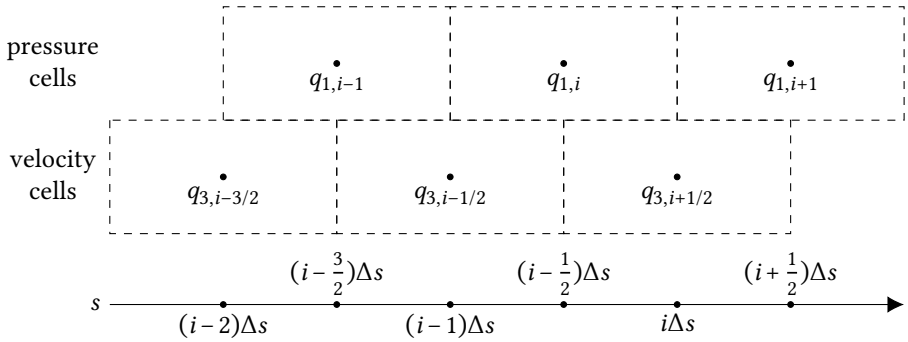

Figure 5.2: Staggered grid layout.

With this notation, the semi-discrete finite volume scheme can be written locally as

$$\frac{\mathrm{d}\mathbf{q}_i}{\mathrm{d}t} + [\![\mathbf{f}_i]\!] + \mathbf{j}_i [\![p_{i-1/2}]\!] = \mathbf{0}, \tag{5.36}$$

with

$$\mathbf{f}_{i-1/2} \coloneqq \begin{bmatrix} f_{1,i-1/2} \\ f_{2,i-1/2} \\ f_{3,i-1} \\ f_{4,i-1} \end{bmatrix} = \begin{bmatrix} \frac{q_{3,i-1/2}}{\Delta s} \\ \frac{q_{4,i-1/2}}{\Delta s} \\ \overline{\left(\frac{q_{3,i-1}}{\overline{q}_{1,i-1}}\right)} \frac{\overline{q}_{3,i-1}}{\Delta s} - \rho_U g_n \widehat{H}_{U,i-1} \\ \overline{\left(\frac{q_{4,i-1}}{\overline{q}_{2,i-1}}\right)} \frac{\overline{q}_{4,i-1}}{\Delta s} - \rho_L g_n \widehat{H}_{L,i-1} \end{bmatrix}, \text{ and } \mathbf{j}_i \coloneqq \begin{bmatrix} j_{1,i} \\ j_{2,i} \\ j_{3,i-1/2} \\ j_{4,i-1/2} \end{bmatrix} = \begin{bmatrix} 0 \\ 0 \\ \frac{\overline{q}_{1,i-1/2}}{\rho_U \Delta s} \\ \frac{\overline{q}_{2,i-1/2}}{\rho_L \Delta s} \end{bmatrix}. \tag{5.37}$$

The semi-discrete version of the volume constraint is given by

$$\frac{q_{1,i}}{\rho_U \Delta s} + \frac{q_{2,i}}{\rho_L \Delta s} = A,$$

which implies the volumetric flow constraint (see chapter 4)

$$[\![Q_i]\!] = 0, \quad \text{with} \quad Q_{i-1/2}(\mathbf{q}_i) \coloneqq \frac{q_{3,i-1/2}}{\rho_U \Delta s} + \frac{q_{4,i-1/2}}{\rho_L \Delta s}. \tag{5.38}$$

5.3.2 Energy conservation for the semi-discrete basic model

The basic TFM, discretized as given above, conserves the following discretized mechanical energy:

$$e_{b,i-1/2} = \rho_U g_n \overline{\widetilde{H}}_{U,i-1/2} \Delta s + \rho_L g_n \overline{\widetilde{H}}_{L,i-1/2} \Delta s + \frac{1}{2} \frac{q_{3,i-1/2}^2}{\overline{q}_{1,i-1/2}} + \frac{1}{2} \frac{q_{4,i-1/2}^2}{\overline{q}_{2,i-1/2}}. \tag{5.39}$$

This result was obtained in chapter 3. Here we will give a concise version of the proof. This is needed as a basis for the extensions of the semi-discrete energy analysis which will be made in the following subsections.

From the energy definition, the $\mathbf{v}_b$ vectors can be calculated as

$$\mathbf{v}_{b,i-1/2,i-1} \coloneqq \left[\frac{\partial e_{b,i-1/2}}{\partial \mathbf{q}_{i-1}}\right]^T = \begin{bmatrix} -\frac{1}{4}\frac{q_{3,i-1/2}^2}{\overline{q}_{1,i-1/2}^2} + \frac{1}{2} g_n \left(\frac{\mathrm{d}\widetilde{H}_U}{\mathrm{d}A_U}\right)_{i-1} \\ -\frac{1}{4}\frac{q_{4,i-1/2}^2}{\overline{q}_{2,i-1/2}^2} + \frac{1}{2} g_n \left(\frac{\mathrm{d}\widetilde{H}_L}{\mathrm{d}A_L}\right)_{i-1} \\ 0 \\ 0 \end{bmatrix},$$

$$\mathbf{v}_{b,i-1/2,i} \coloneqq \left[\frac{\partial e_{b,i-1/2}}{\partial \mathbf{q}_{i}}\right]^T = \begin{bmatrix} -\frac{1}{4}\frac{q_{3,i-1/2}^2}{\overline{q}_{1,i-1/2}^2} + \frac{1}{2} g_n \left(\frac{\mathrm{d}\widetilde{H}_U}{\mathrm{d}A_U}\right)_{i} \\ -\frac{1}{4}\frac{q_{4,i-1/2}^2}{\overline{q}_{2,i-1/2}^2} + \frac{1}{2} g_n \left(\frac{\mathrm{d}\widetilde{H}_L}{\mathrm{d}A_L}\right)_{i} \\ \frac{q_{3,i-1/2}}{\overline{q}_{1,i-1/2}} \\ \frac{q_{4,i-1/2}}{\overline{q}_{2,i-1/2}} \end{bmatrix}.$$

The sum of the dot products of $\mathbf{v}_{b,i-1/2,i-1}$ and $\mathbf{v}_{b,i-1/2,i}$ with equation (5.36) for $\mathbf{q}_{i-1}$ and $\mathbf{q}_i$ respectively is

$$\begin{aligned} \left\langle \mathbf{v}_{b,i-1/2,i-1}, \frac{\mathrm{d}\mathbf{q}_{i-1}}{\mathrm{d}t} \right\rangle + \left\langle \mathbf{v}_{b,i-1/2,i}, \frac{\mathrm{d}\mathbf{q}_{i}}{\mathrm{d}t} \right\rangle + \left\langle \mathbf{v}_{b,i-1/2,i-1}, [\![\mathbf{f}_{i-1}]\!] \right\rangle + \left\langle \mathbf{v}_{b,i-1/2,i}, [\![\mathbf{f}_{i}]\!] \right\rangle \\ + \left\langle \mathbf{v}_{b,i-1/2,i-1}, \mathbf{j}_{i-1} \right\rangle [\![p_{i-3/2}]\!] + \left\langle \mathbf{v}_{b,i-1/2,i}, \mathbf{j}_{i} \right\rangle [\![p_{i-1/2}]\!] = 0. \end{aligned} \tag{5.40}$$

Using the following definitions:

$$\overline{\mathbf{v}}_{b,i,i-1/2} = \frac{1}{2}\left(\mathbf{v}_{b,i-1/2,i-1} + \mathbf{v}_{b,i+1/2,i}\right), \qquad \overline{\mathbf{v}}_{b,i,i+1/2} = \frac{1}{2}\left(\mathbf{v}_{b,i-1/2,i} + \mathbf{v}_{b,i+1/2,i+1}\right),$$

$$[\![\mathbf{v}_{b,i,i-1/2}]\!] = \mathbf{v}_{b,i+1/2,i} - \mathbf{v}_{b,i-1/2,i-1}, \qquad [\![\mathbf{v}_{b,i,i+1/2}]\!] = \mathbf{v}_{b,i+1/2,i+1} - \mathbf{v}_{b,i-1/2,i},$$

and in addition discrete versions of the geometric relations (A.7)[1], the volumetric flow constraint (5.38), and substituting our discretization given by (5.37), it can be shown that

[1] These are only exactly satisfied by geometries with $\mathrm{d}^2 H_L / \mathrm{d}A_L^2 = 0$ (for example the 2D channel geometry).

the terms in (5.40) can be written in conservative form (see chapter 3):

$$\left\langle \mathbf{v}_{b,i-1/2,i-1}, \frac{\mathrm{d}\mathbf{q}_{i-1}}{\mathrm{d}t} \right\rangle + \left\langle \mathbf{v}_{b,i-1/2,i}, \frac{\mathrm{d}\mathbf{q}_{i}}{\mathrm{d}t} \right\rangle = \frac{\mathrm{d}e_{b,i-1/2}}{\mathrm{d}t},$$
$$\left\langle \mathbf{v}_{b,i-1/2,i-1}, [\![\mathbf{f}_{i-1}]\!] \right\rangle + \left\langle \mathbf{v}_{b,i-1/2,i}, [\![\mathbf{f}_{i}]\!] \right\rangle = \left[\!\!\left[h_{f,i-1/2} \right]\!\!\right],$$
$$\left\langle \mathbf{v}_{b,i-1/2,i-1}, \mathbf{j}_{i-1} \right\rangle [\![p_{i-3/2}]\!] + \left\langle \mathbf{v}_{b,i-1/2,i}, \mathbf{j}_{i} \right\rangle [\![p_{i-1/2}]\!] = \left[\!\!\left[h_{p,i-1/2} \right]\!\!\right],$$

with $h_{f,i}$ a discrete version of (5.6)[2]:

$$h_{f,i} = g_n \left(\frac{\mathrm{d}\widetilde{H}_U}{\mathrm{d}A_U} \right)_i \frac{\overline{q}_{3,i}}{\Delta s} + g_n \left(\frac{\mathrm{d}\widetilde{H}_L}{\mathrm{d}A_L} \right)_i \frac{\overline{q}_{4,i}}{\Delta s} + \left(\left[\overline{\left(\frac{q_{3,i}}{\overline{q}_{1,i}} \right)} \right]^2 - \frac{1}{2} \overline{\left(\frac{q_{3,i}^2}{\overline{q}_{1,i}^2} \right)} \right) \frac{\overline{q}_{3,i}}{\Delta s}$$
$$+ \left(\left[\overline{\left(\frac{q_{4,i}}{\overline{q}_{2,i}} \right)} \right]^2 - \frac{1}{2} \overline{\left(\frac{q_{4,i}^2}{\overline{q}_{2,i}^2} \right)} \right) \frac{\overline{q}_{4,i}}{\Delta s}, \quad (5.41)$$

and $h_{p,i}$ a discrete version of (5.7):

$$h_{p,i} = Q(t) p_i. \quad (5.42)$$

The energy analysis of the additional model terms, given in section 5.3.4 onward, will be fit into the same structure. The sum of the dot products of $\mathbf{v}_{b,i-1/2,i-1}$ and $\mathbf{v}_{b,i-1/2,i}$ with the additional model term will yield the resulting addition to the energy equation.

Since each term in (5.40) can be written in conservative form, it reduces to the local energy conservation equation

$$\frac{\mathrm{d}e_{b,i-1/2}}{\mathrm{d}t} + [\![h_{b,i-1/2}]\!] = 0, \quad (5.43)$$

with $h_{b,i} = h_{f,i} + h_{p,i}$. Like in the continuous case, this equation can be integrated over a closed or periodic domain to yield

$$\frac{\mathrm{d}\hat{E}_b}{\mathrm{d}t} = 0, \quad \text{with} \quad \hat{E}_b(t) = \sum_{i=1}^{N_u} e_{b,i-1/2}(t),$$

which means that the discrete mechanical energy defined by (5.39) is a secondary conserved quantity of the semi-discrete model described in section 5.3.1.

5.3.3 Energy equation for the semi-discrete extended model

Having introduced the energy-conserving discretization of the basic TFM and its energy conservation equation, we will propose discretizations of the three additions to the basic model, that retain the energy properties of their continuous counterparts, which were

[2]The given expression for $h_{f,i}$ is different from, but equivalent to, the expression given in chapter 4 (under the current assumptions).

derived in section 5.2. We will present discretizations of friction and diffusion that are strictly dissipative, and a discretization of surface tension that conserves the discretized energy, extended with a discrete version of the surface energy.

Additionally, we will present an upwind discretization of the advective terms that can be shown to be strictly dissipative, in contrast to the energy-conserving discretization of the advective terms given by (5.37). We will then propose to combine this upwind advective flux with the energy-conserving advective flux (using flux limiters), to produce a combined flux that is strictly dissipative, but less dissipative and less diffusive than the purely upwind flux. The combined flux is energy stable, and adds numerical dissipation only where necessary: near strong gradients and discontinuities. This mimics the behavior of weak solutions to the (basic) continuous equations, which instead of the energy equality of section 5.2.2 (that is only valid for smooth solutions), will satisfy an energy inequality.

The semi-discrete model, extended with all the additional terms, is given by

$$\boxed{\frac{\mathrm{d}\mathbf{q}_i}{\mathrm{d}t} + [\![\mathbf{f}_i]\!] + \mathbf{j}_i\,[\![p_{i-1/2}]\!] = [\![\mathbf{d}_i]\!] + \mathbf{s}_i\Delta s + \mathbf{c}_{g,i}\Delta s + \mathbf{c}_{f,i}\Delta s + \mathbf{c}_{p,i}\Delta s} \tag{5.44}$$

with $[\![\mathbf{d}_i]\!]$ representing diffusion, $\mathbf{c}_{f,i}$ representing friction, and $\mathbf{s}_i$ representing surface tension. The expressions for these terms will be given in (5.50), (5.54), and (5.56), respectively. The extended semi-discrete model includes the following contributions from streamwise gravity:

$$\mathbf{c}_{g,i}^T = \begin{bmatrix} 0 & 0 & -g\dfrac{[\![y_{i-1/2}]\!]}{\Delta s}\dfrac{\overline{q}_{1,i-1/2}}{\Delta s} & -g\dfrac{[\![y_{i-1/2}]\!]}{\Delta s}\dfrac{\overline{q}_{2,i-1/2}}{\Delta s} \end{bmatrix} \quad \text{with} \quad \frac{[\![y_{i-1/2}]\!]}{\Delta s} = \big[\sin(\phi)\big]_{i-1/2},$$

and from a constant driving pressure gradient:

$$\mathbf{c}_{p,i}^T = \begin{bmatrix} 0 & 0 & -\dfrac{\overline{q}_{1,i-1/2}}{\rho_U \Delta s}\dfrac{\partial p_{\text{body}}}{\partial s} & -\dfrac{\overline{q}_{2,i-1/2}}{\rho_L \Delta s}\dfrac{\partial p_{\text{body}}}{\partial s} \end{bmatrix}.$$

The energy equation that follows from (5.44) reads

$$\boxed{\frac{\mathrm{d}e_{i-1/2}}{\mathrm{d}t} + [\![h_{i-1/2}]\!] + [\![h_{n,i-1/2}]\!] = -\epsilon_{i-1/2} - \epsilon_{n,i-1/2} + c_{p,i-1/2}} \tag{5.45}$$

with

$$e_{i-1/2} = e_{b,i-1/2} + e_{g,i-1/2} + e_{\sigma,i-1/2}, \tag{5.46}$$

$$h_i = h_{b,i} + h_{g,i} + h_{d,i} + h_{\sigma,i}, \tag{5.47}$$

$$\epsilon_{i-1/2} = \epsilon_{d,i-1/2} + \epsilon_{f,i-1/2}. \tag{5.48}$$

The upcoming subsections will give the expressions (5.52) for $h_{d,i}$, (5.53) for $\epsilon_{d,i-1/2}$, (5.55) for $\epsilon_{f,i-1/2}$, (5.59) for $e_{\sigma,i-1/2}$, and (5.60) for $h_{\sigma,i}$. The contributions from streamwise gravity are given in chapter 4[3]

$$e_{g,i-1/2} = g\overline{\big(y_{i-1/2}\,(q_{1,i-1/2} + q_{2,i-1/2})\big)}, \quad h_{g,i} = g y_i \overline{\left(\frac{q_{3,i}}{\Delta s} + \frac{q_{4,i}}{\Delta s}\right)},$$

[3]The given expression for $h_{g,i}$ is different from, but equivalent to, the expression given in chapter 4.

and the contribution of the driving pressure gradient is given by

$$c_{p,i-1/2} = -Q_{i-1/2}\frac{\partial p_{\text{body}}}{\partial s}\Delta s,$$

which is positive when the body force is aligned with the mean flow. These are all semi-discrete counterparts of the continuous expressions given in section 5.2. The terms with subscript n are specific to the semi-discrete setting, and stem from the energy-stable combined advective flux. The numerical energy flux $h_{n,i}$ will be given by (5.65) and the numerical dissipation $\epsilon_{n,i-1/2}$ will be given by (5.66).

Equation (5.45) is the second main novel result of this work, as it shows that we have obtained a semi-discrete model with the same energy conservation properties as the continuous model. The model additions that were conservative in the continuous setting are discretized in such a way that the energy-conserving behavior is retained, and the model additions that were dissipative in the continuous setting are discretized in such a way that the strictly dissipative behavior is retained. The local energy equation (5.45) can be integrated over a periodic domain to yield the global energy equation[4]

$$\boxed{\frac{\mathrm{d}\hat{E}}{\mathrm{d}t} = -\hat{\mathcal{E}} - \hat{\mathcal{E}}_n + \widehat{C}_p} \quad \text{with} \quad \hat{E}(t) = \sum_{i=1}^{N_u} e_{i-1/2}(t), \quad \hat{\mathcal{E}} = \sum_{i=1}^{N_u} \epsilon_{i-1/2}(t), \tag{5.49}$$

$$\hat{\mathcal{E}}_n = \sum_{i=1}^{N_u} \epsilon_{n,i-1/2}(t), \quad \widehat{C}_p = \sum_{i=1}^{N_u} c_{p,i-1/2}(t) = -Q(t)\frac{\partial p_{\text{body}}}{\partial s}L.$$

This equation determines that the energy of the solution can never increase, except due to an explicitly applied external force (through the source term $\widehat{C}_p$).

Therefore, the novel semi-discrete model is energy stable. It has physical and numerical dissipation rates ($\hat{\mathcal{E}}$ and $\hat{\mathcal{E}}_n$) that can be computed from the solution. These dissipation rates can be integrated in time numerically to find the total dissipated energy due to the different contributions. The total dissipated energy between two points in time should match the difference in energy between these two points in time, as calculated through an evaluation of $\hat{E}$ at those two points in time.

Each term in the semi-discrete model independently results in corresponding terms in the energy equation. The combined result for the complete extended model, discretized in an energy-consistent manner, was given here. In the following subsections we will detail the novel contributions separately.

5.3.4 Physical diffusion

Our first novel contribution in the semi-discrete setting is to propose a discretization of the viscous diffusion terms and prove that it is strictly dissipative, just like its continuous counterpart. The diffusion term that can be added to the RHS of (5.36) is $[\partial \mathbf{d}/\partial s]_i \Delta s$, in which $[\partial \mathbf{d}/\partial s]_i$ is the discrete version of $\partial \mathbf{d}/\partial s$, with $\mathbf{d}$ given by (5.16). We propose the

[4]Note that there is a slight inconsistency between the notation used here and the notation used in earlier chapters. In earlier chapters, $\hat{E}$ is referred to as E_h.

following straightforward central discretization, which yields the diffusion term in (5.44):

$$\left[\frac{\partial \mathbf{d}}{\partial s}\right]_i = \frac{1}{\Delta s}[\![\mathbf{d}_i]\!] = \frac{1}{\Delta s}\left(\mathbf{d}_{i+1/2} - \mathbf{d}_{i-1/2}\right),$$

with

$$\mathbf{d}_{i-1/2} \coloneqq \begin{bmatrix} d_{1,i-1/2} \\ d_{2,i-1/2} \\ d_{3,i-1} \\ d_{4,i-1} \end{bmatrix} = \begin{bmatrix} 0 \\ 0 \\ \nu_{\mathrm{eff},U}\dfrac{q_{1,i-1}}{(\Delta s)^2}\left[\!\left[\dfrac{q_{3,i-1}}{\overline{q}_{1,i-1}}\right]\!\right] \\ \nu_{\mathrm{eff},L}\dfrac{q_{2,i-1}}{(\Delta s)^2}\left[\!\left[\dfrac{q_{4,i-1}}{\overline{q}_{2,i-1}}\right]\!\right] \end{bmatrix} = \begin{bmatrix} 0 \\ 0 \\ \rho_U \nu_{\mathrm{eff},U} A_{U,i-1}\dfrac{[\![u_{U,i-1}]\!]}{\Delta s} \\ \rho_L \nu_{\mathrm{eff},L} A_{L,i-1}\dfrac{[\![u_{L,i-1}]\!]}{\Delta s} \end{bmatrix}. \tag{5.50}$$

With diffusion, no extra term is added to the energy. The steps of the derivation of section 5.3.2 can be simply repeated. With the proposed discretization, the only additional terms in the energy equation (on the LHS) are

$$\begin{aligned}
&-\left\langle \mathbf{v}_{b,i-1/2,i-1}, [\![\mathbf{d}_{i-1}]\!]\right\rangle - \left\langle \mathbf{v}_{b,i-1/2,i}, [\![\mathbf{d}_i]\!]\right\rangle \\
&\quad = -\left[\!\left[\left\langle \overline{\mathbf{v}}_{b,i-1/2,i-1}, \mathbf{d}_{i-1}\right\rangle\right]\!\right] - \left[\!\left[\left\langle \overline{\mathbf{v}}_{b,i-1/2,i}, \mathbf{d}_i\right\rangle\right]\!\right] + \overline{\left\langle [\![\mathbf{v}_{b,i-1/2,i-1}]\!], \mathbf{d}_{i-1}\right\rangle} + \overline{\left\langle [\![\mathbf{v}_{b,i-1/2,i}]\!], \mathbf{d}_i\right\rangle} \\
&\quad = -\left[\!\left[\nu_{\mathrm{eff},U}\frac{q_{1,i-1/2}}{(\Delta s)^2}\overline{\left(\frac{q_{3,i-1/2}}{\overline{q}_{1,i-1/2}}\right)}\left[\!\left[\frac{q_{3,i-1/2}}{\overline{q}_{1,i-1/2}}\right]\!\right]\right]\!\right] + \overline{\left(\nu_{\mathrm{eff},U}\frac{q_{1,i-1/2}}{(\Delta s)^2}\left[\!\left[\frac{q_{3,i-1/2}}{\overline{q}_{1,i-1/2}}\right]\!\right]^2\right)} \\
&\qquad -\left[\!\left[\nu_{\mathrm{eff},L}\frac{q_{2,i-1/2}}{(\Delta s)^2}\overline{\left(\frac{q_{4,i-1/2}}{\overline{q}_{2,i-1/2}}\right)}\left[\!\left[\frac{q_{4,i-1/2}}{\overline{q}_{2,i-1/2}}\right]\!\right]\right]\!\right] + \overline{\left(\nu_{\mathrm{eff},L}\frac{q_{2,i-1/2}}{(\Delta s)^2}\left[\!\left[\frac{q_{4,i-1/2}}{\overline{q}_{2,i-1/2}}\right]\!\right]^2\right)} \\
&\quad = [\![h_{d,i-1/2}]\!] + \epsilon_{d,i-1/2},
\end{aligned} \tag{5.51}$$

with

$$h_{d,i} = -\nu_{\mathrm{eff},U}\frac{q_{1,i}}{(\Delta s)^2}\frac{1}{2}\left[\!\left[\left(\frac{q_{3,i}}{\overline{q}_{1,i}}\right)^2\right]\!\right] - \nu_{\mathrm{eff},L}\frac{q_{2,i}}{(\Delta s)^2}\frac{1}{2}\left[\!\left[\left(\frac{q_{4,i}}{\overline{q}_{2,i}}\right)^2\right]\!\right], \tag{5.52}$$

$$\epsilon_{d,i-1/2} = \overline{\left(\nu_{\mathrm{eff},U}\frac{q_{1,i-1/2}}{(\Delta s)^2}\left[\!\left[\frac{q_{3,i-1/2}}{\overline{q}_{1,i-1/2}}\right]\!\right]^2\right)} + \overline{\left(\nu_{\mathrm{eff},L}\frac{q_{2,i-1/2}}{(\Delta s)^2}\left[\!\left[\frac{q_{4,i-1/2}}{\overline{q}_{2,i-1/2}}\right]\!\right]^2\right)}. \tag{5.53}$$

Here we have used a discrete product rule:

$$a_i[\![b_i]\!] = [\![\overline{a}_i b_i]\!] - \overline{([\![a_i]\!] b_i)},$$

and a discrete chain rule:

$$\overline{a}_{i-1/2}[\![a_{i-1/2}]\!] = \frac{1}{2}[\![a^2_{i-1/2}]\!].$$

These can be derived by substituting the definitions (5.33) and (5.34), and applying some algebraic manipulation.

The result of (5.51) compares directly to the continuous result, given by (5.17). Like the continuous result, it consists of a conservative part, and a strictly dissipative part. The latter is due to $\epsilon_{d,i-1/2}$ being strictly positive, and the minus sign that is added when $\epsilon_{d,i-1/2}$ is moved to the RHS. Therefore, it has been proven that the proposed discretization of the diffusion terms is strictly dissipative with respect to the energy given by (5.46). Moreover, an explicit expression for the dissipation rate has been obtained, that can be used to measure the dissipation taking place in a numerical simulation.

5.3.5 Friction terms

Our second novel contribution in the semi-discrete setting is to show that wall and interface friction result in a strictly dissipative contribution to the semi-discrete energy equation. In (5.44), friction is included through the term $\mathbf{c}_{f,i}\Delta s$, in which $\mathbf{c}_{f,i}$ is the discrete version of (5.20). With reference to the closure relations given in section 5.2.5, we assume the following functional dependencies for the discrete friction terms:

$$\tau_{L,i-1/2} \coloneqq \tau_L(f_{L,i-1/2}, u_{L,i-1/2}), \quad \tau_{U,i-1/2} \coloneqq \tau_U(f_{U,i-1/2}, u_{U,i-1/2}),$$
$$\tau_{\text{int},i-1/2} \coloneqq \tau_{\text{int}}(f_{\text{int},i-1/2}, u_{U,i-1/2}, u_{L,i-1/2}),$$

with primitive variables given by (5.35). Then we propose the following discretization of the friction source terms:

$$\mathbf{c}_{f,i} = \begin{bmatrix} c_{f,1,i} \\ c_{f,2,i} \\ c_{f,3,i-1/2} \\ c_{f,4,i-1/2} \end{bmatrix} = \begin{bmatrix} 0 \\ 0 \\ \tau_{U,i-1/2}P_{U,i-1/2} + \tau_{\text{int},i-1/2}P_{\text{int},i-1/2} \\ \tau_{L,i-1/2}P_{L,i-1/2} - \tau_{\text{int},i-1/2}P_{\text{int},i-1/2} \end{bmatrix}. \tag{5.54}$$

Like with diffusion, adding friction terms to the system does not change the energy definition. Since the friction terms do not involve derivatives, the derivation of the contribution to the energy equation is almost the same as in the continuous case. The only modification to the energy equation is that the following terms are added to the RHS:

$$\begin{aligned} &\langle \mathbf{v}_{b,i-1/2,i-1}, \mathbf{c}_{f,i-1}\Delta s\rangle + \langle \mathbf{v}_{b,i-1/2,i}, \mathbf{c}_{f,i}\Delta s\rangle \\ &\quad = \frac{q_{3,i-1/2}}{\overline{q}_{1,i-1/2}}\left(\tau_{U,i-1/2}P_{U,i-1/2} + \tau_{\text{int},i-1/2}P_{\text{int},i-1/2}\right)\Delta s + \frac{q_{4,i-1/2}}{\overline{q}_{2,i-1/2}}\left(\tau_{L,i-1/2}P_{L,i-1/2} - \tau_{\text{int},i-1/2}P_{\text{int},i-1/2}\right)\Delta s \\ &\quad = -\epsilon_{f,i-1/2}, \end{aligned}$$

with

$$\begin{aligned} \epsilon_{f,i-1/2} = \frac{1}{2}f_{U,i-1/2}\rho_U\left(\frac{q_{3,i-1/2}}{\overline{q}_{1,i-1/2}}\right)^2\left|\frac{q_{3,i-1/2}}{\overline{q}_{1,i-1/2}}\right|P_{U,i-1/2}\Delta s + \frac{1}{2}f_{L,i-1/2}\rho_L\left(\frac{q_{4,i-1/2}}{\overline{q}_{2,i-1/2}}\right)^2\left|\frac{q_{4,i-1/2}}{\overline{q}_{2,i-1/2}}\right|P_{L,i-1/2}\Delta s \\ + \frac{1}{2}f_{\text{int},i-1/2}\rho_U\left(\frac{q_{3,i-1/2}}{\overline{q}_{1,i-1/2}} - \frac{q_{4,i-1/2}}{\overline{q}_{2,i-1/2}}\right)^2\left|\frac{q_{3,i-1/2}}{\overline{q}_{1,i-1/2}} - \frac{q_{4,i-1/2}}{\overline{q}_{2,i-1/2}}\right|P_{\text{int},i-1/2}\Delta s. \end{aligned} \tag{5.55}$$

Since $f_{U,i-1/2}$, $f_{L,i-1/2}$, $f_{\text{int},i-1/2}$, ρ_U, ρ_L, $P_{U,i-1/2}$, $P_{L,i-1/2}$, and $P_{\text{int},i-1/2}$ must be positive, and the rest of the terms are either quadratic or absolute, $\epsilon_{f,i-1/2}$ must always be positive. Therefore, $-\epsilon_{f,i-1/2}$ will act as a sink in the energy equation.

This result allows us, for the first time, to compare the dissipation due to wall and interface friction with the dissipation due to axial diffusion. Both components of the dissipation rate can be computed from the numerical solution, integrated numerically over time, and compared to one another to determine which has dissipated the most energy.

5.3.6 Surface tension

Our third novel contribution in the semi-discrete setting is to propose a discretization of the surface tension, and show that it is energy-conserving. This is key in maintaining the energy-stable nature of the semi-discrete model, while contributing favorably to the linear stability properties of the model; see section 5.4.

Surface tension is included in (5.44) through the term $\mathbf{s}_i \Delta s$, in which $\mathbf{s}_i$ is the discrete version of (5.25). A general form of the surface tension, analogous to (5.25), is given by

$$\mathbf{s}_i = \begin{bmatrix} 0 \\ 0 \\ 0 \\ \frac{\overline{q}_{2,i-1/2}}{\rho_L \Delta s} \frac{1}{\Delta s} \left[\!\left[[\Delta p]_{i-1/2} \right]\!\right] \end{bmatrix}. \tag{5.56}$$

We restrict the analysis to the channel geometry, for which clear results were obtained in the continuous analysis, and propose the following discretization of the pressure jump given in (5.31):

$$\left[\Delta p_{\text{int}}\right]_i = \frac{\sigma}{\Delta s} \left[\!\left[\frac{\left[\!\left[H_{L,i} \right]\!\right]}{\Delta s} \right]\!\right]. \tag{5.57}$$

This constitutes a straightforward discretization of the conventional approximation of the surface tension in the TFM.

With the proposed discretization, the extra terms on the LHS of the energy equation can be written as

$$\begin{aligned}
&- \left\langle \mathbf{v}_{b,i-1/2,i-1}, \mathbf{s}_{i-1} \Delta s \right\rangle - \left\langle \mathbf{v}_{b,i-1/2,i}, \mathbf{s}_i \Delta s \right\rangle \\
&\quad = -\frac{q_{4,i-1/2}}{\rho_L \Delta s} \left[\!\left[\frac{\sigma}{\Delta s} \left[\!\left[\frac{\left[\!\left[H_{L,i-1/2} \right]\!\right]}{\Delta s} \right]\!\right] \right]\!\right] \\
&\quad = -\frac{\sigma}{\rho_L} \left[\!\left[\overline{\left(\frac{q_{4,i-1/2}}{\Delta s} \right)} \frac{1}{\Delta s} \left[\!\left[\frac{\left[\!\left[H_{L,i-1/2} \right]\!\right]}{\Delta s} \right]\!\right] \right]\!\right] + \frac{\sigma}{\rho_L} \overline{\left(\left[\!\left[\frac{q_{4,i-1/2}}{\Delta s} \right]\!\right] \frac{1}{\Delta s} \left[\!\left[\frac{\left[\!\left[H_{L,i-1/2} \right]\!\right]}{\Delta s} \right]\!\right] \right)} \\
&\quad = \left[\!\left[h_{\sigma,i-1/2} \right]\!\right] + \frac{\sigma}{\rho_L} \left[\!\left[\frac{1}{\Delta s} \frac{\mathrm{d} q_{2,i-1/2}}{\mathrm{d} t} \right]\!\right] \frac{\left[\!\left[H_{L,i-1/2} \right]\!\right]}{\Delta s} \\
&\quad = \left[\!\left[h_{\sigma,i-1/2} \right]\!\right] + \sigma \frac{\mathrm{d}}{\mathrm{d} t} \left(\frac{\left[\!\left[H_{L,i-1/2} \right]\!\right]}{\Delta s} \right) \left[\!\left[H_{L,i-1/2} \right]\!\right] \\
&\quad = \left[\!\left[h_{\sigma,i-1/2} \right]\!\right] + \sigma \frac{\mathrm{d} e_{\sigma,i-1/2}}{\mathrm{d} t},
\end{aligned} \tag{5.58}$$

in which, based on (5.31), we have chosen to define the surface energy as:

$$e_{\sigma,i-1/2} = \sigma \Delta s \left(1 + \frac{1}{2} \left(\frac{[\![H_{L,i-1/2}]\!]}{\Delta s} \right)^2 \right), \tag{5.59}$$

with an energy flux of

$$h_{\sigma,i} = \sigma \frac{1}{\Delta s} \left[\!\!\left[\frac{q_{4,i}}{\rho_L \Delta s} \right]\!\!\right] \overline{\left(\frac{[\![H_{L,i}]\!]}{\Delta s} \right)} - \sigma \overline{\left(\frac{q_{4,i}}{\rho_L \Delta s} \right)} \frac{1}{\Delta s} \left[\!\!\left[\frac{[\![H_{L,i}]\!]}{\Delta s} \right]\!\!\right]. \tag{5.60}$$

In this derivation, we have used a discrete version of the product rule that can be derived from (5.33) and (5.34):

$$[\![\overline{a}_{i-1/2} b_{i-1/2}]\!] = \overline{\left([\![a_{i-1/2}]\!] b_{i-1/2} \right)} + a_{i-1/2} [\![b_{i-1/2}]\!],$$

and substituted the semi-discrete mass conservation equation for the lower fluid (the second equation of (5.36)), specified to the 2D channel.

The derivation (5.58) shows that, for the surface tension discretization given by (5.56) and (5.57), the contribution of surface tension to the semi-discrete energy equation can be written in conservative form. This requires adding an extra term to the energy, which must take a specific form that is tied to this discretization. We have succeeded in finding a combination of $\left[\Delta p_{\text{int}}\right]_i$ and $e_{\sigma,i-1/2}$ that is energy-conserving. These results hold for the 2D channel geometry.

Therefore, we have found a way to add surface tension to the semi-discrete model, in such a way that it remains energy stable. Consistent with the physics of the flow, no dissipation (or production) of energy will result from surface tension. All dissipation can be attributed to effects that would physically be expected to yield dissipation: diffusion and wall and interface friction.

5.3.7 Numerical diffusion

In addition to the energy-consistent discretizations of the extra terms in the continuous model, a modification is needed to our discretization of the basic model, as given by (5.37). In this subsection we will propose an upwind discretization of the advective terms in the momentum equations, that can be shown to add a strictly dissipative term to the energy equation, and is therefore energy stable.

This is required because our energy-conserving central advective flux, included in (5.37), is sensitive to discontinuities. At discontinuities, the proofs of energy conservation for the continuous equations no longer hold, and the continuous equations should dissipate energy [61]. However, our energy-conserving flux expressly forbids this. As a result, when discontinuities appear in the solution, numerical oscillations are generated. Adding physical diffusion mitigates the problem, but it acts at small scales, and in order to incorporate its full effect, a high grid refinement is required.

Therefore, it is necessary to introduce some form of (strictly dissipative) numerical diffusion. The adjective 'numerical' indicates that it should be grid-dependent: it is primarily needed at coarse resolutions. Such diffusion can be provided by an upwind discretization of the advective flux.

Different upwind discretizations can be conceived, by taking different interpolations and by upwinding different parts of the numerical flux, see e.g. [60, 67, 74]. Here we present a new upwind discretization that is based on the conservative variables, and closely resembles the energy-conserving flux of (5.37), with the exception that for the advecting velocities we use an upwind interpolation, instead of a central interpolation:

$$f_{3,a,i-1,u} = \left(\frac{q_3}{\overline{q}_1}\right)_{\mathrm{up},i-1} \frac{\overline{q}_{3,i-1}}{\Delta s} = \rho_U u_{U,\mathrm{up},i-1} \overline{\left(\overline{A}_{U,i-1} u_{U,i-1}\right)}, \tag{5.61a}$$

$$f_{4,a,i-1,u} = \left(\frac{q_4}{\overline{q}_2}\right)_{\mathrm{up},i-1} \frac{\overline{q}_{4,i-1}}{\Delta s} = \rho_L u_{L,\mathrm{up},i-1} \overline{\left(\overline{A}_{L,i-1} u_{L,i-1}\right)}, \tag{5.61b}$$

with

$$u_{U,\mathrm{up},i-1} = \begin{cases} u_{U,i-3/2}, & \text{if } \overline{q}_{3,i-1} > 0 \\ u_{U,i-1/2}, & \text{otherwise} \end{cases} \qquad u_{L,\mathrm{up},i-1} = \begin{cases} u_{L,i-3/2}, & \text{if } \overline{q}_{4,i-1} > 0 \\ u_{L,i-1/2}, & \text{otherwise} \end{cases}$$

This upwind flux is atypical in its choice to have u_U and u_L as the upwinded variables instead of q_3 and q_4, and in its choice to base the upwind directions on q_3 and q_4 instead of u_U and u_L. These choices are needed to prove the strictly dissipative property.

We only apply an upwind discretization to the advective terms of the momentum equations, and not to those of the mass equations. The mass equations are left unchanged, since changing these would cause complications in three areas. First, changing the mass advective fluxes would interfere with the coupling between the mass and momentum equations. Second, the discrete form of the volumetric flow constraint would be altered, since it is derived through substitution of the mass equations in the volume constraint. Third, the discrete energy analysis of the streamwise gravity and surface tension terms could be invalidated or require significant modification, since it involves substitution of the mass equations.

We now show that the contribution to the energy equation of these upwind fluxes can be divided into a conservative part and a non-conservative part. To this end, the analysis of section 5.3.2 is repeated, this time with (5.61) taking the place of the momentum advection part of the fluxes given in (5.37). The contribution of the flux terms to (5.40) can then be written as

$$\begin{aligned} &\left\langle \mathbf{v}_{b,i-1/2,i-1}, [\![\mathbf{f}_{i-1}]\!] \right\rangle + \left\langle \mathbf{v}_{b,i-1/2,i}, [\![\mathbf{f}_i]\!] \right\rangle \\ &\quad = \left[\!\left[\left\langle \overline{\mathbf{v}}_{b,i-1/2,i-1}, \mathbf{f}_{i-1} \right\rangle \right]\!\right] + \left[\!\left[\left\langle \overline{\mathbf{v}}_{b,i-1/2,i}, \mathbf{f}_i \right\rangle \right]\!\right] - \overline{\left\langle [\![\mathbf{v}_{b,i-1/2,i-1}]\!], \mathbf{f}_{i-1} \right\rangle} - \overline{\left\langle [\![\mathbf{v}_{b,i-1/2,i}]\!], \mathbf{f}_i \right\rangle} \\ &\quad = \left[\!\left[h_{f,i-1/2} \right]\!\right] + [\![h_{u,i-1/2}]\!] + \epsilon_{u,i-1/2}, \end{aligned}$$

with $h_{f,i}$ given by (5.41), $h_{u,i}$ given by

$$h_{u,i} = -\overline{\left(\frac{q_{3,i}}{\overline{q}_{1,i}}\right)} \left(\overline{\left(\frac{q_{3,i}}{\overline{q}_{1,i}}\right)} - \left(\frac{q_3}{\overline{q}_1}\right)_{\mathrm{up},i} \right) \frac{\overline{q}_{3,i}}{\Delta s} - \overline{\left(\frac{q_{4,i}}{\overline{q}_{2,i}}\right)} \left(\overline{\left(\frac{q_{4,i}}{\overline{q}_{2,i}}\right)} - \left(\frac{q_4}{\overline{q}_2}\right)_{\mathrm{up},i} \right) \frac{\overline{q}_{4,i}}{\Delta s}, \tag{5.62}$$

and $\epsilon_{u,i-1/2}$ given by

$$\epsilon_{u,i-1/2} = \epsilon_{u,U,i-1/2} + \epsilon_{u,L,i-1/2} = \overline{\left(\left[\!\left[\frac{q_{3,i-1/2}}{\overline{q}_{1,i-1/2}}\right]\!\right]\left(\overline{\left(\frac{q_{3,i-1/2}}{\overline{q}_{1,i-1/2}}\right)} - \left(\frac{q_3}{\overline{q}_1}\right)_{\mathrm{up},i-1/2}\right)\frac{\overline{q}_{3,i-1/2}}{\Delta s}\right)} + \overline{\left(\left[\!\left[\frac{q_{4,i-1/2}}{\overline{q}_{2,i-1/2}}\right]\!\right]\left(\overline{\left(\frac{q_{4,i-1/2}}{\overline{q}_{2,i-1/2}}\right)} - \left(\frac{q_4}{\overline{q}_2}\right)_{\mathrm{up},i-1/2}\right)\frac{\overline{q}_{4,i-1/2}}{\Delta s}\right)}. \quad (5.63)$$

We have split $\epsilon_{u,i-1/2}$ into a part pertaining to the upper fluid ($\epsilon_{u,U,i-1/2}$, first line) and a part pertaining to the lower fluid ($\epsilon_{u,L,i-1/2}$, second line).

This shows that the contribution of the upwind flux can be written as the contribution $[\![h_{f,i-1/2}]\!]$ of the energy-conserving flux, plus some extra terms. Some of these terms are completely between double brackets, meaning they are energy-conserving, and can be included in the energy flux $h_{u,i}$. The remaining terms will become source terms in the energy equation.

We will now show that these source terms are strictly dissipative. It is sufficient to only examine the terms pertaining to the upper fluid, since the terms pertaining to the lower fluid have the same structure, so their analysis will yield similar results. The source terms for the upper fluid can be rewritten in the following manner:

$$\epsilon_{u,U,i-1/2} = \frac{1}{2}\left[\!\left[\frac{q_{3,i-1}}{\overline{q}_{1,i-1}}\right]\!\right]\frac{\overline{q}_{3,i-1}}{\Delta s}\left[\overline{\left(\frac{q_{3,i-1}}{\overline{q}_{1,i-1}}\right)} - \left(\frac{q_3}{\overline{q}_1}\right)_{\mathrm{up},i-1}\right] + \frac{1}{2}\left[\!\left[\frac{q_{3,i}}{\overline{q}_{1,i}}\right]\!\right]\frac{\overline{q}_{3,i}}{\Delta s}\left[\overline{\left(\frac{q_{3,i}}{\overline{q}_{1,i}}\right)} - \left(\frac{q_3}{\overline{q}_1}\right)_{\mathrm{up},i}\right].$$

Now, we consider the case that $\overline{q}_{3,i-1} > 0$ and $\overline{q}_{3,i} > 0$, so that $u_{U,\mathrm{up},i-1} = u_{U,i-3/2}$ and $u_{U,\mathrm{up},i} = u_{U,i-1/2}$:

$$\begin{aligned}\epsilon_{u,U,i-1/2} &= \frac{1}{2}\left[\!\left[\frac{q_{3,i-1}}{\overline{q}_{1,i-1}}\right]\!\right]\frac{\overline{q}_{3,i-1}}{\Delta s}\left[\overline{\left(\frac{q_{3,i-1}}{\overline{q}_{1,i-1}}\right)} - \frac{q_{3,i-3/2}}{\overline{q}_{1,i-3/2}}\right] + \frac{1}{2}\left[\!\left[\frac{q_{3,i}}{\overline{q}_{1,i}}\right]\!\right]\frac{\overline{q}_{3,i}}{\Delta s}\left[\overline{\left(\frac{q_{3,i}}{\overline{q}_{1,i}}\right)} - \frac{q_{3,i-1/2}}{\overline{q}_{1,i-1/2}}\right] \\ &= \frac{1}{4}\left[\!\left[\frac{q_{3,i-1}}{\overline{q}_{1,i-1}}\right]\!\right]^2\frac{\overline{q}_{3,i-1}}{\Delta s} + \frac{1}{4}\left[\!\left[\frac{q_{3,i}}{\overline{q}_{1,i}}\right]\!\right]^2\frac{\overline{q}_{3,i}}{\Delta s}.\end{aligned}$$

Clearly, these terms must be positive, given that we have specified that $\overline{q}_{3,i-1} > 0$ and $\overline{q}_{3,i} > 0$.

Similarly, we consider the case that $\overline{q}_{3,i-1} < 0$ and $\overline{q}_{3,i} < 0$, so that $u_{U,\mathrm{up},i-1} = u_{U,i-1/2}$ and $u_{U,\mathrm{up},i} = u_{U,i+1/2}$:

$$\begin{aligned}\epsilon_{u,U,i-1/2} &= \frac{1}{2}\left[\!\left[\frac{q_{3,i-1}}{\overline{q}_{1,i-1}}\right]\!\right]\frac{\overline{q}_{3,i-1}}{\Delta s}\left[\overline{\left(\frac{q_{3,i-1}}{\overline{q}_{1,i-1}}\right)} - \frac{q_{3,i-1/2}}{\overline{q}_{1,i-1/2}}\right] + \frac{1}{2}\left[\!\left[\frac{q_{3,i}}{\overline{q}_{1,i}}\right]\!\right]\frac{\overline{q}_{3,i}}{\Delta s}\left[\overline{\left(\frac{q_{3,i}}{\overline{q}_{1,i}}\right)} - \frac{q_{3,i+1/2}}{\overline{q}_{1,i+1/2}}\right] \\ &= -\frac{1}{4}\left[\!\left[\frac{q_{3,i-1}}{\overline{q}_{1,i-1}}\right]\!\right]^2\frac{\overline{q}_{3,i-1}}{\Delta s} - \frac{1}{4}\left[\!\left[\frac{q_{3,i}}{\overline{q}_{1,i}}\right]\!\right]^2\frac{\overline{q}_{3,i}}{\Delta s}.\end{aligned}$$

Again, these terms must be positive, given that we have specified that $\overline{q}_{3,i-1} < 0$ and $\overline{q}_{3,i} < 0$. The third and fourth options (with differing signs between $\overline{q}_{3,i-1}$ and $\overline{q}_{3,i}$) are just simple recombinations of these two results, so they too will be strictly positive. Move these terms to the RHS, and they become strictly negative source terms. This means that our proposed upwind discretization adds a strictly negative source term to the energy equation, which acts to dissipate the energy given by (5.46).

Comparing this numerical dissipation term to the physical dissipation term given by (5.53), we see that, among other differences, the numerical dissipation has an additional factor Δs. It is proportional to the cell size and will decrease at a first order rate with increasing grid resolution.

Note that alternative upwind fluxes, such as those used by [67, 74], do not yield contributions to the energy equation that can be written as the sum of a conservative term and a strictly negative dissipation term. In contrast, our new upwind advective numerical flux does possess the property of energy stability. However, it may be more dissipative than necessary, and for this reason we will combine it with the energy-conserving flux, in an energy-stable manner.

5

5.3.8 Energy-stable combined advective flux

Our fifth and key novel contribution in the semi-discrete setting is that we combine the strictly dissipative upwind advective flux with the energy-conserving central advective flux, in such a way that the resulting advective flux is energy stable, but less dissipative than a purely upwind discretization. The proposed combination possesses the best properties of both schemes.

Our energy-conserving advective fluxes were defined in (5.37) as

$$f_{3,a,i-1,\mathrm{ec}} = \overline{\left(\frac{q_{3,i-1}}{\overline{q}_{1,i-1}}\right)}\frac{\overline{q}_{3,i-1}}{\Delta s} = \rho_U \overline{u}_{U,i-1}\overline{\left(\overline{A}_{U,i-1}u_{U,i-1}\right)},$$

$$f_{4,a,i-1,\mathrm{ec}} = \overline{\left(\frac{q_{4,i-1}}{\overline{q}_{2,i-1}}\right)}\frac{\overline{q}_{4,i-1}}{\Delta s} = \rho_L \overline{u}_{L,i-1}\overline{\left(\overline{A}_{L,i-1}u_{L,i-1}\right)}.$$

Following the conventional manner of combining low-order and higher-order fluxes [118], we propose the following combination of the energy-conserving fluxes and the upwind fluxes given by (5.61), using flux limiters:

$$f_{3,a,i-1} = \left(1-\phi\left(r_{U,i-1}\right)\right) f_{3,a,i-1,u} + \phi\left(r_{U,i-1}\right) f_{3,a,i-1,\mathrm{ec}}, \tag{5.64a}$$

$$f_{4,a,i-1} = \left(1-\phi\left(r_{L,i-1}\right)\right) f_{4,a,i-1,u} + \phi\left(r_{L,i-1}\right) f_{4,a,i-1,\mathrm{ec}}, \tag{5.64b}$$

with $\phi(r_{U,i-1})$ and $\phi(r_{L,i-1})$ the limiter functions which determine the weighting between the upwind flux and the energy-conserving flux. Here, the upwind flux is a low-order flux, and the energy-conserving flux is a higher-order flux. The limiting coefficients depend on the slope of the solution:

$$r_{U,i-1} = \begin{cases} \frac{q_{3,i-5/2}-q_{3,i-3/2}}{q_{3,i-3/2}-q_{3,i-1/2}}, & \text{if } \overline{u}_{U,i-1} > 0 \\ 1, & \text{if } \overline{u}_{U,i-1} = 0 \\ \frac{q_{3,i-1/2}-q_{3,i+1/2}}{q_{3,i-3/2}-q_{3,i-1/2}}, & \text{if } \overline{u}_{U,i-1} < 0 \end{cases} \qquad r_{L,i-1} = \begin{cases} \frac{q_{4,i-5/2}-q_{4,i-3/2}}{q_{4,i-3/2}-q_{4,i-1/2}}, & \text{if } \overline{u}_{L,i-1} > 0 \\ 1, & \text{if } \overline{u}_{L,i-1} = 0 \\ \frac{q_{4,i-1/2}-q_{4,i+1/2}}{q_{4,i-3/2}-q_{4,i-1/2}}, & \text{if } \overline{u}_{L,i-1} < 0 \end{cases}$$

These coefficients are fed to the limiter functions, for which many options exist. Here we choose the minmod function:

$$\phi(r) = \max[0, \min(r, 1)].$$

The minmod function will always yield a value between 0 and 1, which is an important property that we need to show energy stability of the combined scheme. When the solution is smooth, $\phi(r)$ will be close to 1, and the energy-conserving flux will be used. When the solution is less smooth, the upwind flux will be weighted more heavily. We note that the minmod function could be exchanged for a less dissipative alternative, though most conventional limiter functions are disqualified due to the requirement that the limiter function yield a value between 0 and 1.

The energy analysis of section 5.3.7 can be repeated for the fluxes given by (5.64), with similar results. The contribution of the flux terms to (5.40) can be written as

$$\begin{aligned}
&\left\langle \mathbf{v}_{b,i-1/2,i-1}, [\![\mathbf{f}_{i-1}]\!] \right\rangle + \left\langle \mathbf{v}_{b,i-1/2,i}, [\![\mathbf{f}_i]\!] \right\rangle \\
&\quad = [\![\langle \overline{\mathbf{v}}_{b,i-1/2,i-1}, \mathbf{f}_{i-1} \rangle]\!] + [\![\langle \overline{\mathbf{v}}_{b,i-1/2,i}, \mathbf{f}_i \rangle]\!] - \overline{\langle [\![\mathbf{v}_{b,i-1/2,i-1}]\!], \mathbf{f}_{i-1} \rangle} - \overline{\langle [\![\mathbf{v}_{b,i-1/2,i}]\!], \mathbf{f}_i \rangle} \\
&\quad = \left[\!\!\left[h_{f,i-1/2} \right]\!\!\right] + [\![h_{n,i-1/2}]\!] + \epsilon_{n,i-1/2},
\end{aligned}$$

with $h_{f,i}$ given by (5.41), $h_{n,i}$ given by

$$\begin{aligned}
h_{n,i} = &-\left(1 - \phi\left(r_{U,i}\right)\right) \overline{\left(\frac{q_{3,i}}{\overline{q}_{1,i}}\right)} \left(\overline{\left(\frac{q_{3,i}}{\overline{q}_{1,i}}\right)} - \left(\frac{q_3}{\overline{q}_1}\right)_{\mathrm{up},i} \right) \frac{\overline{q}_{3,i}}{\Delta s} \\
&- \left(1 - \phi\left(r_{L,i}\right)\right) \overline{\left(\frac{q_{4,i}}{\overline{q}_{2,i}}\right)} \left(\overline{\left(\frac{q_{4,i}}{\overline{q}_{2,i}}\right)} - \left(\frac{q_4}{\overline{q}_2}\right)_{\mathrm{up},i} \right) \frac{\overline{q}_{4,i}}{\Delta s},
\end{aligned} \tag{5.65}$$

and $\epsilon_{n,i-1/2}$ given by

$$\begin{aligned}
\epsilon_{n,i-1/2} = &\overline{\left(\left(1 - \phi\left(r_{U,i-1/2}\right)\right) \left[\!\!\left[\frac{q_{3,i-1/2}}{\overline{q}_{1,i-1/2}} \right]\!\!\right] \left(\overline{\left(\frac{q_{3,i-1/2}}{\overline{q}_{1,i-1/2}}\right)} - \left(\frac{q_3}{\overline{q}_1}\right)_{\mathrm{up},i-1/2} \right) \frac{\overline{q}_{3,i-1/2}}{\Delta s} \right)} \\
&+ \overline{\left(\left(1 - \phi\left(r_{L,i-1/2}\right)\right) \left[\!\!\left[\frac{q_{4,i-1/2}}{\overline{q}_{2,i-1/2}} \right]\!\!\right] \left(\overline{\left(\frac{q_{4,i-1/2}}{\overline{q}_{2,i-1/2}}\right)} - \left(\frac{q_4}{\overline{q}_2}\right)_{\mathrm{up},i-1/2} \right) \frac{\overline{q}_{4,i-1/2}}{\Delta s} \right)}.
\end{aligned} \tag{5.66}$$

Since with the minmod limiter function, the factors $\left(1 - \phi\left(r_{U,i}\right)\right)$ and $\left(1 - \phi\left(r_{L,i}\right)\right)$ have values between 0 and 1, this dissipation term has the same positivity property as the upwind dissipation term given by (5.63).

Therefore, our novel advective numerical flux, formed by combining our upwind flux and our energy-conserving flux, is energy stable. The new energy-stable flux will be less dissipative than the pure upwind flux, since it uses the energy-conserving flux where possible. Where the solution is smooth, the continuous equations conserve energy, and our energy-stable flux replicates this property. Where the solution is discontinuous, the energy-stable flux effectively adds numerical diffusion which dissipates energy.

5.4 Stability

In this section, we discuss the stability of the basic and extended TFM. The stability of the TFM is a topic that has received much attention since the discovery of the ill-posedness issue by [81]. Here we focus on providing a detailed motivation for our proposed model additions of physical diffusion and surface tension. Together these effects produce a reliable model that yields convergent solutions under flow conditions where the basic two-fluid model fails. Friction plays a less important role in the model's stability, but is an important physical effect that an accurate model must include, and is included in the stability analysis given here.

The basic two-fluid model, as described in section 5.2.1, is known to be conditionally hyperbolic [87]. In the region of state space where the velocity difference is below the inviscid Kelvin-Helmholtz (IKH) limit, the eigenvalues of the model are real, but outside this region the eigenvalues of the model are complex [74]. Linear stability analysis (see section 5.B) confirms the issue put forward by the characteristic analysis: within the hyperbolic region the model is stable, but in the non-hyperbolic region the (linear) growth rates for small wavelength perturbations tend towards infinity. Therefore the model is said to be (linearly) ill-posed: the common view is that this precludes meaningful solutions to the continuous model, and prevents convergence of numerical solutions [60]. This prevents the use of the basic model in its non-hyperbolic region.

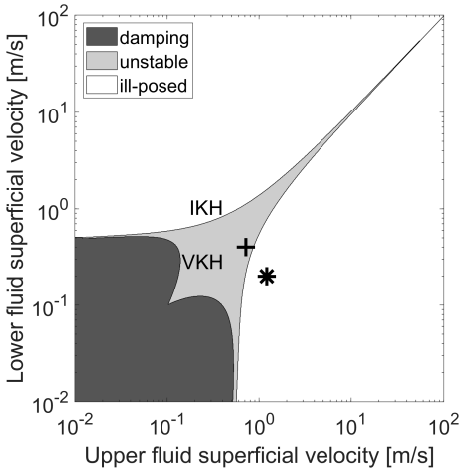

Figure 5.3: A map of the linear stability of perturbations to steady states of the TFM with wall and interface friction, using the basic model without diffusion and surface tension. The state space is divided into regions where perturbations are damped, are unstable with a bounded growth rate, or are unstable with an unbounded growth rate (ill-posed). The inviscid Kelvin-Helmholtz (IKH) and viscous Kelvin-Helmholtz (VKH) stability boundaries are indicated. The symbol + marks the base state given by Table 5.2, and the symbol $*$ marks the base state given by Table 5.3.

Figure 5.3 is a stability map similar to those of [5, 6]. It maps the stability of steady states of the TFM, where friction is balanced by a constant driving pressure gradient (acting as a body force). The parameters are given in Table 5.1 and the geometry is that of a 2D channel. Given the lower fluid superficial velocity $u_L\alpha_L$ and the upper fluid superficial

velocity $u_U(1-\alpha_L)$, the hold-up $\alpha_L = A_L/A$ and driving pressure gradient $\partial p_{\text{body}}/\partial s$ follow from the demand for a fully developed steady state (derivatives to s and t must be zero). For these steady states, the two dispersion relations $\omega(\lambda)$ can be calculated according to section 5.B. For a given perturbation wavelength λ, we consider the dispersion relation for which the imaginary component of ω is largest: this is the most unstable mode for this wavelength. If for this most unstable mode $\text{Im}(\omega(\lambda)) < 0$, the steady state is stable and damping (to perturbations of wavelength λ), if $\text{Im}(\omega(\lambda)) = 0$ it is neutrally stable, and if $\text{Im}(\omega(\lambda)) > 0$ it is unstable. As long as $\text{Im}(\omega(\lambda))$ is bounded as $\lambda \longrightarrow 0$, the state is well-posed. If $\text{Im}(\omega(\lambda)) \longrightarrow \infty$ for $\lambda \longrightarrow 0$, the state is labeled 'ill-posed'.

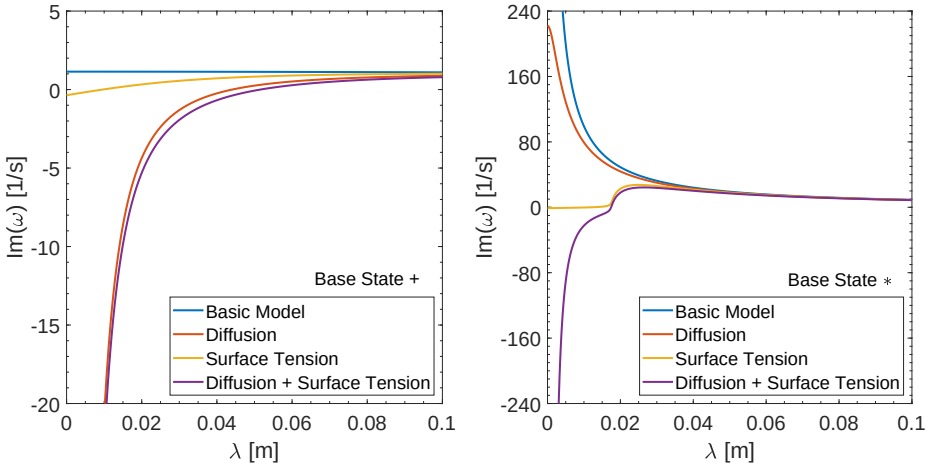

Figure 5.4: Imaginary component of the angular frequency ω for the most unstable mode, for the set of parameters given in Table 5.1, plotted as a function of wavelength $\lambda = 2\pi/k$. All models include wall and interface friction. Left: base state given by Table 5.2, marked by the symbol + in the stability maps. Right: base state given by Table 5.3, marked by the symbol $*$ in the stability maps.

Table 5.1: Parameters used for the linear stability analysis. These resemble the parameters of the Thorpe experiment [117] as described in [46].

Parameter	Symbol	Value	Units
Lower fluid density	ρ_L	1000	kg m^{-3}
Upper fluid density	ρ_U	780	kg m^{-3}
Acceleration of gravity	g	9.81	m s^{-2}
Channel inclination	ϕ	0	degrees
Channel height	H	0.03	m
Lower fluid material viscosity	$\nu_{m,L}$	$1.0 \cdot 10^{-6}$	$\text{m}^2\,\text{s}^{-1}$
Upper fluid material viscosity	$\nu_{m,U}$	$1.9 \cdot 10^{-6}$	$\text{m}^2\,\text{s}^{-1}$
Lower fluid effective viscosity	$\nu_{\text{eff},L}$	$1.13 \cdot 10^{-4}$	$\text{m}^2\,\text{s}^{-1}$
Upper fluid effective viscosity	$\nu_{\text{eff},U}$	$1.21 \cdot 10^{-4}$	$\text{m}^2\,\text{s}^{-1}$
Surface tension	σ	0.04	kg m s^{-2}

Table 5.2: Base state used for the linear stability analysis, corresponding to the left plot in Figure 5.4, and marked with the symbol + in the stability maps.

Variable	Symbol	Value	Units
Initial lower fluid hold-up	$\alpha_{L,0}$	0.4	–
Initial lower fluid velocity	$u_{L,0}$	1	$\mathrm{m\,s^{-1}}$
Initial upper fluid velocity	$u_{U,0}$	1.198	$\mathrm{m\,s^{-1}}$
Driving pressure gradient	$\partial p_{\mathrm{body}}/\partial s$	−204.2	$\mathrm{kg\,m^{-2}\,s^{-2}}$

Table 5.3: Base state used for the linear stability analysis, corresponding to the right plot in Figure 5.4, and marked with the symbol $*$ in the stability maps.

Variable	Symbol	Value	Units
Initial lower fluid hold-up	$\alpha_{L,0}$	0.2	–
Initial lower fluid velocity	$u_{L,0}$	1	$\mathrm{m\,s^{-1}}$
Initial upper fluid velocity	$u_{U,0}$	1.515	$\mathrm{m\,s^{-1}}$
Driving pressure gradient	$\partial p_{\mathrm{body}}/\partial s$	−268.4	$\mathrm{kg\,m^{-2}\,s^{-2}}$

For the basic model without diffusion and surface tension, stability is independent of wavelength [64]: if long wavelengths are unstable then short wavelengths are also unstable (though with different growth rates). This can be seen in Figure 5.4 (similar to figure 3.2 in [76]), which shows the growth rate of the most unstable mode, for two different steady states, and for different versions of the TFM. Therefore the stability map of the basic model in Figure 5.3 is independent of wavelength. It is divided into an ill-posed region and a well-posed region. Without friction the whole well-posed region would be neutrally stable. Friction divides the well-posed region of Figure 5.3 into a region with damping and an unstable region (but with bounded growth rates). The stability boundary with friction is referred to as the viscous Kelvin-Helmholtz (VKH) boundary, while the ill-posedness boundary is referred to as the inviscid Kelvin-Helmholtz (IKH) boundary [5, 6].

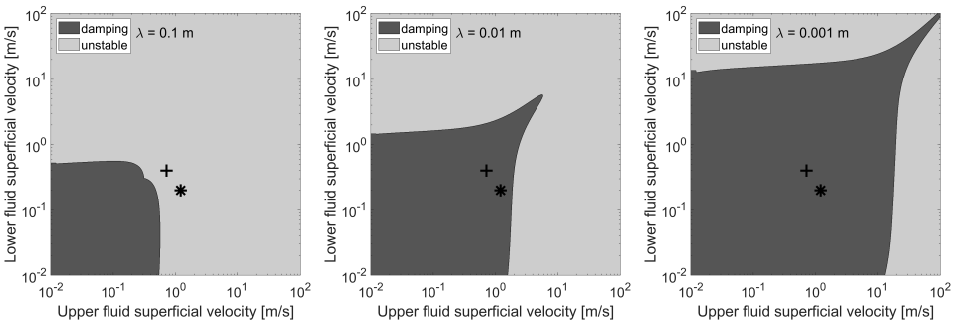

Figure 5.5: Maps of the linear stability of short wavelength perturbations to steady states of the TFM, with wall and interface friction, diffusion, and surface tension. The stability of perturbations with a specific wavelength is shown. Left: $\lambda = 0.1\,\mathrm{m}$. Middle: $\lambda = 0.01\,\mathrm{m}$. Right: $\lambda = 0.001\,\mathrm{m}$. The symbol + marks the base state given by Table 5.2, and the symbol $*$ marks the base state given by Table 5.3.

Adding physical diffusion and surface tension changes the dispersion relations, as can be seen in Figure 5.4. Short wavelength perturbations are stabilized, while at long wavelengths, the dispersion relations are unchanged. The growth rate no longer tends to infinity for short wavelengths, removing the ill-posedness issue. In case only diffusion is added, the growth rate is bounded, but its value still increases rapidly at short wavelengths, which causes short wavelength perturbations to dominate the solution. In a numerical model, upon refining the grid, increasingly unstable scales are resolved, making it impossible to reach convergence [56].

When both physical diffusion and surface tension are added to the model, as suggested by Fullmer et al. [46], a cut-off wavelength is introduced below which perturbations are damped, as can be seen in Figure 5.4 at approximately $\lambda_c = 0.0174\,\mathrm{m}$. This removes the unphysical short wavelength instabilities. Meanwhile, the long wavelength instabilities, which are physical instabilities that are an integral part of the model, can still be resolved dynamically. The removal of the severe short wavelength instabilities means that the impediment to grid convergence is removed, and implies that theoretically all dynamics could be resolved without refining past $\Delta s = \lambda_c/2$. The combination of physical diffusion and surface tension is crucial to achieving the damping effect: with only surface tension the short wavelengths are nearly neutrally stable, with only the shortest wavelengths being very weakly damped, due to the influence of friction.

The cut-off wavelength depends on the state and model parameters. As the difference between the velocities of the two fluids is increased further into the region of instability beyond the IKH limit, the cut-off wavelength is decreased. This is apparent from comparing the stability maps for different wavelengths in Figure 5.5. The marked states in the maps are unstable (with bounded growth rates) to long wavelength perturbations, but stable for short wavelengths, as shown in Figure 5.4. For each possible state there will always be a cut-off wavelength below which damping takes place. Therefore, the extended model is unconditionally well-posed.

This method of regularization leaves intermediate scale perturbations intact that might lie outside of the range of validity of the model dictated by the long-wavelength assumption. An alternative option is to also damp these scales, by using artificial diffusion, added to both the mass and momentum equations [14, 45, 56]. However, the fact that these scales are not modeled to complete accuracy does not mean that it is more accurate to artificially eliminate these perturbations. Our approach is to leave these perturbations intact, for as far as they are not stabilized by physically motivated model components.

Depending on the state, the cut-off wavelength may become quite low and the instability quite severe. For such an unstable state, the solution will be dominated by intermediate scale instabilities, that lie above the cut-off wavelength, but are still of very short wavelength. Practically, the grid resolution required to reach the cut-off wavelength may be prohibitive. Therefore, in engineering applications, it may not be possible to resolve all the dynamics of the model in a numerical simulation. This does not affect the linear well-posedness: if the small scales are not resolved, they will cause no harm, and if they are resolved, they will be regularized by diffusion and surface tension.

The longer scale instabilities that remain present in our extended model have bounded growth rates, but would grow indefinitely, according to the linear stability analysis. In reality, when the perturbations grow large, the assumptions made in the linearization

of the model become invalid, and the behavior of the full model will depart from the behavior of the linearized model. At this point, the nonlinear stability of the model must be considered [76]. Nonlinear effects can bound perturbations that grow initially due to linear instability. Typically, the unstable perturbations develop into shocks, which must be bounded by a dissipative mechanism. In section 5.5.4 we show numerically that physical diffusion plays a crucial role in the nonlinear damping of linear instabilities that develop into shocks. At coarse grid resolutions, this role is taken over by numerical diffusion.

An analytical indication of a form of nonlinear stability, which the model should satisfy even when it is linearly unstable, is given by the energy conservation property. The extended local energy, given by (5.12), can be written in the following primitive form for the 2D channel geometry:

$$e_{\text{ch}} = \frac{1}{2}\rho_U g_n H_U^2 + \rho_U g_n H_U H_L + \frac{1}{2}\rho_L g_n H_L^2 + \frac{1}{2}\rho_U u_U^2 H_U + \frac{1}{2}\rho_L u_L^2 H_L + \rho_U g y H_U + \rho_L g y H_L + \sigma\left(1 + \frac{1}{2}\left(\frac{\partial H_L}{\partial s}\right)^2\right). \quad (5.67)$$

Since H_U and H_L must be positive, each term in this expression is positive. Therefore the global energy equation (5.15) implies a bound on the velocities, the heights, and their spatial derivatives. A numerical model that conserves (or strictly dissipates) this energy can be expected to have solutions that are bounded in this way.

In conclusion, the extended model linearly damps short wavelength perturbations, nonlinearly damps unstable long wavelength perturbations when they grow large, and possesses an energy bound. These properties are achieved by adding only physically derived terms to the basic model (physical diffusion, friction, and surface tension). The end result is a reliable model that can be expected to handle difficult flow states, while still resolving physical instabilities.

5.5 Numerical experiments

5.5.1 Introduction

In this section, the energy stability and well-posedness properties of our new framework are demonstrated through three different numerical experiments. These were conducted using a code based on the spatial discretizations given in section 5.3. The numerical experiments consider a 2D channel geometry, for which the basic discretization described in section 5.3.1 and the surface tension discretization described in section 5.3.6 are exactly energy-conserving.

For the time integration we use the fourth order constraint-consistent Runge-Kutta method described by Sanderse and Veldman [107]. This method is explicit for the mass and momentum equations and implicit for the pressure, requiring the solution of a pressure Poisson equation. It requires the mass and momentum equations to be coupled as has been done by setting the fluxes in the mass equations according to (5.37).

First, in section 5.5.2 we consider a traveling wave solution to the basic TFM without diffusion or surface tension. We show that our novel energy-stable advective flux (described in section 5.3.8) yields smooth solutions without excessive numerical diffusion

or numerical oscillations. We compare this flux to our original energy-conserving flux (described in section 5.3.1) and to our strictly dissipative upwind flux (described in section 5.3.7). Additionally, we compare these to a naive central scheme which is neither energy-conserving nor strictly dissipative.

In section 5.5.3 we repeat the traveling wave case, but with surface tension added according to section 5.3.6. We show that this addition is energy-conserving, as predicted by the analysis.

Last, in section 5.5.4 we consider an unstable perturbation to a shear flow base state that would be ill-posed for the basic TFM. We demonstrate that the complete new framework with friction, diffusion, surface tension, and the energy-stable advective flux, is able to obtain solutions that converge with increasing grid resolution, for this challenging test case. We quantify the contributions of numerical diffusion, physical diffusion and friction to the nonlinear damping by computing the dissipation, using our derived expressions for the dissipation rates.

5.5.2 Traveling wave with the basic model and different schemes

We conduct a test case with a traveling wave, induced as a perturbation upon a uniform base state, for the basic model without diffusion, friction, or surface tension. The base state is given in Table 5.4, and the flow parameters are those of Table 5.1. The perturbation is defined according to the analysis in section 5.B. It is the initial condition for the exact solution to the linearized system, for one of the two modes $\omega(k)$. We set the wavelength of the perturbation to $\lambda = 0.1\,\mathrm{m}$, and select the wave mode $\omega = 39.89\,\mathrm{s}^{-1}$ (the other option is $\omega = 22.94\,\mathrm{s}^{-1}$ and would yield a slower wave). The perturbation is then limited to the range between $s_{\mathrm{pert}} - \lambda/2$ and $s_{\mathrm{pert}} + \lambda/2$, with $s_{\mathrm{pert}} = 2\lambda + \lambda/4$. Outside of this range the base state is kept. The computational domain has length $L = 0.5$ and has periodic boundaries. A pressure projection step is performed on the complete initial condition, adjusting the velocities to ensure that the volumetric flow constraint is satisfied (see [107]).

Table 5.4: Base state for the traveling wave case.

Variable	Symbol	Value	Units
Initial lower fluid hold-up	$\alpha_{L,0}$	0.5	–
Initial lower fluid velocity	$u_{L,0}$	0.5	$\mathrm{m\,s^{-1}}$
Initial upper fluid velocity	$u_{U,0}$	0.5	$\mathrm{m\,s^{-1}}$

The exact solution of the linearized model is a wave traveling to the right without deformation. The solution to the full nonlinear model, using the energy-stable advective flux described in section 5.3.8, is shown in Figure 5.6. We show the hold-up $\alpha_L = A_L/A$ and the upper fluid velocity u_U. The wave travels to the right at constant velocity, with little deformation. At $t = 3.15\,\mathrm{s}$ and $t = 6.30\,\mathrm{s}$, the wave has traveled through the domain an integer number of times (4 and 8 times respectively), and the wave can be compared to the initial perturbation. In the middle of the wave, a slight steepening has taken place, tending towards the formation of a discontinuity. At the edges, the wave has diffused slightly.

In Figure 5.7, we compare results for this test case, using different discretizations of the advective flux in the momentum equations. We compare the energy-stable scheme

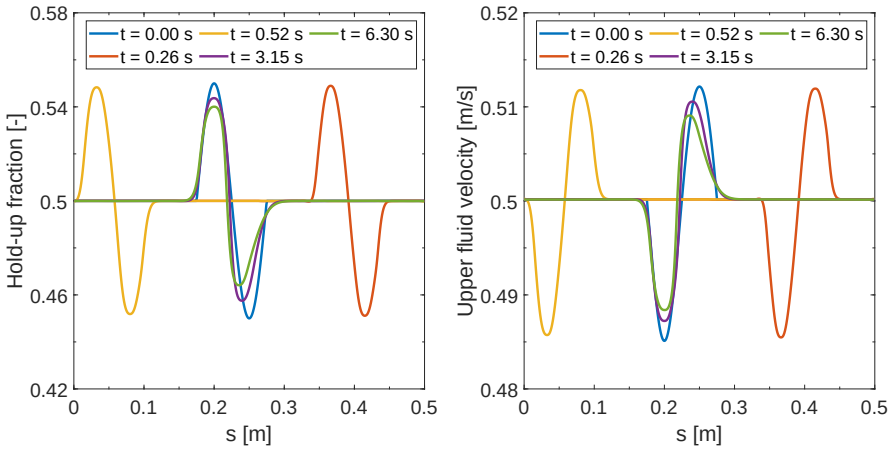

Figure 5.6: Two components of the solution to the traveling wave case for the basic model, using the energy-stable advective flux described in section 5.3.8, with $\Delta s = 10^{-3}$ m and $\Delta t = 10^{-4}$ s.

5

given by (5.64), the upwind scheme given by (5.61), the energy-conserving scheme given in (5.37), and a naive central interpolation scheme in which the momentum advection fluxes are given by

$$f_{3,a,i-1,\text{cen}} = \left[\overline{\left(\frac{q_{3,i-1}}{\overline{q}_{1,i-1}}\right)}\right]^2 \frac{q_{1,i-1}}{\Delta s} = \rho_U \left(\overline{u}_{U,i-1}\right)^2 A_{U,i-1},$$

$$f_{4,a,i-1,\text{cen}} = \left[\overline{\left(\frac{q_{4,i-1}}{\overline{q}_{2,i-1}}\right)}\right]^2 \frac{q_{2,i-1}}{\Delta s} = \rho_L \left(\overline{u}_{L,i-1}\right)^2 A_{L,i-1}.$$

A high-resolution solution ($\Delta s = 1.25 \cdot 10^{-4}$ m and $\Delta t = 1.25 \cdot 10^{-5}$ s), obtained using the energy-stable scheme, is used as a reference. The results show that the central and energy-conserving schemes produce numerical oscillations in the presence of strong gradients, while the upwind scheme is excessively diffusive. The proposed energy-stable scheme yields the most accurate solution, without numerical oscillations and with much less diffusion than the upwind scheme.

This behavior can be understood from the perspective of the (global) energy, of which Figure 5.7 shows the absolute and nondimensional difference with respect to the initial condition. The energy-conserving scheme conserves energy up to a very small time integration error. The energy-stable and upwind schemes lose energy with respect to the initial condition, while the central scheme gains energy (this is not visible since only the absolute difference is plotted). The energy-stable scheme is less dissipative than the upwind scheme, which is reflected in its less diffused solution. Some dissipation is physically necessary near strong gradients or discontinuities, and the lack of this in the central and energy-conserving schemes can be understood to lead to numerical oscillations.

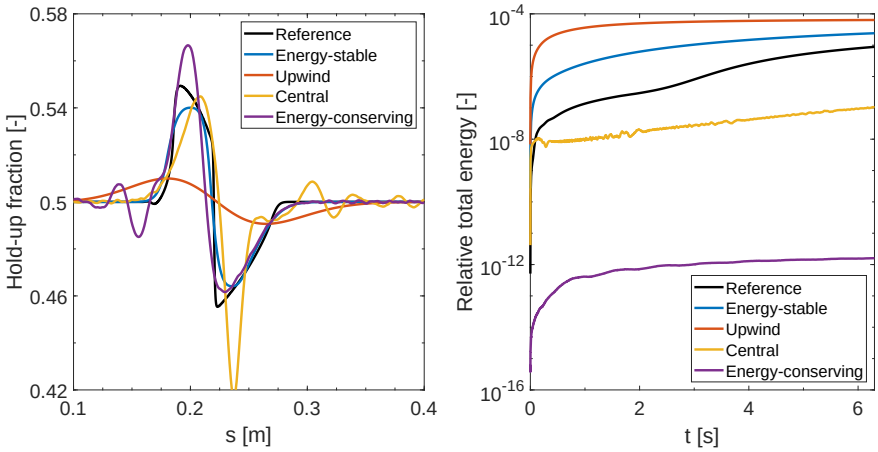

Figure 5.7: Comparison of results of the traveling wave case for the basic model, using different advective flux discretizations. In all cases, $\Delta s = 10^{-3}$ m and $\Delta t = 10^{-4}$ s. The reference is a high-resolution solution ($\Delta s = 1.25 \cdot 10^{-4}$ m and $\Delta t = 1.25 \cdot 10^{-5}$ s) obtained using the energy-stable scheme. Left: the solution for the hold-up at time $t = 6.3$ s. Right: the absolute difference between the energy as a function of time and the initial energy, divided by the initial energy.

5

5.5.3 Traveling wave with surface tension

Adding surface tension to the basic model yields a model that is still energy-conserving, but for the modified energy $e = e_b + e_s$. We repeat the previous case with this model. We test the surface tension implementation described in section 5.3.6 with the energy-conserving advective flux to show that the addition is energy-conserving. We also test the surface tension implementation with the energy-stable flux and show that practically this yields the best results.

The addition of surface tension results in a different angular frequency of $\omega = 40.19\,\mathrm{s}^{-1}$, for $\lambda = 0.1$ m (the other mode is $\omega = 22.64\,\mathrm{s}^{-1}$). The solution at various points in time is shown in Figure 5.8. Due to the slightly increased wave speed, the snapshots at $t = 3.13$ s and 6.25 s are now the points at which the wave has traveled through the domain 4 and 8 times respectively. The addition of surface tension has a dispersive effect: the traveling wave spreads out into smaller oscillations, which are not of numerical origin. This can be determined from the fact that they do not vanish upon grid refinement.

Figure 5.9 shows energy and convergence results using the energy-conserving advective flux. Using the energy-conserving advective flux makes it possible to isolate the effect of the surface tension implementation on the (global) energy. The figure shows how the total energy remains constant in time. This confirms our theoretical analysis: the surface tension implementation is indeed energy-conserving. The different components of the energy (potential, kinetic, and surface energy) are free to increase or decrease, exchanging with one another. The magnitude of the exchange is small.

Figure 5.10 shows energy and convergence results using the energy-stable advective flux. Using this flux, the total energy is not conserved, but decreases monotonically, as discussed in section 5.5.2. A comparison between the right plots of Figure 5.9 and Fig-

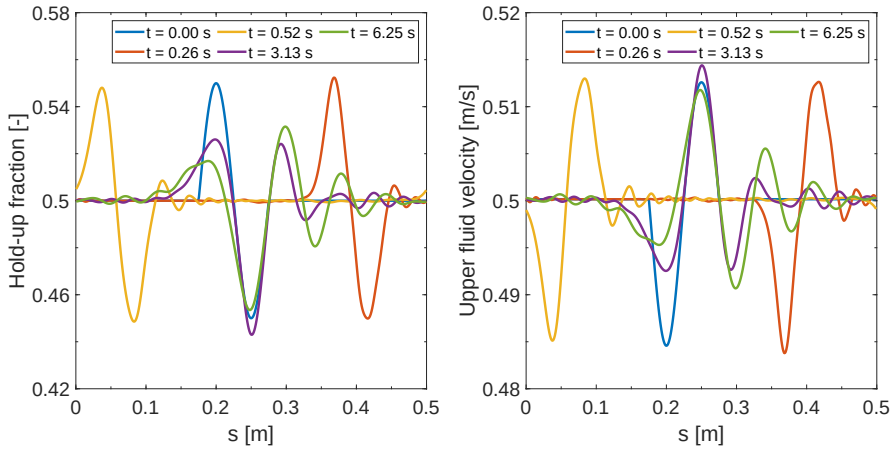

Figure 5.8: Two components of the solution to the traveling wave case for the basic model plus surface tension, using the energy-stable advective flux, with $\Delta s = 10^{-3}$ m and $\Delta t = 10^{-4}$ s.

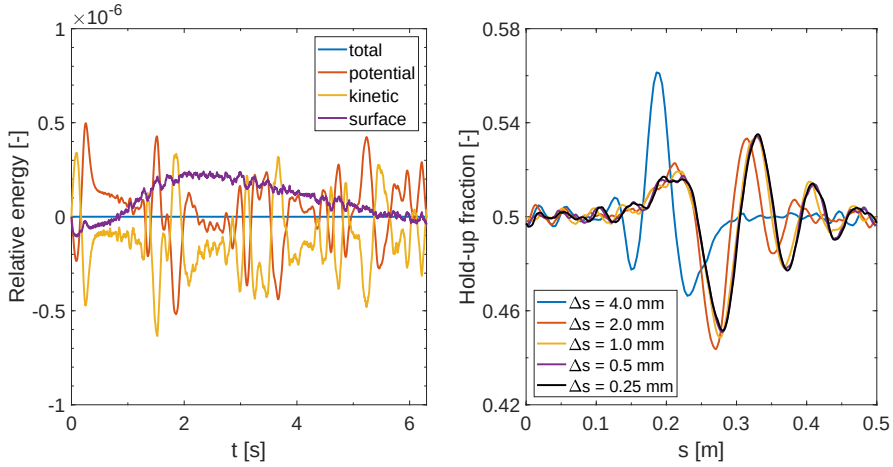

Figure 5.9: Results for the traveling wave case with surface tension, using the energy-conserving advective flux. Left: components of the energy of the solution, with $\Delta s = 10^{-3}$ m and $\Delta t = 10^{-4}$ s. Right: convergence of the hold-up at time $t = 6.3$ s, with a constant ratio $\Delta t/\Delta s = 0.1$ s/m.

ure 5.10 shows that this comes with the advantages of smoother convergence and absence of numerical oscillations. Therefore the energy-stable flux is favored, in combination with the energy-conserving surface tension discretization.

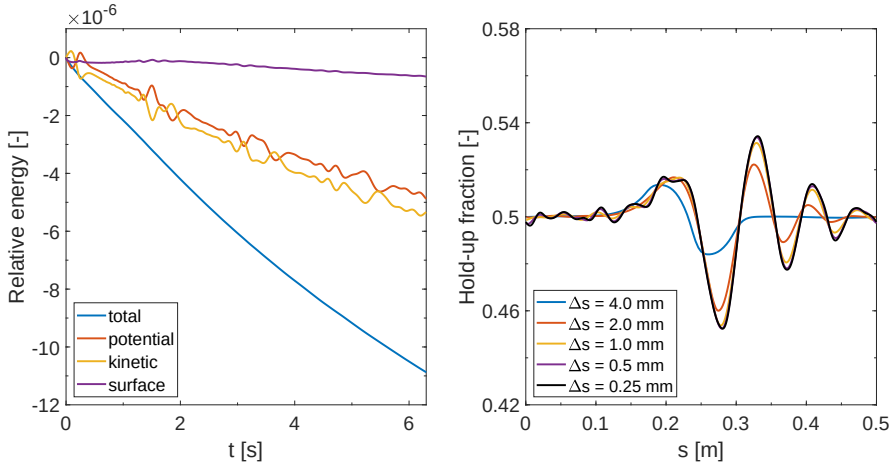

Figure 5.10: Results for the traveling wave case with surface tension, using the energy-stable advective flux. Left: components of the energy of the solution, with $\Delta s = 10^{-3}$ m and $\Delta t = 10^{-4}$ s. Right: convergence of the hold-up at time $t = 6.3$ s, with a constant ratio $\Delta t/\Delta s = 0.1$ s/m.

5.5.4 Shock formation and dissipation in unstable region

In this test case we test our complete proposed framework, with all physical effects and the energy-stable advective flux, on a challenging case involving the rapid growth of a perturbation and development into a shock. The flow is in the region of state space where the basic model is ill-posed: it is marked with the symbol $*$ in the stability maps of section 5.4. However, with our extended model we are able to obtain good convergence and a well-resolved shock.

This test case is inspired by a case from [46], which is in turn derived from [56]. The boundaries are periodic, the flow parameters are given by Table 5.1, and the base state is given by Table 5.3. This base state is altered by a single-period sinusoidal perturbation in the hold-up (with wavelength $\lambda = 0.1$ m and amplitude $\Delta\alpha_L = 0.05$), which determines the initial conditions for q_1 and q_2. The velocities are not explicitly perturbed. Instead, a pressure projection step is performed on the base state plus perturbed hold-up. The projection step perturbs the velocities such that the volumetric flow constraint is satisfied, yielding the initial conditions for q_3 and q_4. Two components of the resulting initial condition (expressed in primitive variables) can be seen in Figure 5.11, along with the evolution of the wave in time. The main difference between this case and the case from [46] is that we add wall and interface friction, so that all sources of dissipation are included in the numerical experiment. The friction is balanced by a driving pressure gradient, with a (constant) value given by Table 5.3, so that the base state is a steady state (see section 5.4). Without the external forcing provided by a driving pressure gradient, the initial perturbation would quickly die out.

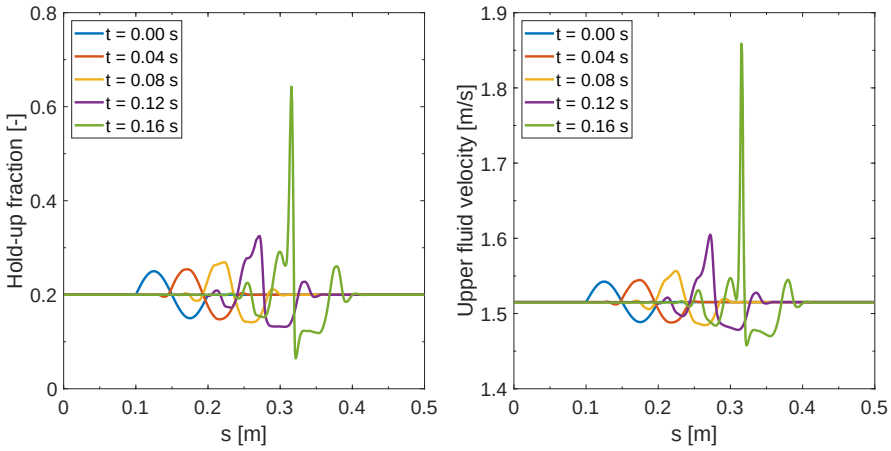

Figure 5.11: Initial condition, and solution over time, for two components of the solution to the unstable shock formation case. Using the energy-stable advective flux, with $\Delta s = 10^{-3}$ m and $\Delta t = 10^{-4}$ s.

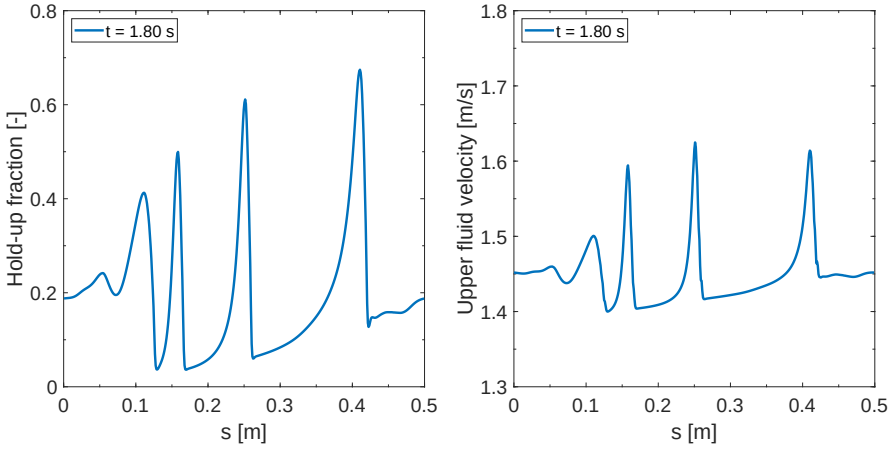

Figure 5.12: Snapshot of two components of the solution to the unstable shock formation case, at time $t = 1.8$ s. Using the energy-stable advective flux, with $\Delta s = 10^{-3}$ m and $\Delta t = 10^{-4}$ s. This figure shows how after the rapid growth depicted in Figure 5.11, the shock breaks up into several roll waves that remain of limited amplitude.

While the basic model possesses an unbounded short wave growth rate for these flow conditions, the extended model damps short wavelength perturbations (see Figure 5.4). The wavelength of the perturbation considered here is still unstable, and indeed the perturbation is observed to grow rapidly in Figure 5.11. Fortunately, as predicted by the linear stability analysis, it grows at a finite rate, and is not dominated by extreme short wavelength instabilities. Finally, after developing into a shock its growth is stopped by nonlinear effects. After this point, secondary perturbations will start to grow, which will continue traveling to the right, through the periodic boundary, to reappear on the left side of the domain. The secondary perturbations also form discontinuities and remain bounded in the same manner as the primary perturbation. Eventually, at much later time, a sequence of roll waves is observed, as shown in Figure 5.12.

The global dissipation as a function of time is shown in Figure 5.13. Here the dissipated energy is calculated using the expressions for the local dissipation – $\epsilon_{d,i-1/2}$, $\epsilon_{f,i-1/2}$, $\epsilon_{n,i-1/2}$ – and the expression for energy production due to a driving pressure gradient – $c_{p,i-1/2}$. These expressions are summed over the domain and integrated in time (numerically) according to (5.49), and their sum yields the total dissipated energy. Since the initial base state is uniform, it has no (physical or numerical) diffusion, but it does have high dissipation due to friction which is balanced by an energy input from the driving pressure gradient. These base state dissipation and production terms have been subtracted so that friction and the driving pressure gradient do not dominate the plot.

In the second plot of Figure 5.13, the instantaneous energy is calculated using the expression for $e_{i-1/2}$, summed over the domain to yield the global energy. The left and right plots of Figure 5.13 show the same decrease in total energy, confirming that the two methods of calculation are consistent.

Figure 5.13 reveals exactly how nonlinear effects bound the amplitude of the shock. The respective contributions of the physical and numerical diffusion to the nonlinear damping can now be quantified, by examining their effect on the energy of the solution. The figure shows that as the shock develops, the physical and numerical diffusion and their resulting dissipation grow large, and decrease the energy of the solution. They act to decrease the kinetic energy of the solution, allowing the potential and surface energy to grow slightly. We note that a calculation of the local dissipation shows the dissipation to be localized around the shock.

The dissipation due to friction also grows with time, but less dramatically, since it is proportional to the size of the wave, not to its steepness. It has a smaller stabilizing effect. Regarding the driving pressure gradient, the energy input remains roughly constant, since it is not dependent on the perturbation but only on the volumetric flow rate, which is a property of the complete flow. Its negative value at $t = 0.16\,\mathrm{s}$ means that the energy input is slightly lower than it was for the initial base state, since the volumetric flow rate has decreased slightly, indicating that the flow has been slowed down slightly.

Figure 5.14 shows how the solution converges with grid resolution, confirming that the extended model is well-posed, as discussed in section 5.4. Also shown in Figure 5.14 is the convergence of the dissipation, divided into its different components. As the grid is refined, the small scales at which the physical diffusion acts are better resolved, allowing the corresponding dissipation to grow and converge to its full physical effect. In contrast, beyond a certain resolution before which the solution is relatively smooth, the numerical

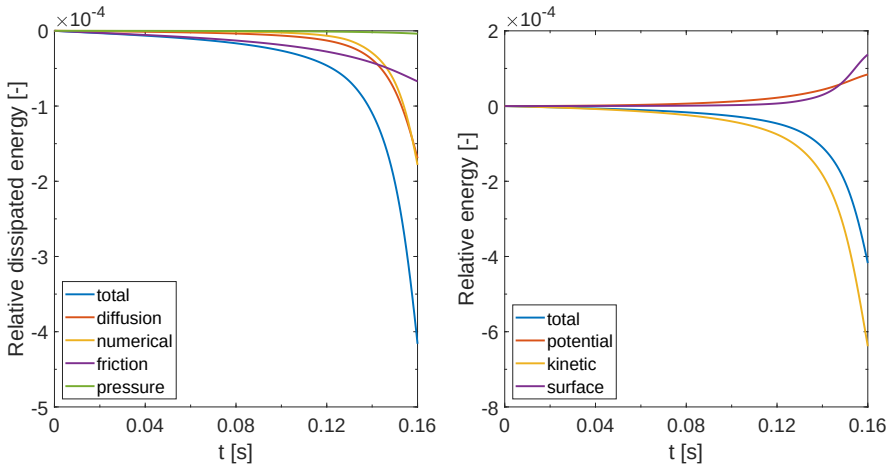

Figure 5.13: For the unstable shock formation case, this figure shows the dissipated energy (left) and the instantaneous energy (right), made non-dimensional by the total energy of the initial condition. Using the energy-stable advective flux, with $\Delta s = 10^{-3}$ m and $\Delta t = 10^{-4}$ s. The total dissipation is divided into contributions from physical diffusion, numerical diffusion, wall and interface friction, and a production term due to an externally applied driving pressure gradient.

dissipation decreases with grid resolution. Only at coarse resolutions, numerical dissipation is needed to compensate for the lack of physical dissipation. Dissipation due to friction only varies slightly with grid resolution, since it is not a small scale phenomenon.

Previous work has described how the linearly unstable wave is bounded by (nonlinear) dissipation in the shock, due to numerical and physical diffusion [46]. However, up to now, dissipation has remained an abstract concept for the TFM. Here we provide definitions for the various components of the dissipation, and specify their effect on a well-defined energy. Therefore, dissipation has become a concrete quantity that can be measured. This provides a stronger basis for discussions of the nonlinear damping of unstable waves. We confirm the conclusions of Fullmer et al. [46], who observe that with only numerical diffusion, the solution fails to converge (with oscillations appearing at high resolutions), due to the lack of numerical diffusion at high grid resolutions. We similarly observe (results not shown here) that physical diffusion without numerical diffusion leads to a less clear convergence, with coarse grid solutions being insufficiently diffused. With Figure 5.14 we have made concrete that with a combination of numerical and physical diffusion, the dissipation in the shock smoothly converges to a finite value, realizing a grid-independent bound on the amplitude of the shock.

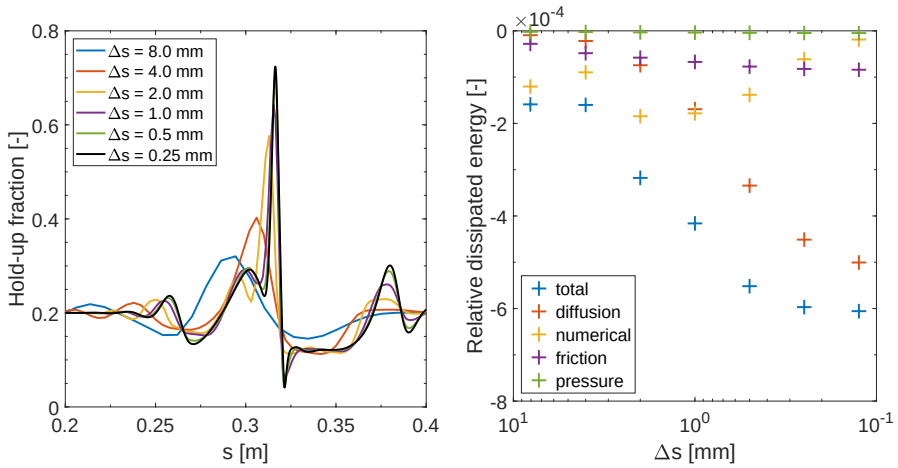

Figure 5.14: For the unstable shock formation case, this figure shows the convergence with grid resolution, of the solution at time $t = 0.16$ s. Using the energy-stable advective flux, with a constant ratio $\Delta t/\Delta s = 0.1$ s/m. Left: hold-up fraction $\alpha_L = A_L/A$. Right: dissipated energy, divided by the total energy of the initial condition.

5

5.6 Conclusions

This chapter has proposed a complete energy-stable framework – including diffusion, friction, surface tension, and an energy-stable advective flux scheme – for reliable simulations with the one-dimensional two-fluid model (TFM). The chapter builds on our earlier work on the energy-conserving basic TFM, which we have extended in an energy-consistent manner. We have shown that for the channel geometry, surface tension can be added to the model in an energy-conserving manner. The additions of friction and momentum diffusion have been shown to be strictly dissipative. Therefore, these extensions yield an energy-stable model.

Besides their implications for energy stability, the additions to the model also solve the basic model's issue of unbounded linear instability at short wavelengths: diffusion and surface tension introduce a cut-off wavelength below which perturbations are damped. The cut-off wavelength is shown to depend on the state: it decreases with increasing velocity difference between the phases. Nevertheless, there exists a cut-off wavelength for any state, rendering the model unconditionally well-posed. These cut-off wavelengths may be shorter than the scales at which the TFM is usually employed, but it is these scales at which the ill-posedness issue of the one-dimensional model resides and it is these scales which need to be stabilized. Diffusion and surface tension offer a clearly physically motivated way to do so. Precisely because diffusion and surface tension are physically motivated, they fit well into our energy-stable framework.

The energy conservation and dissipation properties of the model have been proven to carry over to the semi-discrete model, when the model and its energy are discretized in a specific manner. The semi-discrete model with surface tension is exactly energy-conserving, if the surface energy is added to the basic energy as an extra term. Diffusion and friction add strictly dissipative terms to the local energy conservation equation, with expressions for the dissipation rates that can be evaluated as functions of the local instan-

taneous solution.

However, the key highlight of our semi-discrete model is a new discretization of the advective terms, which combines a previously developed energy-conserving central discretization and a strictly dissipative upwind discretization. These discretizations are combined using flux limiters. The novel combined advective flux is energy stable, and comes with an explicit expression for the numerical dissipation rate, that can be evaluated during a numerical simulation. It is designed to be energy-conserving where the solution is smooth, and dissipative where the solution has strong gradients. This dissipation is motivated by the fact that the energy conservation property of the continuous model does not hold for discontinuous solutions: dissipation is required in this case. The novel energy-stable flux retains the advantages in stability and physical fidelity of the original energy-conserving flux, without the latter's tendency to generate numerical oscillations near discontinuities.

In numerical experiments, spatially exact energy conservation is demonstrated for the basic model extended with surface tension, using the original energy-conserving flux. The upwind and energy-stable advective fluxes are demonstrated to be strictly dissipative, as opposed to a naive central discretization that is neither conservative nor strictly dissipative. The energy-stable scheme is shown to yield smooth solutions without numerical oscillations. It is much less diffusive than a first-order upwind scheme, and this is reflected in the dissipation, which is lower for the energy-stable scheme than for the upwind scheme.

A challenging test of our complete framework is provided by the simulation of an unstable wave in a region of state space where the basic model is linearly ill-posed. Our proposed framework yields a convergent solution, confirming that it is well-posed. The unstable perturbation develops into a shock, which is bounded by nonlinear dissipation. The analytical results of this work enable a precise analysis of the dissipation and better insight into the nonlinear damping taking place. The dissipation due to numerical and physical diffusion are observed to grow as the wave steepens, with numerical dissipation dominating at coarse resolutions and physical dissipation dominating at fine resolutions. Together, numerical and physical diffusion yield a smoothly converging total dissipation, and a smoothly converging solution.

In order to resolve the full effect of the physical diffusion and surface tension and reach convergence, the grid needs to be refined to high resolutions that may be impractical in engineering applications. When the additional computational expense associated with high resolutions is unwanted, our model has the advantage that it can also be used at coarse resolutions, where it provides solutions that are similar to the converged solutions, except that sharp perturbations are diffused. The convergence plots show a monotonic steepening of the waves, without spurious oscillations.

Though the semi-discrete computational model proposed in this chapter is by itself no more computationally expensive than standard discretizations of the basic model, the inclusion of surface tension does place an additional restriction on the time step set in the explicit time integration method. For the basic model the time step only has to satisfy a CFL condition, giving the time step a bound that scales linearly with grid resolution. The addition of surface tension results in a higher order restriction, with an exponent between 1 and 2. Therefore, the addition of surface tension increases the computational effort required for the fully discrete computational model, particularly at higher grid resolutions.

Appendix

5.A Friction closure relations

The wall and interface stresses of the two-fluid model are typically modeled in the following manner [116]:

$$\tau_L = -\frac{1}{2} f_L \rho_L u_L |u_L|, \quad \tau_U = -\frac{1}{2} f_U \rho_U u_U |u_U|, \quad \tau_{\text{int}} = -\frac{1}{2} f_{\text{int}} \rho_U (u_U - u_L)|u_U - u_L|,$$

in which f_L, f_U, and f_{int} are the Fanning friction factors, which require further closure relations. The friction factors depend on the Reynolds numbers

$$\text{Re}_L = \frac{|u_L| D_L}{\nu_{m,L}}, \qquad \text{Re}_U = \frac{|u_U| D_U}{\nu_{m,U}},$$

with hydraulic diameters

$$D_L = \frac{4A_L}{P_L}, \qquad D_U = \frac{4A_U}{P_U + P_{\text{int}}}.$$

In this work we use the Taitel and Dukler friction model [5, 116]

$$f_L = \frac{C}{\text{Re}_L^n}, \qquad f_U = \frac{C}{\text{Re}_U^n}, \qquad f_{\text{int}} = \max\left(f_U, 0.014\right),$$

with coefficients $C = 0.046$ and $n = 0.2$ (valid for turbulent flow).

5.B Linear stability analysis

We conduct a linear stability analysis of the (continuous) model, following [46, 74, 76]. The analysis starts by writing (5.10) in quasilinear matrix form, which can be done by substituting the volume constraint and assuming the solution is smooth:

$$\mathbf{A}(\mathbf{w})\frac{\partial \mathbf{w}}{\partial t} + \mathbf{B}(\mathbf{w})\frac{\partial \mathbf{w}}{\partial s} + \mathbf{E}(\mathbf{w})\frac{\partial^2 \mathbf{w}}{\partial s^2} + \mathbf{G}(\mathbf{w})\frac{\partial^3 \mathbf{w}}{\partial s^3} = \mathbf{c}(\mathbf{w}), \tag{5.68}$$

with

$$\mathbf{w} = \begin{bmatrix} w_1 \\ w_2 \\ w_3 \\ w_4 \end{bmatrix} = \begin{bmatrix} A_L \\ u_L \\ u_U \\ p \end{bmatrix}, \qquad \mathbf{A} = \begin{bmatrix} 1 & 0 & 0 & 0 \\ -1 & 0 & 0 & 0 \\ 0 & 1 & 0 & 0 \\ 0 & 0 & 1 & 0 \end{bmatrix},$$

$$\mathbf{B} = \begin{bmatrix} w_2 & w_1 & 0 & 0 \\ -w_3 & 0 & A - w_1 & 0 \\ -\frac{g_n}{w_1}\frac{\mathrm{d}\widehat{H}_L}{\mathrm{d}A_L} & w_2 - \frac{1}{w_1}\frac{\partial}{\partial s}\left(\nu_{\text{eff},L} w_1\right) & 0 & 1/\rho_L \\ \frac{g_n}{A - w_1}\frac{\mathrm{d}\widehat{H}_U}{\mathrm{d}A_U} & 0 & w_3 - \frac{1}{A - w_1}\frac{\partial}{\partial s}\left(\nu_{\text{eff},U}(A - w_1)\right) & 1/\rho_U \end{bmatrix},$$

$$\mathbf{c} = \begin{bmatrix} 0 \\ 0 \\ -\frac{1}{\rho_L}\frac{\partial p_{\text{body}}}{\partial s} + \frac{\tau_L P_L}{\rho_L w_1} - \frac{\tau_{\text{int}} P_{\text{int}}}{\rho_L w_1} - g_s \\ -\frac{1}{\rho_U}\frac{\partial p_{\text{body}}}{\partial s} + \frac{\tau_U P_U}{\rho_U (A - w_1)} + \frac{\tau_{\text{int}} P_{\text{int}}}{\rho_U (A - w_1)} - g_s \end{bmatrix},$$

$$\mathbf{E} = \begin{bmatrix} 0 & 0 & 0 & 0 \\ 0 & 0 & 0 & 0 \\ \frac{\sigma}{\rho_L}\frac{1}{P_{\text{int}}^2}\frac{\mathrm{d}P_{\text{int}}}{\mathrm{d}A_L}\frac{\partial w_1}{\partial s} & -\nu_{\text{eff},L} & 0 & 0 \\ 0 & 0 & -\nu_{\text{eff},U} & 0 \end{bmatrix}, \qquad \mathbf{G} = \begin{bmatrix} 0 & 0 & 0 & 0 \\ 0 & 0 & 0 & 0 \\ -\frac{\sigma}{\rho_L}\frac{1}{P_{\text{int}}} & 0 & 0 & 0 \\ 0 & 0 & 0 & 0 \end{bmatrix}.$$

Here we have used the second expression in (5.26) for the surface tension, which can be applied to both the 2D channel and the circular pipe geometries.

A general method for the linearization of systems of quasilinear partial differential equations is given by Prosperetti and Tryggvason [95]. The general solution is decomposed into $\mathbf{w} = \bar{\mathbf{w}} + \Delta\mathbf{w}$ with $\Delta\mathbf{w}$ a small disturbance ($\Delta\mathbf{w} \ll \bar{\mathbf{w}}$), and $\bar{\mathbf{w}}$ a base state that is itself also a solution to the equations. Additionally, we assume that the base state is a uniform steady state (its derivatives to s and to t are zero). Then, neglecting terms that are higher order in $\Delta\mathbf{w}$, and subtracting the equation for the base state (which is satisfied by definition), a system of the form (5.68) can be approximated by

$$\mathbf{A}(\bar{\mathbf{w}})\frac{\partial \Delta\mathbf{w}}{\partial t} + \mathbf{B}(\bar{\mathbf{w}})\frac{\partial \Delta\mathbf{w}}{\partial s} + \mathbf{E}(\bar{\mathbf{w}})\frac{\partial^2 \Delta\mathbf{w}}{\partial s^2} + \mathbf{G}(\bar{\mathbf{w}})\frac{\partial^3 \Delta\mathbf{w}}{\partial s^3} = \mathbf{D}_C(\bar{\mathbf{w}})\Delta\mathbf{w}, \tag{5.69}$$

with

$$\mathbf{D}_C(\bar{\mathbf{w}}) = \frac{\partial \mathbf{c}(\bar{\mathbf{w}})}{\partial \bar{\mathbf{w}}}.$$

Here, $\mathbf{D}_C$ is a Jacobian matrix. Due to the assumption of the uniform base state, and the neglecting of higher order terms, the terms in $\mathbf{B}(\bar{\mathbf{w}})$ and $\mathbf{E}(\bar{\mathbf{w}})$ involving partial derivatives to s drop out.

We write $\Delta\mathbf{w}$ as a Fourier series and substitute an arbitrary Fourier mode

$$\Delta\mathbf{w} = \Delta\hat{\mathbf{w}} \exp\left[i(ks - \omega t)\right],$$

with $\Delta\hat{\mathbf{w}}$ the amplitude, k the wavenumber, and ω the angular frequency, into (5.69). This yields the following linear system [46]:

$$\left[-\omega\mathbf{A}(\bar{\mathbf{w}}) + k\mathbf{B}(\bar{\mathbf{w}}) + i\mathbf{D}(\bar{\mathbf{w}}) + ik^2\mathbf{E}(\bar{\mathbf{w}}) - k^3\mathbf{G}(\bar{\mathbf{w}})\right]\Delta\hat{\mathbf{w}} = \mathbf{0}. \tag{5.70}$$

For nontrivial solutions to exist, the determinant of the term between brackets must be zero, and solving for this yields two dispersion relations $\omega(k)$.

The perturbation amplitudes $\Delta\hat{\mathbf{w}}$ corresponding to the found dispersion relations can be found by substituting these in (5.70) and solving for $\Delta\hat{\mathbf{w}}$. This can be understood as, for each dispersion relation, finding the null space of the term between brackets in (5.70), which will consist of one vector. The associated phase angles can be calculated componentwise:

$$\boldsymbol{\theta} = \arctan\left[\mathrm{Im}(\Delta\hat{\mathbf{w}})/\mathrm{Re}(\Delta\hat{\mathbf{w}})\right],$$

where each component of $\boldsymbol{\theta}$ has a range $[-\pi, \pi]$ (use the four-quadrant inverse tangent).

This makes it possible to write the evolution in time of a perturbation as

$$\Delta \mathbf{w} = \sum_j \left| \Delta \hat{\mathbf{w}}_j \right| e^{\mathrm{Im}\{\omega_j\} t} \cos\left(ks - \mathrm{Re}\{\omega_j\} t + \boldsymbol{\theta}_j \right), \tag{5.71}$$

where we take the sum over the different solutions for ω for a given k, and the associated amplitude vectors. If a sinusoidal perturbation is initialized with a given wavenumber k, and an amplitude vector exactly corresponding to one of the two angular frequencies $\omega(k)$, then the sum in (5.71) can be left out and the perturbation will propagate as a single wave with speed $\mathrm{Re}\{\omega\}$ and growth rate $\mathrm{Im}\{\omega\}$. This holds exactly for the linearized system, but solutions to the full nonlinear system will deviate from this solution over time.

6

Conclusions and recommendations

This thesis has proposed computationally efficient, accurate, and nonlinearly stable numerical models and methods for the simulation of waves and instabilities in two-phase pipe flow. The one-dimensional incompressible two-fluid model (TFM) has been shown to satisfy a mechanical energy conservation equation, which offers a new perspective on the model's dynamics and stability. Spatial discretizations have been derived which preserve the energy behavior of the continuous model. The analysis and energy-consistent discretization have also been performed for a new pressure-free version of the TFM, with superior computational efficiency and numerical accuracy. The end result is a robust computational model that yields smoothly converging solutions under difficult conditions, such as the appearance of shocks and the existence of a large velocity difference between the two fluids.

6.1 Conclusions

The basic TFM for horizontal stratified flow, without source terms, was shown in chapter 3 to conserve the sum of the kinetic and potential energy of both fluids. From the mass and momentum conservation equations, a local conservation equation was derived for the mechanical energy, stating that locally the energy can only change due to an imbalance of the inflow and outflow of energy. In periodic or closed domains, this sums up to the statement that the global energy must remain constant. It was thus shown that energy is a secondary conserved quantity of the model, in addition to the primary conserved quantities of mass and momentum.

The derivation of the local energy conservation equation was formulated in such a way as to yield conditions for the momentum advection and level gradient flux terms to be energy-conserving. These were used in the semi-discrete setting, along with the demand that the mass advection fluxes yield a strong pressure-velocity coupling, to derive energy-conserving numerical fluxes in a constructive manner. The thus obtained numerical advective fluxes are energy-conserving for general cross-sectional shapes such as the circular pipe or the 2D channel. Generally energy-conserving expressions were also obtained for the level gradient fluxes, but these have a division by zero issue, and only reduce to a practical form for simple channel-like cross-sectional shapes. The pressure terms of

the discrete model, which are in non-conservative form, are shown to naturally conserve energy due to the use of a staggered grid. The staggered grid makes the choice of the discrete energy non-unique. However, it has been verified through local and global analysis that taking a natural alternative interpolation does not change the conclusions of the discrete energy analysis.

The energy analysis also naturally applies to the pressure-free two-fluid model (PFTFM), which is a model variant that can be directly derived from the original TFM. However, if an assumption is made that is inconsistent with the original model, this can invalidate the energy analysis. In the PFTFM, and also in similar models such as the fixed-flux model (FFM), there is a risk of making such an assumption, due to the need to explicitly set the volumetric flow rate. In chapter 4, we derive an expression for the volumetric flow rate such that the PFTFM retains the energy conservation property of the TFM. This is shown to yield a pressure-free model that is equivalent to the original TFM: any solution to the TFM also satisfies the PFTFM, and any solution to the PFTFM also satisfies the TFM. These results are obtained in both the continuous and semi-discrete settings.

The advantage of the PFTFM over the TFM is that the implicit constraints are removed, yielding a fully explicit model. In addition, our formulation of the PFTFM retains the conservative form of the equations (as needed for correct shock relations), in contrast to existing approaches in literature. The amended PFTFM offers the advantages of an explicit model, while still being completely consistent with the original TFM. The explicit nature of the model offers the concrete advantages of reduced computational cost and reduced numerical error, due to the elimination of the numerically delicate Poisson equation for the pressure.

The energy analysis of the basic model has been extended with several additional terms: streamwise gravity, physical diffusion, wall and interface friction, and surface tension. Physical diffusion and surface tension are short scale effects that are typically neglected in the TFM which primarily models long scale one-dimensional flow, but are included here for their important stabilizing influence. Each of the added terms has been shown to yield either an energy-conserving or a strictly dissipative contribution to the local conservation equation for the mechanical energy. A driving pressure gradient acts as an external source of energy to the flow. Regarding surface tension, a generally energy-conserving form was found, but this only reduced to a physically recognizable form for simple channel-like cross-sectional shapes. The energy and the additional terms were discretized in such a manner that the energy-conserving or energy-dissipating behavior of each term is retained in the numerical model. The result is an energy-stable numerical model, with an upper bound on the global energy.

Since each term in the expression for the energy is positive, the demand that the global energy cannot increase constrains the solution. It therefore can be considered to act as a nonlinear stability bound. The continuous equations naturally satisfy this bound, and the discrete equations will satisfy this bound when the energy-stable discretization is used. This bound still allows linear instability, and may allow significant variation of the solution: it is not as clear as the bound on the L^2 norm of the solution for the Navier-Stokes equations. Regarding linear stability, the higher order additions to the basic model cause short wavelength perturbations to be damped, removing the linear ill-posedness. Longer wavelength perturbations remain unstable, but with a bounded growth rate.

Besides additional physical terms, numerical diffusion has been added to the model through an energy-stable discretization of the advection terms in the momentum equations. This provides the required dissipation at non-smooth parts of the solution, when physical diffusion is absent or not sufficiently resolved (due to a coarse grid). Without any form of dissipation, numerical oscillations appear when the solution becomes discontinuous. With too much dissipation, as provided by a first order upwind discretization, the solution is overly diffused. With the novel energy-stable advective flux, formed as a combination of the energy-conserving advective flux and a strictly dissipative upwind flux, the right amount of dissipation is provided, yielding sharp solutions without oscillations.

In numerical simulations, we demonstrate that the discrete global energy is exactly conserved by the spatial discretization, with only a time integration error remaining. When dissipative terms are added to the model, or the energy-stable advective flux is used, the energy is shown to be strictly decreasing. With the results of the discrete energy analysis, we can measure the dissipation taking place in a numerical simulation, as a function of time and space. When unstable waves grow, they may form shocks, and we observe that this leads to a sharp increase in dissipation, particularly the dissipation attributable to physical and numerical diffusion. The shock is bounded by this dissipation, marking an end to the growth predicted by the linear stability analysis. Our energy analysis has yielded detailed insight into this nonlinear damping and the resulting nonlinear stability.

The final result is a robust computational model. It possesses a form of nonlinear stability, and is free of the linear ill-posedness of the basic model. It resolves shocks without spurious oscillations, and can handle highly unstable flow states. The model can be employed at coarse resolutions, for which short wave instabilities will not be resolved, or at fine resolutions, for which the model smoothly converges to a sharp solution. These properties are achieved through physically motivated additions to the model, and through enhancing the physical fidelity of the numerical model by making its energy conservation properties consistent with the continuous model.

6.2 Recommendations

This thesis has set up a basic framework for energy-stable simulations with the one-dimensional two-fluid model. It has been demonstrated in chapter 5 that the framework can be extended in a modular manner. Several extensions are still envisioned.

- The energy-stable framework of chapter 5 can naturally be applied to the PFTFM. This requires repeating the derivations of chapter 4 with the extended model.
- For simple channel-like cross-sectional shapes, clear and practical energy-consistent discretizations were obtained for all terms. But for a circular cross-sectional shape (i.e. a pipe), the level gradient and surface tension terms require further work to find energy-conserving discretizations that are both numerically robust and physically sound. The constructive derivations given in this thesis offer the possibility to try out different energy definitions and find the matching energy-conserving expression for the model term.
- In this thesis, we have focused on making the spatial discretization energy-conserving. Ideally, this would be supplemented by an energy-conserving time integration

method. For the Navier-Stokes equations energy-conserving time integration can be achieved for example by applying the implicit midpoint method [52]. This relies on the fact that the energy is a simple quadratic function of the solution. For the TFM, the energy is a complex nonlinear function of the solution, so that existing time integration methods such as implicit midpoint will not be energy-conserving, and a more complex method will be needed. It could perhaps be based on an energy-conserving time integration method for the related two-layer shallow water equations [15].

- For the TFM, unlike for the incompressible Navier-Stokes equations, the energy is not directly an L^2 norm of the solution. It might be possible to rewrite the model into a form with different dependent variables, such that the L^2 norm of these variables constitutes the energy. This has been done for the *compressible* Navier-Stokes equations, using so-called 'square-root variables' [101].

- An alternative approach to obtaining more rigorous nonlinear stability results is to attempt to show that the energy is a convex entropy function of the TFM. For the energy to be a convex entropy function, its Hessian with respect to the vector of dependent variables must be symmetric positive definite. We can attempt to obtain such a result by reformulating the energy and the model. For systems of hyperbolic conservation laws, the existence of a convex entropy function implies that the system is symmetrizable, and is tied to the existence of a global stability estimate [32, 85, 98, 114]. Initial work has been done to apply the theory of entropy stability to the two-layer shallow water equations, which like the TFM is a non-conservative system that may attain complex eigenvalues [15, 24].

- An important issue with applying the TFM to slug capturing is the handling of phase disappearance, which takes place when one of the two fluids locally fills the pipe or channel. Possible approaches include manipulating certain model terms so the volume fractions are limited to a certain range (not allowing them to become zero) [10], or explicitly truncating the volume fractions so they can not go below a certain threshold value [3]. Alternatively, the volume fraction can be allowed to go below the threshold value, upon which the model can be switched to a single phase flow model locally [67]. In a phase disappearance algorithm, special attention needs to be paid to retaining the conservation properties of the discrete model, which would be lost by simple truncation of the volume fraction. In order to combine well with the current work, a phase disappearance algorithm should not only conserve mass and momentum, but also the mechanical energy of the isothermal TFM.

- A final desired extension is to make our energy-conserving discretization applicable to non-uniform grids. This could improve computational efficiency, by allowing coarse grids to be used where the flow is smooth, and fine grids where the flow develops into shocks or slugs. In order to conserve energy on a non-uniform grid, the interpolations used in our discretization will need to be generalized in a specific manner, similar to the way it has been done for an energy-conserving discretization of the shallow water equations [122].

A

Geometric relations

We treat the model equations in a way that is general to arbitrary duct geometries, using general geometric quantities which can be substituted for expressions that are specific to certain duct cross-sectional shapes. The most important general geometric terms are the H-variables, of which we have three for each fluid: H_U, $\widehat{H}_U$, $\widetilde{H}_U$, H_L, $\widehat{H}_L$, $\widetilde{H}_L$. We use H (implying something like a height) for each of these variables because they are all functions only of A_U and A_L respectively, and these functions all depend only on the cross-sectional duct shape. They are all distinct though, and the relations between these geometric quantities (which hold for arbitrary geometries) are crucial to the results of this work. This appendix will give these geometric relations.

The equations are written in terms of the cross-sectional areas occupied by each fluid, which in general can be defined to be related to the interface height H_L via

$$A_L = \int_0^{H_L} w(h)\,\mathrm{d}h, \qquad A_U = \int_{H_L}^{H} w(h)\,\mathrm{d}h, \tag{A.1}$$

with h the vertical coordinate, and $w(h)$ the local duct width. Note that $w(H_L) = P_{\text{int}}$, where P_{int} is the (generalized) interface perimeter. The geometric quantities $\widehat{H}_L$ and $\widehat{H}_U$ which appear in the governing equations of the two-fluid model, also have general definitions:

$$\widehat{H}_L \coloneqq \int_0^{H_L} (h - H_L) w(h)\,\mathrm{d}h, \qquad \widehat{H}_U \coloneqq \int_{H_L}^{H} (h - H_L) w(h)\,\mathrm{d}h. \tag{A.2}$$

Besides $\widehat{H}_L$ and $\widehat{H}_U$, the following geometric quantities are used in the energy definition:

$$\widetilde{H}_L \coloneqq \int_0^{H_L} h\, w(h)\,\mathrm{d}h = \widehat{H}_L + H_L A_L, \qquad \widetilde{H}_U \coloneqq \int_{H_L}^{H} h\, w(h)\,\mathrm{d}h = \widehat{H}_U + (H - H_U) A_U. \tag{A.3}$$

In order to calculate derivatives of these quantities, we need to use the Leibniz integral rule:

$$\frac{d}{dx}\left(\int_{a(x)}^{b(x)} f(x,t)\,dt\right) = f\big(x,b(x)\big)\cdot\frac{d}{dx}b(x) - f\big(x,a(x)\big)\cdot\frac{d}{dx}a(x) + \int_{a(x)}^{b(x)}\frac{\partial}{\partial x}f(x,t)\,dt.$$

This rule can be applied to (A.1), yielding

$$\begin{aligned}\frac{\mathrm{d}A_L}{\mathrm{d}H_L} &= \frac{\mathrm{d}}{\mathrm{d}H_L}\int_0^{H_L} w(h)\,\mathrm{d}h \\ &= w(H_L)\frac{\mathrm{d}H_L}{\mathrm{d}H_L} - w(0)\frac{\mathrm{d}0}{\mathrm{d}H_L} + \int_0^{H_L}\frac{\mathrm{d}w(h)}{\mathrm{d}H_L}\,\mathrm{d}h \\ &= w(H_L)\frac{\mathrm{d}H_L}{\mathrm{d}H_L} = P_{\mathrm{int}},\end{aligned}$$

$$\begin{aligned}\frac{\mathrm{d}A_U}{\mathrm{d}H_U} &= \frac{\mathrm{d}}{\mathrm{d}H_U}\int_{H_L}^{H} w(h)\,\mathrm{d}h \\ &= w(H)\frac{\mathrm{d}H}{\mathrm{d}H_U} - w(H_L)\frac{\mathrm{d}H_L}{\mathrm{d}H_U} + \int_{H_L}^{H}\frac{\mathrm{d}w(h)}{\mathrm{d}H_U}\,\mathrm{d}h \\ &= -w(H_L)\frac{\mathrm{d}H_L}{\mathrm{d}H_U} = P_{\mathrm{int}},\end{aligned}$$

where we have taken $\mathrm{d}H_L/\mathrm{d}H_L = 1$, $\mathrm{d}H/\mathrm{d}H_U = 0$, and $\mathrm{d}H_L/\mathrm{d}H_U = -1$, since $H = H_L + H_U$ and H is constant.

Applying the same technique to (A.2) and (A.3) yields

$$\frac{\mathrm{d}\widehat{H}_L}{\mathrm{d}H_L} = -A_L, \qquad \frac{\mathrm{d}\widehat{H}_U}{\mathrm{d}H_U} = A_U,$$
$$\frac{\mathrm{d}\widetilde{H}_L}{\mathrm{d}H_L} = H_L P_{\mathrm{int}}, \qquad \frac{\mathrm{d}\widetilde{H}_U}{\mathrm{d}H_U} = (H - H_U)P_{\mathrm{int}},$$

which leads to

$$\frac{\mathrm{d}\widehat{H}_L}{\mathrm{d}A_L} = \frac{\mathrm{d}\widehat{H}_L}{\mathrm{d}H_L}\left[\frac{\mathrm{d}A_L}{\mathrm{d}H_L}\right]^{-1} = -\frac{A_L}{P_{\mathrm{int}}}, \qquad \frac{\mathrm{d}\widehat{H}_U}{\mathrm{d}A_U} = \frac{\mathrm{d}\widehat{H}_U}{\mathrm{d}H_U}\left[\frac{\mathrm{d}A_U}{\mathrm{d}H_U}\right]^{-1} = \frac{A_U}{P_{\mathrm{int}}}, \tag{A.4}$$

$$\frac{\mathrm{d}\widetilde{H}_L}{\mathrm{d}A_L} = \frac{\mathrm{d}\widetilde{H}_L}{\mathrm{d}H_L}\left[\frac{\mathrm{d}A_L}{\mathrm{d}H_L}\right]^{-1} = H_L, \qquad \frac{\mathrm{d}\widetilde{H}_U}{\mathrm{d}A_U} = \frac{\mathrm{d}\widetilde{H}_U}{\mathrm{d}H_U}\left[\frac{\mathrm{d}A_U}{\mathrm{d}H_U}\right]^{-1} = H - H_U. \tag{A.5}$$

Since the mappings between A_L and H_L and between A_U and H_U are generally one-to-one, (A.4) can alternatively be written as

$$\frac{\mathrm{d}\widehat{H}_L}{\mathrm{d}A_L} = -A_L\frac{\mathrm{d}H_L}{\mathrm{d}A_L}, \qquad \frac{\mathrm{d}\widehat{H}_U}{\mathrm{d}A_U} = A_U\frac{\mathrm{d}H_U}{\mathrm{d}A_U}. \tag{A.6}$$

A similar calculation, in which we assume that H is constant with s, yields

$$\frac{\partial\widehat{H}_L}{\partial s} = -A_L\frac{\partial H_L}{\partial s}, \qquad \frac{\partial\widehat{H}_U}{\partial s} = -A_U\frac{\partial(H - H_U)}{\partial s}.$$

Finally, comparison to (A.5) yields

$$\frac{\partial \widehat{H}_L}{\partial s} = -A_L \frac{\partial}{\partial s}\left(\frac{\mathrm{d}\widetilde{H}_L}{\mathrm{d}A_L}\right), \qquad \frac{\partial \widehat{H}_U}{\partial s} = -A_U \frac{\partial}{\partial s}\left(\frac{\mathrm{d}\widetilde{H}_U}{\mathrm{d}A_U}\right), \tag{A.7}$$

and these geometric relations are critical to deriving the local energy conservation equation.

Two geometries of particular interest are the 2D channel and the circular pipe. For a 2D channel geometry, $w(h) = 1$, and the following substitutions can be made in the equations:

$$\begin{aligned} A_L &= H_L, & A_U &= H_U, \\ P_L &= 1, & P_U &= 1, \\ A &= H, & P_{\text{int}} &= 1. \end{aligned}$$

For a pipe geometry we have, as in [2],

$$\begin{aligned} H_L &= R(1-\cos(\theta)), & H_U &= R(1+\cos(\theta)), \\ P_L &= 2R\theta, & P_U &= 2R(\pi-\theta), \\ A &= \pi R^2, & P_{\text{int}} &= 2R\sin(\theta), \\ A_L &= R^2\left(\theta - \frac{1}{2}\sin(2\theta)\right), & A_U &= R^2\left(\pi - \theta + \frac{1}{2}\sin(2\theta)\right). \end{aligned}$$

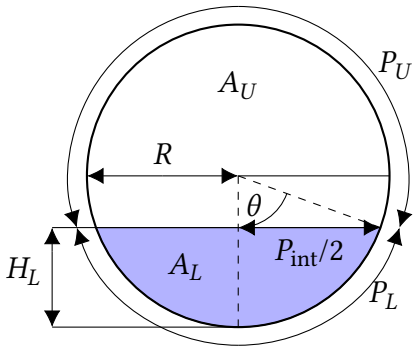

Figure A.1: A schematic of a circular pipe cross-section.

In Figure A.1 we show how the wetted angle θ is defined for the pipe geometry. If $\alpha = A_L/A$, then $\pi\alpha = \theta - \frac{1}{2}\sin(2\theta)$, and this equation must be solved iteratively in order to obtain θ from A_L, so that the remaining geometric quantities can be calculated. Alternatively, the following approximation can be used [12]:

$$\theta \approx \pi\alpha + \left(\frac{3\pi}{2}\right)^{1/3}\left(1 - 2\alpha + \alpha^{1/3} - (1-\alpha)^{1/3}\right) - \frac{1}{200}\alpha(1-\alpha)(1-2\alpha)\left[1 + 4\left(\alpha^2 + (1-\alpha)^2\right)\right].$$

The general geometric quantities $\widehat{H}_L$ and $\widehat{H}_U$ can also be evaluated for specific geometries. For a 2D channel geometry, (A.2) evaluates to

$$\widehat{H}_L = -\frac{1}{2}H_L^2, \qquad \widehat{H}_U = \frac{1}{2}H_U^2,$$

where we have substituted $H_L = H - H_U$. For the pipe geometry, we make the transformation $h = R(1-\cos(\theta^*))$, with θ^* the integration variable, to get [106]

$$\widehat{H}_L = \left[(R-H_L)A_L - \frac{1}{12}P_{\text{int}}^3\right], \qquad \widehat{H}_U = -\left[(R-H_U)A_U - \frac{1}{12}P_{\text{int}}^3\right].$$

The general geometric quantities that appear in the energy definition also have specific forms for different geometries. For the channel geometry, the general expressions (A.3) evaluate to

$$\widetilde{H}_L = \frac{1}{2}H_L^2, \qquad \widetilde{H}_U = \frac{1}{2}H_U^2 + H_U H_L.$$

For the pipe geometry the results are

$$\widetilde{H}_L = \left[RA_L - \frac{1}{12}P_{\text{int}}^3\right], \qquad \widetilde{H}_U = \left[RA_U + \frac{1}{12}P_{\text{int}}^3\right].$$

References

[1] R. Abgrall and S. Karni. Two-layer shallow water system: A relaxation approach. *SIAM Journal on Scientific Computing*, 31(3):1603–1627, 2009.

[2] A. H. Akselsen. *Efficient Numerical Methods for Waves in One-Dimensional Two-Phase Pipe Flows*. PhD thesis, Norwegian University of Science and Technology, Trondheim, 2016.

[3] A. Ashrafizadeh, C. B. Devaud, and N. U. Aydemir. A Jacobian-free Newton–Krylov method for thermalhydraulics simulations. *International Journal for Numerical Methods in Fluids*, 77(10):590–615, 2015.

[4] P. Aursand, M. Hammer, S. T. Munkejord, and Ø. Wilhelmsen. Pipeline transport of CO2 mixtures: Models for transient simulation. *International Journal of Greenhouse Gas Control*, 15:174–185, 2013.

[5] D. Barnea and Y. Taitel. Kelvin-Helmholtz stability criteria for stratified flow: Viscous versus non-viscous (inviscid) approaches. *International Journal of Multiphase Flow*, 19(4):639–649, 1993.

[6] D. Barnea and Y. Taitel. Interfacial and structural stability of separated flow. *International Journal of Multiphase Flow*, 20:387–414, 1994.

[7] K. H. Bendiksen, D. Maines, R. Moe, and S. Nuland. The dynamic two-fluid model OLGA: Theory and application. *SPE Production Engineering*, 6(2):171–180, 1991.

[8] R. A. Berry, L. Zou, H. Zhao, H. Zhang, J. W. Peterson, R. C. Martineau, S. Y. Kadioglu, and D. Andrs. RELAP-7 Theory Manual. Technical Report INL/EXT-14-31366, Idaho National Laboratory, 2014.

[9] D. Bestion. The physical closure laws in the CATHARE code. *Nuclear Engineering and Design*, 124:229–245, 1990.

[10] D. Bestion. The phase appearance and disappearance in the CATHARE code. In *Proceedings of the Workshop on Trends in Numerical and Physical Modelling for Industrial Multiphase Flows*, Cargèse, France, 2000.

[11] D. Bestion. The structure of system thermal-hydraulic (SYS-TH) code for nuclear energy applications. In F. D'Auria, editor, *Thermal-Hydraulics of Water Cooled Nuclear Reactors*, pages 639–727. Woodhead Publishing, 2017.

[12] D. Biberg. An explicit approximation for the wetted angle in two-phase stratified pipe flow. *The Canadian Journal of Chemical Engineering*, 77(6):1221–1224, 1999.

[13] M. Bonizzi. *Transient One-Dimensional Modelling of Multiphase Slug Flows*. PhD thesis, Imperial College London, United Kingdom, 2003.

[14] A. Bonzanini, D. Picchi, and P. Poesio. Simplified 1D incompressible two-fluid model with artificial diffusion for slug flow capturing in horizontal and nearly horizontal pipes. *Energies*, 10(9):1372, 2017.

[15] F. Bouchut and T. Morales de Luna. An entropy satisfying scheme for two-layer shallow water equations with uncoupled treatment. *ESAIM: Mathematical Modelling and Numerical Analysis*, 42(4):683–698, 2008.

[16] F. Bouchut and V. Zeitlin. A robust well-balanced scheme for multi-layer shallow water equations. *Discrete & Continuous Dynamical Systems - B*, 13(4):739, 2010.

[17] N. Brauner and D. Moalem Maron. Stability analysis of stratified liquid-liquid flow. *International Journal of Multiphase Flow*, 18(1):103–121, 1992.

[18] J. Buist, B. Sanderse, Y. van Halder, B. Koren, and G. van Heijst. Machine learning for closure models in multiphase flow applications. In *Proceedings of the 3rd International Conference on Uncertainty Quantification in Computational Sciences and Engineering (UNCECOMP 2019)*, pages 379–399, Crete, Greece, 2019.

[19] J. F. H. Buist. Machine Learning for Closure Models in Multiphase-Flow Applications. Master's thesis, Eindhoven University of Technology, The Netherlands, 2019.

[20] J. F. H. Buist, B. Sanderse, S. Dubinkina, R. A. W. M. Henkes, and C. W. Oosterlee. Energy-conserving formulation of the two-fluid model for incompressible two-phase flow in channels and pipes. *Computers & Fluids*, 244:105533, 2022.

[21] J. F. H. Buist, B. Sanderse, S. Dubinkina, C. W. Oosterlee, and R. A. W. M. Henkes. Energy-consistent formulation of the pressure-free two-fluid model. *International Journal for Numerical Methods in Fluids*, 95(5):869–898, 2023.

[22] J. F. H. Buist, B. Sanderse, S. Dubinkina, C. W. Oosterlee, and R. A. W. M. Henkes. Energy-stable discretization of the one-dimensional two-fluid model. *International Journal of Multiphase Flow*, 174:104756, 2024.

[23] J. C. Butcher. *Numerical Methods for Ordinary Differential Equations*. Wiley, Chichester, England, 2003.

[24] M. J. Castro, U. S. Fjordholm, S. Mishra, and C. Parés. Entropy conservative and entropy stable schemes for nonconservative hyperbolic systems. *SIAM Journal on Numerical Analysis*, 51(3):1371–1391, 2013.

[25] M. J. Castro-Díaz, E. D. Fernández-Nieto, J. M. González-Vida, and C. Parés-Madroñal. Numerical treatment of the loss of hyperbolicity of the two-layer shallow-water system. *Journal of Scientific Computing*, 48(1):16–40, 2011.

[26] J. Chahed, V. Roig, and L. Masbernat. Eulerian–Eulerian two-fluid model for turbulent gas–liquid bubbly flows. *International Journal of Multiphase Flow*, 29(1):23–49, 2003.

[27] A. Chiapolino and R. Saurel. Models and methods for two-layer shallow water flows. *Journal of Computational Physics*, 371:1043–1066, 2018.

[28] S. W. Churchill. Friction factor equation spans all fluid flow regimes. *Chemical Engineering*, 84:91–92, 1977.

[29] G. Coppola, F. Capuano, and L. de Luca. Discrete energy-conservation properties in the numerical simulation of the Navier–Stokes equations. *Applied Mechanics Reviews*, 71(1):010803, 2019.

[30] R. Courant and D. Hilbert. *Methods of Mathematical Physics*, volume 2. Wiley, Singapore, 1962.

[31] B. Cushman-Roisin. Environmental Fluid Mechanics. Available online at: `https://cushman.host.dartmouth.edu/books/EFM.html`, last accessed on 22-11-2023.

[32] C. M. Dafermos. *Hyperbolic Conservation Laws in Continuum Physics*. Springer, Berlin, 3rd edition, 2010.

[33] T. J. Danielson and K. M. Bansal. LEDA: The next multiphase flow performance simulator. In *Proceedings of the 12th International Conference on Multiphase Production Technology*, pages 477–492, Barcelona, Spain, 2005.

[34] T. N. Dinh, R. R. Nourgaliev, and T. G. Theofanous. Understanding the ill-posed two-fluid model. In *Proceedings of the 10th International Topical Meeting on Nuclear Reactor Thermal Hydraulics (NURETH-10)*, Seoul, Korea, 2003.

[35] D. A. Drew and S. L. Passman. *Theory of Multicomponent Fluids*. Springer, New York, 1999.

[36] A. Etrati and I. A. Frigaard. A two-layer model for buoyant inertial displacement flows in inclined pipes. *Physics of Fluids*, 30(2):022107, 2018.

[37] S. Evje and T. Flåtten. Hybrid flux-splitting schemes for a common two-fluid model. *Journal of Computational Physics*, 192(1):175–210, 2003.

[38] J. Fabre. Gas-Liquid Slug Flow. In V. Bertola, editor, *Modelling and Experimentation in Two-Phase Flow*, pages 117–156. Springer, Vienna, 2003.

[39] I. Faille and E. Heintzé. A rough finite volume scheme for modeling two-phase flow in a pipeline. *Computers & Fluids*, 28(2):213–241, 1999.

[40] J. H. Ferziger and M. Perić. *Computational Methods for Fluid Dynamics*. Springer, Berlin, 3rd edition, 2002.

[41] U. S. Fjordholm. Energy Conservative and Stable Schemes for the Two-layer Shallow Water Equations. In *Hyperbolic Problems*, volume 17 & 18 of *Series in Contemporary Applied Mathematics*, pages 414–421. World Scientific Publishing, 2012.

[42] U. S. Fjordholm, S. Mishra, and E. Tadmor. Energy Preserving and Energy Stable Schemes for the Shallow Water Equations. In F. Cucker, A. Pinkus, and M. J. Todd, editors, *Foundations of Computational Mathematics, Hong Kong 2008*, pages 93–139. Cambridge University Press, 2009.

[43] U. S. Fjordholm, S. Mishra, and E. Tadmor. Well-balanced and energy stable schemes for the shallow water equations with discontinuous topography. *Journal of Computational Physics*, 230(14):5587–5609, 2011.

[44] W. Fullmer, M. Lopez de Bertodano, and V. H. Ransom. The Kelvin-Helmholtz instability: Comparisons of one- and two-dimensional simulations. In *Proceedings of the 14th International Topical Meeting on Nuclear Reactor Thermal Hydraulics (NURETH-14)*, Toronto, Canada, 2011.

[45] W. D. Fullmer, S. Y. Lee, and M. A. Lopez de Bertodano. An artificial viscosity for the ill-posed one-dimensional incompressible two-fluid model. *Nuclear Technology*, 185(3):296–308, 2014.

[46] W. D. Fullmer, V. H. Ransom, and M. A. Lopez de Bertodano. Linear and nonlinear analysis of an unstable, but well-posed, one-dimensional two-fluid model for two-phase flow based on the inviscid Kelvin–Helmholtz instability. *Nuclear Engineering and Design*, 268:173–184, 2014.

[47] G. J. Gassner, A. R. Winters, and D. A. Kopriva. A well balanced and entropy conservative discontinuous Galerkin spectral element method for the shallow water equations. *Applied Mathematics and Computation*, 272:291–308, 2016.

[48] A. Goldszal, T. J. Danielson, K. M. Bansal, Z. L. Yang, S. T. Johansen, and G. Depay. LedaFlow 1D: Simulation results with multiphase gas/condensate and oil/gas field data. In *Proceedings of the 13th International Conference on Multiphase Production Technology*, pages 17–31, Edinburgh, United Kingdom, 2007.

[49] L. E. Gomez, O. Shoham, Z. Schmidt, R. N. Chokshi, A. Brown, and T. Northug. A unified mechanistic model for steady-state two-phase flow in wellbores and pipelines. In *Proceedings of the SPE Annual Technical Conference and Exhibition*, page 56520, Houston, Texas, 1999.

[50] B. Gustafsson, H.-O. Kreiss, and J. Oliger. *Time Dependent Problems and Difference Methods*. Wiley, Hoboken, New Jersey, 2nd edition, 2013.

[51] F. Ham, K. Mattsson, G. Iaccarino, and P. Moin. Towards Time-Stable and Accurate LES on Unstructured Grids. In S. C. Kassinos, C. A. Langer, G. Iaccarino, and P. Moin, editors, *Complex Effects in Large Eddy Simulations*, pages 235–249. Springer, Berlin, 2007.

[52] F. E. Ham, F. S. Lien, and A. B. Strong. A fully conservative second-order finite difference scheme for incompressible flow on nonuniform grids. *Journal of Computational Physics*, 177(1):117–133, 2002.

[53] C. Hirsch. *Numerical Computation of Internal and External Flows: Fundamentals of Computational Fluid Dynamics*, volume 1. Butterworth-Heinemann, Oxford, United Kingdom, 2nd edition, 2007.

[54] H. Holmås. *Numerical Simulation of Waves in Two-Phase Pipe Flow Using 1D Two-Fluid Models*. PhD thesis, University of Oslo, Norway, 2008.

[55] H. Holmås. Numerical simulation of transient roll-waves in two-phase pipe flow. *Chemical Engineering Science*, 65(5):1811–1825, 2010.

[56] H. Holmås, T. Sira, M. Nordsveen, H. P. Langtangen, and R. Schulkes. Analysis of a 1D incompressible two-fluid model including artificial diffusion. *IMA Journal of Applied Mathematics*, 73(4):651–667, 2008.

[57] M. Ishii. *Thermo-Fluid Dynamic Theory of Two-Phase Flow*. Eyrolles, Paris, 1975.

[58] M. Ishii and T. Hibiki. *Thermo-Fluid Dynamics of Two-Phase Flow*. Springer, New York, 2nd edition, 2011.

[59] M. Ishii and K. Mishima. Two-fluid model and hydrodynamic constitutive relations. *Nuclear Engineering and Design*, 82:107–126, 1984.

[60] R. I. Issa and M. H. W. Kempf. Simulation of slug flow in horizontal and nearly horizontal pipes with the two-fluid model. *International Journal of Multiphase Flow*, 29(1):69–95, 2003.

[61] A. Jameson. The construction of discretely conservative finite volume schemes that also globally conserve energy or entropy. *Journal of Scientific Computing*, 34(2):152–187, 2008.

[62] A. Jameson. Formulation of kinetic energy preserving conservative schemes for gas dynamics and direct numerical simulation of one-dimensional viscous compressible flow in a shock tube using entropy and kinetic energy preserving schemes. *Journal of Scientific Computing*, 34(2):188–208, 2008.

[63] G. W. Johnson. *A Study of Stratified Gas-Liquid Pipe Flow*. PhD thesis, University of Oslo, Norway, 2005.

[64] A. V. Jones and A. Prosperetti. On the suitability of first-order differential models for two-phase flow prediction. *International Journal of Multiphase Flow*, 11(2):133–148, 1985.

[65] B. L. Keyfitz. Mathematical properties of nonhyperbolic models for incompressible two-phase flow. In *Proceedings of the ICMF*, New Orleans, Louisiana, 2001.

[66] B. L. Keyfitz, R. Sanders, and M. Sever. Lack of hyperbolicity in the two-fluid model for two-phase incompressible flow. *Discrete and Continuous Dynamical Systems - B*, 3(4):541–563, 2003.

[67] B. I. Krasnopolsky and A. A. Lukyanov. A conservative fully implicit algorithm for predicting slug flows. *Journal of Computational Physics*, 355:597–619, 2018.

[68] H.-O. Kreiss and J. Lorenz. *Initial-Boundary Value Problems and the Navier-Stokes Equations*. Number 47 in Classics in Applied Mathematics. Society for Industrial and Applied Mathematics, Philadelphia, Pennsylvania, 2004.

[69] H.-O. Kreiss and J. Yström. Parabolic problems which are ill-posed in the zero dissipation limit. *Mathematical and Computer Modelling*, 35(11):1271–1295, 2002.

[70] H.-O. Kreiss and J. Yström. A note on viscous conservation laws with complex characteristics. *BIT Numerical Mathematics*, 46(S1):55–59, 2006.

[71] P. K. Kundu, I. M. Cohen, D. R. Dowling, and G. Tryggvason. *Fluid Mechanics*. Academic Press, 6th edition, 2016.

[72] P. D. Lax and R. D. Richtmyer. Survey of the stability of linear finite difference equations. *Communications on Pure and Applied Mathematics*, 9(2):267–293, 1956.

[73] R. J. Leveque. *Finite Volume Methods for Hyperbolic Problems*. Cambridge University Press, United Kingdom, 2002.

[74] J. Liao, R. Mei, and J. F. Klausner. A study on the numerical stability of the two-fluid model near ill-posedness. *International Journal of Multiphase Flow*, 34(11):1067–1087, 2008.

[75] M.-S. Liou, L. Nguyen, C.-H. Chang, S. Sushchikh, R. Nourgaliev, and T. Theofanous. Hyperbolicity, discontinuities, and numerics of two-fluid models. In H. Deconinck and E. Dick, editors, *Proceedings of the Fourth International Conference on Computational Fluid Dynamics (ICCFD4)*, pages 625–630, Ghent, Belgium, 2006.

[76] M. López de Bertodano, W. Fullmer, A. Clausse, and V. H. Ransom. *Two-Fluid Model Stability, Simulation and Chaos*. Springer International Publishing, Cham, Switzerland, 2017.

[77] M. Lopez de Bertodano, W. D. Fullmer, and A. Clausse. One-dimensional two-fluid model for wavy flow beyond the Kelvin–Helmholtz instability: Limit cycles and chaos. *Nuclear Engineering and Design*, 310:656–663, 2016.

[78] M. Louaked, L. Hanich, and C. P. Thompson. Well-posedness of incompressible models of two- and three-phase flow. *IMA Journal of Applied Mathematics*, 68:595–620, 2003.

[79] R. Lteif. Well-balanced numerical resolution of the two-layer shallow water equations under rigid-lid with wet–dry fronts. *Computers & Fluids*, 235:105277, 2022.

[80] R. W. Lyczkowski. *The History of Multiphase Science and Computational Fluid Dynamics*. Mechanical Engineering Series. Springer, Cham, Switzerland, 2018.

[81] R. W. Lyczkowski, D. Gidaspow, C. W. Solbrig, and E. D. Hughes. Characteristics and stability analyses of transient one-dimensional two-phase flow equations and their finite difference approximations. *Nuclear Science and Engineering*, 66(3):378–396, 1978.

[82] J. M. Mandhane, G. A. Gregory, and K. Aziz. A flow pattern map for gas-liquid flow in horizontal pipes. *International Journal of Multiphase Flow*, 1(4):537–553, 1974.

[83] J. M. Masella, Q. H. Tran, D. Ferre, and C. Pauchon. Transient simulation of two-phase flows in pipes. *International Journal of Multiphase Flow*, 24(5):739–755, 1998.

[84] R. M. M. Mattheij, S. W. Rienstra, and J. H. M. Ten Thije Boonkkamp. *Partial Differential Equations: Modeling, Analysis, Computation*. Number 10 in SIAM Monographs on Mathematical Modeling and Computation. Society for Industrial and Applied Mathematics, Philadelphia, Pennsylvania, 2005.

[85] M. L. Merriam. An entropy-based approach to nonlinear stability. Technical Memorandum 101086, NASA, 1989.

[86] P. Milewski, E. Tabak, C. Turner, R. Rosales, and F. Menzaque. Nonlinear stability of two-layer flows. *Communications in Mathematical Sciences*, 2(3):427–442, 2004.

[87] M. Montini. *Closure Relations of the One-Dimensional Two-Fluid Model for the Simulation of Slug Flows*. PhD thesis, Imperial College London, United Kingdom, 2011.

[88] C. Morel. *Mathematical Modeling of Disperse Two-Phase Flows*, volume 114 of *Fluid Mechanics and Its Applications*. Springer International Publishing, Cham, Switzerland, 2015.

[89] K. W. Morton and D. F. Mayers. *Numerical Solution of Partial Differential Equations*. Cambridge University Press, United Kingdom, 2nd edition, 2005.

[90] S. T. Munkejord. *Analysis of the Two-Fluid Model and the Drift-Flux Model for Numerical Calculation of Two-Phase Flow*. PhD thesis, Norwegian University of Science and Technology, Trondheim, 2006.

[91] H. Ockendon and J. R. Ockendon. How to mitigate sloshing. *SIAM Review*, 59(4):905–911, 2017.

[92] C. Omgba-Essama. *Numerical Modelling of Transient Gas-Liquid Flows (Application to Stratified & Slug Flow Regimes)*. PhD thesis, Cranfield University, United Kingdom, 2004.

[93] C. L. Pauchon, H. Dhulesia, G. Binh-Cirlot, and J. Fabre. TACITE: A transient tool for multiphase pipeline and well simulation. In *Proceedings of the SPE 69th Annual Technical Conference and Exhibition*, pages 311–326, New Orleans, Louisiana, 1994.

[94] A. Prosperetti and A. V. Jones. The linear stability of general two-phase flow models—II. *International Journal of Multiphase Flow*, 13(2):161–171, 1987.

[95] A. Prosperetti and G. Tryggvason. *Computational Methods for Multiphase Flow*. Cambridge University Press, 2007.

[96] J. D. Ramshaw and J. A. Trapp. Characteristics, stability, and short-wavelength phenomena in two-phase flow equation systems. *Nuclear Science and Engineering*, 66:93–102, 1978.

[97] V. H. Ransom and D. L. Hicks. Hyperbolic two-pressure models for two-phase flow. *Journal of Computational Physics*, 53(1):124–151, 1984.

[98] D. Ray, P. Chandrashekar, U. S. Fjordholm, and S. Mishra. Entropy stable scheme on two-dimensional unstructured grids for Euler equations. *Communications in Computational Physics*, 19(5):1111–1140, 2016.

[99] R. A. Remmerswaal. *Numerical Modelling of Variability in Liquid Impacts*. PhD thesis, University of Groningen, The Netherlands, 2023.

[100] R. D. Richtmyer and K. W. Morton. *Difference Methods for Initial-Value Problems*. Interscience Publishers, New York, 2nd edition, 1967.

[101] W. Rozema. *Low-Dissipation Methods and Models for the Simulation of Turbulent Subsonic Flow*. PhD thesis, University of Groningen, The Netherlands, 2015.

[102] B. Sanderse. *Energy-Conserving Discretization Methods for the Incompressible Navier-Stokes Equations*. PhD thesis, Eindhoven University of Technology, The Netherlands, 2013.

[103] B. Sanderse. Energy-conserving Runge–Kutta methods for the incompressible Navier–Stokes equations. *Journal of Computational Physics*, 233:100–131, 2013.

[104] B. Sanderse. Governing equations of single- and multi-phase flow in one-dimensional pipelines. Technical Report SR.13.13992, Shell Global Solutions International, Amsterdam, The Netherlands, 2013.

[105] B. Sanderse, J. F. H. Buist, and R. A. W. M. Henkes. A novel pressure-free two-fluid model for one-dimensional incompressible multiphase flow. *Journal of Computational Physics*, 426:109919, 2021.

[106] B. Sanderse, I. E. Smith, and M. H. W. Hendrix. Analysis of time integration methods for the compressible two-fluid model for pipe flow simulations. *International Journal of Multiphase Flow*, 95:155–174, 2017.

[107] B. Sanderse and A. E. P. Veldman. Constraint-consistent Runge–Kutta methods for one-dimensional incompressible multiphase flow. *Journal of Computational Physics*, 384:170–199, 2019.

[108] J. Shaha. *Phase Interactions in Transient Stratified Flow*. PhD thesis, Imperial College London, United Kingdom, 1999.

[109] J. H. Song and M. Ishii. The well-posedness of incompressible one-dimensional two-fluid model. *International Journal of Heat and Mass Transfer*, 43(12):2221–2231, 2000.

[110] J. H. Song and M. Ishii. On the stability of a one-dimensional two-fluid model. *Nuclear Engineering and Design*, 204:101–115, 2001.

[111] H. B. Stewart and B. Wendroff. Two-phase flow: Models and methods. *Journal of Computational Physics*, 56(3):363–409, 1984.

[112] B. Straughan. *The Energy Method, Stability, and Nonlinear Convection*. Springer, New York, 2nd edition, 2004.

[113] J. C. Strikwerda. *Finite Difference Schemes and Partial Differential Equations*. Society for Industrial and Applied Mathematics, Philadelphia, Pennsylvania, 2nd edition, 2004.

[114] E. Tadmor. Entropy stability theory for difference approximations of nonlinear conservation laws and related time-dependent problems. *Acta Numerica*, 12:451–512, 2003.

[115] E. Tadmor and W. Zhong. Energy-Preserving and Stable Approximations for the Two-Dimensional Shallow Water Equations. In H. Munthe-Kaas and B. Owren, editors, *Mathematics and Computation, a Contemporary View*, volume 3, pages 67–94. Springer, Berlin, 2008.

[116] Y. Taitel and A. E. Dukler. A model for predicting flow regime transitions in horizontal and near horizontal gas-liquid flow. *AIChE Journal*, 22(1):47–55, 1976.

[117] S. A. Thorpe. Experiments on the instability of stratified shear flows: Immiscible fluids. *Journal of Fluid Mechanics*, 39(1):25–48, 1969.

[118] E. F. Toro. *Riemann Solvers and Numerical Methods for Fluid Dynamics: A Practical Introduction*. Springer, Berlin, 1999.

[119] G. Tryggvason, R. Scardovelli, and S. Zaleski. *Direct Numerical Simulations of Gas-Liquid Multiphase Flows*. Cambridge University Press, 2011.

[120] G. K. Vallis. *Essentials of Atmospheric and Oceanic Dynamics*. Cambridge University Press, 2019.

[121] M. van Reeuwijk. A mimetic mass, momentum and energy conserving discretization for the shallow water equations. *Computers & Fluids*, 46(1):411–416, 2011.

[122] B. van 't Hof and A. E. P. Veldman. Mass, momentum and energy conserving (MaMEC) discretizations on general grids for the compressible Euler and shallow water equations. *Journal of Computational Physics*, 231(14):4723–4744, 2012.

[123] B. van 't Hof and M. J. Vuik. Symmetry-preserving finite-difference discretizations of arbitrary order on structured curvilinear staggered grids. *Journal of Computational Science*, 36:101008, 2019.

[124] A. E. P. Veldman. A general condition for kinetic-energy preserving discretization of flow transport equations. *Journal of Computational Physics*, 398:108894, 2019.

[125] A. E. P. Veldman. Supraconservative finite-volume methods for the Euler equations of subsonic compressible flow. *SIAM Review*, 63(4):756–779, 2021.

[126] R. W. C. P. Verstappen and A. E. P. Veldman. Symmetry-preserving discretization of turbulent flow. *Journal of Computational Physics*, 187(1):343–368, 2003.

[127] G. B. Wallis. *One-Dimensional Two-Phase Flow*. McGraw-Hill, New York, 1969.

[128] J. R. Welty, G. L. Rorrer, and D. G. Foster. *Fundamentals of Momentum, Heat and Mass Transfer*. Wiley, Singapore, 6th edition, 2015.

[129] P. Wesseling. *Principles of Computational Fluid Dynamics*. Springer, Berlin, 2001.

[130] G. B. Whitham. *Linear and Nonlinear Waves*. Wiley, New York, 1999.

[131] L. Zou, H. Zhao, and H. Zhang. Implicitly solving phase appearance and disappearance problems using two-fluid six-equation model. *Progress in Nuclear Energy*, 88:198–210, 2016.

[132] N. Zuber and J. A. Findlay. Average volumetric concentration in two-phase flow systems. *Journal of Heat Transfer*, 87(4):453–468, 1965.

Curriculum Vitae

Jurriaan Frederick Hubert Buist

26-07-1995 Born in Boxmeer, The Netherlands

Education

2007–2013 Voorbereidend Wetenschappelijk Onderwijs (VWO)
2College Durendael, Oisterwijk

2013–2016 Bachelor of Science in Applied Physics
Eindhoven University of Technology

2016–2019 Master of Science in Applied Physics (cum laude)
Eindhoven University of Technology

2019–2024 PhD Candidate
Centrum Wiskunde & Informatica, Delft University of Technology

List of Publications

- J. F. H. Buist, B. Sanderse, S. Dubinkina, C. W. Oosterlee, and R. A. W. M. Henkes. Energy-stable discretization of the one-dimensional two-fluid model. *International Journal of Multiphase Flow*, 174:104756, 2024.
- J. F. H. Buist, B. Sanderse, S. Dubinkina, C. W. Oosterlee, and R. A. W. M. Henkes. Energy-consistent formulation of the pressure-free two-fluid model. *International Journal for Numerical Methods in Fluids*, 95(5):869–898, 2023.
- J. F. H. Buist, B. Sanderse, S. Dubinkina, R. A. W. M. Henkes, and C. W. Oosterlee. Energy-conserving formulation of the two-fluid model for incompressible two-phase flow in channels and pipes. *Computers & Fluids*, 244:105533, 2022.
- B. Sanderse, J. F. H. Buist, and R. A. W. M. Henkes. A novel pressure-free two-fluid model for one-dimensional incompressible multiphase flow. *Journal of Computational Physics*, 426:109919, 2021.
- J. Buist, B. Sanderse, Y. van Halder, B. Koren, and G. van Heijst. Machine learning for closure models in multiphase flow applications. In *Proceedings of the 3rd International Conference on Uncertainty Quantification in Computational Sciences and Engineering (UNCECOMP 2019)*, pages 379–399, 2019.